Modeling the Alaskan Continental Shelf Waters

Shiao-Kung Liu, J. J. Leendertse

RAND

The research described in this report was sponsored by the National Oceanic and Atmospheric Administration under Contract 03-6-022-35249. Preparation of this report was funded by The RAND Corporation as part of its program of public service.

ISBN: 0-8330-0827-7

Published by The RAND Corporation
1700 Main Street, P.O. Box 2138, Santa Monica, CA 90406-2138

R-3567-NOAA/RC

Modeling the Alaskan Continental Shelf Waters

Shiao-Kung Liu, J. J. Leendertse

October 1987

Prepared for the
National Oceanic and Atmospheric Administration

RAND

PREFACE

This report gives an account of studies made over a period of six years under a contract between the National Oceanic and Atmospheric Administration (NOAA) and The RAND Corporation. Preparation of this report was funded by The RAND Corporation.

RAND's initial modeling studies supported investigations made by other scientists of NOAA and universities concerning the physical processes in and on the waters of the Alaskan outer continental shelf. Gradually it became clear that probabilistic oil spill trajectory simulations directly usable in impact analysis were needed in addition to the field investigations of physical oceanographic processes. Efforts were then redirected from a scientific modeling study (aiming to obtain a better understanding of the complicated hydrodynamic processes of the Alaskan continental shelf) to analysis and simulations directly usable for impact assessments. Most of the study results were submitted in digital form to the Minerals Management Service.

In modeling studies made to better understand the physical processes, generally only a limited part of the system is modeled. This type of modeling is well understood and accepted by most, since the physical processes can be quite clearly formulated in mathematical expressions. Modeling for impact assessments and policy analysis is different. Here, scenarios have to be selected and processes have to be screened as to their relevance in the final results, and the modeling requires the execution of a large number of modeling steps in sequence.

Few modeling studies of this type have been made for the environmental impact assessment of Arctic waters. For this reason, in this report the authors particularly emphasize descriptions of the processes that were included and how these processes are incorporated in the overall analysis. Thus with this study the authors intend to support the environmental impact assessments made by others by stating what was considered here and how all of the results have been combined.

In making the analyses reported here, the authors made extensive use of computer simulations, but most of the critical analyses were made by conventional means. The analyses of the Alaskan coastal system have been more difficult and tedious than other analyses made of other coastal areas. The primary reason for this difficulty has been the lack of field data. For example, parts of the Beaufort Sea beneath the permanent polar ice cap are not charted. Carrying out a monitoring program in the large remote offshore areas of Alaska is difficult and expensive, particularly as the presence of sea ice poses unique problems. Many instrument packages were lost during the data collection efforts.

Even with these difficulties, the modeling studies have been very rewarding to the authors. Many times the analyses were confirmed by field data collected after a certain area had been modeled.

The authors found the hydrodynamic and weather systems in the study areas very complicated, but valued the opportunity to study the major dynamic processes involved. Obviously, there is still much to be learned about the hydrodynamics of one of the widest continental shelves in the world.

SUMMARY

This report presents the development of three-dimensional numerical models of the Bering Sea, the Chukchi Sea, the Beaufort Sea, and the Gulf of Alaska. These models are formulated on ellipsoidal horizontal grids and variable vertical grids covering a total area of more than three million square kilometers and slightly more than half of the entire U.S. coastline.

The hydrodynamic model is coupled to a two-dimensional stochastic weather model and an oil spill trajectory/weathering model. The former also simulates stochastically the cyclogenetic/cyclolytic processes within the modeled area.

The report also compares the computed results with available field data. These include tides, baroclinic circulation, ice distribution/movement, and the partition of kinetic energetics in the frequency domain.

ACKNOWLEDGMENTS

The study was supported by the Minerals Management Service, Department of the Interior, through an interagency agreement with the National Oceanic and Atmospheric Administration, under which a multiyear program responding to the needs of petroleum development of the Alaskan continental shelf is managed by the Outer Continental Shelf Environmental Assessment Program (OCSEAP) office.

The execution of this study would not have been possible without our RAND colleague A. B. Nelson. With much skill he prepared the programs and the numerous program modifications that were used in the analyses. We thank him for his effort and for the time he spent at RAND outside normal office hours to accomplish his tasks and to meet the close deadlines imposed by the project.

The report was reviewed by five anonymous reviewers outside RAND and also by RAND colleagues F. Murray and M. Juncosa. We would like to thank them for their efforts.

We also want to thank Geni R. Coughlan who expertly and professionally prepared the drafts and final report with great patience.

CONTENTS

PREFACE iii

SUMMARY v

ACKNOWLEDGMENTS vii

FIGURES xi

TABLES xvii

Chapter

1. INTRODUCTION 1

2. THE THREE-DIMENSIONAL MODELING SYSTEM 3

3. MODELING COASTAL HYDRODYNAMIC PROCESSES 15
   - Modeling Tides, Residuals, and Baroclinic Circulation in the Alaskan Outer Continental Shelf 15
   - Modeling Tides in the Gulf of Alaska Shelf 17
   - Modeling Tides in the Eastern Bering Sea 27
   - Modeling Tides in the Chukchi Sea 33
   - Modeling Tides in the Beaufort Sea 36
   - Modeling Wind-Induced Circulations 39
   - Modeling the Density Field and the Residual Circulation 41

4. MODELING WIND FIELDS 60
   - Stochastic Analysis of Regional Weather System 60
   - Modeling Wind Speed and Direction 62
   - Modeling Storms 67
   - Computing Cyclonic Surface Wind 71

5. MODELING PACK ICE MOVEMENTS 79
   - Objectives 79
   - Ice Conditions and the Dynamics of Ice Pack 79
   - Computational Formulas and Data Requirements 81
   - Ice/Water Interaction under the Forces of Wind and Currents 86

6. MODELING OIL TRAJECTORIES 91
   - Objectives 91
   - The Modeling Approach for Long Duration Wind Driven Currents 91
   - Computing Oil Behavior under Ice 92
   - Modeling Oil Spill Trajectories 95
   - Determining the Oil Concentration Field 105

7. CONCLUSIONS 118

Appendix: COMPUTED RESIDUAL CURRENTS IN THE BERING AND CHUKCHI SEAS 121

BIBLIOGRAPHY 127

FIGURES

2.1. Location of variables 4
2.2. Comparison of mean flow velocity component u, computed by numerical method, to nonviscous fluid, computed by analytical solution 10
2.3. Vertical distribution of velocity component u in the middle of the homogeneous oscillating basin (logarithmic vertical scale) 10
2.4. Driven only with M2 tide (monochromatic wave) at the open boundary, the proposed numerical scheme can produce the cascade of energy distribution according to the universal "minus five-third" through the model's nonlinear advective process (Hinze, 1959) 12
2.5. For the stratified fluid, the computed spectra of the vertical displacements (in the surface layer, within pycnocline and near bottom) and significant energy distribution agree with the observed spectra of the first mode of internal waves (Gordon, 1978) 12
2.6. When driven with the predicted tide, the computed subsurface currents in the Bering Sea agree fairly well with the observed subsurface currents, both in magnitude and in direction (Liu and Leendertse, 1979) 13
2.7. Comparison of relative turbulence intensities between the three-dimensional model for stratified flow field and the standard verification curve of air flow measured in a pipe (Laufer, 1954) 14
3.1. Coverage of the Alaskan coastal area by various models and submodels 16
3.2. A submodel of the Bering Sea covering the area of Bristol Bay and a portion of the Gulf of Alaska. Insert map at the lower right corner is another submodel of this one, covering the area of Izembak Lagoon 18
3.3. The rise and fall of water levels and the computed tidal currents in the model of the western Gulf of Alaska. The figure illustrates the falling of water level (□) over the shelf and within part of the Cook Inlet. In the meantime, the water level near Anchorage is still rising (+) 19
3.4. Three-dimensional perspective diagrams illustrate the along-shore view of higher modes in the water-level variation with the highest point at the head of Cook Inlet near Anchorage (upper diagram). The lower diagram shows the cross-shore variation 20
3.5. Computed co-tidal chart for the semidiurnal component (primarily M2). Each 10° in phase represents approximately 20 minutes lag relative to the Greenwich mean phase. The maximum tidal amplitudes, reaching 250 cm, are found in the Cook Inlet 21
3.6. The computed east-west velocity components at six representative layers near the mouth of Cook Inlet (Portlock Bank) 22
3.7. The computed north-south velocity components at six representative layers near the mouth of Cook Inlet (Portlock Bank) 22
3.8. The computed vertical velocity components at six representative layers near the mouth of Cook Inlet (Portlock Bank) 23
3.9. The computed turbulent energy densities at six representative layers near the mouth of Cook Inlet (Portlock Bank) 23
3.10. Comparison between the computed hodograph and the measured surface tidal current ellipse 24
3.11. Vertical distribution of magnitude of the computed currents illustrated in the hodograph (near Cook Inlet) 24

3.12. Computed tidal ellipses (at 5 m level) in the Gulf of Alaska using a plotting scale of 200 cm/sec per grid spacing. Maximum tidal excursions are found in the middle of Cook Inlet where the tidal currents can reach 140 cm/sec in either direction. Currents over the shelf break near Kodiak are of elliptical rotary-type and can reach a maximum speed of 70 cm/sec 25
3.13. Computed tidal residual circulation (at 5 m level) in the Gulf of Alaska using a plotting scale of 5 cm/sec per computational grid. Maximum residual current in the middle of Cook Inlet can reach a speed of 7.5 cm/sec, which is approximately 5.5 percent of the local maximum tidal current. Over the shelf break and in the Shalikof Strait, residual currents flow primarily toward the southwest 26
3.14. Bathymetric schematization of the three-dimensional model of the Bering and Chukchi Seas 28
3.15. Computed instantaneous tidal currents and water-level distributions in the Bering/Chukchi Sea system. + denotes that water level rises; □ indicates that local water level falls 29
3.16. Computed co-tidal chart for the semidiurnal tidal component using the three-dimensional model of the Bering/Chukchi Sea 30
3.17. Co-tidal chart for the semidiurnal tidal component M2 compiled by NOAA according to existing data 30
3.18. Computed co-tidal chart for the diurnal tidal component using the three-dimensional model of the Bering/Chukchi Seas 31
3.19. Co-tidal chart for the diurnal tidal component (K1) compiled by NOAA according to existing data 31
3.20. Computed 12.5 hr tidal ellipses in the first layer (at 2.5 m level) using a plotting scale of 86 cm/sec per horizontal grid spacing 32
3.21. Computed velocities (U = E/W, V = N/S components) in six representative layers at a station in the Bering Strait 34
3.22. Computed vertical velocity (w) and the turbulent energy intensities in six representative layers at a station in the Bering Strait 34
3.23. Computed horizontal tidal velocity components (u = E/W, v = N/S) at station NC6 35
3.24. Computed vertical tidal velocity component w and tide-induced sub-grid-scale energy densities at station NC6 35
3.25. Computed co-tidal chart for the semidiurnal component in the Beaufort Sea showing amplitudes in centimeters and Greenwich phase in degrees. Maximum amplitudes are located near Cape Halkett and Mackenzie Bay 37
3.26. Computed tidal current ellipses in the surface layer (at 2.5 m level) of the Beaufort Sea model with a plotting scale of 15 cm/sec per grid spacing. Magnitudes of tidal currents are inversely proportional to the local depth, whereas the shape of the tidal ellipses reflects the shore effects 38
3.27. Nontidal oscillations in the east-west velocity component of the observed currents at station LD-5 after applying the numerical filter which filters out energies in the primary and higher tidal modes 40
3.28. Nontidal oscillations in the north-south velocity component of the observed currents at station LD-5 after applying the numerical filter which filters out energies in the primary and higher tidal modes 40
3.29. Surface water particle trajectories in the Chukchi Sea induced by tide and 10 knot wind blowing from the south for 24 hours. Particles were traced for a total of 48 hours from the beginning to include the transient and inertial dynamics. Trajectories launched near the coastal areas between Point Lay and Icy Cape clearly indicate the development of coastal jets 42

3.30. Surface water particle trajectories in the Chukchi Sea induced by tide and 10 knot wind blowing from the north for 24 hours. Particles were traced for a total of 48 hours from the beginning to include the transient and inertial dynamics. Trajectories launched near the coastal areas between Point Lay and Icy Cape clearly indicate the development of coastal jets 43
3.31. Enlarged section of surface water particle trajectories near the coast between Point Lay and Icy Cape showing the coastal jet. The left shows the trajectories induced by tide and wind from the south (with water movements in the north to east directions); the right shows the trajectories induced by tide and wind from the north (with water movements in the west and south directions) 44
3.32. Surface salinity distribution superimposed on the computed tidal circulation pattern at 1200 hours (Greenwich Mean Time) on August 2, 1976. Areas of low salinity are located near the Yukon River and the eastern Siberian Shelf 45
3.33. Surface temperature distribution superimposed on the computed tidal flow pattern at 1200 hours (Greenwich Mean Time) on August 2, 1976. Areas of warmer temperature are generally located near Yukon Delta and the eastern shelf areas of the Bering and Chukchi Seas 46
3.34 Vertical salinity distributions through two cross-sections of the model. In the north/south section, the shallow pycnocline to the left is located near the Yukon Delta. Because of counterclockwise circulation within Norton Sound, the mixing causes deepening of the pycnocline before reaching the Bering Strait. In the east/west cross-section, fresher water is generally located near the Siberian shelf. The depth of pycnocline is approximately between 7 to 15 meters 47
3.35. Vertical temperature distributions through two cross-sections of the model 48
3.36. Vertical distribution of salinity, temperature, and currents through a cross-section of the eastern Bering shelf showing the pycnocline, frontal structure, and local density instability where heavier water could stay above lighter water temporarily 50
3.37. Inferred geostrophic circulation pattern, based on 5500 hydrographic data, as reported by Arsen'ev (1967) 53
3.38. Computed geostrophic circulation pattern based on a CTD cast by the Japanese fishing fleet, as reported by Takenouti and Ohtani (1974) 53
3.39. Baroclinically induced residual currents at 5 m level after the initial 5-day spin-up. To reflect the realistic energy level over the continental shelf, astronomical tides are included in the computation and subsequently filtered with a two-dimensional numerical tidal eliminator 54
3.40. Comparison between (A), the computed long-term transport, and (B), observed long-term movement of water masses as compiled by Drury et al. (1981) 56
3.41. Observed current components through the Bering Strait with the tidal bands filtered out. The general trend of northward flow is caused mainly by storm events and baroclinic and other residual transport. Sampling period covers November 4, 1982, through January 14, 1983 (by Dr. J. Schumacher of the PMEL, NOAA) 57
3.42. Horizontal distribution of water temperature in the middle of the second layer (7.5 m level) of the Beaufort Sea model 58
3.43. Computed residual circulation in the surface layer with the plotting scale of 2 cm/sec per grid spacing 59
4.1. Typical baric pattern where Alaska is dominated by a flat weak low with several centers over Alaska or near the coast 65
4.2. Typical baric pattern where low is at the west over Siberia plus a ridge over Alaska 65

4.3. Abstract diagram showing transition of stochastic weather state in conjunction with the parameterized physicostochastic model of a cyclone 68
4.4. Monthly occurrences of extra-tropical cyclones by subareas (January 1966–December 1974) 69
4.5. Normalized frequency distribution of intensity based on synoptic characteristics of five-year January daily weather maps at 1230Z during 1949-1953. The sampling period is within the 19-year period when the identical weather charts were used for deriving the transition probability matrices. The original synoptic analyses were made by Schutz (1975) 72
4.6. Normalized frequency distribution of forward speed and persistence based on synoptic characteristics of five-year January daily weather maps at 1230Z during 1949-1953. The sampling period is within the 19-year period when the identical weather charts were used for deriving the transition probability matrices. The original synoptic analyses were made by Schutz (1975) 73
4.7. Typical baric pattern where a pronounced low existed over the modeled area. In this case, the Eastern Low coexisted with a Siberian High. This pressure pattern creates strong southerly air flow near the Bering Strait and thus may induce an ice breakout through the Strait 74
4.8. Surface-temperature-enhanced infrared satellite (NOAA-5) images showing two events of ice breakout through the Bering Strait. The left is for March 20, 1978; the right is for January 31, 1977. Both were adapted from Ahlnas and Wendler (1979). These images imply that ice could pass either to the east or to the west of St. Lawrence Island 75
4.9. Monthly Meridinal average sea-level pressure over the northern Bering Sea at 65°N latitude 77
4.10. Monthly average air-sea temperature difference over the eastern Bering Sea 77
4.11. Comparison between the observed wind roses at three land-based stations (Brower et al., 1977) for July, and typical marine winds at nearby locations obtained by long-term (2000) weather sequences interrupted by moving storms . . . 78
5.1. Spatial distribution of ice concentration and thickness as compiled from existing data for the summer period 80
5.2. Spatial distribution of average pack ice thickness in the Bering/Chukchi Sea model near the end of January 82
5.3. Initial distribution of ice thickness. Area near the Yukon Delta and at the head of the Sound is covered by shore-fast ice. Areas near Golovin Bay and south of it are ice-producing areas 88
5.4. Ice floe movement under northeast wind (10 kn) combined with tidal movement. Displacements immediately neighboring shore-fast ice zones are limited with rotational behavior induced by strong ice-ice interactions 88
5.5. Water movements beneath the ice. They are driven by tidal forces and wind stresses transmitted through the ice 89
5.6. 24-hour ice trajectories, driven by tidal excursion and 10 kn wind from the northeast for the first 12 hours 89
5.7. 24-hour net ice displacements, induced by tidal-residual current and 10 kn wind from the northeast for the first 12 hours. Daily displacements under 24-hour wind stress would be approximately twice the amount shown 90
5.8. Pattern of daily ice floe movement of 30-31 March 1976 (Stringer and Hufford, 1980) when the pressure difference between Barrow and Nome was approximately 0.4 inches 90
6.1. Response function components 93

6.2. Flow chart showing importance of both the three-dimensional hydrodynamic and the weather model to the oil spill trajectory model. These parameters are difficult and expensive to measure over the entire coastal waters. Observed wind roses, if available can still be used to drive the trajectory model in its simplest mode 97
6.3. Daily movements of oil originated from launch points 21 through 40 98
6.4. Three groups of ice drift data (A) Coast Guard drogues for 3 months during the summer of 1979; (B) composite trajectories compiled using data from 1893-1972 by Colony and Thorndike (1984); and (C) trajectories of automatic data buoys (1979-1982), also from Colony and Thorndike (1984) 100
6.5 Comparison between (A) trajectories of five satellite-tracked buoys deployed by the U.S. Coast Guard August to October, 1979, from eastern Mackenzie Bay, Canada, and (B) 30-day trajectories launched from five locations and computed by the RAND oil trajectory model and the two-dimensional stochastic weather simulation model 101
6.6. Composite oil-spill trajectory map showing the general direction of movements launched from stations 1, 8, and 17 during winter. The staggered launch scheme represents an equally likely chance of spill during the long winter period. The residence time within the modeled area is approximately two to three months . . . 102
6.7. Spatial distribution of oil contact frequencies. If oil is trapped in a near-shore lagoon, a continuous contact is assumed for the remaining period. Analysis is made using two-hour counting method. Plotting scale for the circle 21211, two-hour exposure periods equal one latitudinal grid spacing for the radius of the circle 103
6.8. Spatial distribution of oil contact frequencies excluding near-shore entrapments. Latitudinal grid spacing equals 1872 two-hour contact periods for the radius of a circle 104
6.9. Pathways of particle groups released in different layers of the model. Partially insulated by the pycnocline, 24-hour trajectories of particle groups released in the upper five layers experience less turbulent diffusion than the lower layers when the system is forced only with tidal energies 106
6.10. Submodels are used to improve the near-shore resolution of the trajectory computation. The computational grids of the submodel are nested within the larger model's computational grid (Liu and Leendertse, 1984) 107
6.11. Displacements of the one-part-per billion concentration envelope every five days for an instantaneous release of 700,000 barrels of crude oil from five hypothetical launch points during the summer. The variability of local advective and diffusive mechanisms is illustrated by the changing speed and direction of the oil's movements 108
6.12. Oil spill trajectory launched in the middle of the Bering Strait under a 30-day stochastic weather scenario during the summer. (A) illustrates progressive daily displacements of the 1 part per billion concentration envelope for the continuous discharge of 2000 barrels of crude oil. The traveling speed of oil is governed by the evolutionary weather state as well as the local circulation pattern. (B) illustrates the concentration contour of the oil. Notice the cumulation effects when the oil reaches the coastal area where the on-shore current components drop and the along-shore currents strengthen. This near-shore effect tends to redirect the oil while slowing it down somewhat 109
6.13. Location of 46 launch points specified for the oil spill trajectory computation. Barrow Arch lease area (No. 109) 111

6.14. Five sets of randomly selected trajectories from launch points 10, 13, 16, 28, and 39; under the staggered-launch mode, each spill has about an equally likely chance of occurrence during the winter. Spill launched near the Bering Strait can move either south or north depending on the weather sequence 112
6.15. Current roses analyzed from twenty-one 30-day oil spill trajectories for winter, launched near a point between St. Lawrence Island and the Gulf of Anadyr, USSR (see insert map). Local residual and the relative distance from the shore-fast ice make the oil containing ice move differently from the free-drifting pack ice. Consequently, there are more random ice motions under the local wind stress than the oil movements in the water column resulting resulting from inertia and momentum filtering effects 113
6.16. Spatial distribution of oil contact frequencies during winter. Latitudinal grid spacing equals 3161 two-hour contact periods for the long axis of the ellipse 114
6.17. Spatial distribution of oil contact frequencies during summer. Latitudinal grid spacing equals 12722 two-hour contact periods for the long axis of the ellipse 115

TABLES

3.1. Data Groups Adapted for Estimating the Net Circulation Near the Bering Shelf Break and the Updating Process 52
4.1. Cumulative Distribution of Transitional Probability Matrix Associated with the 11 Weather Types Used for Simulating Oil Trajectories, June-August Period 63
4.2. Synoptic Characteristics for the Summar Baric Types 64
4.3. Synoptic Characteristics for the Winter Baric Types 64
4.4. Determination of Standard Deviation for Wind Speed Simulation at Point Barrow for the Month of January (Sample Period, 19 Years) 66
4.5. Spatial Distribution of PDF (x10000) of Low Pressure Centers 70
6.1. Chukchi Sea Winter Oil Spill Trajectory Analyses (Sale 109). Tabulated "Trace-Back" of Oil Spill Contact Between Contact Location and Launch Point. "*" Indicates Landfall and "#" Indicates Trajectory Moved Out of the Modeled Area 116
6.2. Chukchi Sea Summer Oil Spill Trajectory Analyses (Sale 109). Tabulated "Trace-Back" of Oil Spill Contact Between Contact Location and Launch Point. "*" Indicates Landfall and "#" Indicates Trajectory Moved Out of the Modeled Area 117
A.1. Computed East-West Component of Tidal/Baroclinic Residual Currents in the Bering and Chukchi Seas 121
A.2. Computed East-West Component of Tidal/Baroclinic Residual Currents in the Bering and Chukchi Seas 122
A.3. Computed East-West Component of Tidal/Baroclinic Residual Currents in the Bering and Chukchi Seas 123
A.4. Computed North-South Component of Tidal/Baroclinic Residual Currents in the Bering and Chukchi Seas 124
A.5. Computed North-South Component of Tidal/Baroclinic Residual Currents in the Bering and Chukchi Seas 125
A.6. Computed North-South Component of Tidal/Baroclinic Residual Currents in the Bering and Chukchi Seas 126

1. INTRODUCTION

This report presents modeling studies of the hydrodynamic and related physical processes of the Alaskan coastal waters for impact assessments of the exploration and exploitation of oil reserves on the Alaskan outer continental shelf.

At present, the Prudhoe Bay field in northern Alaska contributes a substantial amount of the current domestic oil production of the United States. Oil is also expected to be present on the continental shelf of Alaska, and it is estimated that approximately 28 percent of the total U.S. oil reserve is located beneath the shallow ice-covered seas of the Alaskan continental shelf (Weeks and Weller, 1984). To explore and to exploit these rich oil resources, engineers must confront hostile oceanographic conditions such as high tides, waves, strong currents, and dangerous working conditions associated with the sea ice. Results from the modeling work reported here will provide useful information on the environmental factors affecting the design of engineering works for the exploration and exploitation of these oil reserves.

The Alaskan continental shelf is rich in fishery resources. Being one of the most productive fishing grounds in the northern Pacific, the potential ecological impact of an oil spill is also of major concern. Another major concern is the impact of oil spills on wildlife, particularly in those areas where wildlife congregate during certain periods of the year. As a result, the major application of the models we developed during our studies has been for the assessment of risk associated with petroleum development within the region. For this reason, a major part of this report describes the methodology used for the computation of oil dispersion, weathering, and movements, and the results of these computations.

Initially our studies were limited to the determination of water movements resulting from tides and the distribution of densities in the considered water bodies. Soon after we began our modeling work, we realized that results of a hydrodynamic model cannot provide much data for environmental assessment without regional weather information and models for the computation of the movement, dispersion, and weathering of oil spills.

The studies reported here were made in conjunction with environmental research studies performed by others. The work includes all the waters of the Alaskan continental shelf, but some areas were covered with more geographic detail than others.

In each chapter of this report, studies for each particular process are presented. Thus in each chapter the formulation of the model is described and results are presented for the different application areas.

Chapter 2 outlines the mathematical formulation and the solution scheme of the hydrodynamic modeling system. Because of the strong buoyancy effects caused by ice melting in the water column, and because of the intense momentum transfer process associated with frequent storm activity, a new turbulence closure scheme is used. The scheme is somewhat different from the traditional approach and is described in Chapter 2. Also represented are the behavior and performance of the numerical model. Particularly important is the model's verification on the partition of energy in the frequency domain for both homogeneous and nonhomogeneous tubulent flows. This is an essential step in model development.

Chapter 3 describes the modeling of hydrodynamic processes including tides, wind-driven currents, and the residual circulation induced by the baroclinic field. The Alaskan coastal waters are part of three major oceanic systems—the Arctic Ocean, the Bering Sea,

and the Gulf of Alaska. Each system has its own distinct characteristics, but they interact in a complex, yet interesting way. These important features are also presented in this chapter.

One special feature of the Alaskan coastal waters is the frequent presence of storms. These large moving storms produce strong winds that alter the areawide hydrodynamic processes through long-period oscillation within the system. The intense storms not only pose a threat to the offshore, oil related activities but also play a significant role in environmental risk analyses such as the reversal of ice transport between the Bering Sea and the Arctic Ocean. The cyclogenetic/cyclolytic processes associated with these extratropical storms are complex and stochastic in nature. The probabilities associated with the storm-related parameters have to be considered together with the environmental risk factors. Because of this, stochastic models are developed to estimate the weather elements associated with the modeling systems such as the variability of wind fields. These analyses are presented in Chapter 4.

Another special feature of the Alaskan coastal waters we included in our studies is the presence of ice. Chapter 5 gives a description of the ice modeling work. Nearly half of our modeled area lies within the Arctic Circle. In this region the waters can be completely free of ice at some time of year and completely covered with ice at other times. The presence of ice complicates the modeling work considerably, particularly when the knowledge of polar ice is incomplete.

In Chapter 6 we describe the transport, dispersion, and weathering of spilled oil. To provide information for oil spill risk analyses, the movements of spilled oil were computed for at least one month under summer conditions. If simulated spills occurred during winter, the simulation period had to be extended, sometimes for several months. In the computational methods we developed for this purpose, we accounted for the movements of oil under ice.

Wind is a major input to the oil trajectory computations. The wind model described in Chapter 4 is used for this purpose. In some instances, information had to be provided on the distribution of oil in the water after a spill. With excellent cooperation from other research institutions, we were able to develop a model for the dispersion of oil that included the oil weathering process. The procedures for these oil dispersion computations are also presented in Chapter 6.

2. THE THREE-DIMENSIONAL MODELING SYSTEM

In the modeling system, the three-dimensional hydrodynamic model is one of the most important models. This model is formulated according to the equations of motion for water and ice, continuity, state, the balance of heat, salt, pollutant, and turbulent energy densities, on a three-dimensional finite grid. The vertical momentum, mass, heat, and turbulent energy exchange coefficients are computed from the turbulent energy, thus the model contains a turbulence closure computation. Turbulent energy dissipation resulting from the mixing of heavier water with lighter water is accounted for in the turbulence closure.

For the derivation of basic equations, the reader is referred to Liu and Leendertse (1978), in which aspects such as open boundary conditions, numerical stability, solution discontinuity, and conservation properties are also described.

In the present model, the horizontal grid conforms to the earth's ellipsoidal coordinates and the arbitrary vertical grid spacing approximates the bottom topography of the modeled area. The results are subsequently transformed into the Universal Mercator projection for graphical representation. For simplicity, the system of modeling equations is presented here using the standard finite difference notation on a regular spatial grid network in the horizontal direction, and on an irregular grid in the vertical (Fig. 2.1). The coordinates i, j, k, and n are used to denote discrete points in the x, y, z, and t domain. The finite difference formulation adapted for the computation takes the following form:

$$\overline{\delta_t \zeta}^{t} = -\sum_k \left[\delta_x\left(\bar{h}^{x} u\right) + \delta_y\left(\bar{h}^{y} v\right)\right] \quad \text{at } i, j, n \tag{2.1}$$

where the variation of the water level ζ is derived from the continuity equation by vertical integration, and h is the layer thickness. The momentum equation in the x-direction:

$$\overline{\delta_t\left(\bar{h}^{x} u\right)}^{t} = -\delta_x\left(\overline{\bar{h}^{x} u\, \bar{u}^{x}}^{x}\right) - \delta_y\left(\overline{\bar{h}^{y} v\, \bar{u}^{y}}^{x}\right) - \bar{h}^{x}\delta_z\left(\bar{u}^{z}\bar{w}^{x}\right) + f\bar{h}^{x}\bar{v}^{xy} - \frac{1}{\bar{\rho}^{x}}\bar{h}^{x}\delta_x p$$

$$+ \frac{1}{\bar{\rho}^{x}}\left[h\delta_z\left(E_x\delta_z\bar{u}^{2t}\right) + \delta_x\left(hA_x\delta_x u\right)_{-} + \delta_y\left(\overline{\bar{h}^{x}\overline{A_y}^{x}}^{y}\delta_y u\right)_{-}\right]$$

$$\text{at } i+\tfrac{1}{2}, j, k, n \tag{2.2}$$

where E_x is the vertical momentum exchange coefficient, and A_x, A_y are the horizontal exchange coefficients in x-direction and y-direction, respectively.

The momentum equation in the y-direction:

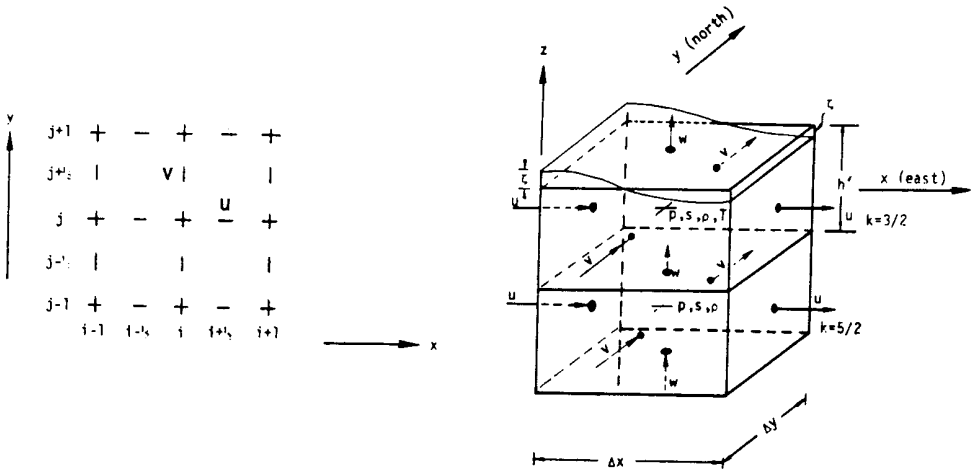

Space-staggered computation grid and relative position of variables

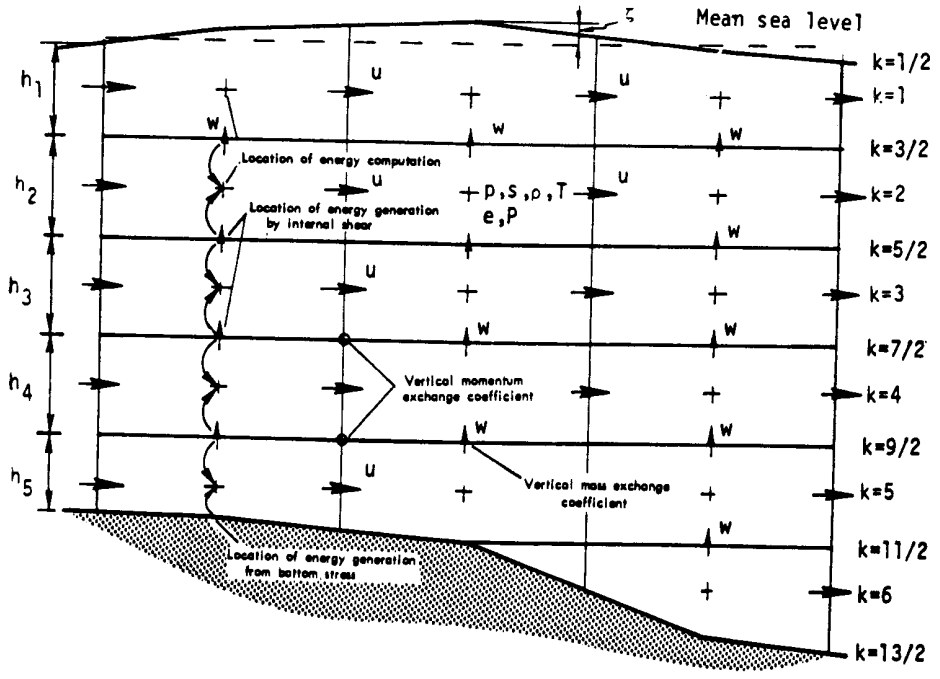

Location of variables on the X-Z plane

Fig. 2.1—Location of variables.

$$\overline{\delta_t\left(\bar{h}^y v\right)}^t = -\delta_x\left(\overline{\bar{h}^x u\, \bar{v}^x}^y\right) - \delta_y\left(\overline{\bar{h}^y v\, \bar{v}^y}^y\right) - \bar{h}^y \delta_z\left(\bar{v}^z \bar{w}^y\right) - f\bar{h}^y \bar{u}^{xy} - \frac{1}{\bar{\rho}^y}\bar{h}^y \delta_y p$$

$$+ \frac{1}{\bar{\rho}^y}\left[h\delta_z\left(E_y \delta_z \bar{v}^{2t}\right) + \delta_x\left(\overline{\bar{h}^y \overline{A_x}^y}^x \delta_x v\right)_- + \delta_y\left(hA_y \delta_y v\right)_-\right]$$

$$\text{at } i, j + \tfrac{1}{2}, k, n \tag{2.3}$$

The mass-balance equation for salt,

$$\overline{\delta_t\left(hs\right)}^t = -\delta_x\left(\bar{h}^x u\bar{s}^x\right) - \delta_y\left(\bar{h}^y v\bar{s}^y\right) - h\delta_z\left(w\bar{s}^z\right)$$
$$+ \delta_x\left(\bar{h}^x D_x \delta_x s\right)_- + \delta_y\left(\bar{h}^y D_y \delta_y s\right)_- - hs_z\left(\kappa\delta_z \bar{s}^{2t}\right)$$

$$\text{at } i, j, k, n \tag{2.4}$$

where D_x and D_y are the horizontal diffusion coefficients, s is the salinity (salt concentration), and κ is the vertical mass exchange coefficient. For temperature:

$$\overline{\delta_t\left(hT\right)}^t = -\delta_x\left(\bar{h}^x u\overline{T}^x\right) - \delta_y\left(\bar{h}^y v\overline{T}^y\right) - h\delta_z\left(w\overline{T}^z\right)$$

$$+ \delta_x\left(\bar{h}^x D_x \delta_x T\right)_- + \delta_y\left(\bar{h}^y D_y \delta_y T\right)_- + h\delta_z\left(\kappa'\delta_z \overline{T}^{2t}\right)$$

$$\text{at } i, j, k, n \tag{2.5}$$

where κ' is the vertical thermodiffusion coefficient.

For the SGS energy density in the system,

$$\overline{\delta_t\left(he\right)}^t = -\delta_x\left(\bar{h}^x u\bar{e}^x\right) - \delta_y\left(\bar{h}^y v\bar{e}^y\right) - h\delta_z\left(w\bar{e}^z\right)$$

$$+ \delta_x\left(\bar{h}^x D_x \delta_x e\right)_- + \delta_y\left(\bar{h}^y D_y \delta_y e\right)_- + h\delta_z\left(E_e \delta_z \bar{e}^{2t}\right) + h\overline{S_e}^z - D_e h$$

$$\text{at } i, j, k, n \tag{2.6}$$

where E_e is the vertical momentum exchange coefficient. For the pollutant constituent concentration:

$$\overline{\delta_t(hP)}^t = -\delta_x\left(\bar{h}^x u\bar{P}^x\right) - \delta_y\left(\bar{h}^y v\bar{P}^y\right) - h\delta_z\left(w\bar{P}^z\right)$$

$$+ \delta_x\left(\bar{h}^x D_x\delta_x P\right)_- + \delta_y\left(\bar{h}^y D_y\delta_y P\right)_- + h\delta_z\left(\kappa\delta_z\bar{P}^{2t}\right) + hS_P - D_P h$$

$$\text{at } i, j, k, n \tag{2.7}$$

The equation of state is approximated by:

$$\rho = \frac{\left[5890 + 38T - 0.375T^2 + 3s\right]}{\left[(1779.5 + 11.25T - 0.0745T^2) - (3.8 + 0.01T)s + 0.698(5890 + 38T - 0.375T^2 + 3s)\right]}$$

$$\text{at } i, j, k, n + l \tag{2.8}$$

The continuity equation is used to compute the vertical velocity:

$$\delta_z w = -\delta_x\left(\bar{h}^x u\right) - \delta_y\left(\bar{h}^y v\right) \qquad \text{at } i, j, k, n + l \tag{2.9}$$

Similar equations for velocity components u and v can be written for the top and bottom layers, but now the effects of wind and bottom friction must be considered. We have at the surface:

$$\overline{\delta_t\left(\bar{h}^x u\right)}^t = -\delta_x\left(\overline{\bar{h}^x u}^x\,\bar{u}^x\right) - \delta_y\left(\overline{\bar{h}^y v}^x\,\bar{u}^y\right) - \bar{h}^x\delta_z\left(\bar{u}^z\bar{w}^x\right) + f\bar{h}^x\bar{v}^{xy} - \frac{1}{\bar{\rho}^x}\bar{h}^x\delta_x P$$

$$+ \frac{1}{\bar{\rho}^x}\left[\Theta\rho_a w_a^2\sin\psi - \left(E_x\delta_z\bar{u}^{2t}\right)_{k-3/2} + \delta_x\left(hA_x\delta_x u\right)_- + \delta_y\left(\overline{\bar{h}^x\overline{A_y}^x}^y\delta_y u\right)_-\right]$$

$$\text{at } i + \tfrac{1}{2}, j, l, n \tag{2.10}$$

where ψ is the clockwise angle between the model's y-axis and the direction toward which the wind is blowing and where Θ represents the wind-stress coefficient. In the y-direction, the momentum equation becomes:

$$\overline{\delta_t(\bar{h}^y v)}^t = -\delta_x\left(\overline{\bar{h}^x u}^y\,\bar{v}^x\right) - \delta_y\left(\overline{\bar{h}^y v}^y\,\bar{v}^y\right) - \bar{h}^y\delta_z\left(\bar{u}^z\bar{w}^y\right) - f\bar{h}^y\bar{v}^{xy} - \frac{1}{\bar{\rho}^y}\bar{h}^y\delta_y p$$

$$+ \frac{1}{\bar{\rho}^y}\left[\Theta\rho_a w_a^2\cos\psi - \left(E_y\delta_z\bar{v}^{2t}\right)_{k-3/2} + \delta_x\left(\overline{\bar{h}^y\overline{A_x}^y}^x\delta_x v\right)_- + \delta_y\left(hA_y\delta_y v\right)_-\right]$$

$$\text{at } i, j, + \tfrac{1}{2}, l, n \tag{2.11}$$

where w_a is wind speed, and ρ_a represents the density of air. At the bottom layer the momentum equations become:

$$\overline{\delta_t(\bar{h}^x u)}^t = -\delta_x\left(\overline{\bar{h}^x u\,\bar{u}^x}^x\right) - \delta_y\left(\overline{\bar{h}^y v\,\bar{u}^y}^x\right) - \bar{h}^x\delta_z\left(\bar{u}^z\bar{w}^x\right) + f\bar{h}^x\bar{v}^{xy} - \frac{1}{\bar{\rho}^x}\bar{h}^x\delta_x p$$

$$+ \frac{1}{\bar{\rho}^x}\left\{\left(E_x\delta_z\bar{u}^{2t}\right)_{k-K-1/2} - \bar{\rho}^x g u_-\left[u_-^2 + \left(\bar{v}_-^{xy}\right)^2\right]^{1/2}\Big/\left(\bar{C}^x\right)^2\right.$$

$$\left. + \delta_x\left(hA_x\delta_x u\right)_- + \delta_y\left(\overline{\bar{h}^{xy}A_y}^y\delta_y u\right)_-\right\} \quad \text{at } i+\tfrac{1}{2}, j, K, n$$

$$\overline{\delta_t(\bar{h}^y v)}^t = -\delta_x\left(\overline{\bar{h}^x u\,\bar{v}^x}^y\right) - \delta_y\left(\overline{\bar{h}^y v\,\bar{v}^y}^y\right) - \bar{h}^y\delta_z\left(\bar{v}^z\bar{w}^y\right) - f\bar{h}^{xy}\bar{u}^{xy} - \frac{1}{\bar{\rho}^y}\bar{h}^y\delta_y p \qquad (2.12)$$

$$+ \frac{1}{\bar{\rho}^x}\left\{\left(E_y\delta_z\bar{v}^{2t}\right)_{k-K-1/2} - \bar{\rho}^y g v_-\left[\left(\bar{u}_-^{xy}\right)^2 + v_-^2\right]^{1/2}\Big/\left(\bar{C}^y\right)^2\right.$$

$$\left. + \delta_x\left(\overline{\bar{h}^{xy}A_x}^x\delta_x v\right)_- + \delta_y\left(hA_y\delta_y v\right)_-\right\} \quad \text{at } i, j+\tfrac{1}{2}, K, n \qquad (2.13)$$

where C is the Chezy coefficient:

In the modeled area, each vertical motion of water mass has to work against buoyancy forces induced by the density gradient. If the available kinetic energy of the turbulent motion is insufficient to overcome this stabilizing effect, turbulence is inhibited and suppressed. As a consequence, the process of momentum and mass-heat exchange will be lower than the neutral stability condition. The criteria for the onset of this turbulence-suppressing process in the system can be obtained from the local density gradient and turbulent energy level. Therefore, the variability of the vertical exchange coefficients in the model is computed by a turbulence closure technique using local turbulence intensity, e:

$$E_y = \bar{\rho}^{yz}\,\overline{L\sqrt{e_-}}^{xz} \qquad (2.14)$$

$$E_x = \bar{\rho}^{xz}\,\overline{L\sqrt{e_-}}^{xz} \qquad (2.15)$$

$$E_e = a_1\,\overline{L\sqrt{e_-}}^{z} \qquad (2.16)$$

$$\kappa = a_4\,\overline{L\sqrt{e_-}}^{z} \qquad (2.17)$$

where a_1 , a_4 are turbulence closure constants and L denotes the length scale, which can be approximated by an additional transport equation (Rodi, 1980), or by a parametric expression based on work by Kranenberg (1984, 1985) and Joppe (1985).

$$\frac{1}{L} = \frac{1}{\ell_m} + \frac{1}{\ell_s} \tag{2.18}$$

where

$$\ell_m = \kappa' z (1 - z/d)^{1/2}$$

$$\ell_s = C_s (\kappa \rho_o / (g \partial \rho / \partial z) \tag{2.19}$$

κ' is the von Karman constant, z represents the vertical distance from the bottom to the point considered, and d is the vertical distance from the surface to the bottom.

In the horizontal direction, the exchange coefficient is computed in two parts as a function of the local vorticity gradient and the local grid dimension. The first part is:

$$A = \gamma \left| \left(\delta_x \bar{\omega}^y + \delta_y \bar{\omega}^x \right) \right| \left(\Delta \ell \right)^3 \tag{2.20}$$

where ω is the vorticity, γ is a coefficient, and $\Delta \ell$ is the local grid size. This part represents the exchange for a wave number lower than the spatial Nyquist frequency. The second part represents the contribution from the homogeneous subgrid scale turbulence above the spatial Nyquist frequency, which can be computed according to Kolmogorov's turbulence spectrum theory. The gross horizontal exchange coefficient is therefore:

$$D_x = \bar{A}^x + a_5 \Delta \ell^{4/3} \tag{2.21}$$

$$D_y = \bar{A}^y + a_5 \Delta \ell^{4/3} \tag{2.22}$$

where a_5 is a function of the energy dissipation rate. In a strict sense, molecular diffusion, which is quite small (and a property of the fluid), could be added as the third part. These three parts thus cover the turbulent dispersion/diffusion process over the entire spectral partition without overlapping.

In the model the amount of reduction in the vertical exchange resulting from stratification is based on the direct computation of the local gain in potential energy induced by vertical mixing. The exact amount is then taken out of the local turbulent (kinetic) energy budget. In the equation of energy (Eq. (2.6)), the generation and dissipation terms become:

$$\overline{S_e^z} - D_e = \underbrace{a_3 \overline{L\sqrt{e}}^z \left[\left(\delta_z \bar{u}^x\right)^2 + \left(\delta_z \bar{v}^y\right)^2\right]}_{(1)} + \underbrace{a_3 \overline{L\sqrt{e}}^z \frac{g}{\bar{h}^z \bar{\rho}} \left(\delta_z \bar{\rho}^z\right)}_{(2)} \tag{2.23}$$

$$\underbrace{- a_2 e^{3/2}/L}_{(3)}$$

where the first term denotes production, the second term represents the portion supplied that is used in potential energy increase, and the third term is dissipation.

The model algorithm allows a variable layer thickness to be used. In all models the thickness of the upper two layers is roughly half the mixed layer depth. Near the pycnocline the layer thickness is reduced to obtain the vertical resolution that is needed to model the mass and momentum exchanges and the dynamics with the appropriate accuracy.[1] These processes are of primary importance in our modeling work and are one of the major reasons why three-dimensional models were used in our analyses.

For oil spill trajectory computations and for computations of the dispersion of oil on the surface of the sea, surface currents are needed. These currents can be obtained by an extrapolation starting in the middle of the top layer. An analytical solution similar to the solution by Ekman (see Neumann and Pierson, 1966) is used. Ekman uses a fixed vertical eddy coefficient in his computations, whereas in our work this coefficient is variable. These time- and spatially varying coefficients are derived from simulations with the three-dimensional model by means of the turbulence closure procedure described above.

During the development stage of the modeling system, subsurface currents have been computed by means of vertical turbulent closure of both first- and second-order schemes, similar to that described by Launder and Spalding (1972). During tests, in the absence of a wind-induced free-surface energy source, both one- and two-equation models have worked well. However, under variable wind (or storm) conditions, and sometimes with floating ice, there is little experimental information on the surface effects of wind-induced turbulence that could be used as the basis for providing parameters for specifying length scale (Rodi, 1980).

As illustrated in Figs. 2.2 and 2.3, the model produces logarithmic vertical velocity profiles in homogeneous oscillating flow (straight line on a semilog plot). It can also reproduce nonviscous analytical solutions when all diffusion coefficients are set to zero.

Consider the turbulent closure computation when the model is driven at the open boundary by a monochromatic wave, in this case, a semidiurnal M2 tidal component into the Chesapeake Bay (see Fig. 2.4). In the model's interior, the scheme can produce the cascade of

[1]We did not introduce vertical coordinate transformations in which the layers are a fixed fraction of the full ocean depth even though such an approach reduces the programming effort considerably, as boundary conditions are very much simplified. When such transformations are used, the model loses its effectiveness, as this procedure introduces artificial mixing. This can be visualized by considering a deep point and an adjacent shallow point of the grid with water of low salinity. When the currents have a direction from the shallow area to the deeper area, then the water at the bottom layer of the shallow area is moved directly into the bottom layer in the deeper area and we obtain strong artificial mixing.

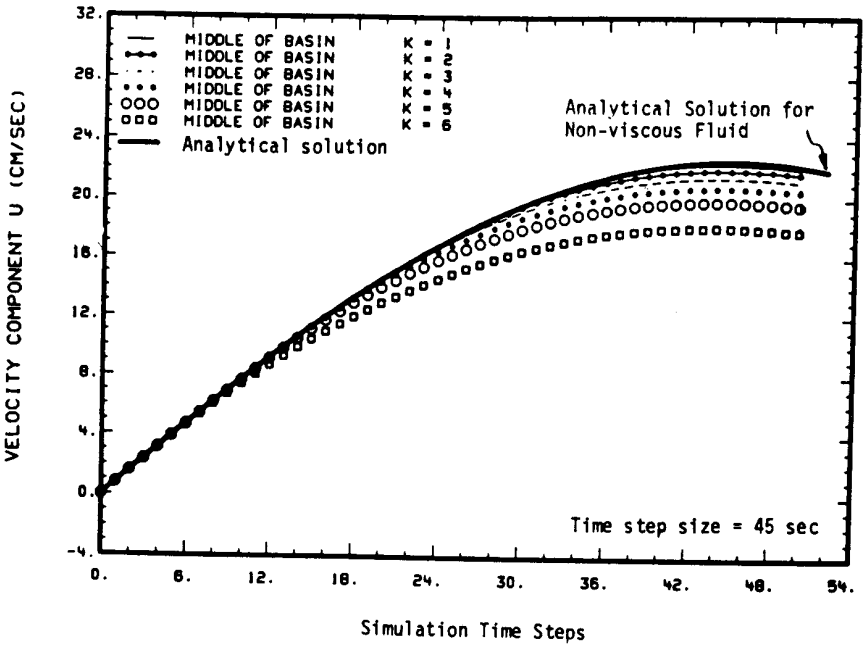

Fig. 2.2—Comparison of mean flow velocity component u, computed by numerical method, to nonviscous fluid, computed by analytical solution.

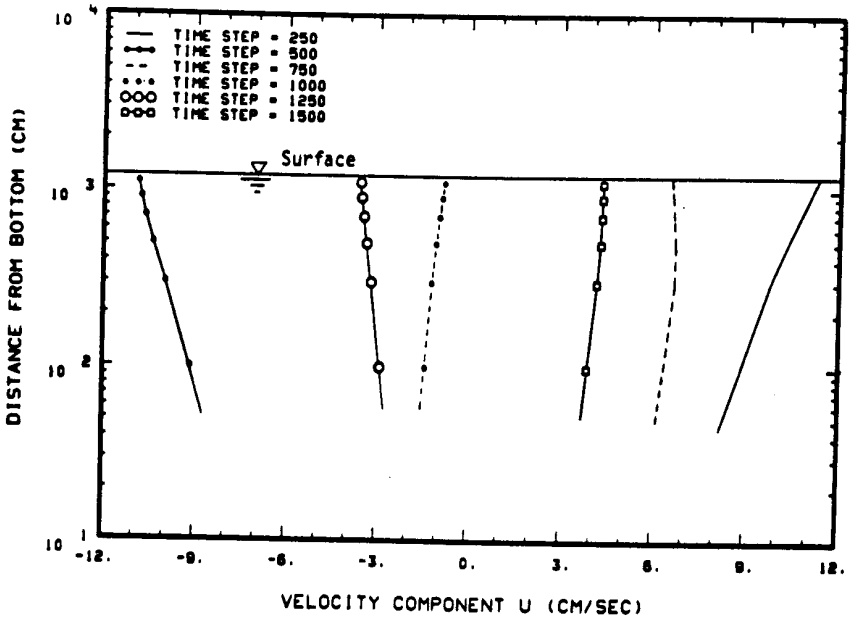

Fig. 2.3—Vertical distribution of velocity component u in the middle of the homogeneous oscillating basin (logarithmic vertical scale).

energy distribution according to the universal "minus five-third power law" (Hinze, 1959) through the model's nonlinear advective process. (Also, see the recent measurements by Heathershaw, 1979, and Elliott, 1984.)

In stratified geophysical flow, the density-induced vertical exchange often has a time scale much shorter than its horizontal baroclinic counterpart. It also plays an important role in the coastal ecological balance via the euphotic/energetic processes. It, therefore, creates stringent demands on the accuracy of modeling. On one hand, advances made in other disciplines, such as aerodynamic modeling, can often be applied to the geophysical flows, but, on the other hand, the differences in the free-surface and other boundary treatments make the closure technique not necessarily identical for stratified flows because coastal flows are primarily two-dimensional. Recent findings on the nonequilibrium statistical characteristics of turbulence have shown that the universal Kolmogorov-constant of the turbulence spectrum has to be modified for two-dimensional turbulence. Peaks of the spectra for two-dimensional turbulence are not uniquely located; however, they depend on the energy input and the relative location from the boundary (the so-called localization factor). Models relying on the Richardson-number-related parameters are especially susceptible to field measurement inaccuracies.

Consequently, over the past several years we have modified our earlier models that required Richardson-number-related parameters to an energy balance approach (Eq. (2.23)).

For the stratified fluid, when the computed spectra of the vertical displacements (in the surface layer, within pycnocline and near bottom, Liu and Leendertse, 1979) are plotted on a log-log scale (Fig. 2.5), the distribution of significant energy within this spectra agrees with the observed spectra of the first-mode internal wave (Gordon, 1978).

When the Bering Sea model reported herein is driven with the predicted tide (not measured), the computed subsurface current in the model's interior point agrees fairly well with the observed subsurface current both in magnitude and in direction (Fig. 2.6). When the computed velocities and the relative turbulence intensities at 15 layers are normalized with respect to the bottom, the vertical distribution of relative turbulence intensities (circles in Fig. 2.7) is nearly the same when compared with the standard NACA (later NASA) calibration curve of air flow measured in a brass pipe. In that graph, the insulation of momentum transfer across the pycnocline is evident.

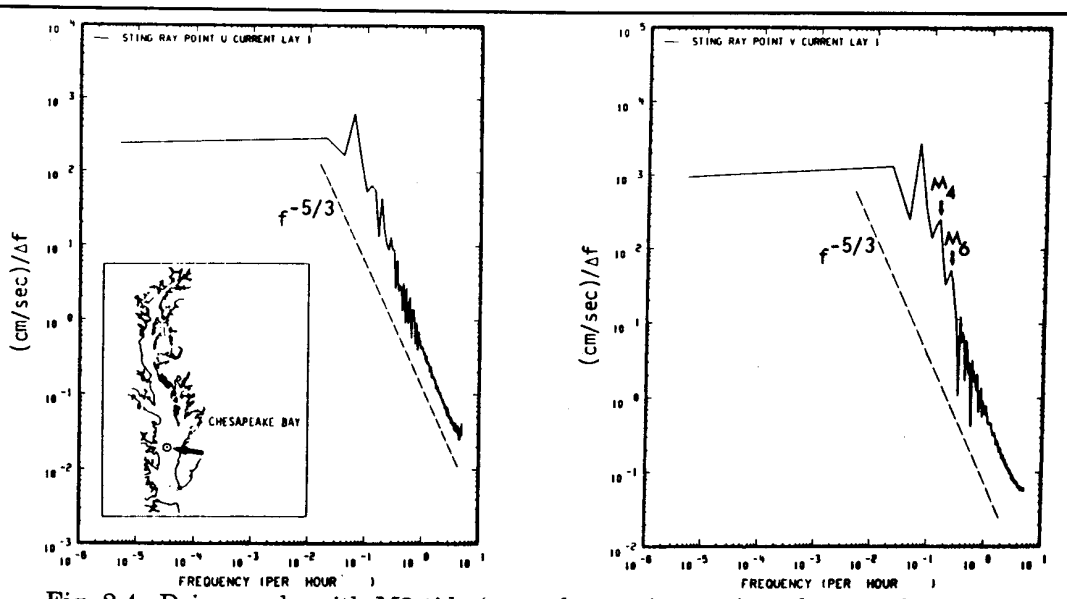

Fig. 2.4—Driven only with M2 tide (monochromatic wave) at the open boundary, the proposed numerical scheme can produce the cascade of energy distribution according to the universal "minus five-third" through the model's nonlinear advective process (Hinze, 1959).

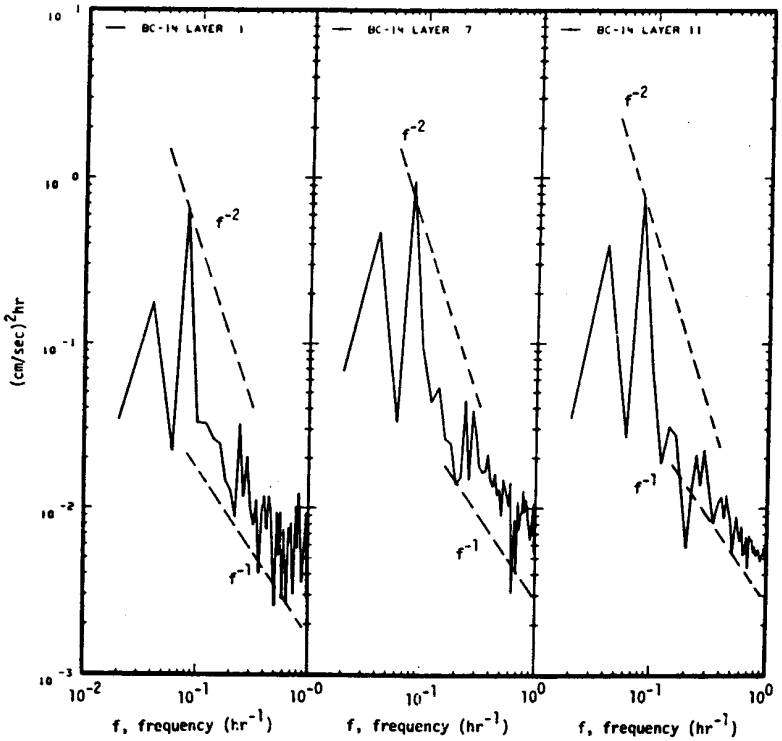

Fig. 2.5—For the stratified fluid, the computed spectra of the vertical displacements (in the surface layer, within pycnocline and near bottom) and significant energy distribution agree with the observed spectra of the first mode of internal waves (Gordon, 1978).

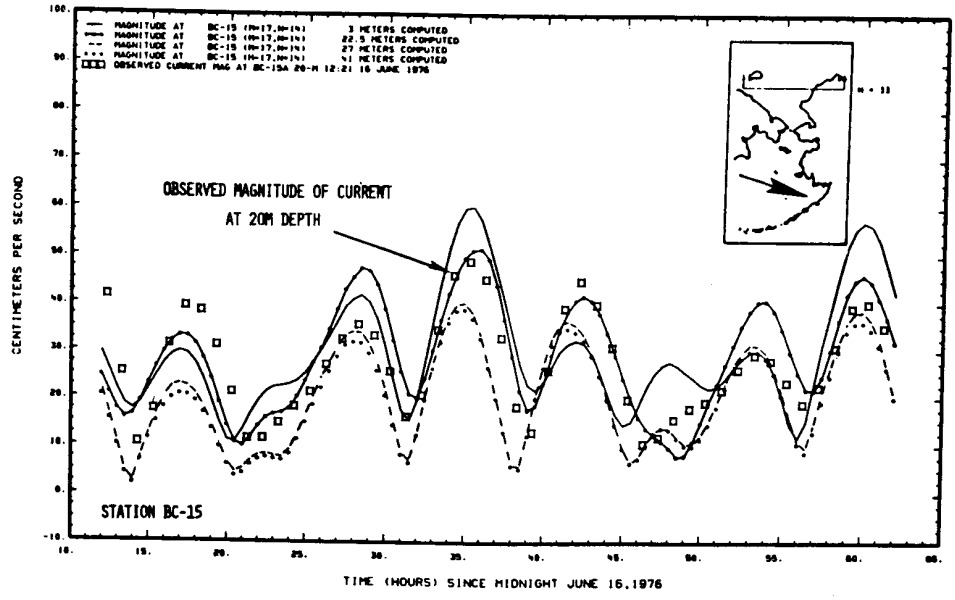

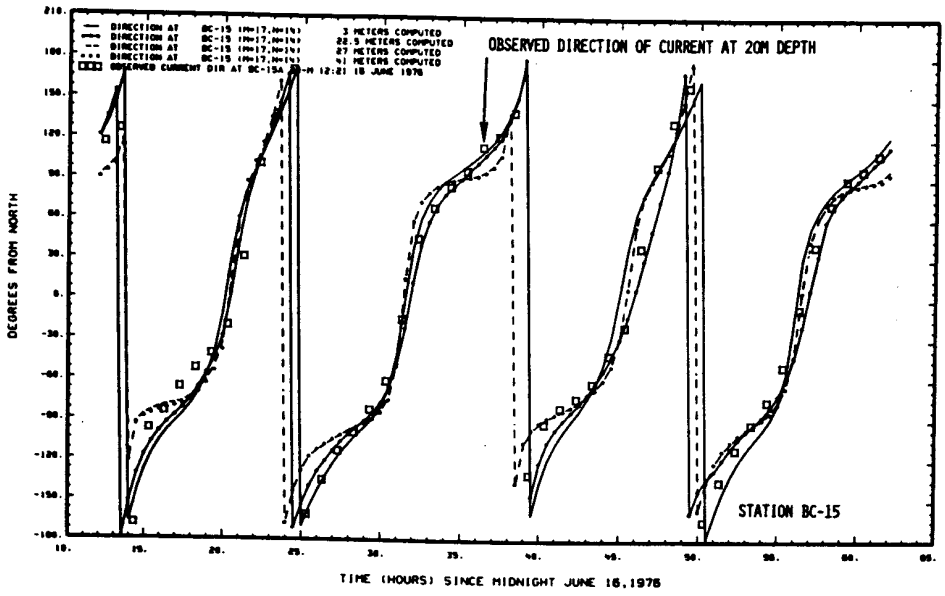

Fig. 2.6—When driven with the predicted tide, the computed subsurface currents in the Bering Sea agree fairly well with the observed subsurface currents, both in magnitude and in direction (Liu and Leendertse, 1979).

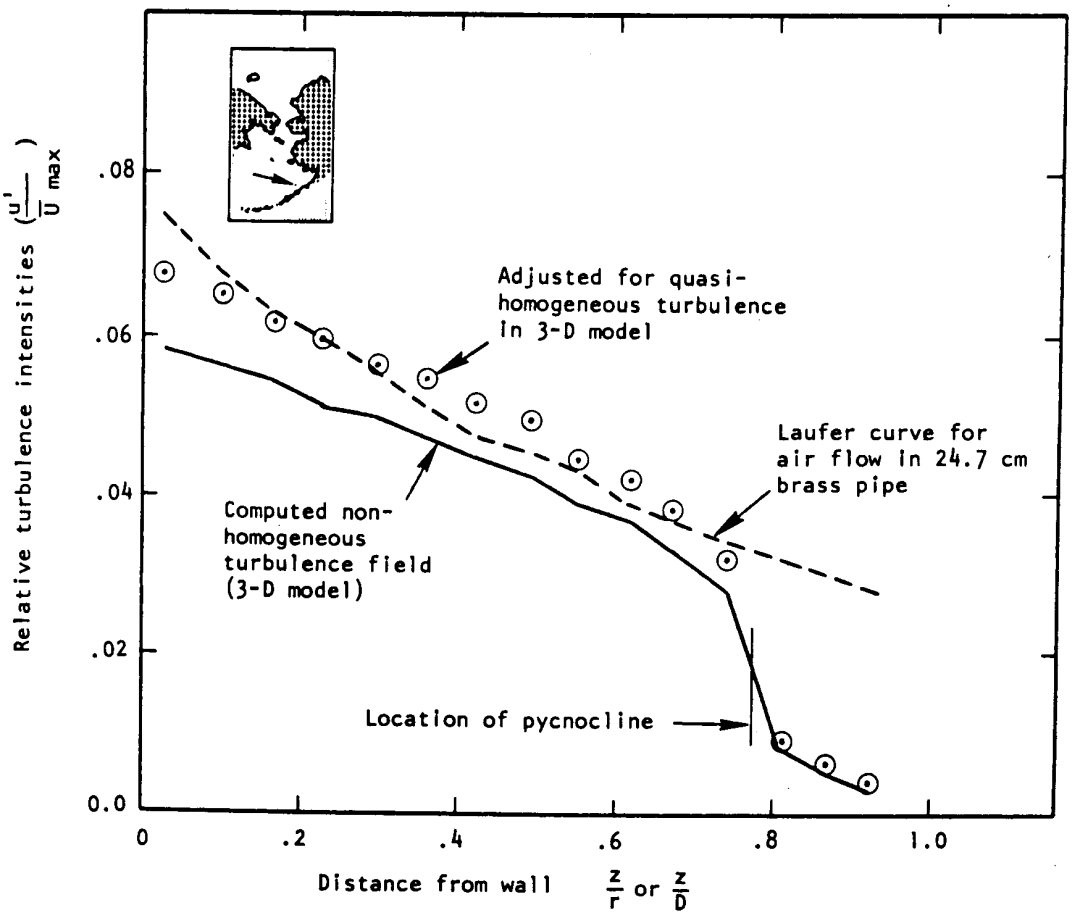

Fig. 2.7—Comparison of relative turbulence intensities between the three-dimensional model for stratified flow field and the standard verification curve of air flow measured in a pipe (Laufer, 1954).

3. MODELING COASTAL HYDRODYNAMIC PROCESSES

MODELING TIDES, RESIDUALS, AND BAROCLINIC CIRCULATION IN THE ALASKAN OUTER CONTINENTAL SHELF

Tides are probably the most important and consistent driving force in the Alaskan shelf waters. For example, about 90 percent of current energies over the Bering shelf are of tidal origin. Tides over these shelves are driven primarily by astronomical tides of the Pacific Ocean and of the Arctic Ocean. Amplitudes of the Pacific tides are substantially larger than the Arctic tides and they penetrate through the Aleutian Islands, entering the Bering Sea. The two tidal systems encounter each other near the Bering Strait where exchange of water masses takes place. Tides are believed to be one of three major factors that cause the exchange of water. Other than atmospheric forcing and density-induced circulation, the difference in tidal characteristics between the Bering Sea and the Chukchi Sea is that they also induce residual currents through the Bering Strait.

When in deep water, tides do not generate significant tidal currents. Consequently, bottom dissipation and the shore's effects are minimal. Tides, as a long wave, tend to maintain their characteristics without much deformation until they reach the continental shelf. When tides propagate through the shallow shelf area, the nonlinear advection terms in the equation of motion generate higher harmonics of the fundamental frequency. When bottom dissipation is not considered, the second harmonic increases in amplitude with the distance of propagation into the coastal zone. On the other hand, bottom friction generates odd harmonics. A sloping bottom and configuration of the shoreline induce the dispersion of tidal energy across frequencies by the mechanism of nonlinear advective transport. These higher-order mechanisms not only modify tidal levels along the coastline, but more important, they create residual transport responsible for carrying floating and soluble substances for longer time periods, which was of particular importance to the impact studies.

Thus models were built to simulate the tides in the Alaskan coastal waters. The models used in our studies are shown in Fig. 3.1. As this figure indicates, we developed submodels in some of the model areas. The areas covered by these submodels were of particular interest in the impact studies and required more geographical detail or were intended to provide estimates of tides and currents to plan field surveys in subsequent years.

The model for the Gulf of Alaska extends westerly to 165°W with its southern boundaries at 52°. Water-level boundary conditions from Muench and Schumacher (1980) and Schwiderski (1978) were used at all seaward extremities of the modeled area. The grid size in latitudinal direction was 0.25°, and in longitudinal direction 0.5°. The model has ten layers in the vertical direction.

The submodel of the western Gulf extended to the edge of the continental shelf and had more resolution. The grid size on latitudinal direction was 0.125°, and in longitudinal direction 0.25°. The water-level boundary conditions were obtained from the Gulf of Alaska model.

For the investigation of the hydrodynamic processes in the eastern Bering Sea, the primary model was of the continental shelf of the Bering Sea together with the Chukchi Sea (Fig. 3.1). The Chukchi Sea was included in the model as the tides of the Pacific Ocean interact with the tides of the Arctic Ocean near the Bering Strait, and it was expected that

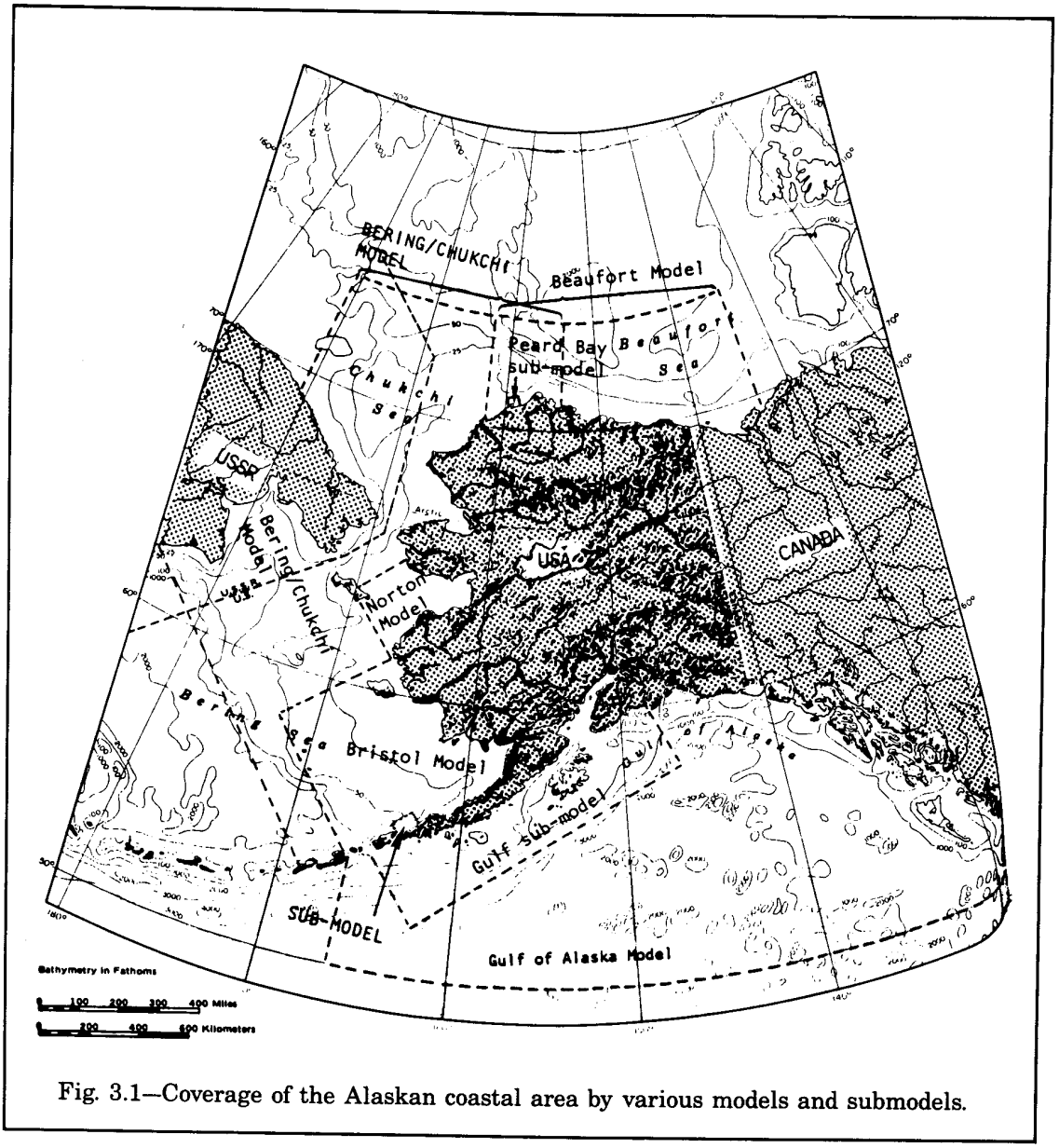

Fig. 3.1—Coverage of the Alaskan coastal area by various models and submodels.

this interaction would generate nonlinear residual currents. The model extends from 54°N to 74°N, and from 178°E to 156°W. The grid size in a northerly direction was 0.5° and in the longitudinal direction 1° was chosen. The model has a boundary running very close to the continental shelf break (Fig. 3.1). The tidal boundary conditions were based upon published data and water-level boundaries were used at all open boundaries. This three-dimensional model has ten layers in the vertical in the deeper sections. The seaward boundaries were

obtained from tide gauge measurements obtained by the Pacific Marine Environmental Laboratory (Pearson et al., 1981a, 1981b) in the vicinity of the model boundary.

The model of the Beaufort Sea covers the waters north of Alaska to 73°N. The western boundary is at 162°W and overlaps part of the Chukchi Sea model. The eastern boundary extends to the Mackenzie River delta at 133°W. The grid size in latitudinal direction is 0.16666° and in longitudinal direction 0.5°.

Even though our final interest is the residual circulation, the basic tidal mechanisms over these shelf areas are the first to be determined. We will proceed with the analyses from the southern coast, thence to the west coast, and finally to the northern Beaufort Sea.

MODELING TIDES IN THE GULF OF ALASKA SHELF

The model of the Gulf of Alaska is the largest model covering the Alaskan coastal waters developed by the authors. Because of the complex coastal features, a series of nested submodels is needed to resolve the circulation dynamics of the near-shore lagoons and the ecologically sensitive passage (Figs. 3.2 and 3.3). The embayment in the northeast corner of Fig. 3.2 is Cook Inlet, where the largest astronomical tides in the Pacific are found—sometimes reaching 13 meters. Also present are strong currents and residual circulation induced by nonlinear interaction between the advective mechanism and the bathymetry of the coast. The three-dimensional perspective diagram in the upper part of Fig. 3.4 illustrates the along-shore view of higher modes in the water-level variation with the highest point at the head of Cook Inlet, whereas the lower diagram shows cross-shore variations. Figure 3.5 shows the computed co-tidal chart for the semidiurnal component and the comparison between the computed amplitudes and phases at four locations where observed data are available (Schumacher and Muench, 1980). Figures 3.6 through 3.9 present the computed horizontal/vertical velocity components and the turbulent energy densities at levels 1, 3, 5, 7, 8, and 9 at a location near the opening of Cook Inlet (Portlock Bank). At that location the computed hodograph in Fig. 3.10 nearly matches the observed current ellipse. The vertical distribution of the magnitude of the computed current (Fig. 3.11) indicates that the vertical variability departs substantially from the logarithmic distribution commonly present in a shallow tidal embayment.

The computed tidal ellipses for the entire Gulf of Alaska (from Vancouver Island to the Aleutian Islands) are presented in Fig. 3.12. To show the strong tidal currents within Cook Inlet and over shelf areas, the plotting scale is set at 200 cm/sec per grid spacing. The maximum tidal currents can reach 140 cm/sec in either direction. Computed tidal residual current distribution within the Gulf of Alaska is presented in Fig. 3.13. In Fig. 3.13 the maximum residual current in Cook Inlet is approximately 7.5 cm/sec, which is 5.5 percent of the local maximum tidal current. Over the shelf and in Shalikof Strait the direction of the residual current is primarily to the southwest. Results from the model of the Gulf of Alaska have been reported in Liu and Leendertse (1987) in which aspects of the partitioning of tidally induced energetics are discussed.

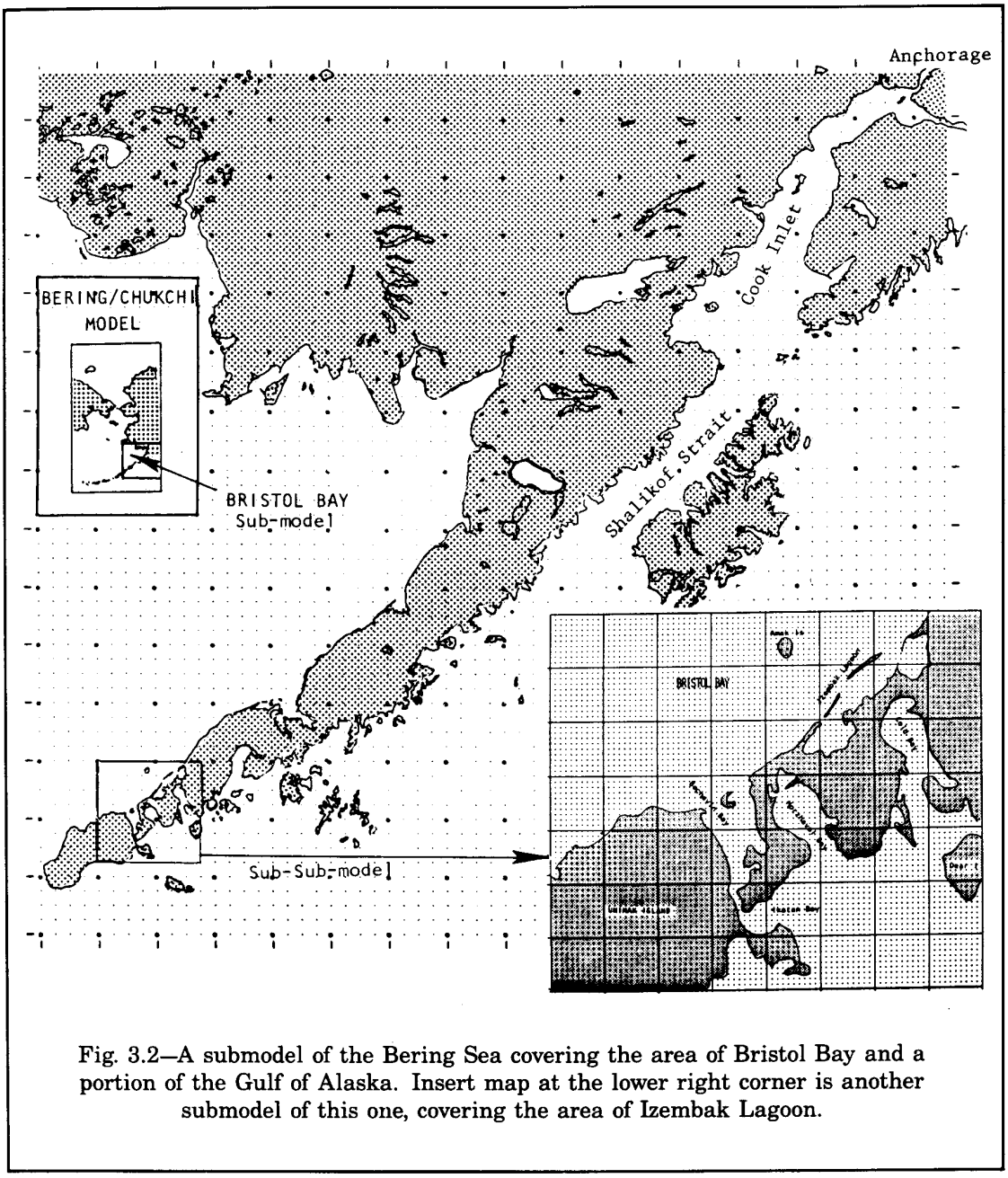

Fig. 3.2—A submodel of the Bering Sea covering the area of Bristol Bay and a portion of the Gulf of Alaska. Insert map at the lower right corner is another submodel of this one, covering the area of Izembak Lagoon.

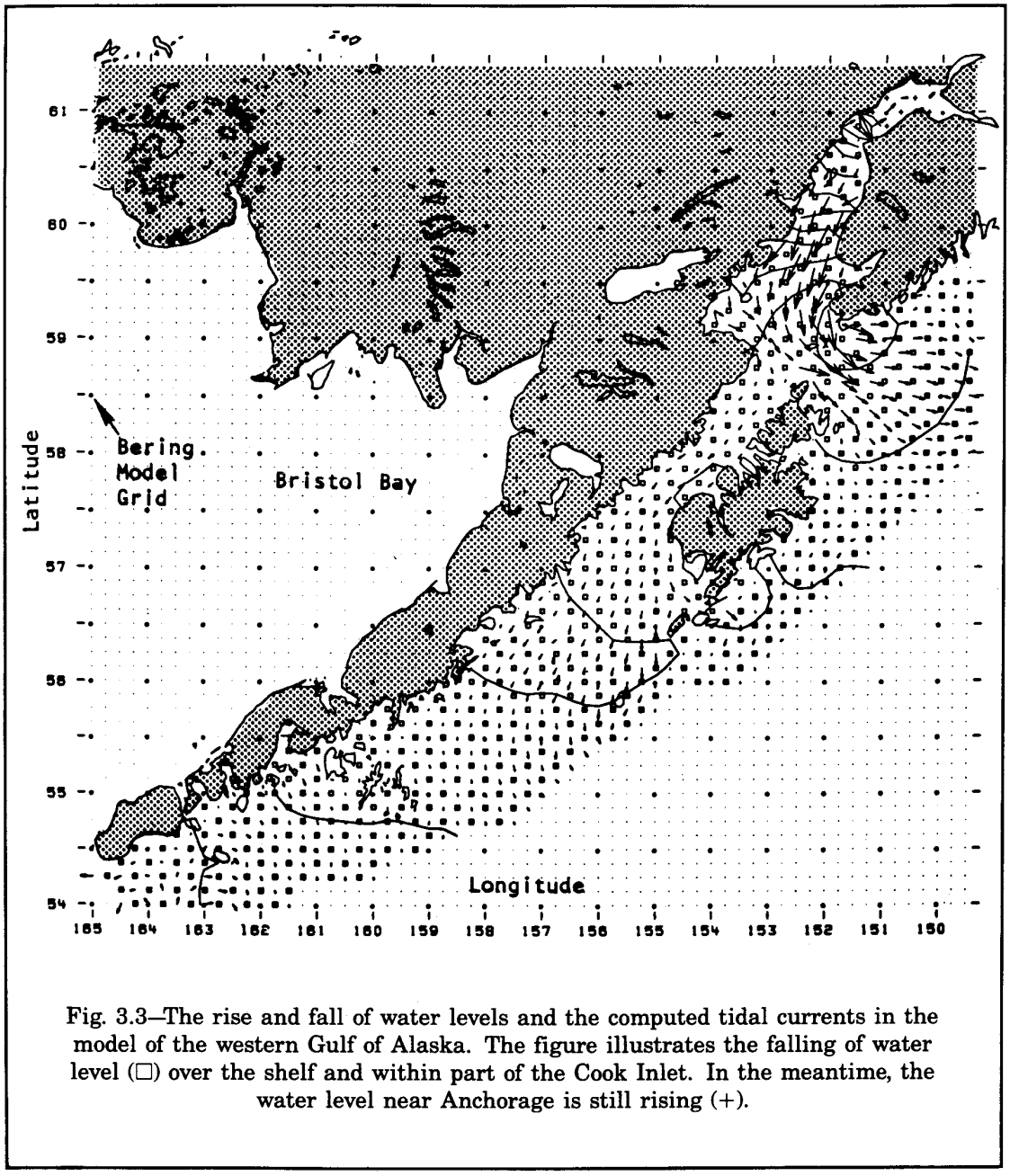

Fig. 3.3—The rise and fall of water levels and the computed tidal currents in the model of the western Gulf of Alaska. The figure illustrates the falling of water level (□) over the shelf and within part of the Cook Inlet. In the meantime, the water level near Anchorage is still rising (+).

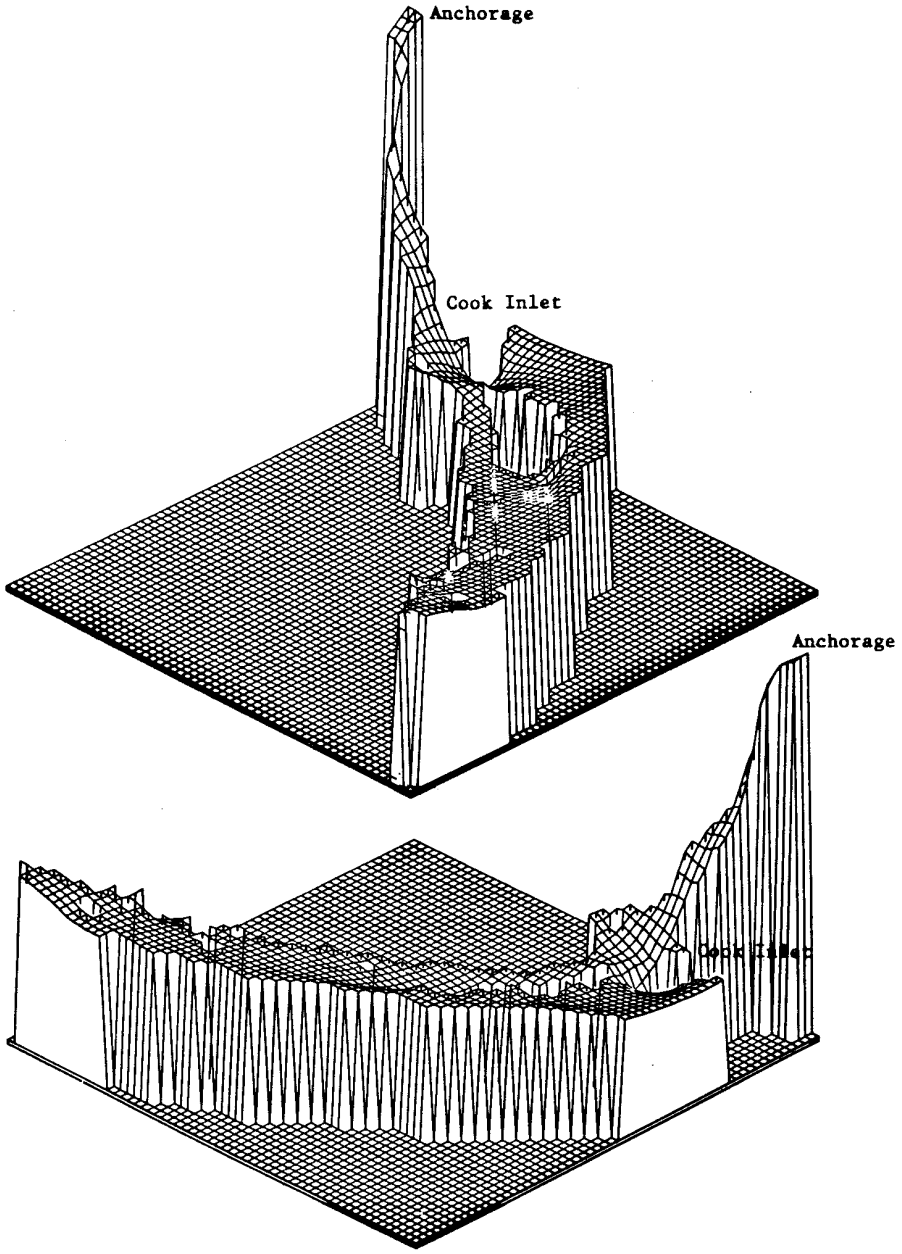

Fig. 3.4—Three-dimensional perspective diagrams illustrate the along-shore view of higher modes in the water-level variation with the highest point at the head of Cook Inlet near Anchorage (upper diagram). The lower diagram shows the cross-shore variation.

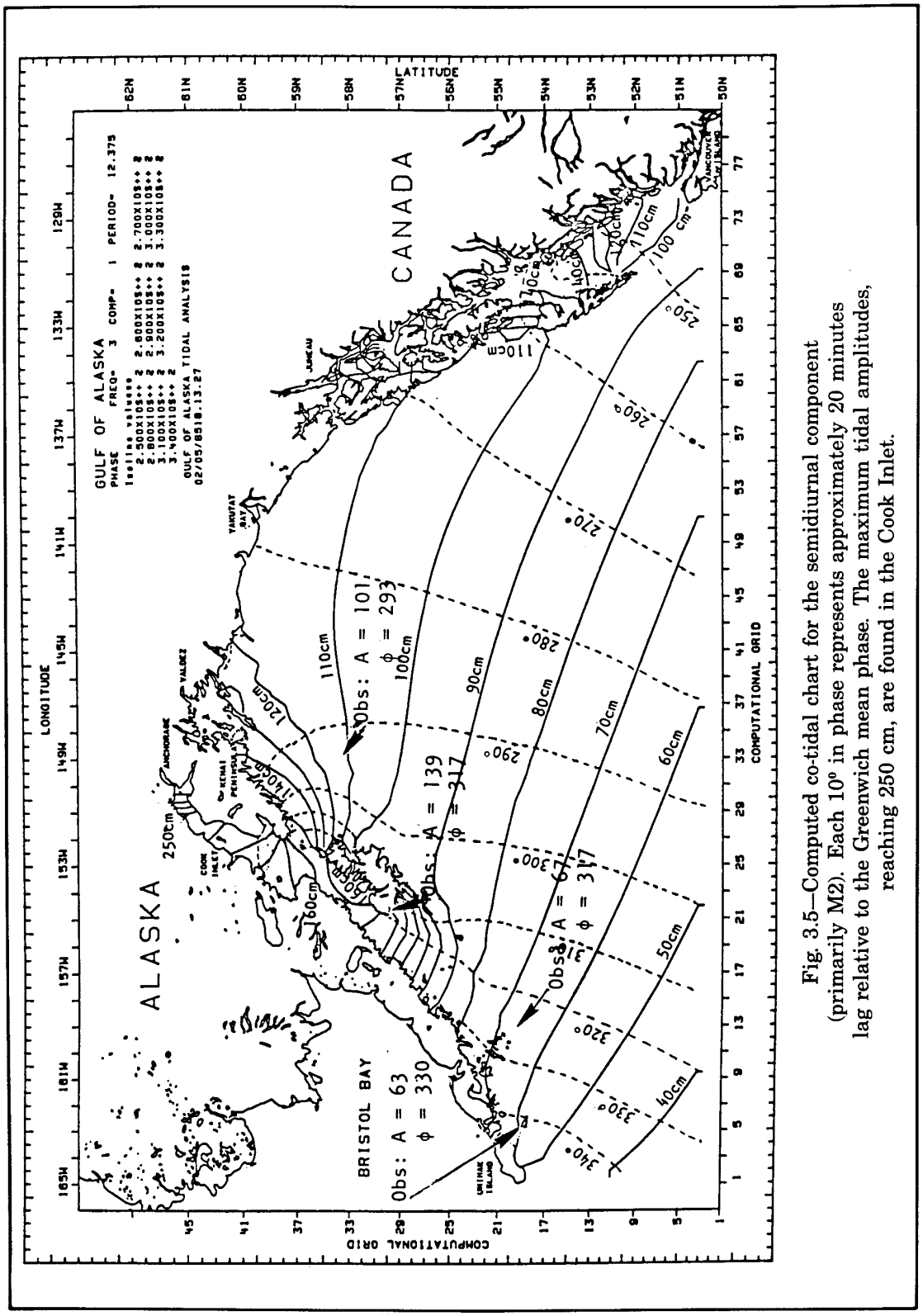

Fig. 3.5—Computed co-tidal chart for the semidiurnal component (primarily M2). Each 10° in phase represents approximately 20 minutes lag relative to the Greenwich mean phase. The maximum tidal amplitudes, reaching 250 cm, are found in the Cook Inlet.

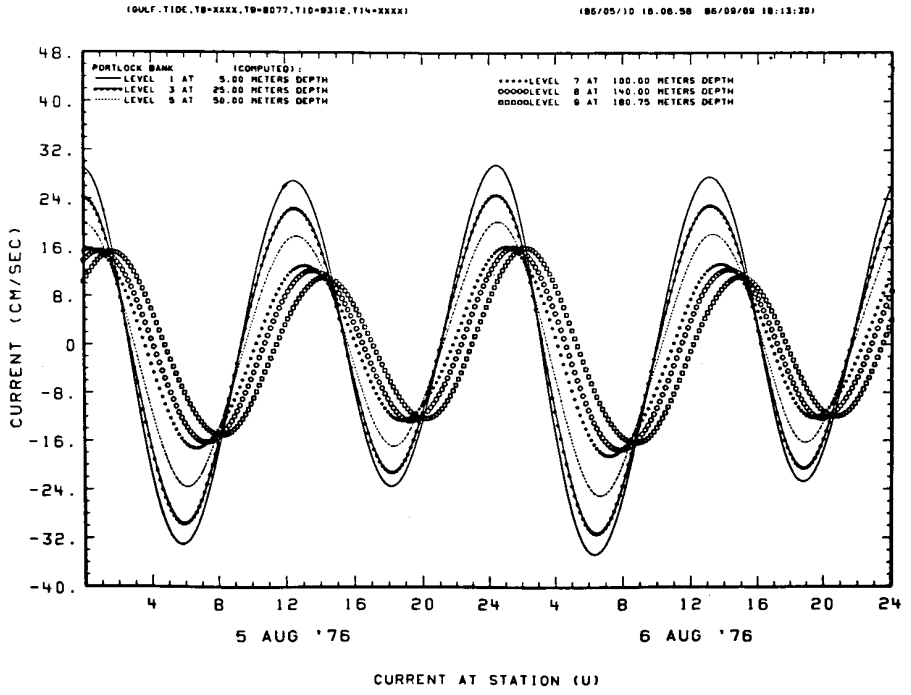

Fig. 3.6—The computed east-west velocity components at six representative layers near the mouth of Cook Inlet (Portlock Bank).

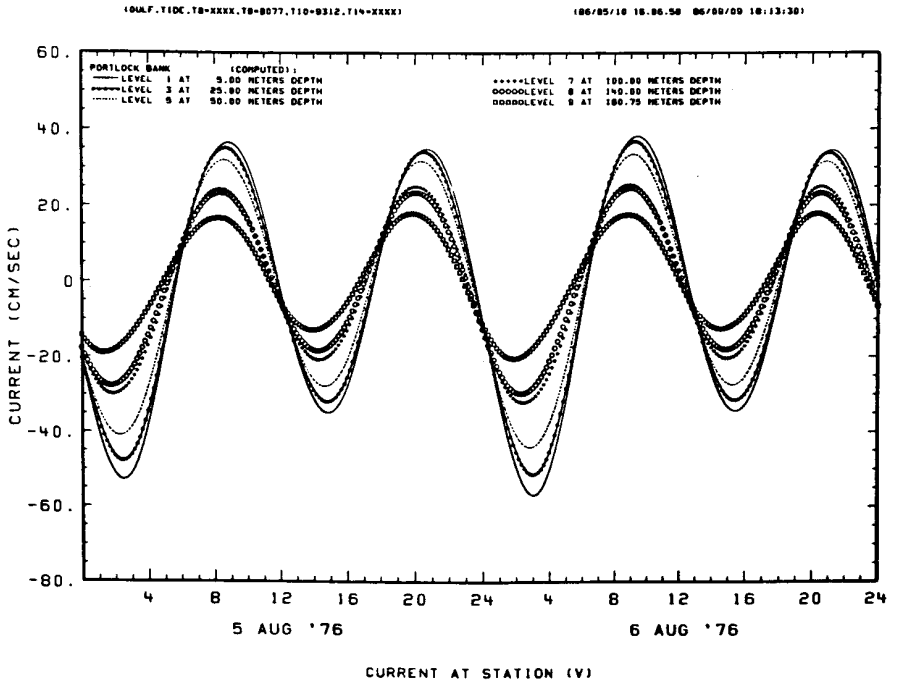

Fig. 3.7—The computed north-south velocity components at six representative layers near the mouth of Cook Inlet (Portlock Bank).

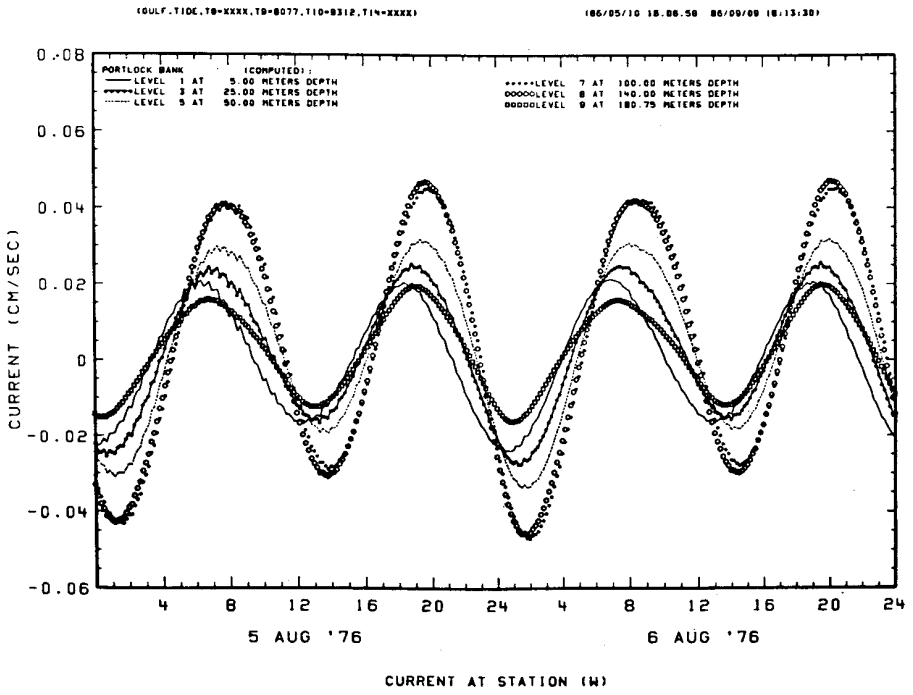

Fig. 3.8—The computed vertical velocity components at six representative layers near the mouth of Cook Inlet (Portlock Bank).

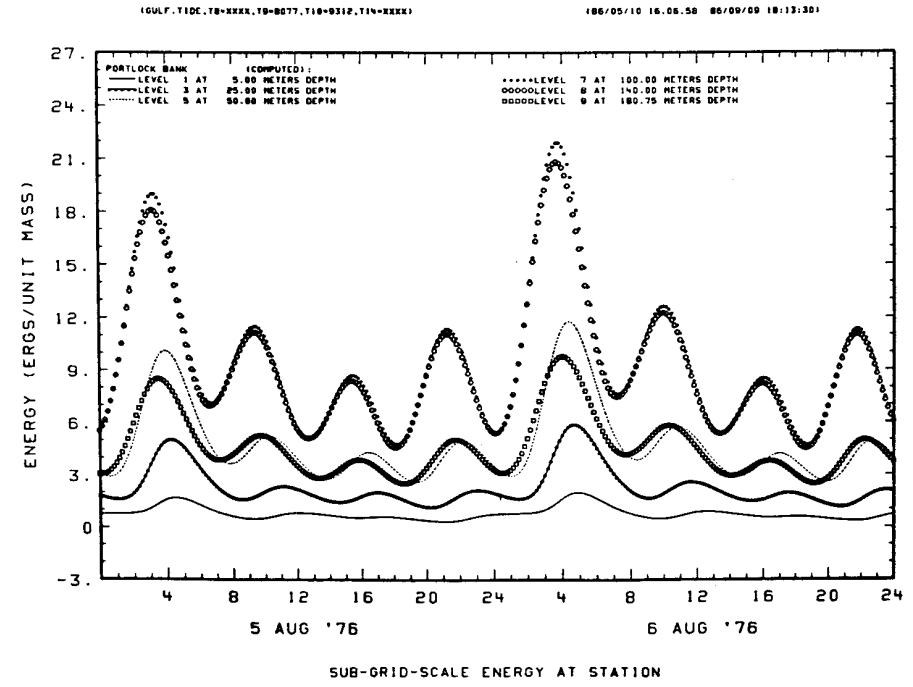

Fig. 3.9—The computed turbulent energy densities at six representative layers near the mouth of Cook Inlet (Portlock Bank).

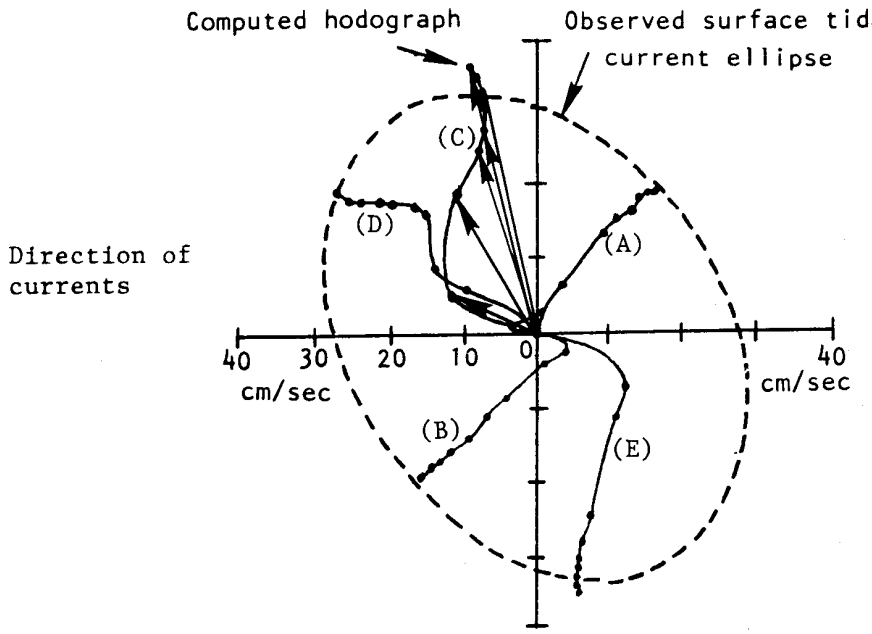

Fig. 3.10—Comparison between the computed hodograph and the measured surface tidal current ellipse.

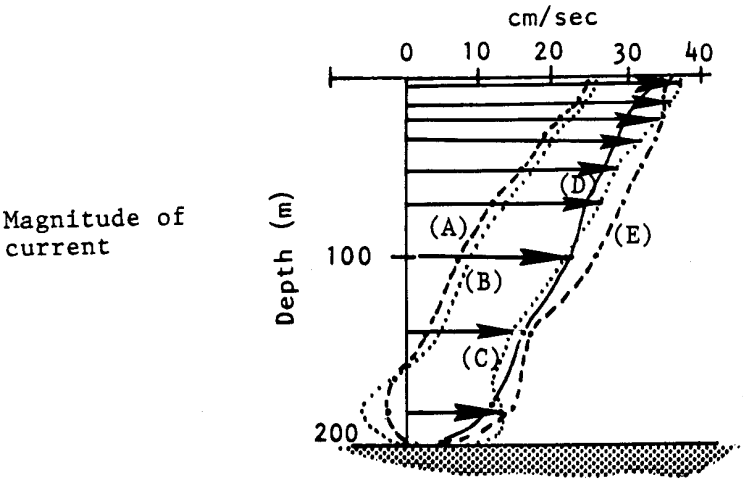

Fig. 3.11—Vertical distribution of magnitude of the computed currents illustrated in the hodograph (near Cook Inlet).

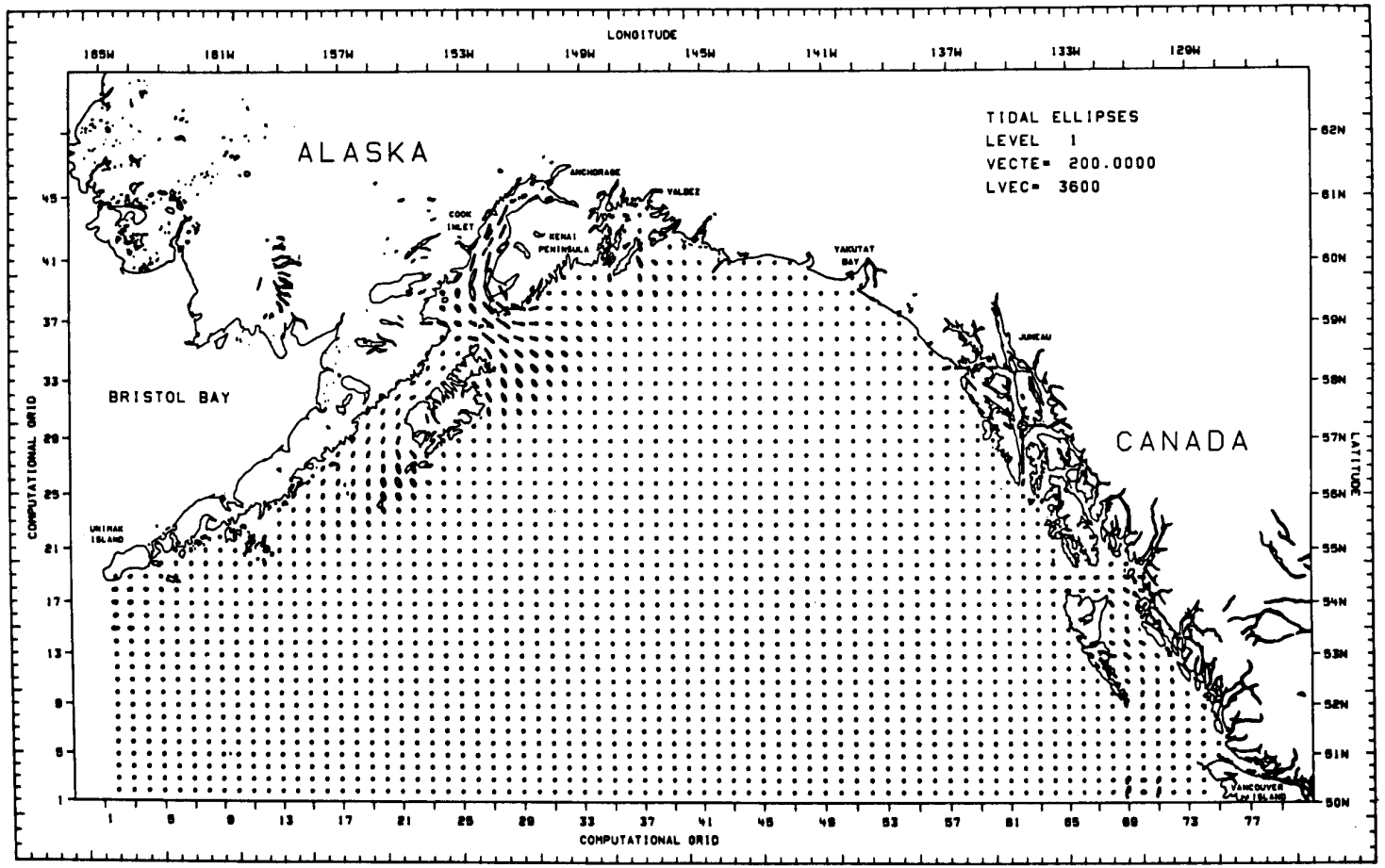

Fig. 3.12—Computed tidal ellipses (at 5 m level) in the Gulf of Alaska using a plotting scale of 200 cm/sec per grid spacing. Maximum tidal excursions are found in the middle of Cook Inlet where the tidal currents can reach 140 cm/sec in either direction. Currents over the shelf break near Kodiak are of elliptical rotary-type and can reach a maximum speed of 70 cm/sec.

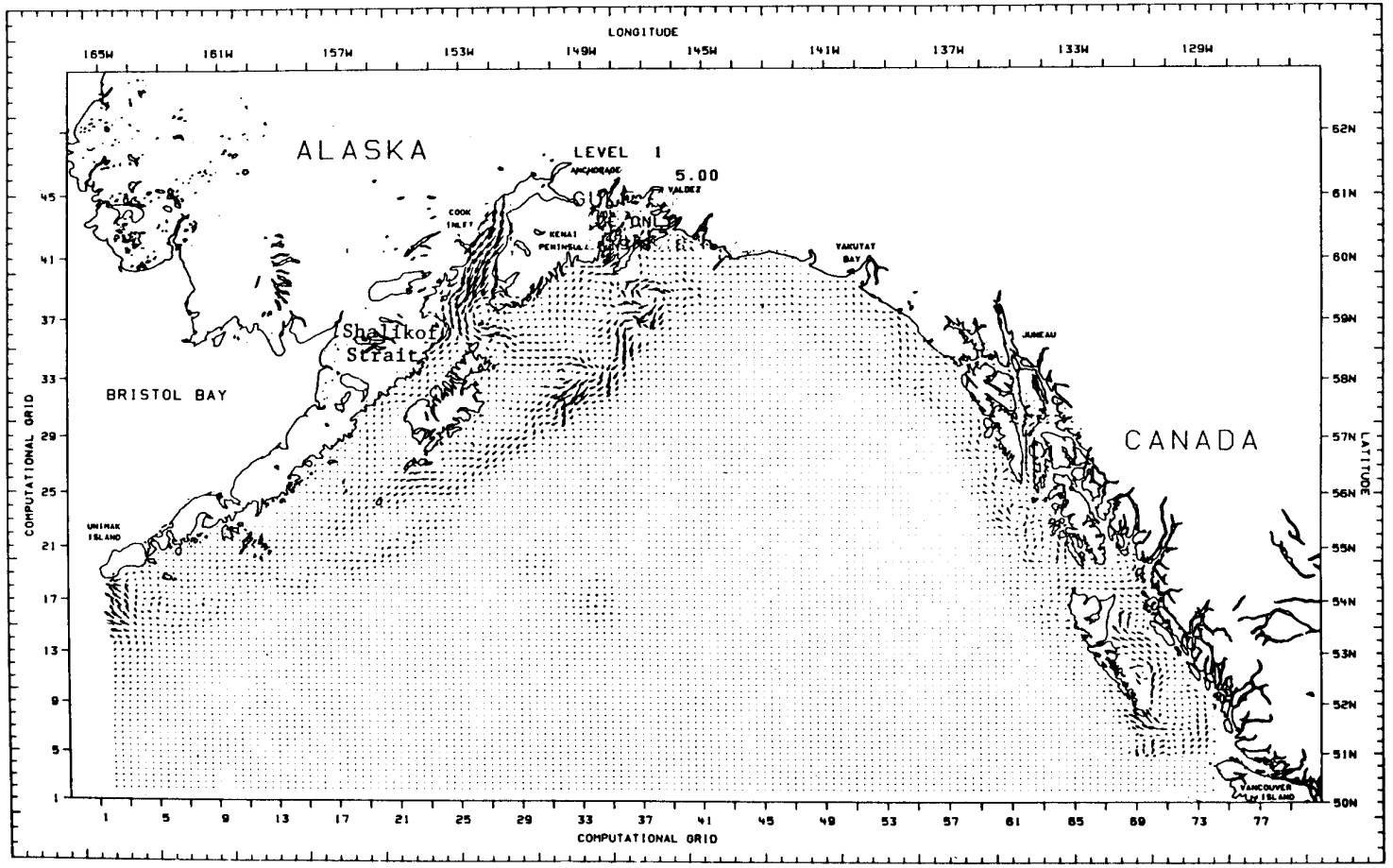

Fig. 3.13—Computed tidal residual circulation (at 5 m level) in the Gulf of Alaska using a plotting scale of 5 cm/sec per computational grid. Maximum residual current in the middle Cook Inlet can reach a speed of 7.5 cm/sec, which is approximately 5.5 percent of the local maximum tidal current. Over the shelf break and in the Shalikof Strait, residual currents flow primarily toward the southwest.

MODELING TIDES IN THE EASTERN BERING SEA

The propagation of tides in the study area is dominated by the bathymetry and to a certain extent is influenced by the vertical density structure. The bathymetric representation of the three-dimensional model is shown in Fig. 3.14. For the study of tide propagation during the summer when the deeper shelf waters are stratified, a simulation period in early August 1976 was selected. Figure 3.15 shows an instantaneous distribution of computed tidal currents and water levels plotted on a chart based upon the Mercator projection. The computed distributions reflect the conditions on August 2, 1976, at 6:00 A.M., but the simulation results do not reflect any influence of wind, as no inputs for the wind field were used. The figure shows conditions at ebb over the shelf break with falling water levels. The simulation results indicate rising water levels in the eastern part of Bristol Bay, in Norton Sound, and over most of the Chukchi Sea.

Figure 3.16 shows the co-tidal chart for the semidiurnal tidal component M2 obtained from a simulation of several days. Several amphidromic points will be noted. This chart is in agreement with a co-tidal chart of the M2 tide component compiled from field data by NOAA (Pearson et al., 1981a, 1981b) shown as Fig. 3.17. As to be expected the amplitudes in the model, which are the apparent amplitudes during the simulation period due to all semidiurnal constituents, are generally larger than shown in Fig. 3.17, which is only due to the M2 component.

The analysis of the semidiurnal component made from model simulations indicated two amphidromic points from which we found no previous reference in the literature, namely, one located at the opening of the Gulf of Anadyr, and the other between St. Lawrence Island and the Bering Strait.

The computed co-tidal chart for the diurnal tide component is shown in Fig. 3.18. On the shelf in the Bering Sea two counterclockwise amphidroms are found near the entrance of Bristol Bay and Norton Sound. This is in agreement with the co-tidal chart compiled by NOAA from field data (Fig. 3.19, Pearson et al., 1981a).

Co-tidal charts provide good insight into the up and down movement of the water surface, but they do not reveal comprehensive information on tidal currents. This information could be obtained by making charts of tidal ellipses such as shown in Fig. 3.20. In this graph, the end points of the computed current vectors in the second layer of the model are shown over a period of 12.5 hours of a simulation. It will be noted that in some parts of the system tidal ellipses are elongated, thus in those areas the tidal currents will be quite small during certain phases of a tidal cycle.

Results from a modeling also confirm two important tidal characteristics of the Bering Sea suggested by Harris (1904) based only on a small number of observations nearly 80 years ago. He suggested that after the tide enters from the Pacific the wave is retarded by the shallow shelf area while moving in a northeasterly direction. He also indicated that the shallow shelf section from Cape Navarin to the Pribilof Islands simply co-oscillates with the tide in the deep Bering Basin in the southwest. He continued to postulate that there would be a counterclockwise amphidrom at the opening of Norton Sound. His analysis, based on very limited field data, is remarkably in agreement with our findings and the field data collected by various surveys.

When comparing computed co-tidal charts with those derived from observed data it should be kept in mind that propagation of the tide is influenced by the vertical density structure. When a sharp pycnocline exists, the momentum transfer between the water

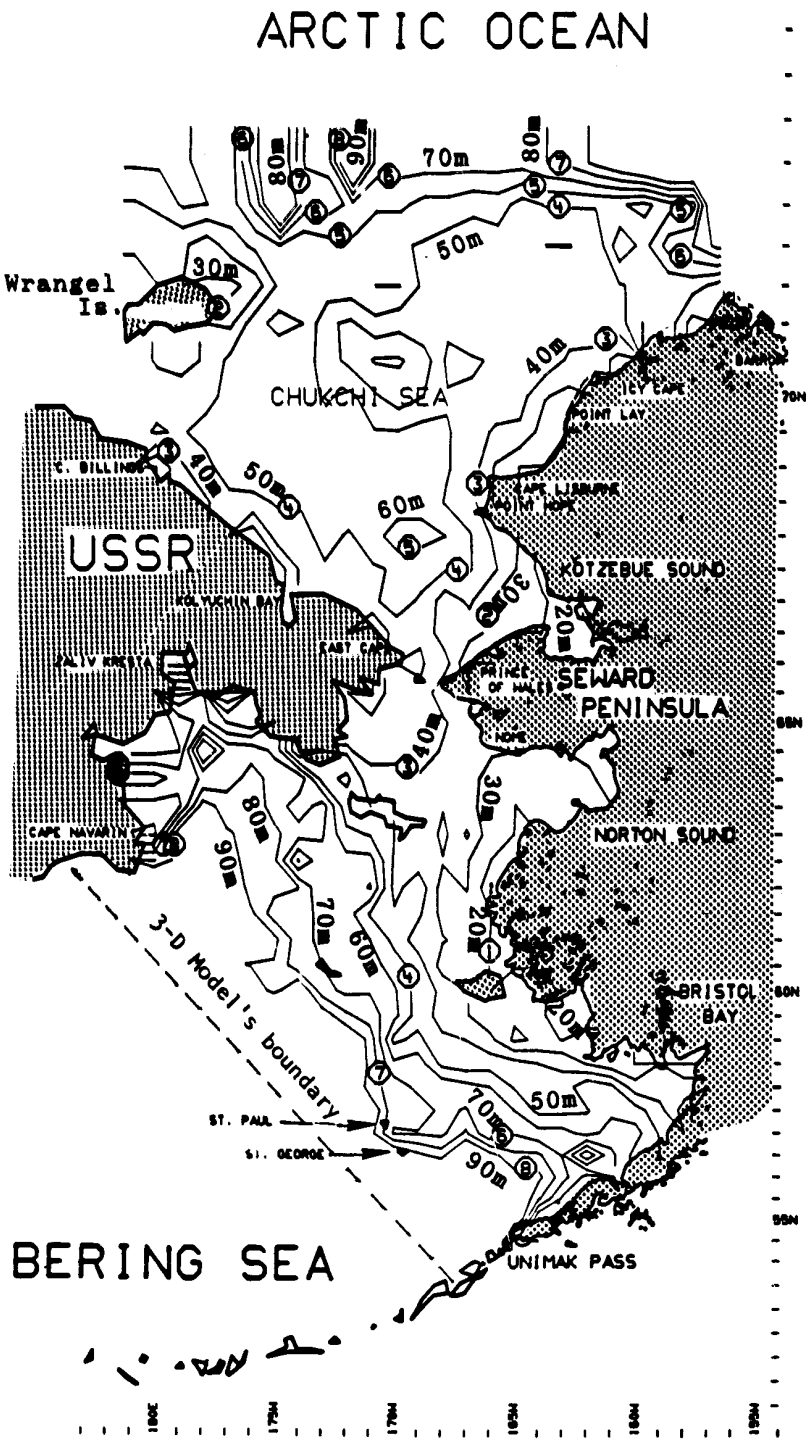

Fig. 3.14—Bathymetric schematization of the three-dimensional model of the Bering and Chukchi Seas.

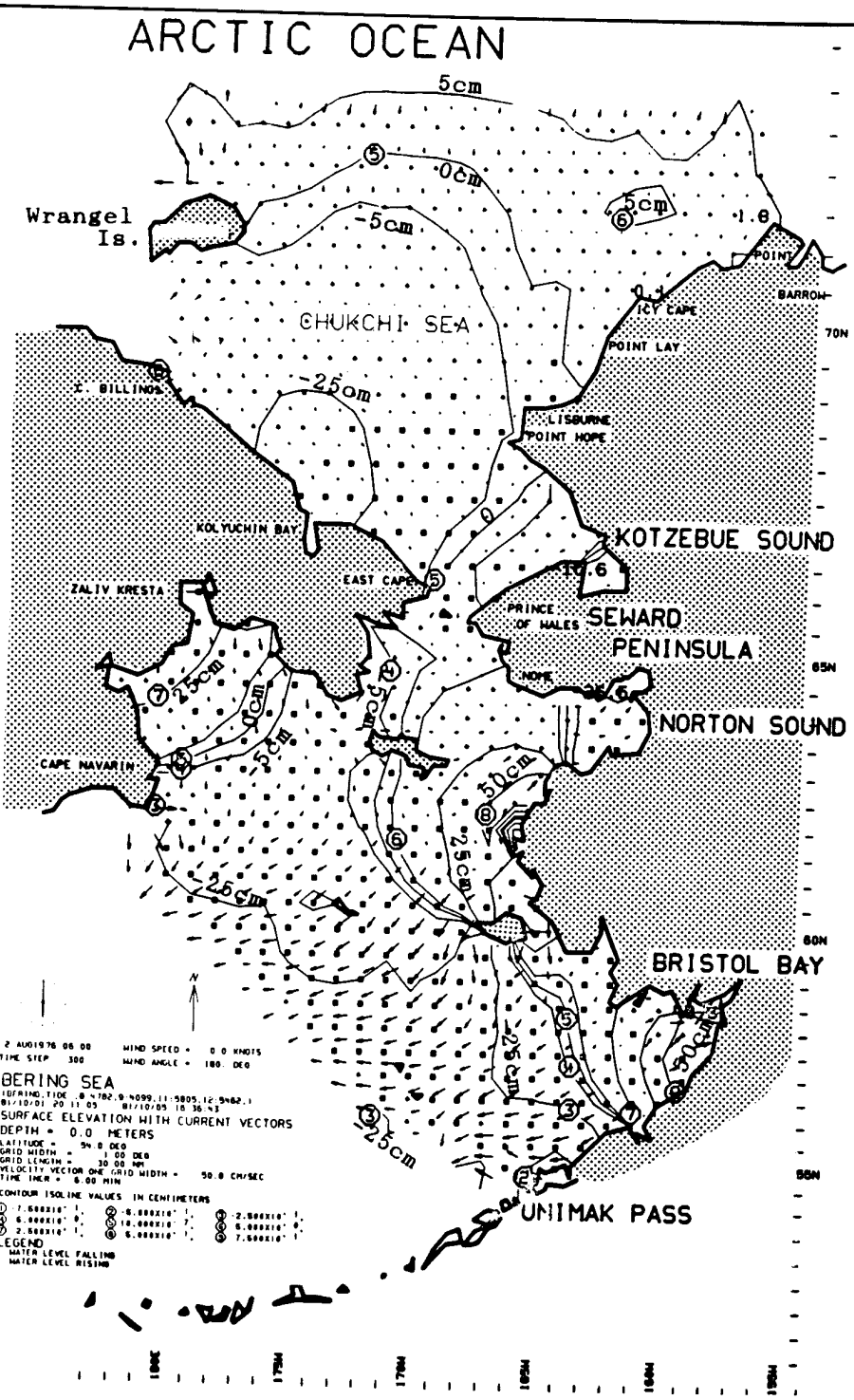

Fig. 3.15—Computed instantaneous tidal currents and water-level distributions in the Bering/Chukchi Sea system. + denotes that water level rises; □ indicates that local water level falls.

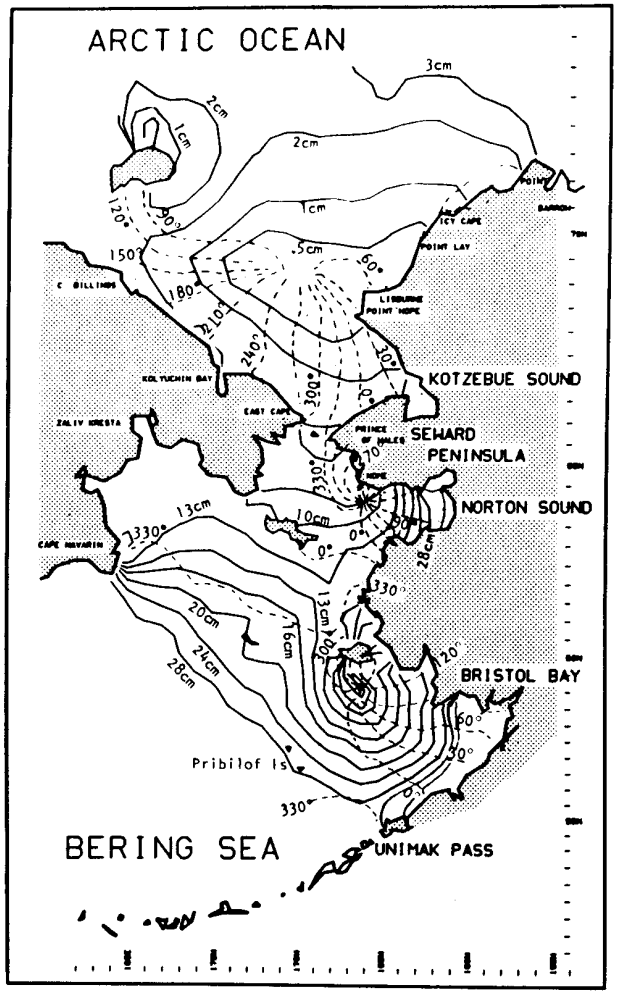

Fig. 3.16—Computed co-tidal chart for the semidiurnal tidal component using the three-dimensional model of the Bering/Chukchi Sea.

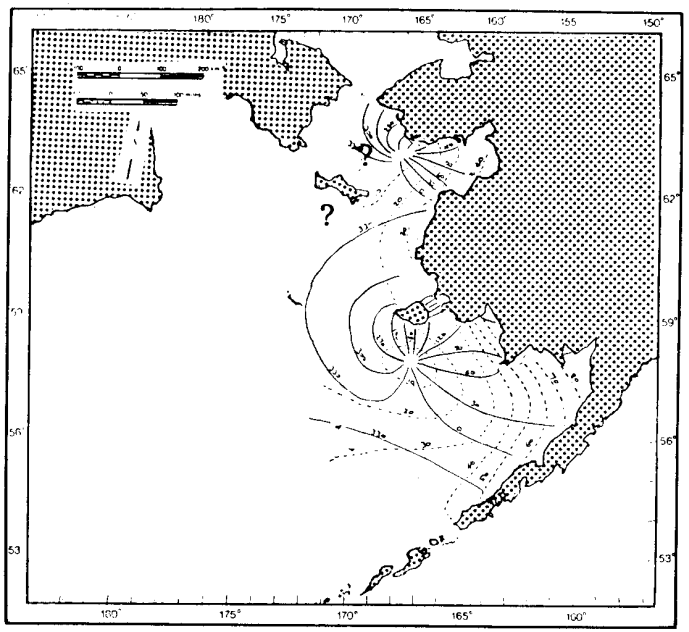

Fig. 3.17—Co-tidal chart for the semidiurnal tidal component M2 compiled by NOAA according to existing data (Pearson et al., 1981a).

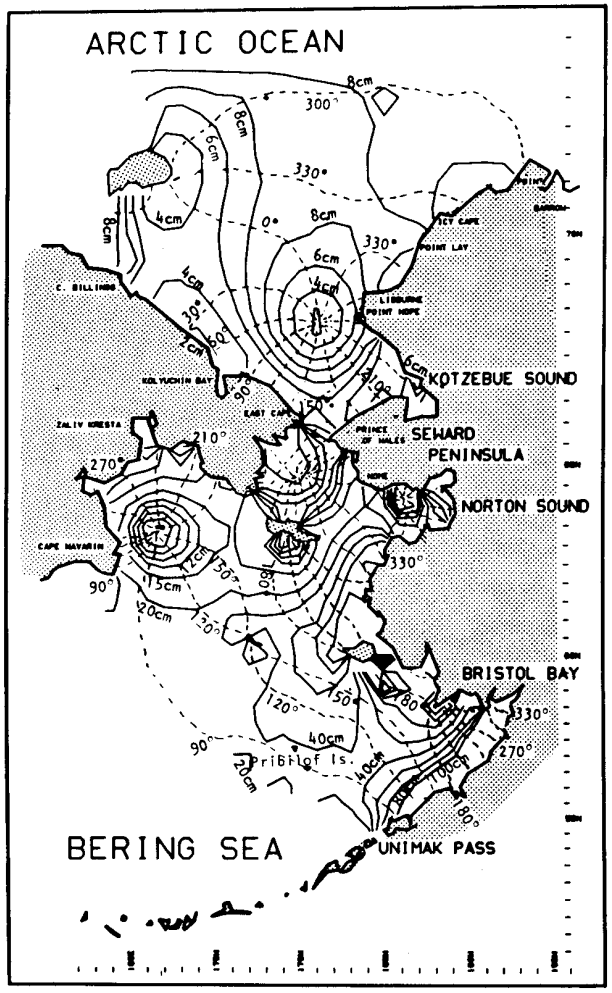

Fig. 3.18—Computed co-tidal chart for the diurnal tidal component using the three-dimensional model of the Bering/Chukchi Seas.

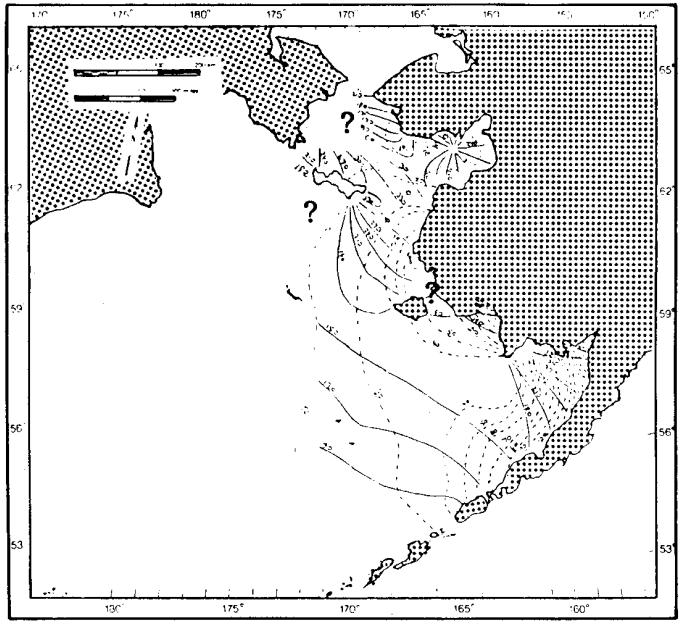

Fig. 3.19—Co-tidal chart for the diurnal tidal component (K1) compiled by NOAA according to existing data (Pearson et al., 1981a).

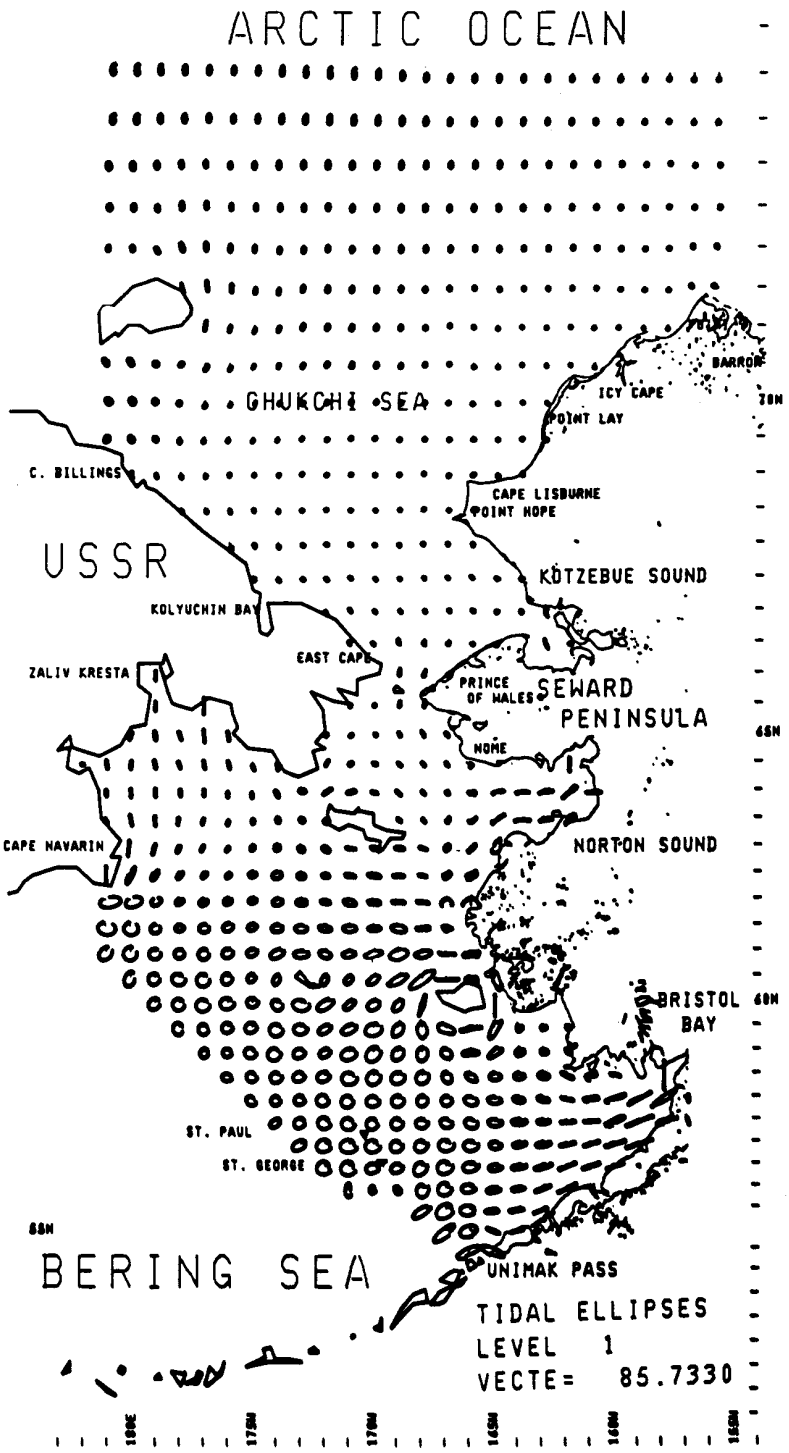

Fig. 3.20—Computed 12.5 hr tidal ellipses in the first layer (at 2.5 m level) using a plotting scale of 86 cm/sec per horizontal grid spacing.

masses above and underneath the pycnocline is reduced compared to the well-mixed situation. It is known that some of the amphidromic points in the Alaskan waters shift in position when the sea makes the transition from a well-mixed sea to a stratified sea. For this reason considerable effort was made to obtain temperature and salinity data that would be consistent with the periods that were simulated. Aspects of salinity and temperature distributions will be discussed at the end of this chapter.

MODELING TIDES IN THE CHUKCHI SEA

Unlike tides in the Bering Sea, tides in the Chukchi Sea are a subsystem of the Arctic tides that enter the shallow Chukchi shelf from the east. The propagation of tides in the Chukchi Sea is dominated by the bathymetry and coastal configuration, and to a certain extent is influenced by vertical density structure. The latter was known to cause shifting of the location of amphidromic points during summer when a strong pycnocline existed. Under an average summer condition, model results indicate that an amphidromic system exists in the southern Chukchi Sea for both diurnal and semidiurnal tides. The findings were reported in Liu and Leendertse (1982).

Tides in the Chukchi Sea are substantially weaker than in the Bering Sea. The presence of ice and the weather systems sometimes dominates local energetics. However, when the influence of the weather is weak, tides dominate the circulation pattern in the vicinity of the Bering Strait and the southern Chukchi Sea.

Connecting two vastly different tidal systems, dynamics of circulation near the Bering Strait have been a focal point of interest for many years. We conducted numerical experiments with the three-dimensional model of the Bering Sea and the Chukchi Sea by forcing it only with tide and baroclinic fields associated with the summer salinity/temperature distribution described in more detail at the end of this chapter.

The computational results from the experiment were analyzed and the computed currents are shown in Fig. 3.21. The east-west component of the velocities are predominantly eastward and the flow reverses only during a short period in the tidal cycle.

The north-south components of the velocities are nearly always directed toward the north. The maximum north-south velocity component is in the surface layer and is 22 cm/sec. The magnitude of the current at that time is approximately 23 cm/sec, and the direction is approximately 17° from the north. Higher modes (overtides) can be noticed in the computed currents. They appear mainly in the lower layers where frictional effects are strong and the velocities lag behind those in the upper layers. These characteristics are more obvious in the computed vertical velocity components (top graph, Fig. 3.22). Friction retards bottom currents and thus induces vertical mass transport.

Turbulence variation in the bottom layer leads to variation in the upper layers, as the momentum transfer is inefficient because of the vertical pycno-structure, as shown in the bottom graph of Fig. 3.22. Note that the greatest turbulence intensity exists in the bottom layer and it is represented by small squares.

From similar graphs for a coastal station near Point Lay (Figs. 3.23 and 3.24), it can be found that during flood tide, a bottom long shore tidal current of 7.8 cm/sec is flowing in a direction that is 17° from the north. At the same time, the surface current has a speed of 6.1 cm/sec and is flowing in a direction 31° from the north. During ebb tide a bottom current of 2.2 cm/sec exists, which is flowing 144° from the north, whereas the surface current is approximately 2 cm/sec to the south. Consequently, the direction of the net tidal transport is along the shore to the north.

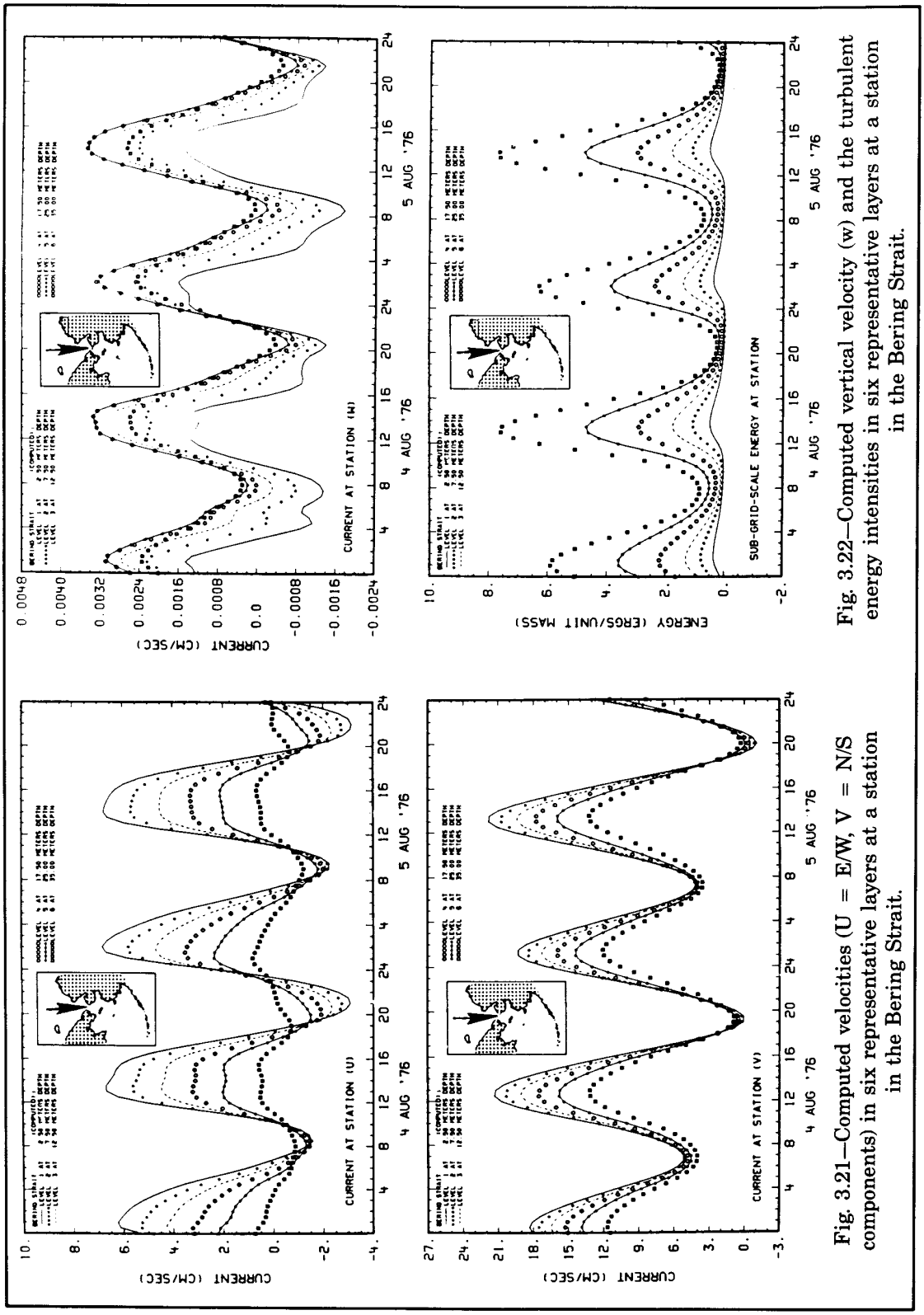

Fig. 3.21—Computed velocities (U = E/W, V = N/S components) in six representative layers at a station in the Bering Strait.

Fig. 3.22—Computed vertical velocity (w) and the turbulent energy intensities in six representative layers at a station in the Bering Strait.

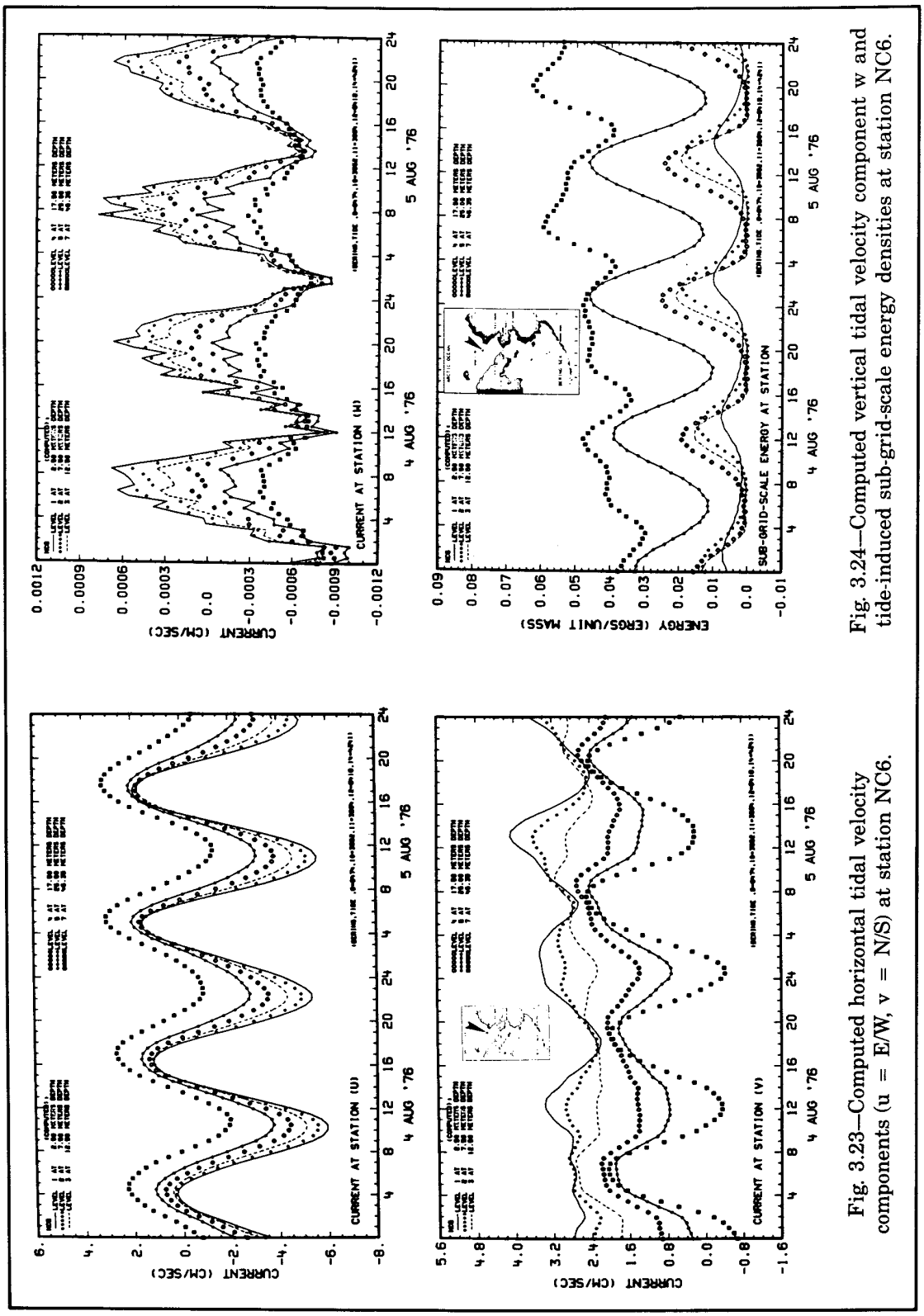

Fig. 3.23—Computed horizontal tidal velocity components (u = E/W, v = N/S) at station NC6.

Fig. 3.24—Computed vertical tidal velocity component w and tide-induced sub-grid-scale energy densities at station NC6.

The simulation results of the two stations described above are characteristic for the model area.

MODELING TIDES IN THE BEAUFORT SEA

The propagation of tides in the Beaufort Sea is strongly influenced by the bathymetry. The tidal currents are mostly weak, and tidal currents of appreciable magnitude are present only near the large flat shelf area northwest of Point Barrow and in several embayments. The tidal amplitudes are also small and the maximum semidiurnal tide in the model area with an amplitude of approximately 10 cm is near the head of Mackenzie Bay.

Even though the magnitude of tides in the Beaufort Sea is small, compared to other modeled areas, the residual currents in many areas reach similar magnitudes to those in other areas and are more complicated. As these residuals are of considerable significance in modeling studies of the dispersion and transport of spilled oil, considerable effort was made to obtain a good representation of the tide.

In addition to the bathymetry, the very shallow pycnocline, ice coverage, and Coriolis effects associated with the high latitude influence the propagation of the tide. During most of the year the Beaufort Sea is covered with ice; only during the summer are there open areas close to shore. Thus ice had to be considered in all simulations.

The simulations with the model were made initially as a guide for the design of a field survey. From these simulations tidal charts were prepared from which the semidiurnal co-tidal chart is shown in Fig. 3.25. Several tide gauges were installed in the summer of 1983, and in 1984 results of the analysis of the tidal records obtained by Pitman (1984) became available. In the co-tidal chart, we have shown observed and computed semidiurnal tidal components at the location of the gauges. The agreement was good except near Hershel Island where the measured amplitude is 2 cm higher than the computed amplitude. This difference is very likely due to local effects; the computed amplitude is for the sea offshore, whereas the tide gauge was deployed behind a barrier island to protect it against ice scour.

In the literature we found another reference to tidal amplitudes in the Beaufort Sea (Kusunoki et al., 1962), namely, measurements obtained from the grounded Fletcher's Ice Island (T3). Observations made on this ice island are considered most suitable to study tides and storm surges, as the depth in the vicinity of the grounded island was very uniform. The location northwest of Point Barrow was far removed from land and thus was removed from shore effects. The agreement between this observation and our simulation was very good.

The simulations for summer conditions indicated that tidal currents near shore were highly influenced by shore effects, particularly where pack ice is present. This can be seen from the chart of tidal ellipses abstracted from a simulation and shown in Fig. 3.26. At those locations the fresh water beneath the ice and sharp pycnocline limits the vertical momentum transfer. The movement of ice is not in phase with the movement of the water underneath, and the nonlinear momentum transfer generates higher harmonics in the tide in addition to those generated by the shallowness of the coastal water. Later we will see that residual currents are generated in those regions. Note that tidal ellipses from Cape Halkett to Prudhoe Bay, in particular, have very unusual shapes.

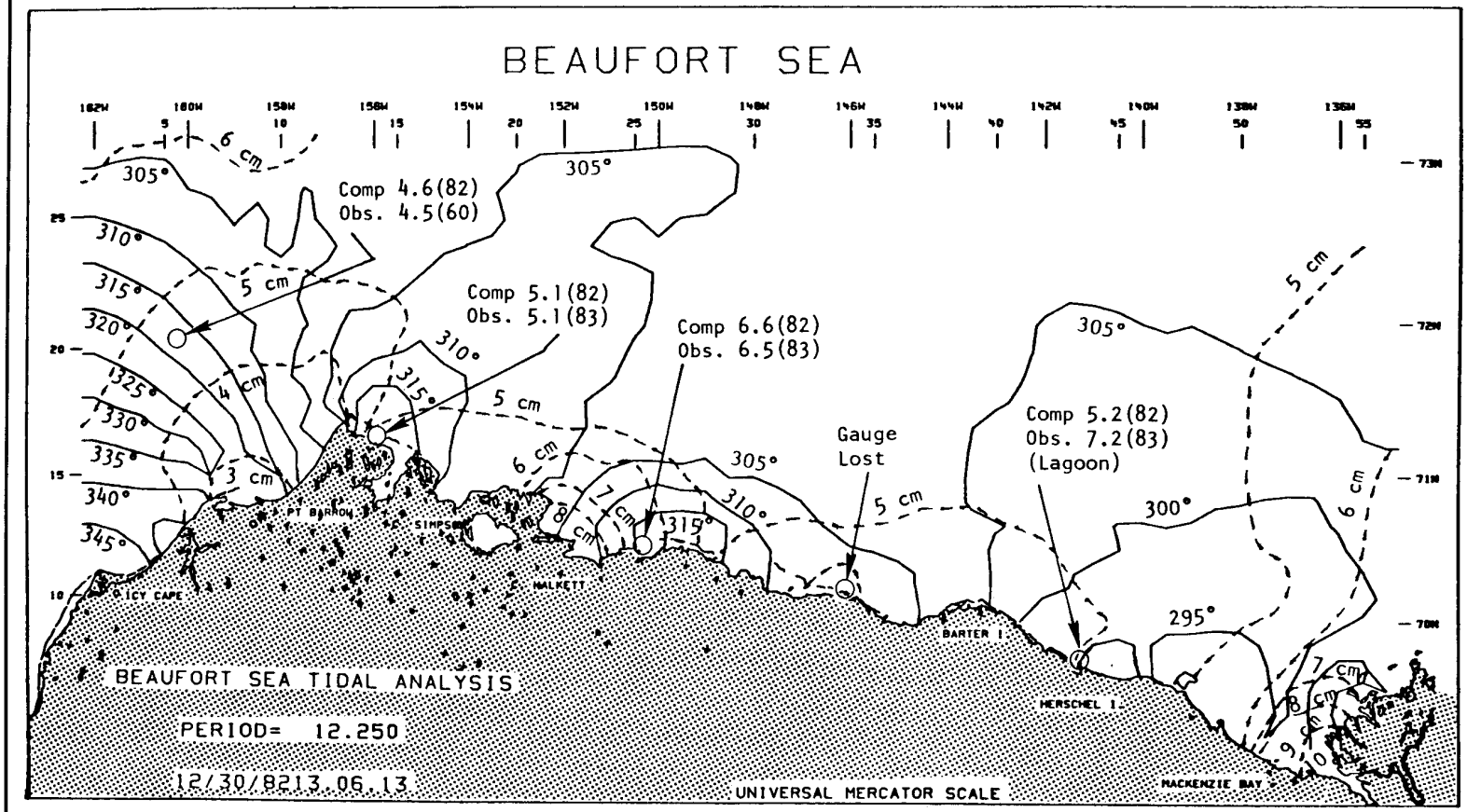

Fig. 3.25—Computed co-tidal chart for the semidiurnal component in the Beaufort Sea showing amplitudes in centimeters and Greenwich phase in degrees. Maximum amplitudes are located near Cape Halkett and Mackenzie Bay.

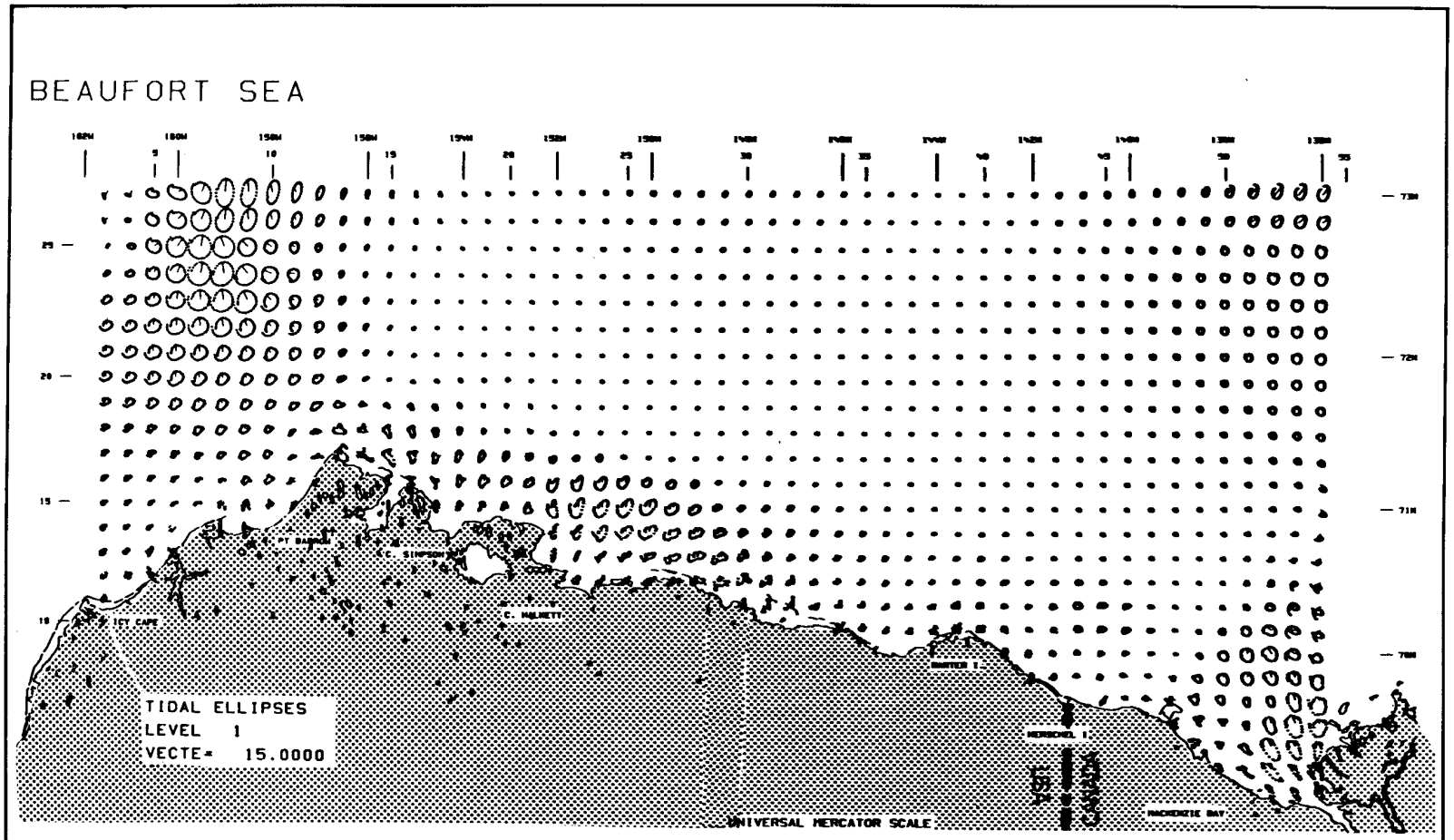

Fig. 3.26—Computed tidal current ellipses in the surface layer (at 2.5 m level) of the Beaufort Sea model with a plotting scale of 15 cm/sec per grid spacing. Magnitudes of tidal currents are inversely proportional to the local depth, whereas the shape of the tidal ellipses reflects the shore effects.

MODELING WIND-INDUCED CIRCULATIONS

Other than tides, winds are the next most important driving force in the coastal hydrodynamic process. If the area covered by the model is small, and if there is no need to take into account wind effects generated outside the model area, the computation of wind-induced flow is relatively straightforward. The wind field can be assumed to have the same speed and direction over an entire modeled area; however, when a large model area is involved, the wind field to be used varies in time and space.

For the study of the water movements resulting from wind in the eastern Bering Sea and the Chukchi Sea, the primary model contained the entire continental shelf. The need for a model of such a large area comes about because a storm passing through the southern Bering Sea may influence the hydrodynamics of the northern Bering Shelf, and vice versa. This became clearly evident when a 40-day current data series of a station in Norton Sound was analyzed.[1] Figures 3.27 and 3.28 show persistent nontidal oscillations in the current components after a numerical tidal eliminator was applied. The period of this oscillation is approximately 50 hours. This oscillation (seiching) of Norton Sound is generated by storms passing over the continental shelf. Such a storm passed over the recording station approximately 650 hours after the beginning of the record. The maximum nontidal current was approximately 30 cm/sec.

The passage of storms over the coastal waters of Alaska is very common, particularly over the eastern Bering Sea. The predominant direction of the cyclonic tracks is toward the northeast with an average passage time of one and a half to two days. Observation of such wind fields are generally difficult to obtain, as a dense network of weather stations is required for a good spatial resolution.

For the computation of wind-induced circulation with the three-dimensional model, the source terms in the turbulent energy balance equation and momentum equations are of major importance. The source for the energy balance equations is computed from the kinetic energy associated with the wind/wave field. For the case where the local water depth decreases, computations with the turbulent energy equation will then show that energy in the water column increases with a decrease in depth. Thus the model accounts for more intense mixing and dissipation, and larger bottom stress. When sufficient resolution is used in the model, these computations can even be extended up to the near-shore as all important physical processes are incorporated in the model formulation. Even though the model code is programmed to handle radiation boundary conditions, for the majority of the simulation, absorbing boundary conditions were imposed at the shelf break where water is much deeper than at the shelf.

Results of simulations with wind have been extensively used to determine the movement and dispersal of spilled oil, and these results will be presented in that context in Chapter 6. However, it seems appropriate to present some results and to illustrate the effects of the coastal configuration on wind drift in the eastern Chukchi Sea. Navigators in the eastern Chukchi Sea have noticed high currents in this area and have termed them the *coastal jets of the Chukchi Sea* (Wiseman and Rouse, 1980). To analyze this phenomenon, simulations were made with winds from the north as well as from the south, together with the tides. A wind speed of 10 knots was selected. After the run-in period of the simulation, we placed particles in the surface layer of the model at every grid point, followed these particles over a period of 48 hours, and made pathway plots of each particle.

[1] Original data were supplied by Dr. J. Schumacher of NOAA.

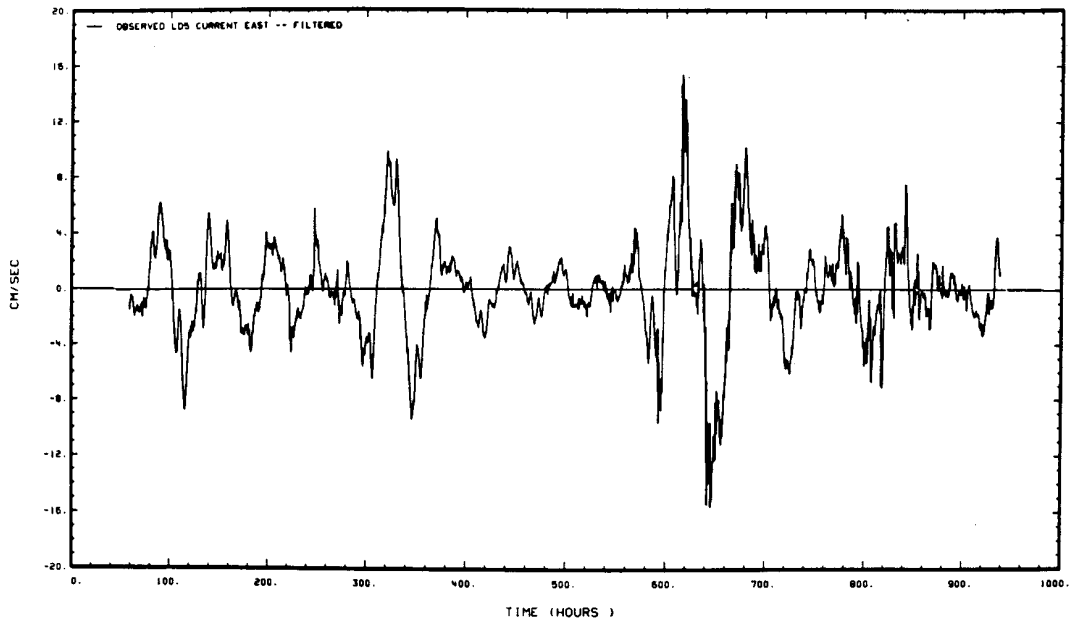

Fig. 3.27—Nontidal oscillations in the east-west velocity component of the observed currents at station LD-5 after applying the numerical filter which filters out energies in the primary and higher tidal modes.

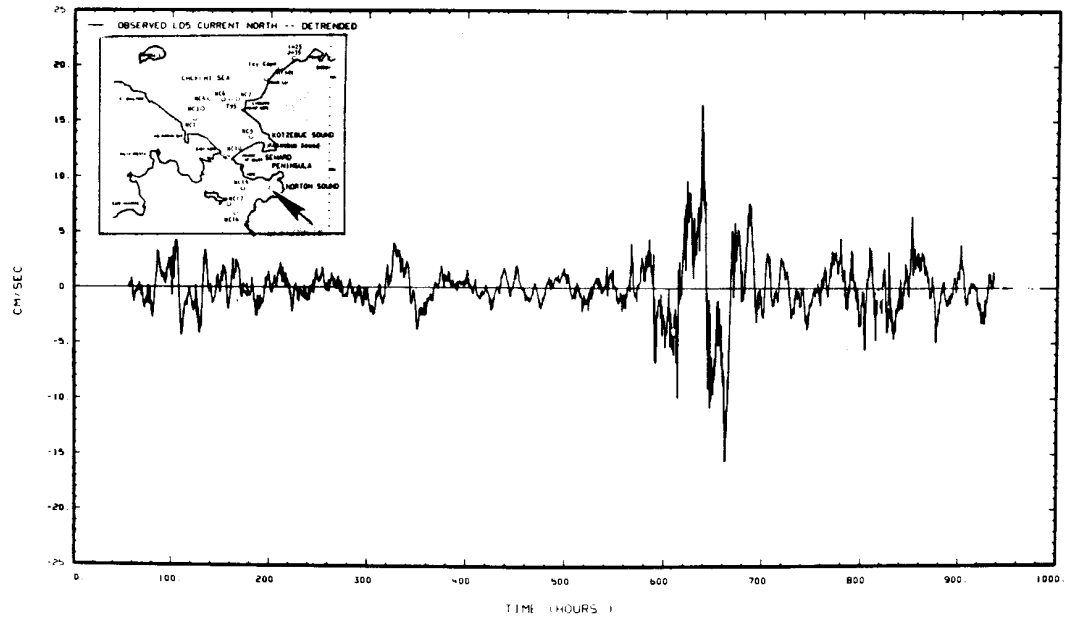

Fig. 3.28—Nontidal oscillations in the north-south velocity component of the observed currents at station LD-5 after applying the numerical filter which filters out energies in the primary and higher tidal modes.

When the wind blows from the south, areas with the largest particle displacements are in the Bering Strait and offshore Icy Cape (Fig. 3.29). However, when the wind direction is reversed and blowing from the north (Fig. 3.30) the area in the eastern Chukchi Sea with the largest displacement is still near Icy Cape. Note that the particle displacements in the Bering Strait, now small because of residuals, are in the opposite direction of the wind-generated current.

Figure 3.31 presents enlarged sections of water particle trajectories of the two previous figures. It is quite clear that a band of high speed coastal jet currents is present regardless of the wind direction. We will see below that this coastal jet would have a considerable effect on the movements of spilled oil in that area.

MODELING THE DENSITY FIELD AND THE RESIDUAL CIRCULATION

The hydrodynamic model used to compute the water motions contains the mathematical formulations for the evolvement of the salinity, temperature, and flow field in time. To start a simulation for a particular model area, the initial salinity and temperature fields are required. These data are furnished by the NODC project office. Figure 3.32 shows the salinity distribution in the surface layer of the model for the Bering Sea and the Chukchi Sea during a simulation of typical summer conditions. The lowest salinity (less than 20 g/kg) is located near the Yukon River Delta where fresh water from the river mixes with saline water of Norton Sound. Water of much higher salinity (approximately 29 g/kg) is found in the surface layer in the northwestern part of the Sound near Nome. Water in lower layers of the model have higher salinities, generally in the range of 29 to 34 g/kg.

In Fig. 3.33, the temperature distribution in the surface layer of the same simulation is shown. The highest temperatures are found in Norton Sound. At the head of the Sound (Norton Bay), summer temperatures can reach 14°C in the surface layer because of local solar heating. In the Chukchi Sea, temperatures vary over a large range in the surface layer for these summer conditions. In Kotzebue Sound, the temperature is 10°C and 2°C around Point Barrow.

The density structure in the vertical is as important as the horizontal distribution for its effects on the residual circulation. The vertical density structure is also important for dispersion processes on a relatively short time scale. To obtain an insight into the vertical distributions of salinity and temperature, cross-sectional graphs were made of simulation results. Figure 3.34 shows vertical salinity distributions through two sections of the model. Note that near the Bering Strait, water in the surface layer has a higher salinity than in the surface layers of the Bering Sea and Chukchi Sea. If we look at the east-west section at 70°N, it can be seen that near the Siberian coast, water has a much lower salinity than the sea near the Alaskan coast. The salinity distribution in this section shows that vertical salinity gradients are present in the whole section.

The graphs of the temperature distributions (Fig. 3.35) in the same vertical sections show the thermocline much more clearly than the graphs of the salinity distributions. This is due, in part, to the larger number of contour lines that are shown. In the longitudinal section, note that the temperatures decrease with higher latitudes, as was to be expected. The depth of the pycnocline is generally between 7 m and 15 m. This pycnocline is also present in the Chukchi Sea.

During summer several frontal systems are present. In the eastern Bering shelf area these frontal systems generally occur near the 50 m isobath. In the shallower area between

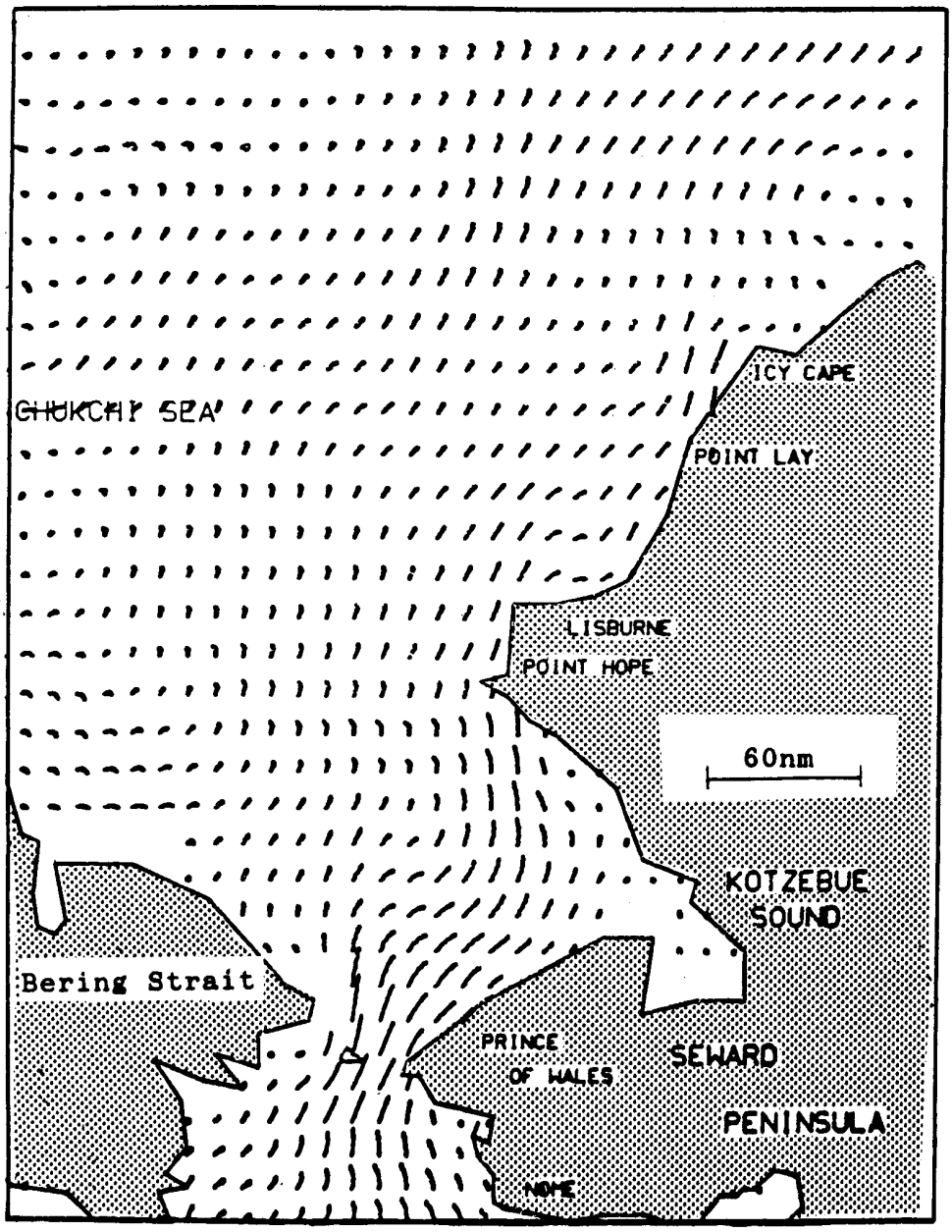

Fig. 3.29—Surface water particle trajectories in the Chukchi Sea induced by tide and 10 knot wind blowing from the south for 24 hours. Particles were traced for a total of 48 hours from the beginning to include the transient and inertial dynamics. Trajectories launched near the coastal areas between Point Lay and Icy Cape clearly indicate the development of coastal jets.

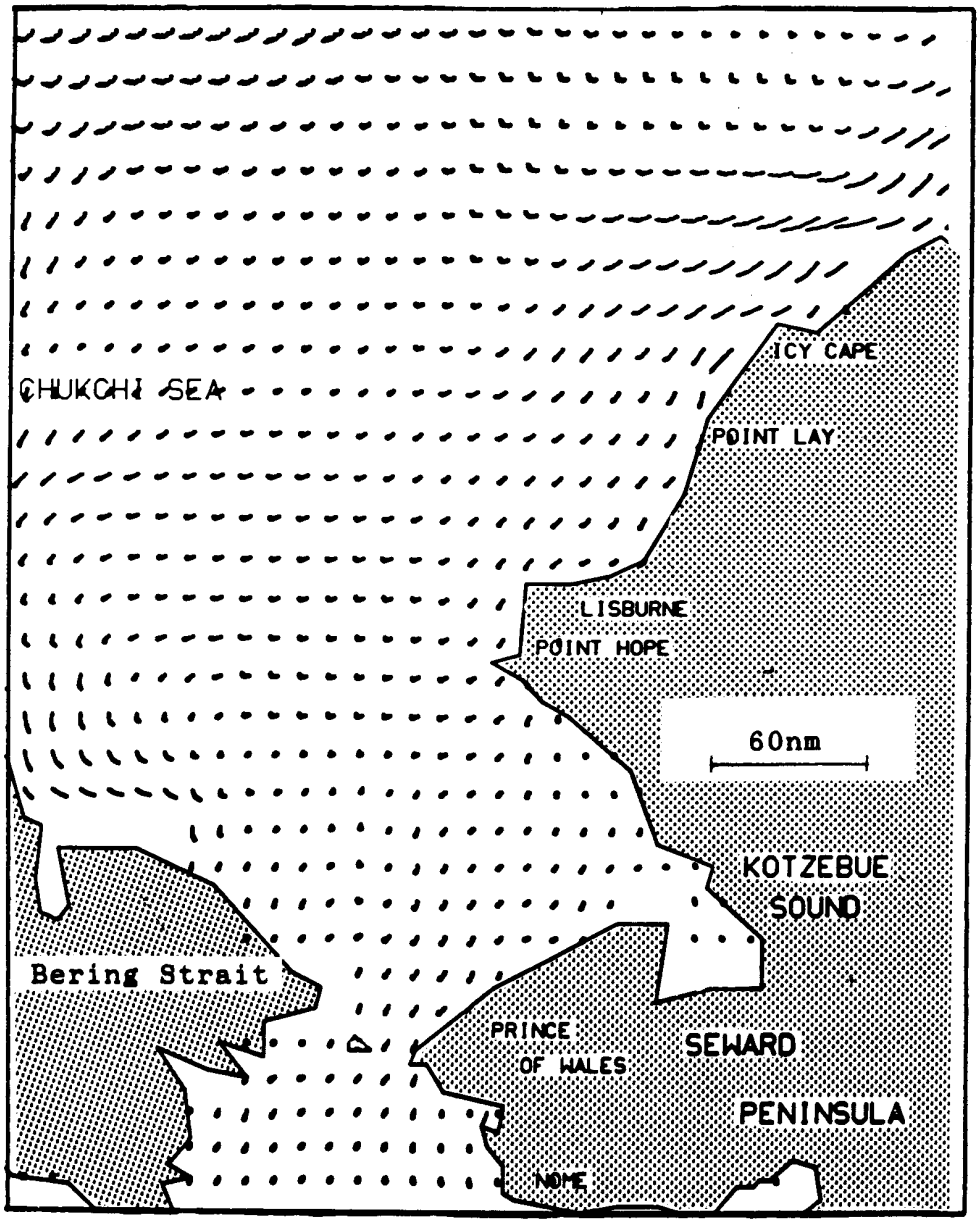

Fig. 3.30—Surface water particle trajectories in the Chukchi Sea induced by tide and 10 knot wind blowing from the north for 24 hours. Particles were traced for a total of 48 hours from the beginning to include the transient and inertial dynamics. Trajectories launched near the coastal areas between Point Lay and Icy Cape clearly indicate the development of coastal jets.

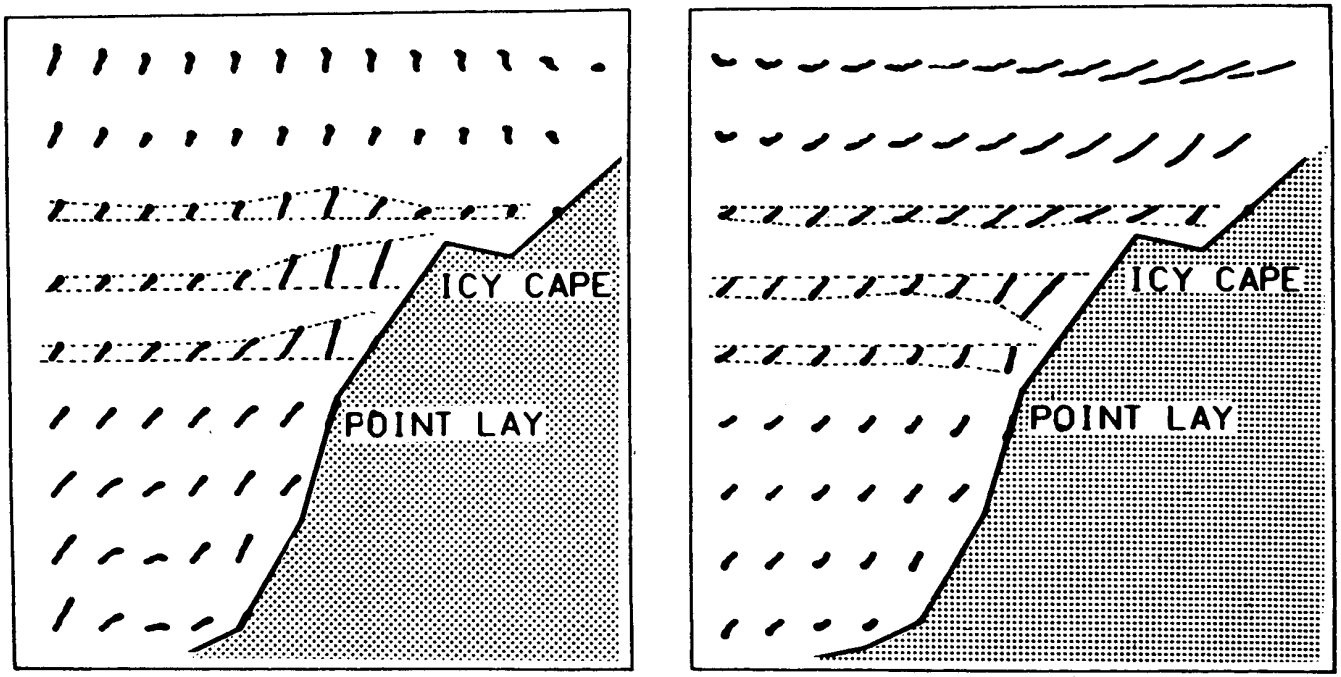

Fig. 3.31—Enlarged section of surface water particle trajectories near the coast between Point Lay and Icy Cape showing the coastal jet. The left shows the trajectories induced by tide and wind from the south (with water movements in the north to east directions); the right shows the trajectories induced by tide and wind from the north (with water movements in the west and south directions).

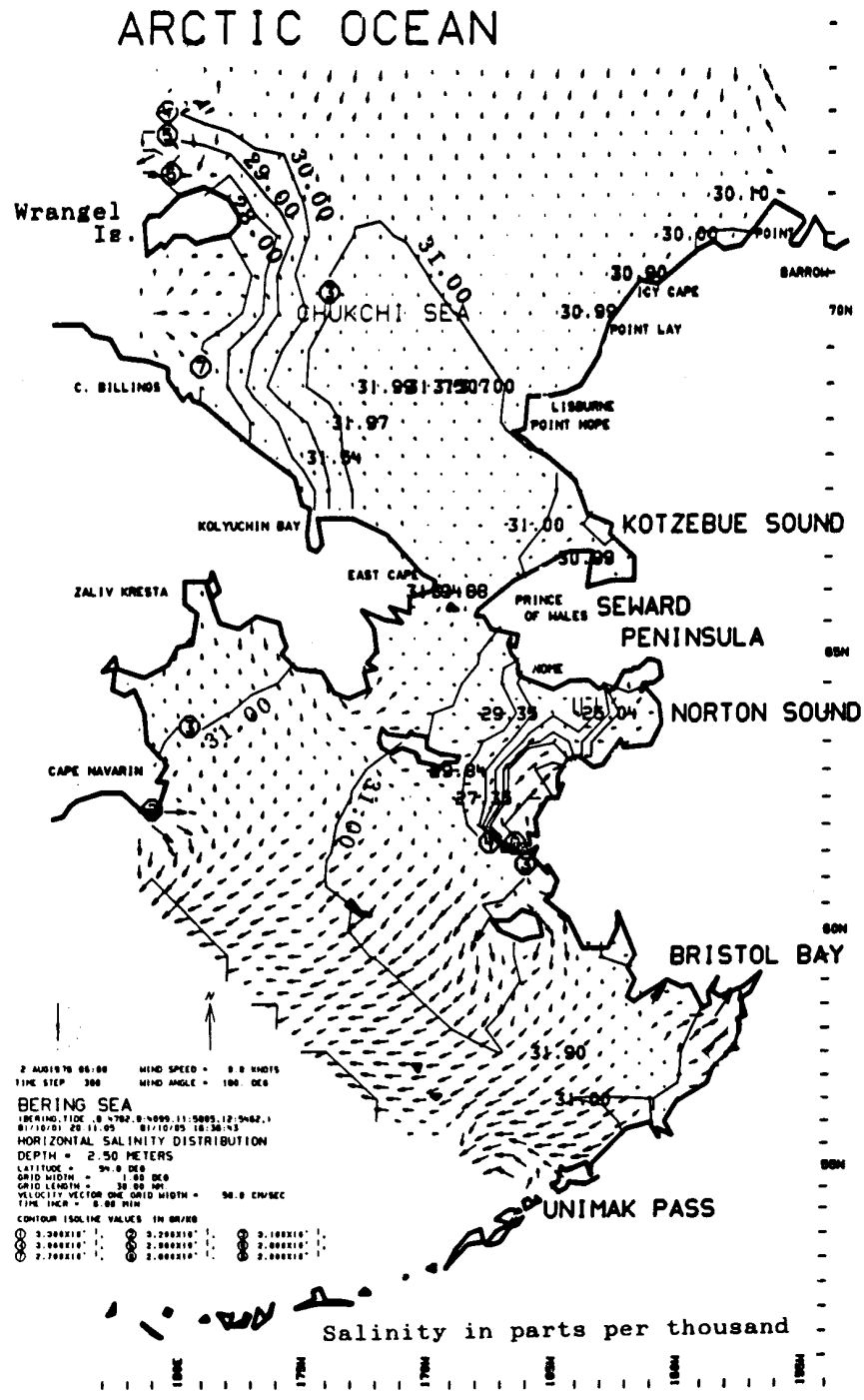

Fig. 3.32—Surface salinity distribution superimposed on the computed tidal circulation pattern at 1200 hours (Greenwich Mean Time) on August 2, 1976. Areas of low salinity are located near Yukon River and the eastern Siberian Shelf.

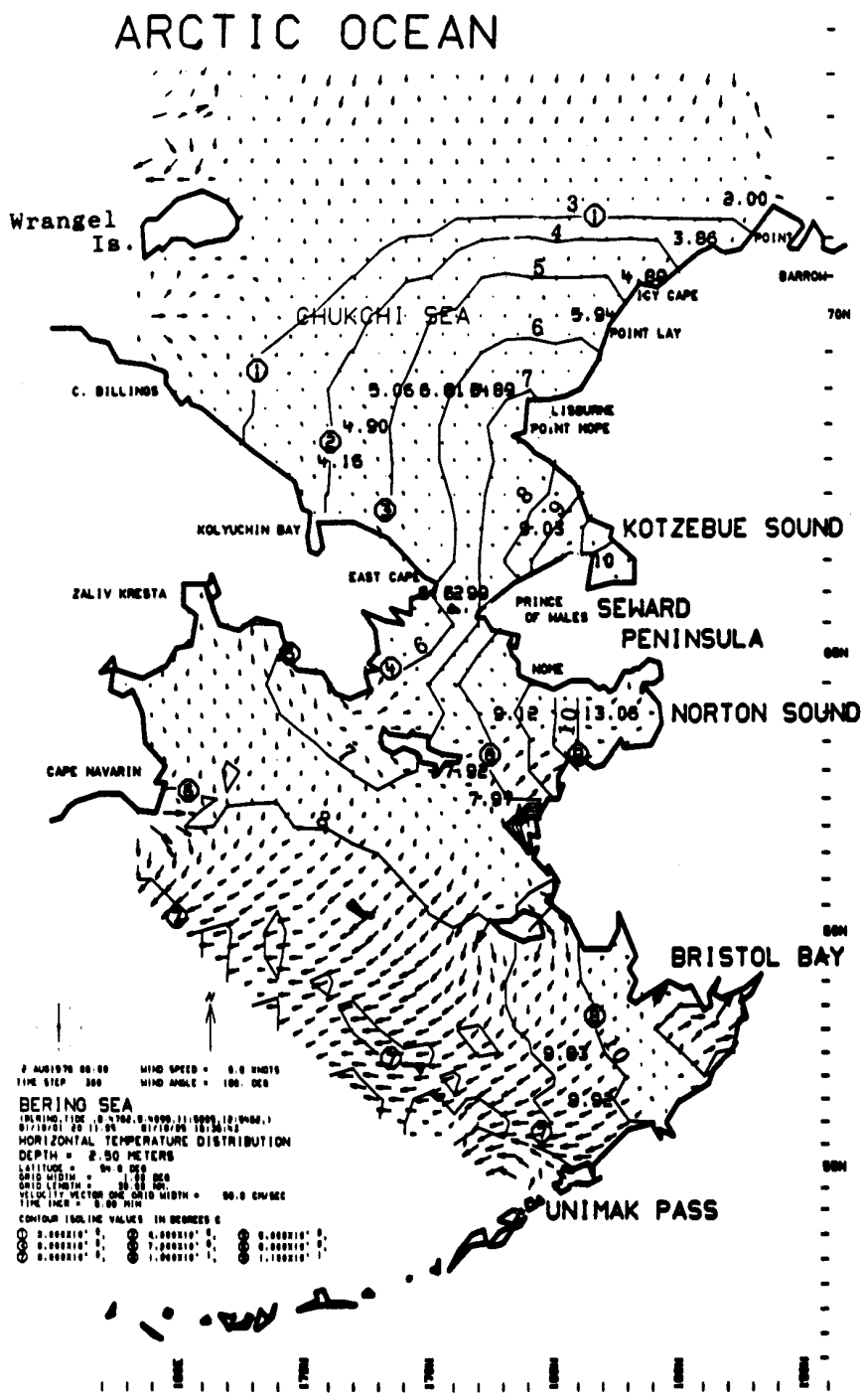

Fig. 3.33—Surface temperature distribution superimposed on the computed tidal flow pattern at 1200 hours (Greenwich Mean Time) on August 2, 1976. Areas of warmer temperature are generally located near Yukon Delta and the eastern shelf areas of the Bering and Chukchi Seas.

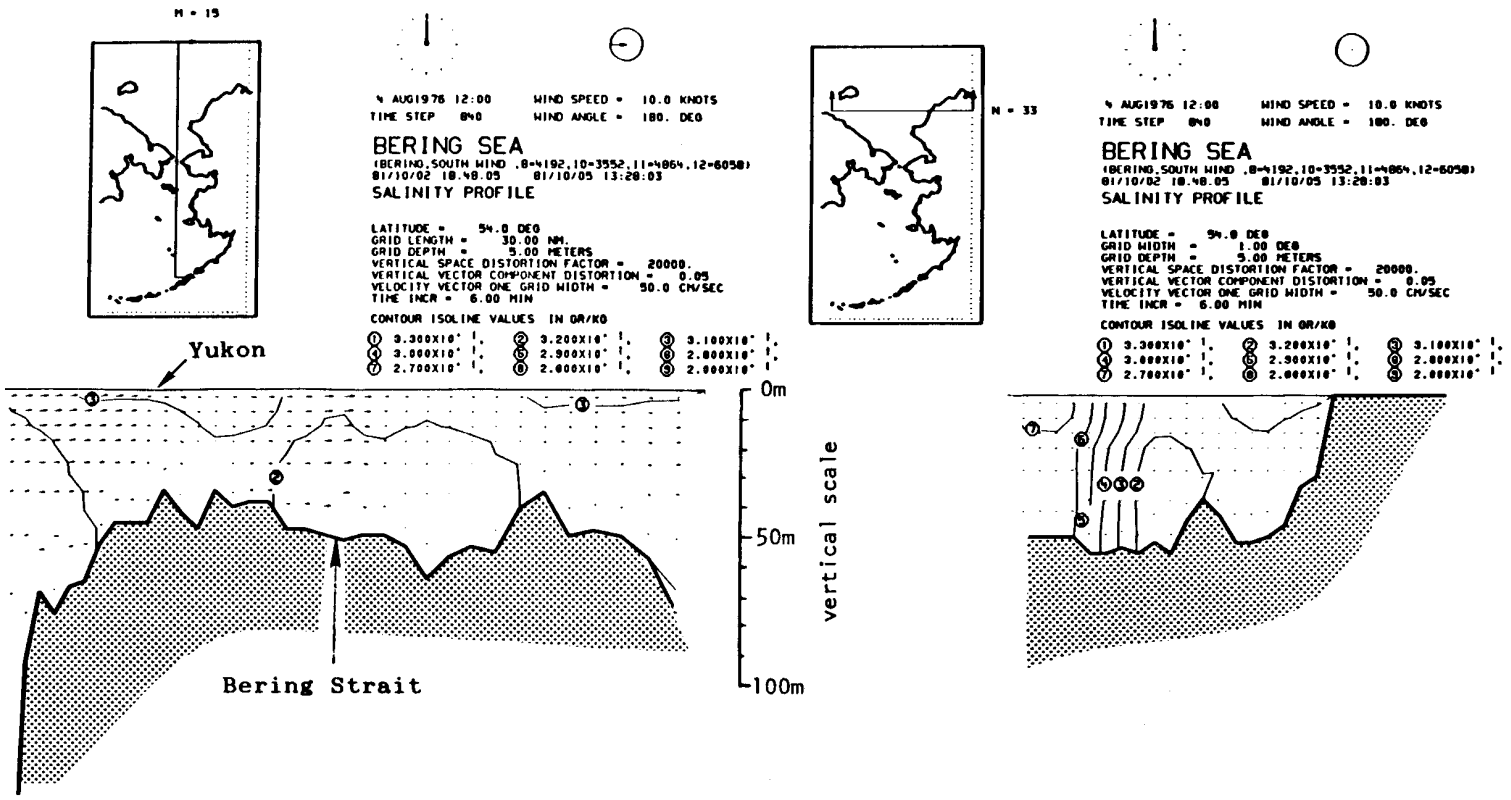

Fig. 3.34—Vertical salinity distributions through two cross-sections of the model. In the north/south section, the shallow pycnocline to the left is located near the Yukon Delta. Because of counterclockwise circulation within Norton Sound, the mixing causes deepening of the pycnocline before reaching the Bering Strait. In the east/west cross-section, fresher water is generally located near the Siberian shelf. The depth of pycnocline is approximately between 7 to 15 meters.

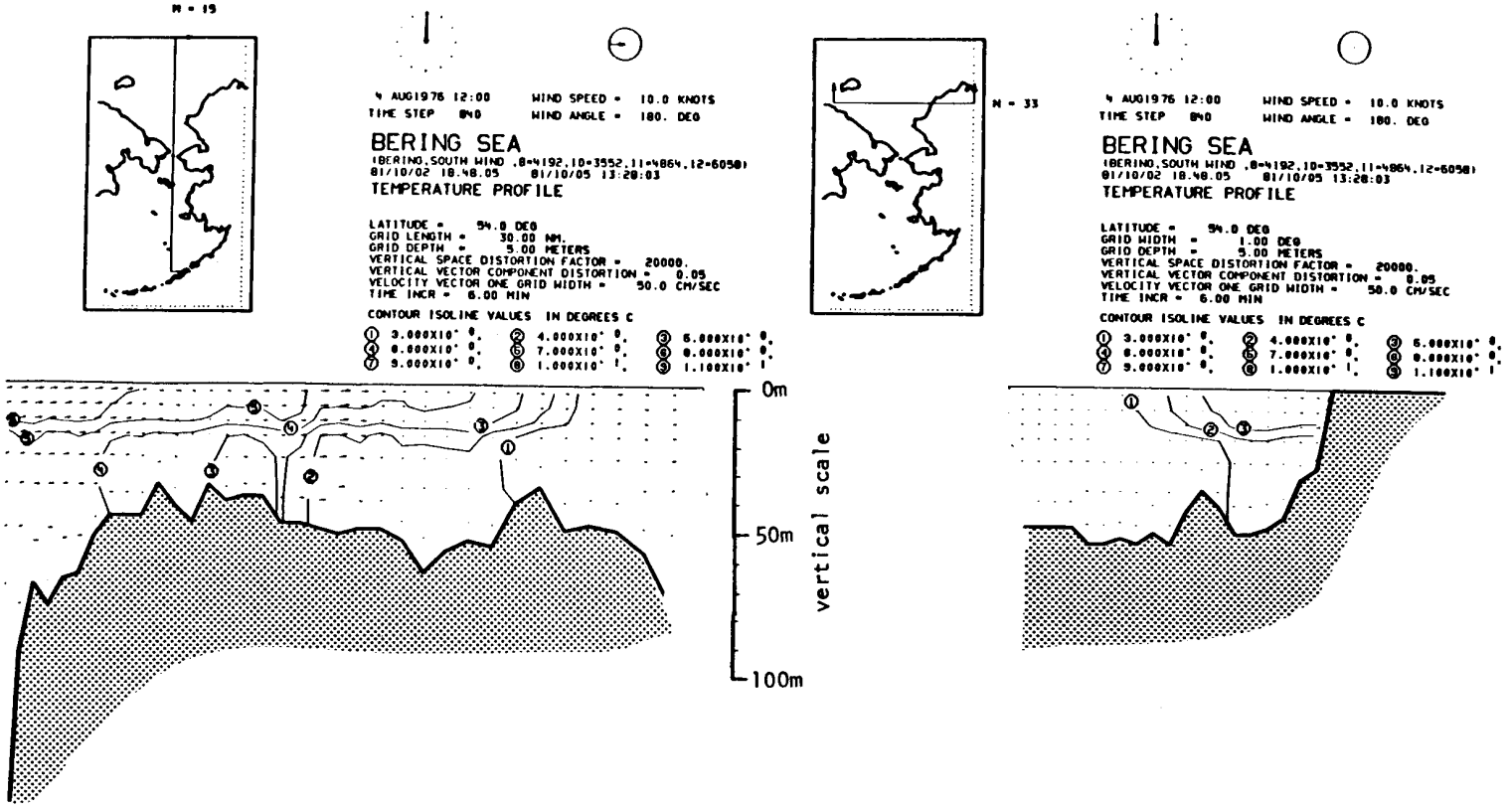

Fig. 3.35—Vertical temperature distributions through two cross-sections of the model.

50 m depth and the coast, water is well-mixed. A pycnocline exists in deeper water. The turbulence generated by tidal currents is not strong enough to mix water in the upper layer with water at a greater depth. The turbulence generated by wind causes the water above the pycnocline to be mixed and with a strong wind the pycnocline deepens. These effects can be seen very clearly in the salinity and temperature distributions in a vertical section of a submodel of the Bering Sea and Chukchi Sea model (Fig. 3.36).

The hydrographical structure of the Alaskan coastal waters is very complex, and many papers have been written on the subject (Mountain et al., 1976; Schumacher et al., 1979; Kinder et al., 1980; Coachman and Aagaard, 1981; Aagaard et al., 1981; Schumacher and Kinder, 1983; Salo et al., 1983; Reed and Schumacher, 1984). As the density field contributes considerably to the generation of the baroclinic currents and is very important for the dispersion computations of spilled oil, a major effort was made to obtain the appropriate salinity and temperature field for our studies and to have a good formulation of the turbulence closure computation when a pycnocline is present. It appears that in highly stratified regions, saltier water may sometimes stay on top of less saline water. In such a case the higher temperature more than compensates for the top-heavy distribution of the salinity. An example is shown by arrows in Fig. 3.36. In the absence of wind the layer can be temporarily stable until disturbed. Turner (1967) indicated that in nature in such a double diffusion convection case, salt fingers in the water column are formed. In principle the computation procedure is also able to model double diffusion convection instabilities, since different coefficients for the vertical diffusion transport in the mass balance equation of salt and heat are used, but we have not made an analysis of this phenomenon in our simulation results.

Now consider the propagation of tide in a homogeneous body of water where no density gradient exists. The bathymetry and bottom friction generate residual circulation through the nonlinear advective mechanisms in the equation of motion. The tidal residual in homogeneous water is different from the tidal residual of stratified water. In stratified water the vertical momentum transfer is suppressed, the vertical velocity profiles are different, and a different nonlinear advection and dissipation generates a different residual. Thus the seasonal change in the density structure produces a seasonal change in the tidal residual. The influence of the velocity distribution on the residual also shows near the vertical fronts that were discussed above. Near the front the water-level gradients are essentially the same, but the nonlinear processes that generate the residual are not the same. Consequently, a transition in the residual is generated that shows as a band of higher residual currents near the frontal area. Because the frontal area is located at the 50 m isobath, the residual more or less follows this isobath. A similar process exists near the shelf break. On the other hand, without tides the horizontal density gradient generates baroclinic circulation in seeking a geostrophic balance. Over the Alaskan coastal shelf, both tidal forces and density gradient are significant and dynamically coupled. One cannot, therefore, compute them separately.

It has been a useful analytical procedure to compute oceanic circulation using geostrophic balance according to the hydrographic data. Results from this type of diagnostic calculation would yield a pattern of currents relative to a "level of no motion" typically at 1200–1500 meter depths. The computed geostrophic currents represent the distance between the density (pressure) gradient and the Coriolis force. In the deep ocean when tidal currents are weak, the density-driven current is the primary circulation in the absence of local wind force.

However, over the shallow shelf of the Alaskan coastal waters a major portion of the kinetic energies are within tidal frequency bands (Mofjeld et al., 1984; Pearson et al., 1981a,

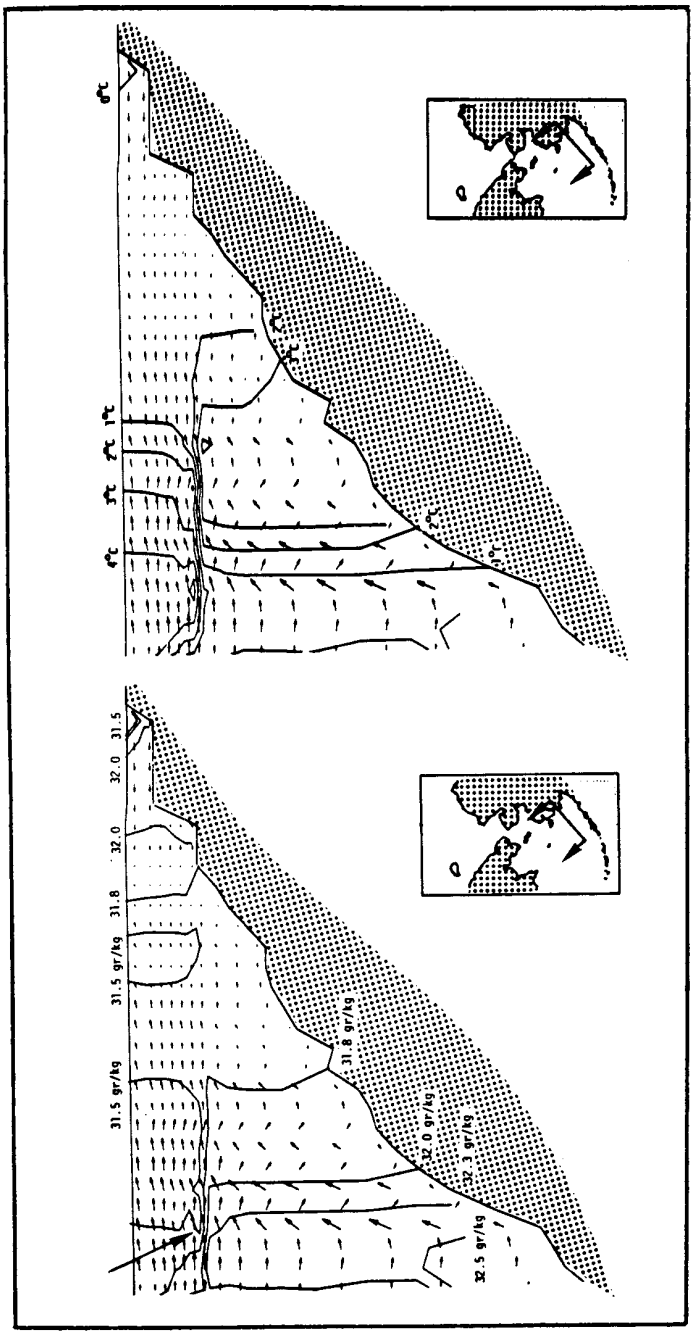

Fig. 3.36—Vertical distribution of salinity, temperature, and currents through a cross-section of the eastern Bering shelf showing the pycnocline, frontal structure, and local density instability where heavier water could stay above lighter water temporarily.

1981b). Consequently, in computing the density-induced circulation one has to include tides in the computation. If they are not included, the computed density currents are restrained by very weak bottom stress because of the quadratic relation between velocity and frictional dissipation. This would overestimate the density currents. Also, as a result, a deep-water density current when close to the shelf break, would extend over the shelf and the velocities gradually decrease landward. It is unlikely that any frontal eddies at the shelf break would be generated by the model. On the other hand, if tides are included in the computation, tidal currents are generated on the shelf, and these currents are damped by the bottom stress, which is much larger than in simulations without tide. The water movements on the shelf are then practically uncoupled from the density currents in the deep Bering basin, and sharp transitions are generated in the model.

Currents computed with tides and density field would include primarily baroclinic circulation with "tidal residuals" if energies at tidal frequencies are "filtered." The spin-up time required to establish a baroclinic balance is approximately five to ten days. This is reasonable when compared to the spin-up time required for the Atlantic Ocean (Anderson and Killworth, 1977), which takes between ten to 16 days.

At the beginning of our modeling study extensive field cruises were made to establish networks of conductivity, temperature, and depth (CTD) stations and to emplace current meters and bottom pressure recorders. The field studies were conducted by Drs. Kinder, Muench, Tripp, Schumacher, and Mofjeld (see the Bibliography). Because of practical difficulties, most of the gauge deployments were stopped at the shelf break, even though it had been requested to extend coverage further offshore into the deep Bering Basin. As compensation, more CTD profiles were cast near the shelf break. It was decided in a project technical review meeting to compute the baroclinic circulation over the shelf break using the three-dimensional model according to the CTD cast as mentioned above. The geostrophic currents at the northeast part of the Bering Basin were deduced from the 5500 hydrographic profiles (developed for the years 1874–1959, by Arsen'ev, 1967) and computed from a CTD cast made by a Japanese fishing fleet (Takenouti and Ohtani, 1974). The pattern was supplemented by the estimated transport computed from five CTD transects developed by Kinder et al. (1975). The net transport through the Unimak Pass was measured by Schumacher et al. (1982). Data groups were adapted for estimating the net circulation near the Bering Shelf break and this information is shown in Table 3.1. The general direction of geostrophic transport along the shelf break flows toward the northwest. This northwesterly flowing current along the shelf break has been called the "transverse current" by Russian oceanographers (e.g., Arsen'ev, 1965, Fig. 3.37) and the "Bering Slope currents" by American scientists (e.g., Kinder et al., 1975). This current is coupled with the cyclonic circulation in the eastern Bering Basin (Fig. 3.38 by Takenouti and Ohtani, 1974). Based on the measured density field and tidal forcing, a series of computations using three-dimensional dynamic computation were made in 1979 and 1980. The rationale to include tidal energy in the computation and then later filter it out was presented above. After filtering out the tidal components, the remaining baroclinic residual transport along the shelf break (with tidal residual also included) also flows toward the northwest, as shown in Fig. 3.39. (See also the Appendix.) Thus this agrees with the compiled data sets.

Furthermore, the baroclinic current tends to pass St. Lawrence Island not only through the western passage but is also to the south, passing through the eastern passage near Norton Sound. This computed pattern agrees with two earlier studies by the Russian and Japanese groups. For oil trajectory computations, baroclinic circulation near and beyond the shelf break was compiled from the sources listed in Table 3.1.

Table 3.1

DATA GROUPS ADAPTED FOR ESTIMATING THE NET CIRCULATION NEAR THE BERING SHELF BREAK AND THE UPDATING PROCESS

Data Group	Observation Period	Data Type	Author	Publication Date	Methods and Comments
1	1874–1959	CTD[a]	Arsen'ev	1967	Diagnostic comp. (Sparce data in the area of interest, qualitative.)
2	1959–1965	CTD	Takenouti and Ohtani	1974	Diagnostic comp.
3	8/2–13, 72	CTD	Kinder et al.	1975	Diagnostic comp.
4	8/14–21, 72	Drogue	Kinder et al.	1975	Parachute drogue at 150 m and 750 m
5	June 1976	CTD	Data: Kinder model: Liu and Leendertse	1977 1979	3-D dynamic computation (Liu and Leendertse, 1979) using this group of CTD casts
6	1981	Meter	Schumacher et al.	1982	Net flow through Unimak Pass
7	1982	Meter	Muench and Schumacher	1985	Marginal ice zone study
8	10/82–5/83	CTD meter	Muench and Schumacher	1985	Direct observation and diagnostic comp.
9	1983	CTD and drogue	Schumacher and Kinder	1983	Direct observation and inferred geostrophic flow
10	1982–1983	Drogue	Royer and Emery	1984	Window-shade drogue, broken (to give rough estimate at 30 m level).

[a]Conductivity, temperature, and depth.

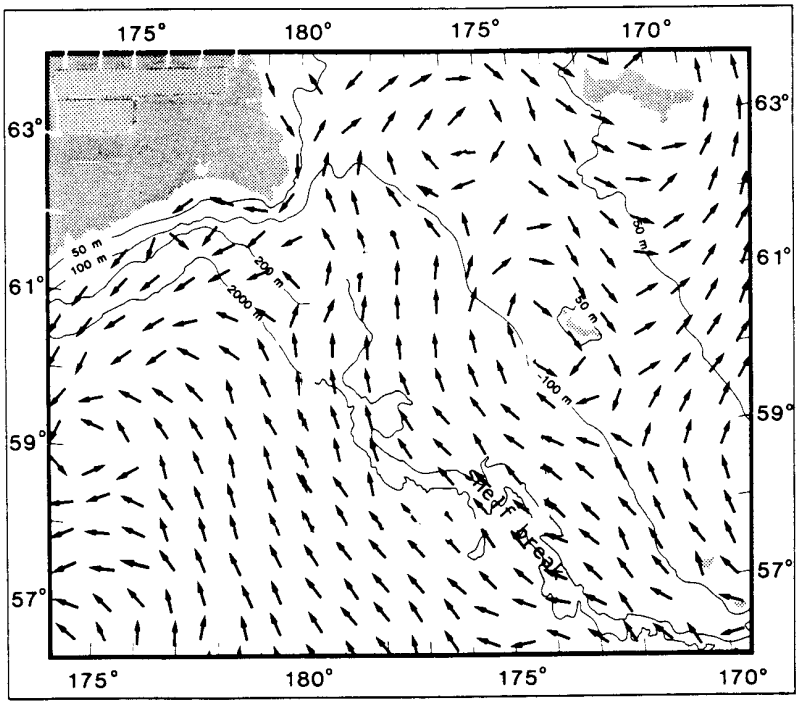

Fig. 3.37—Inferred geostrophic circulation pattern, based on 5500 hydrographic data, as reported by Arsen'ev (1967).

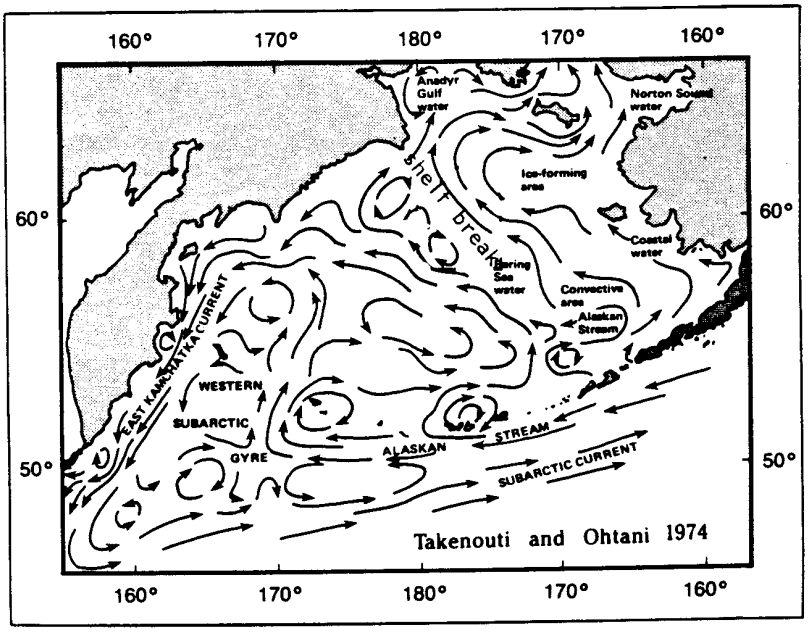

Fig. 3.38—Computed geostrophic circulation pattern based on a CTD cast by the Japanese fishing fleet, as reported by Takenouti and Ohtani (1974).

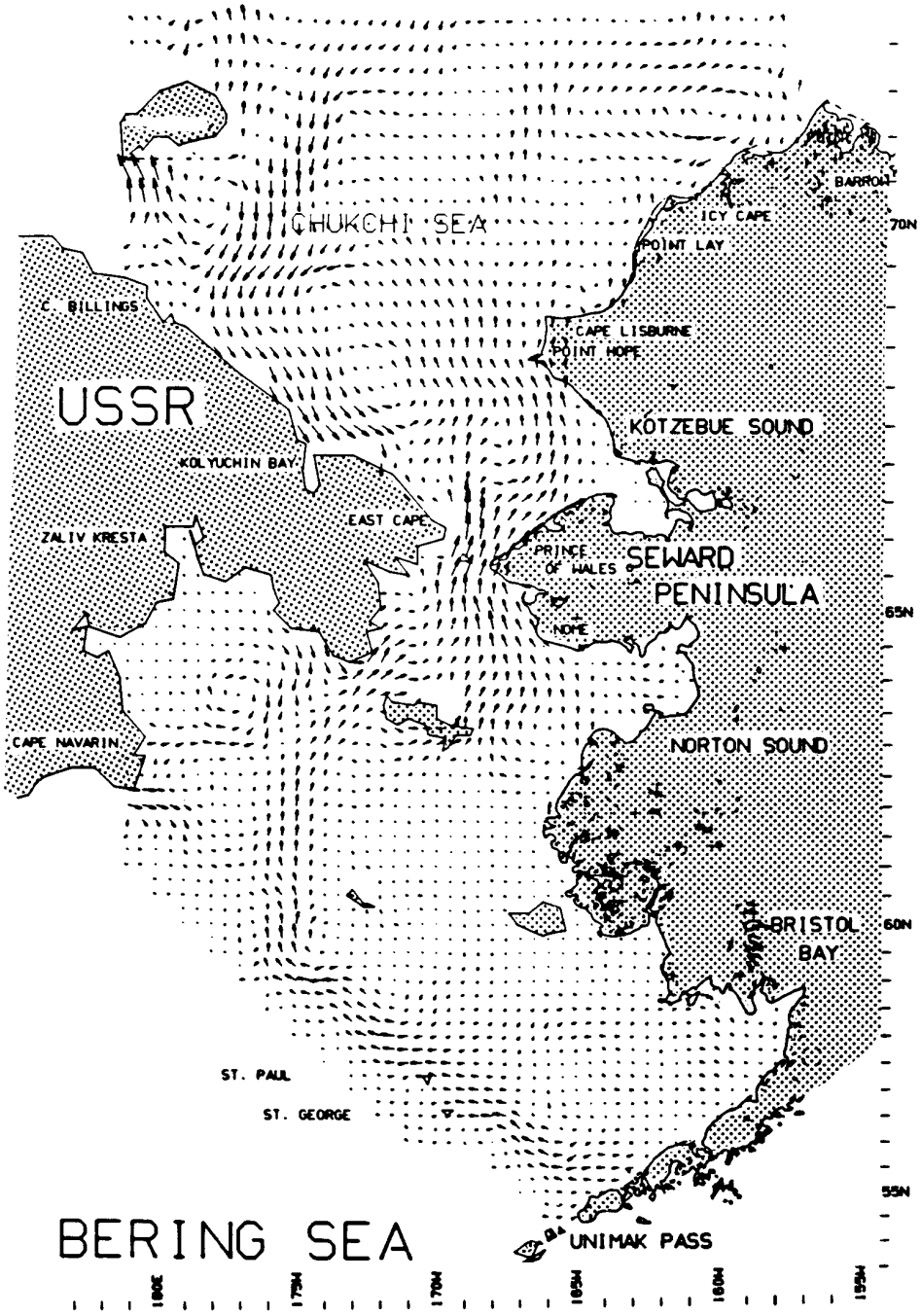

Fig. 3.39—Baroclinically induced residual currents at 5 m level after the initial 5-day spin-up. To reflect the realistic energy level over the continental shelf, astronomical tides are included in the computation and subsequently filtered with a two-dimensional numerical tidal eliminator.

Another noteworthy feature is the eddy structure west of Unimak Pass where an anticyclonic eddy is followed by a cyclonic eddy in the surface layer of a higher resolution model of Bristol Bay (Liu and Leendertse, 1979, e981a). Also of some interest is the baroclinic circulation near the Bering Strait (Fig. 3.40) where the computed surface pattern agrees extremely well with the observed long-term movement of water masses as compiled by Drury et al. (1981).

Even though the predominant transport through the Bering Strait is to the north, an atmospheric pressure difference across the Strait such as induced by a Siberian high or Bering cyclones could cause a temporary current reversal. Observed current through the Bering Strait with tidal bands filtered out (Fig. 3.41) reveals the northward transport with occasional reversals resulting from storms. The Bering and Chukchi Seas are relatively well studied in comparison with the Beaufort Sea, which is accessible for navigation only during a very short period in the summer, if conditions are favorable. Initial conditions were very difficult to obtain. A typical temperature distribution several meters under the water surface in the middle of the second layer of the model (7.5 m below the surface) is shown in Fig. 3.42. The water in a major part of the model is colder than 0°C.

From the simulations of the Beaufort Sea described earlier in this chapter, the density and tidal residual current field was determined by application of a low-pass filter on half-hourly data. Figure 3.43 shows this computed residual circulation. Even though the tides are weak in the Beaufort Sea, the combined density and tidal residual currents range between 2 to 6 cm/sec in a band near the Alaskan coast. Larger currents are found near the shallow areas around Mackenzie Bay and northeast of Point Barrow. The near-shore residual current for the Gulf of Alaska shelf is presented in Fig. 3.13. The offshore current (Alaskan stream) flows toward the southwest. Some field measurements have been made by Schumacher and Muench (1980).

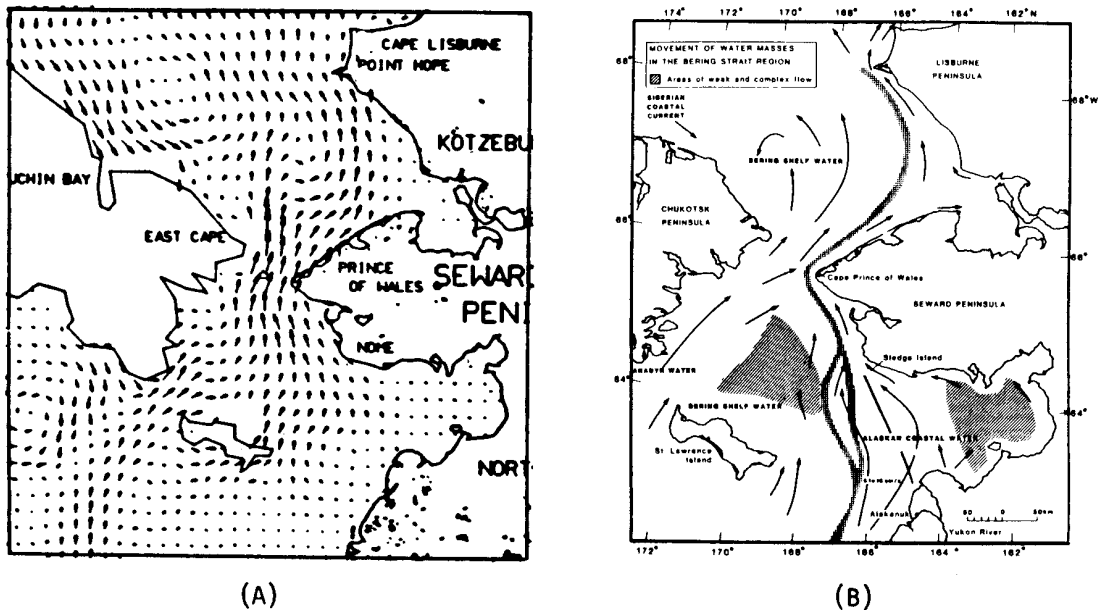

Fig. 3.40—Comparison between (A), the computed long-term transport, and (B), observed long-term movement of water masses as compiled by Drury et al. (1981).

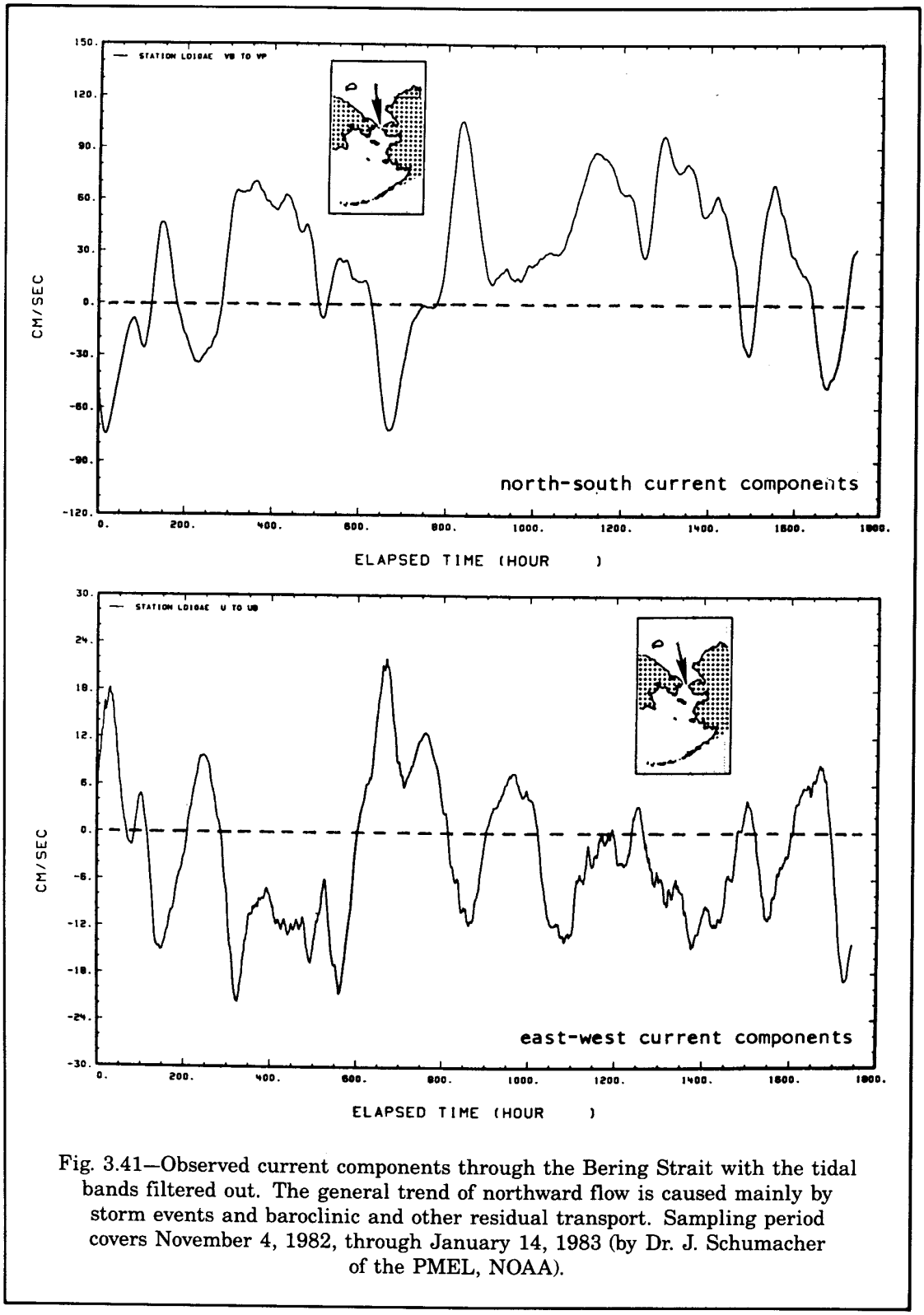

Fig. 3.41—Observed current components through the Bering Strait with the tidal bands filtered out. The general trend of northward flow is caused mainly by storm events and baroclinic and other residual transport. Sampling period covers November 4, 1982, through January 14, 1983 (by Dr. J. Schumacher of the PMEL, NOAA).

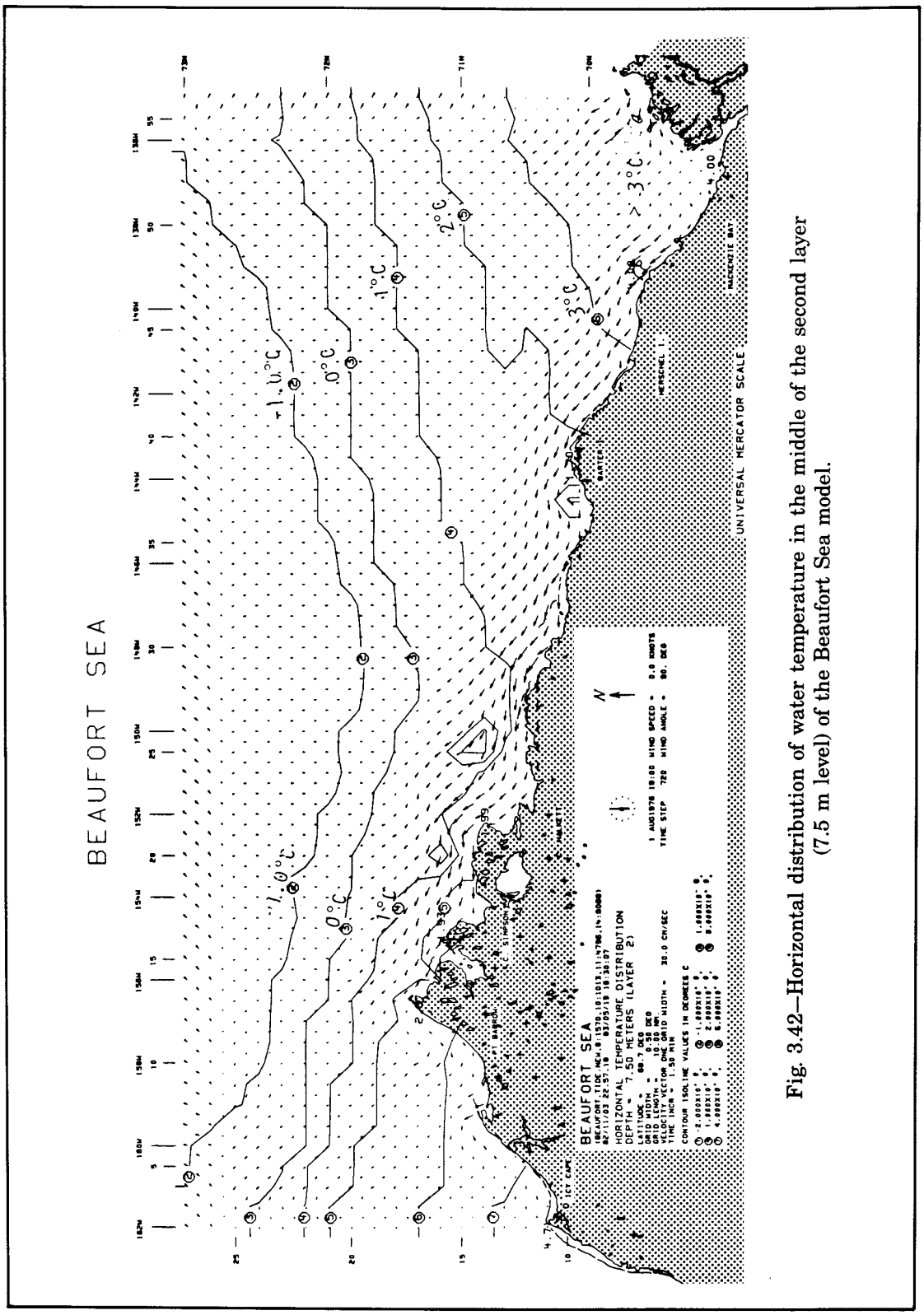

Fig. 3.42—Horizontal distribution of water temperature in the middle of the second layer (7.5 m level) of the Beaufort Sea model.

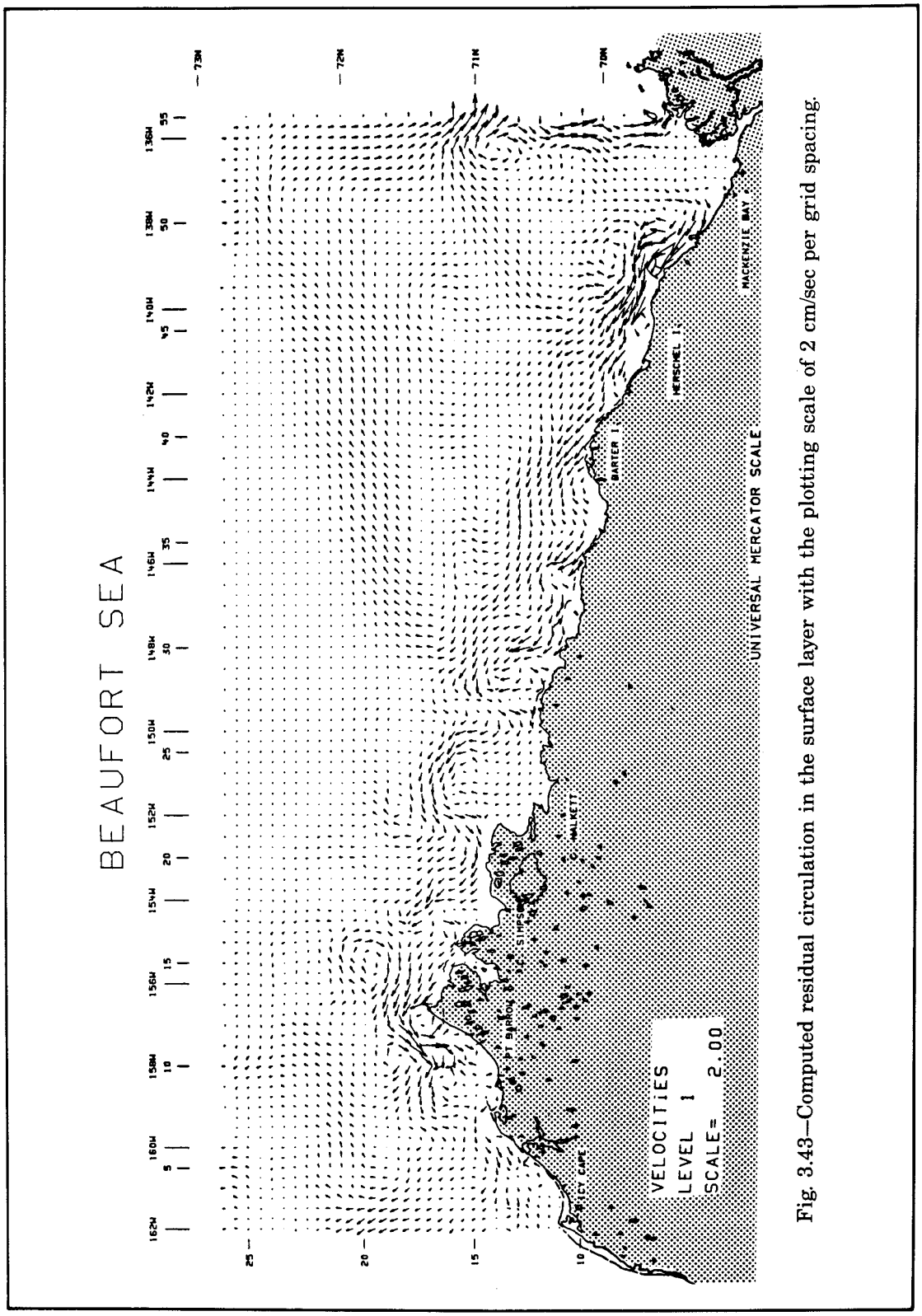

Fig. 3.43—Computed residual circulation in the surface layer with the plotting scale of 2 cm/sec per grid spacing.

4. MODELING WIND FIELDS

When an area in which the wind field is to be determined is small and located in the open ocean, a wind model is relatively simple to develop. Under such conditions a model can be built using random sampling according to a measured steady-state wind rose if observed data are available.

Another possibility is to use the mesoscale numerical weather model data to compute the wind field. Unfortunately, the strong winds of the extratropical cyclonic storms frequently occurring in this area cannot be simulated with this approach, which does not generate realistic winds in the computed wind fields. Therefore, the drift speed of the oil trajectories computed with this approach will also be inaccurate.

A high resolution of the wind field is required, as the area to be modeled is in one of two major extratropical depression tracks in the northern hemisphere, namely, the Aleutian Low, and the average radius of an Alaskan extratropical cyclone is about 500 km.

For example, when the sea-level pressure data from the National Center for Atmospheric Research (NCAR) are used, the spatial resolution is about 3.4° latitude (381 km) at 60°N (Overland et al., 1980; Macklin, 1984; Jenne, 1975; Holl, 1971), and a typical Alaskan extratropical cyclone would be represented by less than two grid points. With such a resolution realistic wind speeds cannot be generated, as the exponential pressure distribution within the cyclonic structure needs to be adequately resolved. Recent experiences (Dell'osso and Bengtsson, 1985) indicated that for large cyclones even with a fine mesh model, the computed cyclonic central pressure deficit is approximately 40 percent of the measured value.

Accurate modeling of the wind field of these depressions is very important, as high winds create large surface water movements, which are crucial in oil spill risk analysis. As the deterministic approach to obtain the time varying wind field is not feasible, a stochastic model was developed.

STOCHASTIC ANALYSIS OF REGIONAL WEATHER SYSTEM

Before entering the detailed computational methods it is perhaps more appropriate to give a general overview of the approach by which the wind data over the study area are analyzed and modeled. The basic approach involves three steps:

1. An analysis and determination of the baric types within the study area;
2. An assessment of measured weather elements at weather stations in relation to these baric types;
3. Computation of the circulation patterns belonging to the baric types by use of dynamic balances.[1]

These, in fact, constitute the three basic techniques of *synoptic climatology* (Barry and Perry, 1973). Because of the observed weather element whose probabilistic characteristic changes not only in space but also over time, the analysis is "stochastic" in nature.

[1]For oil spill trajectory computations, wind fields are required at intervals shorter than those at which the baric types are determined. These wind fields are obtained from dynamic balances of baric pressure fields obtained by interpolation of the two successive pressure fields.

In developing the model we first treat the weather system over the modeled area as a stochastic process whose evolution is represented by a series of transitions between certain "states" of the process. Previous analysis of the Alaskan weather system and of the Aleutian Low indicated that the residence time of a weather system is approximately between one to three days. It is plausible that the process is of the Markovian type. If one considers that the present weather state contains all essential elements that caused the weather to evolve from the previous state to the present state then the stochastic process is of the first order Markov type. It can be described or simulated if the probabilities of transition are known via the matrix of transitional probability

$$P\{p(ij)\} = \begin{bmatrix} p(1,1) & p(1,2) & \ldots . p(1,k) \\ p(2,1) & p(2,2) & \ldots . p(2,k) \\ \cdot & \cdot & \\ \cdot & \cdot & \\ \cdot & \cdot & \\ p(j,1) & p(j,2) & \ldots . p(j,k) \end{bmatrix} \tag{4.1}$$

$$0 \le p(ij) \le 1 \text{ and } \sum_{j=1}^{k} p(ij) = 1 \quad i = 1,2,\ldots . k$$

in which k represents the total number of possible outcomes, with $p_{i\,j}$ denoting the probability from the weather state i evolved into the weather state j. Each weather state can represent, for example, an atmospheric pressure pattern over Alaska.

Also analyzed are the steady-state behavior of the process and the amount of occupation time of each weather state (within the state-space of the stochastic process).

The physical rationales behind the stochastic-synoptic approach are as follows:

1. Weather over a particular region, being a part of the global circulation system, possesses climatic characteristics unique to that area;
2. Governed by physical laws, the transition between one weather type to the next tends not to have an equally likely chance toward all possible types (i.e., it is not a purely random process). It must obey the dynamic elements associated with the evolutionary process;
3. The present weather state contains all essential elements that caused the weather to evolve from the previous state to the present state, thence to the next state.

The climatic characteristics of the Alaskan coastal area are unique. The climate is often dominated by low pressure centers over the Bering Sea and over the Gulf of Alaska, namely, the Aleutian Low. In an extensive effort, Putnins (1966) analyzed nearly 20 years of daily weather charts. As a result, he classified the baric pattern over Alaska into 22 types. In the classification, he also took into consideration the upper-level circulation. For each baric type, observed wind data at ground stations are summarized for each month. Raw data on the occurrence of each pressure type subsequently followed by another weather type are also tabulated. Transitional probability can then be calculated from these data.

In the classification of weather types by Putnins, surface pressures and upper-level pressures were used. To simplify the task, the original 22 weather types are condensed into 11 types for each season. Table 4.1 is an example of a transitional probability matrix tabulated in the form of a cumulative probability distribution. The transitional probability analyses are divided into spring/summer and fall/winter periods. Most pressure types exist in both seasons and 14 pressure types are considered. Altogether this covers approximately 98 percent of the original classification.

Tables 4.2 and 4.3 list the synoptic characteristics associated with each of the baric types. Figure 4.1 illustrates a typical type-1 summer baric pattern, whereas Fig. 4.2 shows a typical type-5 pattern.

For each weather type, speed and direction of the monthly mean value for each station are tabulated. Spatial interpolation between the stations are weighted according to the inverse square of the distances. Supplementary buoy data from the National Oceanic Data Center (NODC), as well as other triangulation analyses (Kozo, 1984), are also used.[2]

The variabilities of winds from the mean speed and direction associated with each pressure pattern are first analyzed at each individual station before spatial interpolation. The method to determine the statistical parameter of wind speed and direction needed for the simulation is described next.

MODELING WIND SPEED AND DIRECTION

The variability of wind speed from a given set of records is usually expressed in terms of its variance or standard deviation. The characteristic of wind speed variability is that it has a lower limit of zero. In the higher ranges, the variability decreases as the wind speed increases. This behavior is typically a physical process that fits an extreme-value probability distribution. Most commonly applied distributions in this class of problems are exponential, lognormal, Weibull, Rayleigh, and Gumbel probability distributions. For wind speed they are lognormal and Weibull distributions (Finzi et al., 1984; SethuRaman and Tichler, 1977; Kolmogorov, 1962; Oboukhov, 1962; Monin and Yaglom, 1975; Smith, 1971; Conradsen et al. 1984). The lognormal distribution was selected for the wind speed distribution not only because of its strong physical justification[3] but also for many of its convenient features—one of which is the ability to estimate its variance from the extreme value. In other words, we are able to estimate its standard deviation using its extreme value and the sample size. This was necessary because only the mean and maximum wind speed data were available from each of the ground stations during the 19-year period when data were used to derive the weather state transitional probability matrices. The procedure is as follows (see Table 4.4). For each weather station, the observed frequency of the maximum wind is computed from the number of wind speed observations associated with each weather type for that month. Frequency is simply the reciprocal of the total number of observations made during the 19-year period from the monthly station data.

By the nature of lognormal distribution, standardized units can be computed as shown in Table 4.4. The standardized normal units can be found in most mathematical tables (e.g.,

[2]Under contract from NOAA, Dr. Kozo has made special analyses to correlate wind parameters from coastal stations to offshore locations using buoy data. Results from these studies have been used extensively in the modeling work reported here.

[3]From a physical point of view, lognormality has been treated by Kolmogorov to "represent any essential positive characteristics" and became his third "well known hypothesis."

Table 4.1

CUMULATIVE DISTRIBUTION OF TRANSITIONAL PROBABILITY MATRIX ASSOCIATED WITH THE 11 WEATHER TYPES USED FOR SIMULATING OIL TRAJECTORIES, JUNE-AUGUST PERIOD

Weather Type	1	2	3	4	5	6	7	8	9	10	11
1	.6810	.7083	.7778	.8971	.9166	.9246	.9853	.9853	.9853	.9853	1.0000
2	.0195	.5135	.5663	.5749	.5901	.7391	.7391	.7391	.8560	.8560	1.0000
3	.2795	.4061	.8875	.9036	.9274	.9519	.9757	.9757	.9757	.9757	1.0000
4	.2610	.3586	.4397	.9158	.9995	.9995	1.0000	1.0000	1.0000	1.0000	1.0000
5	.4028	.4028	.4028	.4866	1.0000	1.0000	1.0000	1.0000	1.0000	1.0000	1.0000
6	.1701	.3351	.3544	.4069	.5188	.9020	.9020	.9020	.9020	.9020	1.0000
7	.3570	.4745	.5245	.5245	.5245	.5245	1.0000	1.0000	1.0000	1.0000	1.0000
8	.0000	.0555	.1111	.2061	.2061	.2894	.3310	.8208	1.0000	1.0000	1.0000
9	.0000	.1516	.1668	.1668	.1668	.3065	.3065	.3216	.9173	.9470	1.0000
10	.0000	.0000	.2500	.2500	.2500	.2500	.2500	.5000	.5000	1.0000	1.0000
11	.3895	.3895	.3895	.3895	.6006	.7434	.7434	.7434	.7434	.7434	1.0000

Table 4.2

SYNOPTIC CHARACTERISTICS FOR THE SUMMER BARIC TYPES

Type	Baric Characteristics
1	Entire area is dominated by a flat low with several centers over Alaska or near the coast
2	Low is at the east, plus a ridge over the Alaskan Peninsula
3	Low is stretched from the southwest toward the northeast. A high is located at the south or southeast of Alaska
4	Modeled area is part of the extensive low belt in the latitudinal direction
5	A pronounced low-pressure center occurs at the southwest of the Bering Sea moving toward the middle
6	A low is over Siberia
7	Low is centered over the Gulf of Alaska (southeast coast) plus a ridge over the northwest and north (over the Chukchi Sea)
8	A ridge dominates the Alaskan Peninsula, plus a low over the Gulf of Alaska
9	A high dominates the eastern section of Alaska
10	A trough from the east, plus a high over Siberia
11	Low in the west, plus a low over the Gulf of Alaska

Table 4.3

SYNOPTIC CHARACTERISTICS FOR THE WINTER BARIC TYPES

Type	Baric Characteristics
1	A flat low dominates the entire modeled area with several centers over Alaska or near the coast
2	Low is centered at the southeast coast, plus a ridge over the northwest and north (over the Chukchi Sea)
3	A belt of several lows occurs over the southern Bering Sea
4	A pronounced low-pressure center occurs at the southwest of the Bering Sea moving toward the middle
5	A high dominates the north over the Chukchi Sea
6	A high dominates the eastern Alaskan Peninsula
7	Dominated by a pronounced central low
8	Low at west plus a southern low over the Gulf of Alaska
9	Low is in east, plus a ridge over Alaska
10	Low centered at the southwest but stretched toward the northeast. A high is located at the south or southeast
11	Low centered at the southwest but stretched toward the northeast. A high is located at the south or southeast (over the Gulf of Alaska)

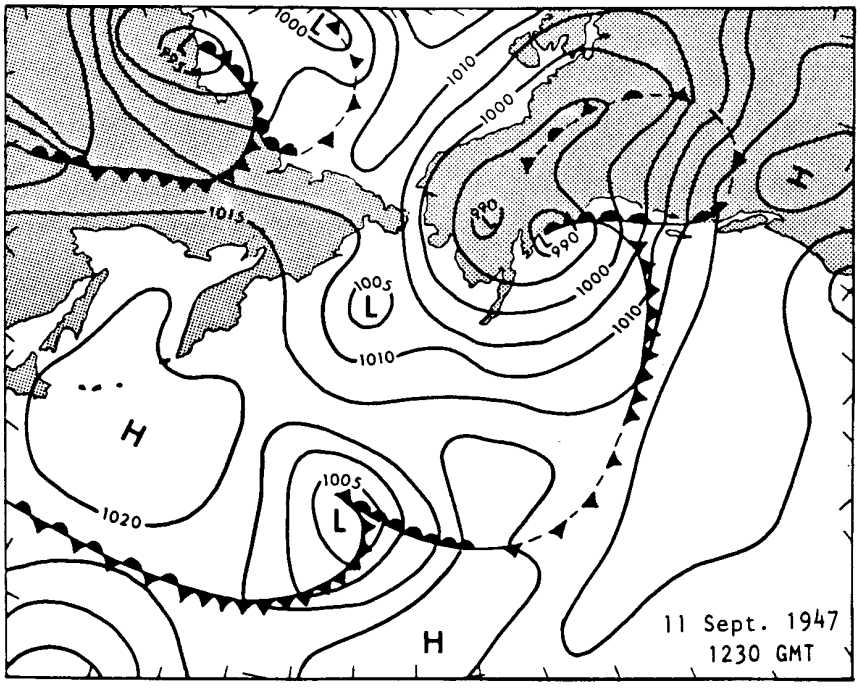

Fig. 4.1—Typical baric pattern where Alaska is dominated by a flat weak low with several centers over Alaska or near the coast.

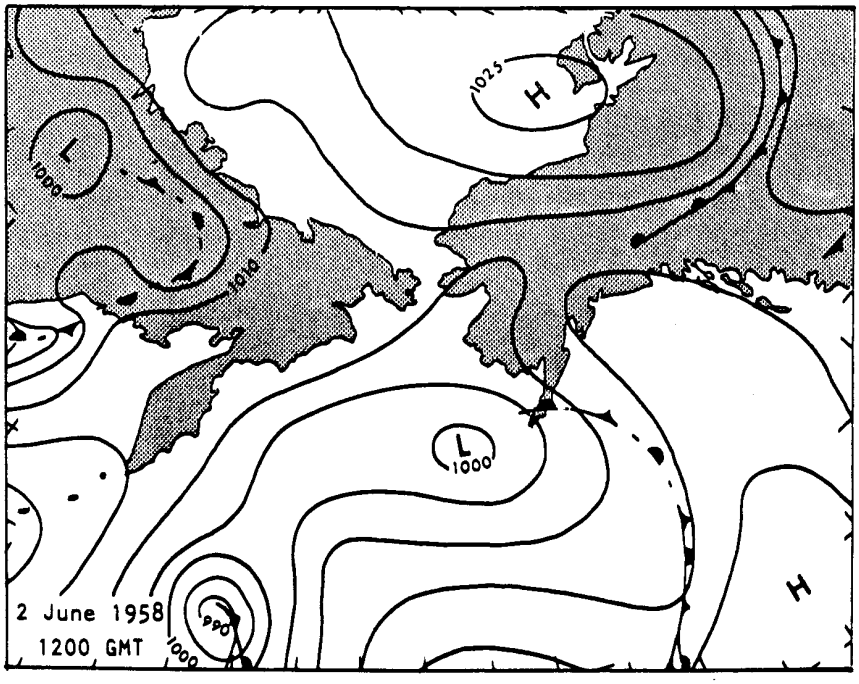

Fig. 4.2—Typical baric pattern where low is at the west over Siberia plus a ridge over Alaska.

Table 4.4

DETERMINATION OF STANDARD DEVIATION FOR WIND SPEED SIMULATION AT POINT BARROW FOR THE MONTH OF JANUARY (SAMPLE PERIOD, 19 YEARS)

Baric Type	Observed Frequency of Maximum Wind	Standardized $Z(q)$	Observed Wind				Adjusted Marine Wind Speed		$\ln \sigma = [ln(max.) - ln(\sigma)]$	σ
			Direction (T)	Deviation (2σ)	Speed μ	(kn) Max.	$ln(\mu)$	$ln(max.)$	$Z(q)$	kn
1	0.00340	2.71	45	(90)	9	(28)	2.379	3.514	0.418	1.52
2	0.00393	2.66	225	(90)	7	(25)	2.128	3.401	0.478	1.61
3	0.00362	2.69	67.5	(90)	8	(25)	2.262	3.401	0.423	1.52
4	0.00363	2.69	90	(90)	13	(38)	2.747	3.820	0.399	1.49
5	0.00746	2.43	90	(90)	10	(34)	2.485	3.708	0.503	1.65
6	0.00216	2.86	101	(22.5)	10	(34)	2.485	3.708	0.427	1.53
7	0.00109	2.29	90	(45)	9	(34)	2.379	3.708	0.580	1.78
8	0.00387	2.66	270	(135)	8	(25)	2.262	3.401	0.428	1.53
9	0.00909	2.36	101	(67.5)	11	(33)	2.580	3.679	0.465	1.59
10	0.00704	2.46	90	(90)	11	(30)	2.580	3.583	0.407	1.50
11	0.00980	2.34	56	(112)	7	(27)	2.128	3.478	0.576	1.78

Abramowitz and Stegun, 1964). For better accuracy in the lower frequencies, tabulated values were obtained by rational approximation using Chebyshev polynomials (Hastings, 1955).

From the land-based station data, adjusting factors of 1.2 and 10° were used for marine wind speed and direction. These factors were determined from a field monitoring program relating land-based wind data (Nome) and the marine wind data (Norton Sound) carried out by the Pacific Marine Environmental Laboratory (PMEL, NOAA) (Overland, 1980).

As shown in Table 4.4, the standard deviation of wind speed is then computed by subtracting the logarithms of the maximum and the mean wind speed divided by the standardized normal units. The same procedure is used for each pressure pattern, each month, and each station.

To verify and adjust the probabilistic model of wind speed, data at Nome (from December 1, 1906, to December 31, 1980) were used and compared with the simulated data near Norton Sound. The simulated data were drawn at half-hour intervals. Each group of 1440 samples that represented a simulation period of 30 days was compared with the long-term monthly wind statistics. During this comparison, previously mentioned correlation factors between land-based wind data and marine wind conditions were considered. A total of 60 simulations were compared with the long-term data each of sample size 1440. The difference between the simulated wind speed and the observed wind speed for a winter period (December through May) was 3.0 percent too high. The difference for the summer period (June through September) was 3.7 percent too high. For the fall period (October through November) a simulated mean wind was 2.3 percent too low. These discrepancies were subsequently used for the final adjustments of mean wind speed for each of the weather types for that area.

In the case where a prevailing wind direction exists under a given pressure pattern, it is usually assumed that the prevailing direction is normally distributed with nonzero mean and a given variance (Riera et al., 1977; McWilliams and Sprevak, 1980, 1985). When winds are weak or from no prevailing direction, the distribution reduces to uniform distribution (McWilliams and Sprevak, 1980, 1985). In modeling wind direction, observed data of each

weather type for that particular month were simulated with normal distribution. However, when data were categorized as "weak and variable," then a uniform distribution was used.

MODELING STORMS

In treating the Alaskan regional weather as a Markov stochastic process, we are, in essence, defining the weather and the regional wind field onto a finite set of stochastic states. Each state processes certain unique physical behavior characteristic of its baric pattern. The state of having an extratropical cyclone exist within a modeled area is one of the possible outcomes of the finite states of the stochastic weather system.

The principle of the computational procedure can be illustrated using a simple diagram (Fig. 4.3) in which the realization of a stochastic weather sequence is depicted. Starting from the lower left corner of the diagram, an initial state is selected from the steady-state probability distribution of all the weather types. Suppose the weather pattern type 4 is selected out of all possible outcomes. The next draw will be from the transitional matrix $P = \{P_{ij}\}$. The probability of selecting a weather sequence 8 would be $p_{4,8}$, as shown in the diagram. The same weather type can also be selected at the probability $p_{2,2}$, which is the second diagonal element of the probability matrix. In the subsequent draws, solid lines represent outcomes of the random selection.

Suppose a type-5 weather pattern is selected. The sea-level pressure distribution associated with this particular weather type is a pronounced low pressure center occurring at the southwest of the Bering Sea moving toward the middle (Table 4.2). Under this condition, the simulation program would divert the computation to a subprogram handling the probabilistic simulation of a moving extratropical cyclone. In the subprogram, parameters associated with the cyclone are derived from synoptic analyses using a subset of the 19-year data from which the transitional matrices are derived. Essential parameters for the computation of a moving cyclonic wind field are, namely, the spatial distribution of the cyclogenetic process, the distribution of central pressure, the forwarding speed, and persistency. The last parameter would govern the number of consecutive weather states in which a cyclone exists until a cyclolytic process prevails. Under this condition a weather state that has the highest probability of following a cyclonic state is likely to be selected within the state transitional matrix.

To determine parameters of the Aleutian Low, several groups of climatological data were analyzed. For the frequency of occurrence, synoptic data between January 1966 and December 1974 (Brower et al., 1977) were used. Figure 4.4 gives the spatial distribution of cyclonic events in each subarea. The area west of 160°W and north of 50°N is classified as the southern Bering area, since its cyclonic flow dominates the entire southern Bering Sea. Figure 4.4 shows no major seasonal trend in the number of occurrences of the cyclonic activities over the modeled area. Table 4.5 gives the two-dimensional probability density function ($pdf \times 10000$) of the occurrences over the computational grid for the weather simulation. The spatial resolution of the grid network is deemed necessary to provide an accurate wind field considering the pressure distribution of a typical extratropical cyclone.

For the probability distribution of the intensity, daily synoptic data for five years (1949–1953) were adapted. The original data were analyzed by Schutz (1975) for the climatological modeling work conducted at The RAND Corporation. In the analysis the normalized (using the pdf of the mean value = unity) frequency distribution of intensity based on synoptic characteristics of five-year January data is shown in Fig. 4.5. This sampling period is within the 19-year period when identical weather data were used to derive the weather state

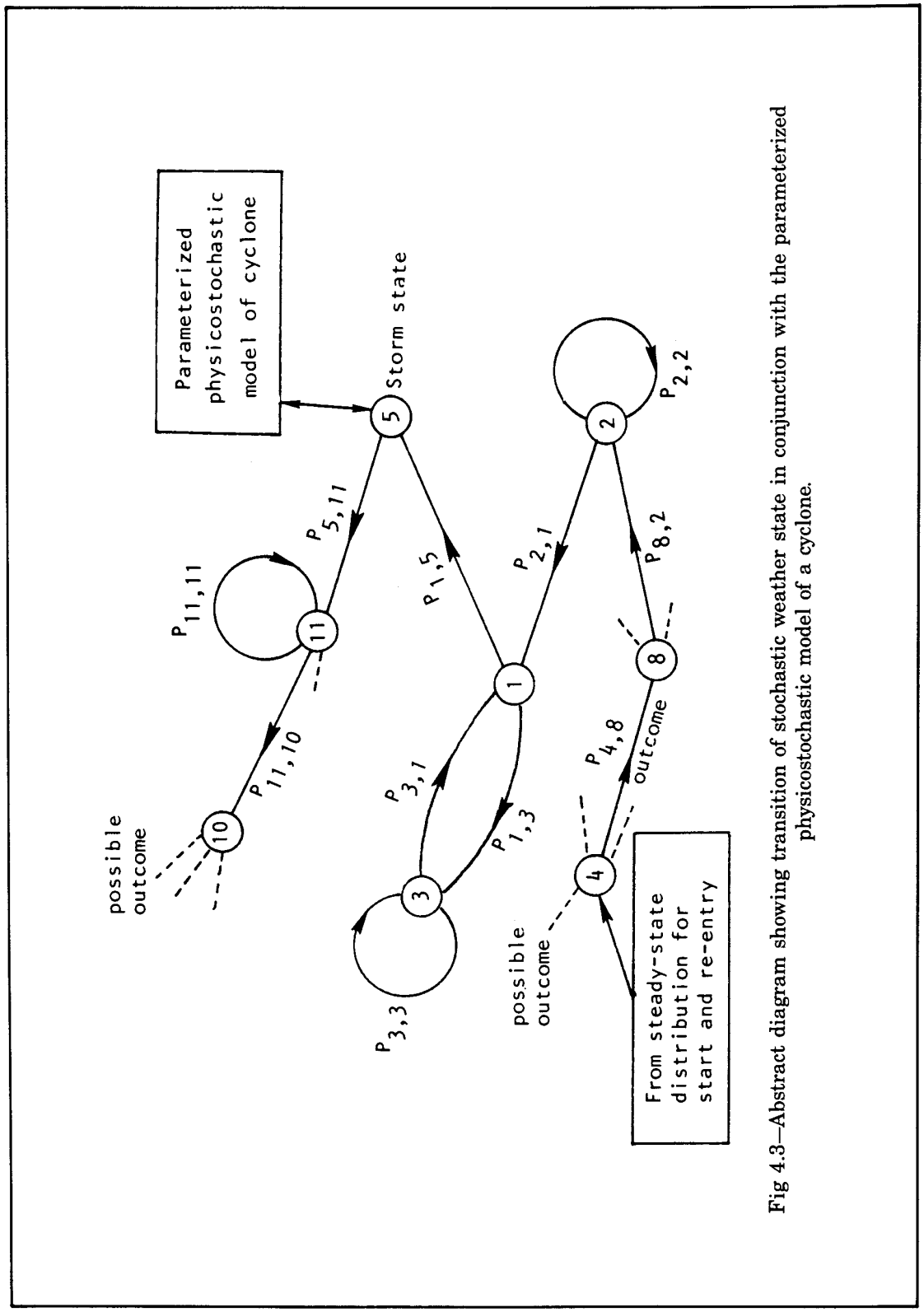

Fig 4.3—Abstract diagram showing transition of stochastic weather state in conjunction with the parameterized physicostochastic model of a cyclone.

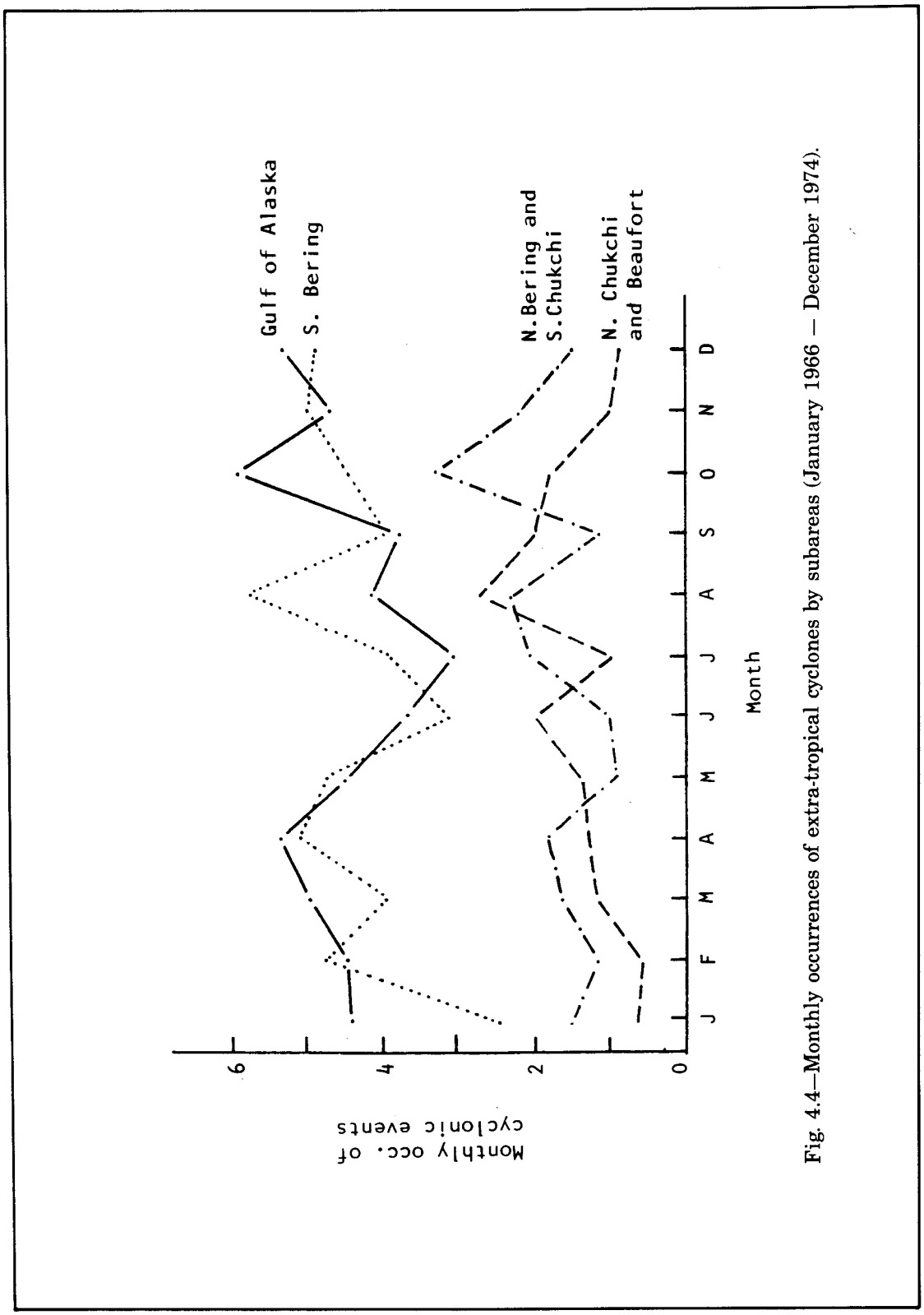

Fig. 4.4—Monthly occurrences of extra-tropical cyclones by subareas (January 1966 — December 1974).

Table 4.5

SPATIAL DISTRIBUTION OF PDF (x10000) OF LOW PRESSURE CENTERS

Latitude	180°W			170°W						160°W						150°W						140°W					130°W	Σ
80°N	1	0	0	0	1	1	1	1	1	3	1	1	1	2	0	1	1	2	0	3	1	1	0	0	0	0	23
	2	1	0	3	1	0	1	1	1	2	1	0	0	0	0	2	1	2	1	1	3	2	1	0	1	0	27
	1	1	1	2	0	2	0	2	0	0	0	2	3	0	0	1	4	1	0	1	2	1	1	1	1	0	27
	1	1	1	1	0	0	0	1	0	0	1	2	3	2	0	0	0	1	1	1	1	4	0	0	0	0	20
	1	1	1	2	0	1	1	2	3	2	1	2	0	2	0	0	0	1	1	1	1	1	2	0	0	0	26
	1	0	3	0	1	1	0	1	0	3	0	1	3	1	2	1	0	0	1	2	2	0	0	0	1	0	24
	1	1	1	2	2	2	1	0	0	0	0	0	0	2	1	0	0	1	1	2	3	1	3	1	0	2	27
	0	2	0	0	2	0	1	1	1	1	1	1	4	0	3	0	2	0	2	5	2	1	0	0	0	0	29
	2	0	1	1	1	1	1	3	2	1	2	2	0	4	2	2	2	1	3	1	3	2	2	1	0	0	40
	3	4	1	0	2	1	1	1	0	0	4	1	1	1	1	2	3	0	0	0	1	1	2	3	0	0	33
	1	1	1	2	2	3	3	1	3	2	4	0	1	4	2	2	0	3	2	1	3	1	1	2	1	0	46
	4	2	4	2	5	2	1	3	2	3	6	0	3	2	1	4	1	2	2	3	0	3	1	4	1	0	61
	4	3	1	2	3	4	6	2	2	4	1	2	2	3	1	1	6	3	3	2	4	3	2	4	5	0	73
	2	3	4	4	1	3	1	1	3	1	0	1	3	6	2	1	4	1	4	4	4	2	1	2	1	1	60
	4	5	3	3	7	2	3	3	3	2	3	5	2	2	0	6	1	1	3	3	2	5	4	0	1	0	73
70°N	6	1	5	5	3	1	5	3	6	2	4	2	2	3	0	2	1	4	2	4	2	3	4	5	3	0	78
	2	5	4	3	6	4	8	2	2	5	4	6	4	5	5	1	2	3	2	5	4	5	4	0	2	2	95
	1	2	3	6	4	6	8	2	8	6	2	4	5	3	3	5	2	5	4	6	8	7	6	0	4	0	110
	1	3	7	7	1	7	5	10	7	8	6	5	5	2	5	4	3	5	8	7	3	1	4	7	3	1	125
	6	7	8	2	6	6	5	1	6	4	4	0	6	3	4	7	5	5	3	7	3	5	10	4	6	0	123
	6	10	7	7	8	7	15	4	5	2	3	4	4	3	5	11	6	4	7	7	4	6	4	2	1	0	142
	2	4	12	4	10	9	12	7	8	6	10	6	3	2	7	5	5	3	3	7	7	8	6	6	7	2	161
	4	9	10	5	4	9	9	5	10	6	7	5	8	3	8	7	9	8	6	4	11	4	6	1	3	2	163
	9	7	7	5	9	4	5	8	3	9	7	5	6	6	8	5	7	7	17	8	5	4	5	8	4	1	169
	10	7	14	7	7	12	12	8	7	8	7	10	9	5	7	7	7	9	3	8	5	10	10	12	3	3	207
	10	4	10	6	6	6	3	4	8	6	4	8	8	10	8	5	13	9	3	5	14	8	10	13	6	3	190
	8	5	11	9	14	4	5	6	10	9	5	10	11	11	12	6	8	6	6	12	16	10	7	12	9	2	224
	6	9	14	12	18	8	14	13	13	7	6	12	17	3	12	10	10	9	11	6	11	12	12	10	9	2	266
	11	9	11	17	13	8	8	7	12	9	11	7	12	10	12	7	10	10	11	14	9	9	9	3	5	2	246
	9	8	14	19	9	10	8	6	16	5	17	7	9	2	8	3	8	10	10	10	13	12	9	8	4	4	238
60°N	7	9	11	11	14	13	16	15	11	9	12	14	12	10	14	9	11	12	9	5	15	15	8	4	8	1	275
	13	13	13	11	14	14	10	16	9	10	14	18	10	12	8	15	10	11	9	19	12	9	17	7	6	2	302
	11	14	17	11	13	14	14	16	15	14	12	7	8	11	17	16	14	15	8	8	16	5	18	15	8	1	318
	19	16	17	12	10	16	13	19	10	11	7	12	14	14	24	15	17	15	20	13	21	11	8	20	8	5	367
	13	14	20	26	14	17	18	20	14	10	19	15	22	12	10	16	14	14	18	12	13	20	14	12	11	1	389
	18	20	19	20	16	18	17	19	15	17	17	15	11	19	15	23	16	10	15	16	10	20	20	11	14	4	415
	21	12	18	26	22	19	22	10	17	19	19	17	17	7	15	15	19	19	18	19	21	12	17	12	16	3	432
	18	18	15	24	16	13	18	19	16	19	14	21	18	18	17	25	24	13	19	23	16	20	21	23	15	4	467
	12	21	19	24	23	16	21	24	27	13	16	17	17	15	17	24	25	23	34	25	21	24	18	14	13	0	503
	15	18	18	31	20	17	16	16	17	20	22	30	20	16	20	25	18	31	24	23	23	16	15	22	20	4	517
	21	20	34	20	21	22	19	28	23	23	13	22	18	15	11	17	26	19	24	30	24	16	17	8	18	5	514
	20	32	17	25	15	30	25	24	23	24	21	19	21	21	17	24	24	27	37	25	20	16	18	15	13	2	555
	20	18	20	20	28	28	15	21	21	22	23	16	31	27	26	20	20	29	26	22	22	25	23	10	16	11	560
	18	32	36	36	31	29	31	18	23	21	22	21	20	27	32	32	26	24	40	29	35	28	24	26	19	8	688
50°N	25	29	31	26	25	26	23	17	20	16	28	17	16	16	22	23	27	18	27	36	23	25	17	16	19	4	572
Σ	370	401	464	461	428	416	421	391	403	364	381	372	390	342	384	407	412	395	448	445	439	394	381	324	285	82	

transitional probability matrices as well as the wind statistics collected at all coastal stations. A mean value of 975.0 mb with a standard deviation of 10.66 mb was obtained from the synoptic analyses of the Aleutian Low.

The average forward speed and frequency of persistence of cyclones are shown in Fig. 4.6. Each 36-hour period is treated as a time unit that is subdivided into three 12-hour periods for the convenience of later convolution. From Fig. 4.6, the storm duration with the highest probability of occurrence is 1.0 to 2.0 days. This is followed by 3.0, 4.0, and 6.0 days, in a descending order.

The steady-state probability distribution of storm events can also be represented by transitional probability statistics in which a storm having longer persistence is equivalent to a "storm" weather state followed by another "storm" weather state. During a simulation, events like this are treated by continuing the storm track with new speed and direction sampled according to the observed statistical parameters associated with the Aleutian Low.

In certain aspects more refinements of the general approach are desirable. This usually requires more data as well as more detailed analyses. Dominant weather features like the persistent Aleutian Low make the synoptic weather analyses an effective way to simulate its behavior; without such prominent weather features this method would be less effective.

A unique weather feature in the modeled area is a pronounced low pressure center coexisting with a quasi-stationary Siberian High (Fig. 4.7). Because of the characteristic relationship between a pressure field and the veering angle of the surface wind field, the wind direction at sea level near the Bering Strait would have a direction of nearly due south. If a strong wind field persists long enough, a substantial amount of ice would migrate southward through the Bering Strait thus creating an "ice breakout" condition (Ahlnas and Wendler, 1979). As shown in Fig. 4.8 for a typical winter ice condition, under a wind stress of 0.5 pascal, it requires a fetch of 200 km to cause a breakout (Reiner, 1979). This corresponds approximately to a critical wind speed of 26 kn blowing over ice. Using 19-year observed wind data from the nearby weather station (Kotzebue) resulted in a probability of 2.3 events per each winter period (from November through June).

COMPUTING CYCLONIC SURFACE WIND

Surface wind speeds and directions associated with a cyclonic baric pattern are computed according to the following procedures. The pressure distribution in the cyclonic field is schematized with the pressures at the center and the outermost closed-isobar according to an exponential function often used to describe the cyclones.

The pressure at the center is selected at random according to the mean and the standard deviation associated with the Aleutian Low (Fig. 4.5). The outer pressure is selected by the long-term monthly average sea-level pressure in the modeled area (Fig. 4.9). The continuous pressure distribution is of the form:

$$P(r) = p_c + (p_n - p_c) \exp(-A/r^B) \tag{4.2}$$

where p_c is the central pressure and p_n is the ambient pressure. For the average extratropical cyclones in this area, the value of A is selected to be 30 nautical miles (i.e., 0.5° latitude). Slight modifications can be made because of the eccentricity associated with extratropical cyclones. But they were not implemented for the oil spill trajectory simulations.

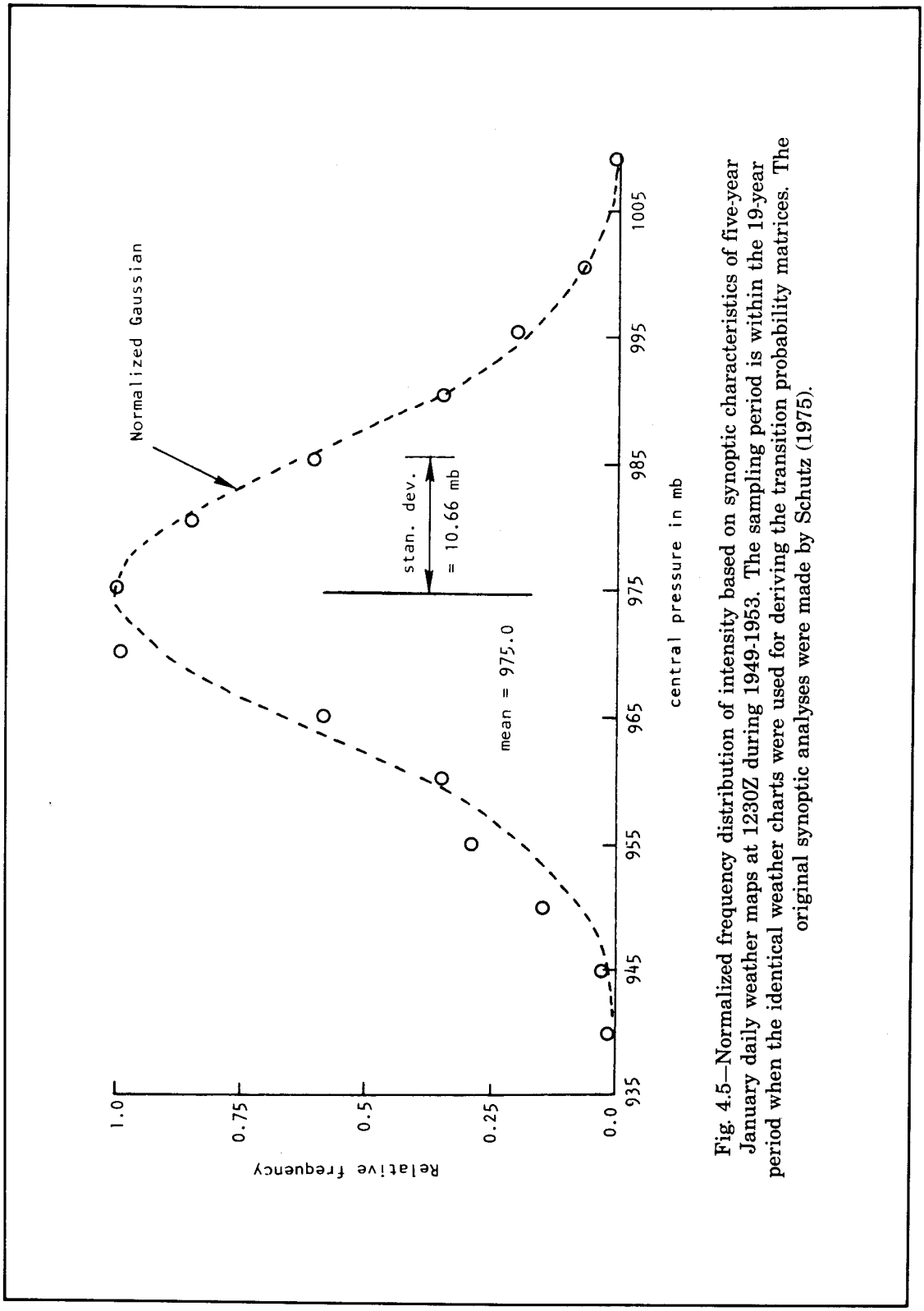

Fig. 4.5—Normalized frequency distribution of intensity based on synoptic characteristics of five-year January daily weather maps at 1230Z during 1949-1953. The sampling period is within the 19-year period when the identical weather charts were used for deriving the transition probability matrices. The original synoptic analyses were made by Schutz (1975).

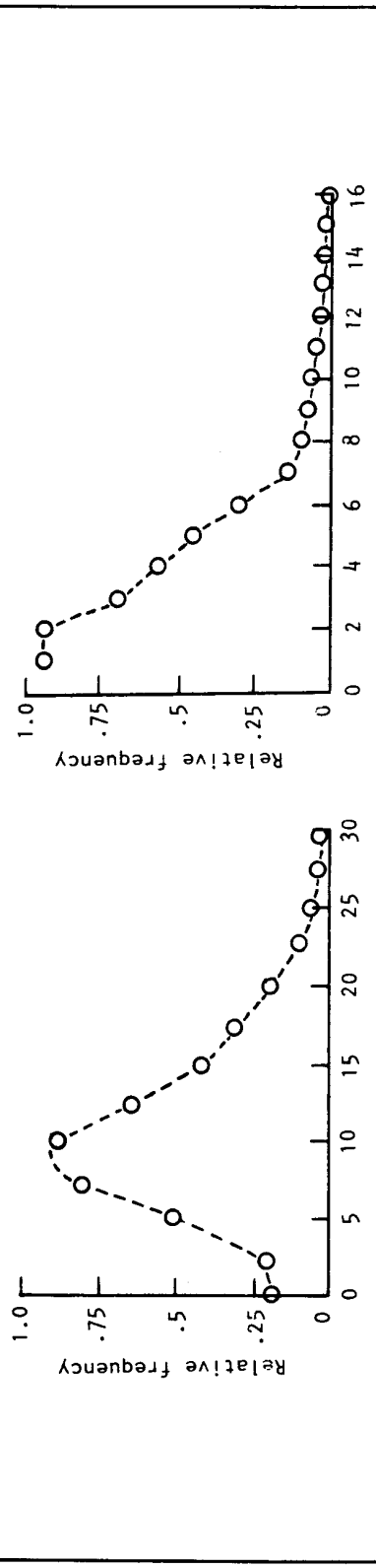

Fig. 4.6—Normalized frequency distribution of forward speed and persistence based on synoptic characteristics of five-year January daily weather maps at 1230Z during 1949-1953. The sampling period is within the 19-year period when the identical weather charts were used for deriving the transition probability matrices. The original synoptic analyses were made by Schutz (1975).

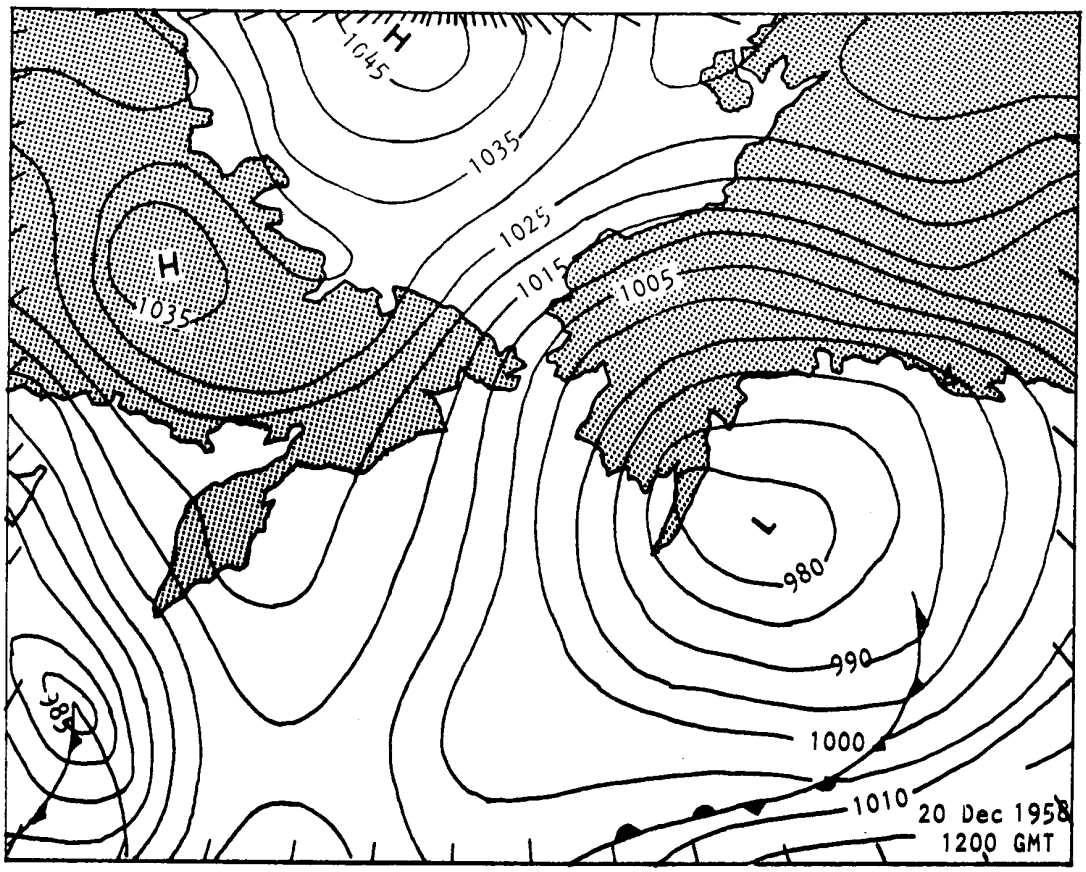

Fig. 4.7—Typical baric pattern where a pronounced low existed over the modeled area. In this case, the Eastern Low coexisted with a Siberian High. This pressure pattern creates strong southerly air flow near the Bering Strait and thus may induce an ice breakout through the Strait.

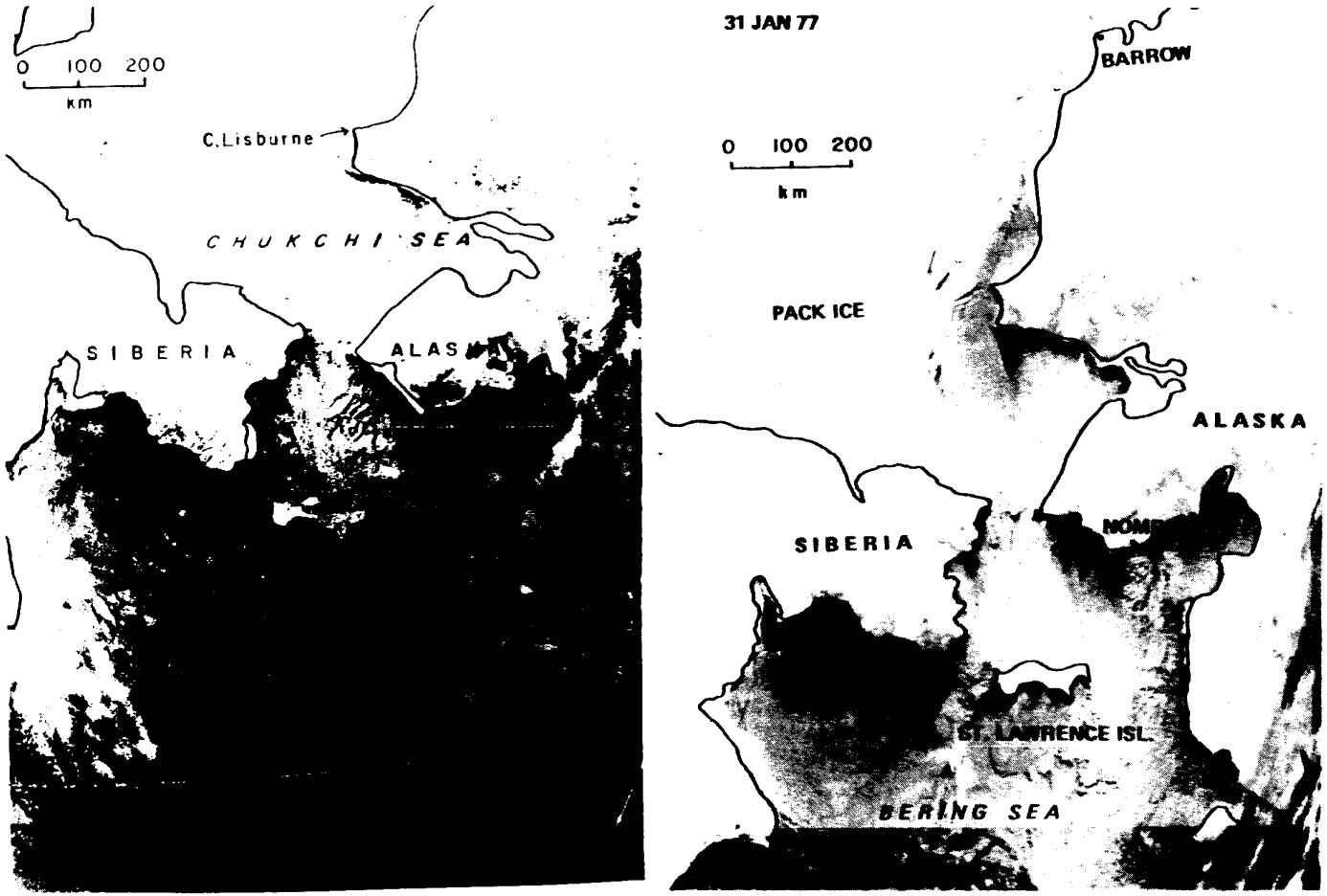

Fig. 4.8—Surface-temperature-enhanced infrared satellite (NOAA-5) images showing two events of ice breakout through the Bering Strait. The left is for March 20, 1978; the right is for January 31, 1977. Both were adapted from Ahlnas and Wendler (1979). These images imply that ice could pass either to the east or to the west of St. Lawrence Island.

The value of coefficient B is taken as 1.0. Higher values are often selected for a tropical cyclone. The average distance between the center and the outer closed isobar is approximately 5° latitude. The sea-level pressure at the outer closed isobar is obtained from the long-term monthly average SLP for the modeled area. The gradient wind speed is then computed using:

$$V_{gr}^2 + fr\ V_{gr} = \frac{r}{\rho_a} \frac{dp}{dr} \tag{4.3}$$

where f is the Coriolis parameter, r is radius, and dp/dr is the local pressure gradient. During the oil spill trajectory simulation, the wind field is computed every half hour. Finally, the computed gradient winds are adjusted for speeds and directions to obtain winds at sea surface (10 m level). For the adjustment, the method of Hesse (1974) and Hesse and Wagner (1971) was used. The method was selected because it was derived from extensive field data associated with the extratropical cyclones. For other models, the reader is referred to the work of Cardon (1969) and Brown and Liu (1982).

The bulk momentum transfer coefficients are computed according to the air-sea temperature difference (Fig. 4.10) and the results compiled by Kondo (1975) and Garratt (1977), and later the updated results were compiled by Wu (1982). The eccentricity associated with the extratropical cyclones was investigated. It was found, however, that synoptic analyses could not provide enough data to support a definite asymmetric parameter so that the gradient wind field can be modified. This aspect is worth further study.

With the methods described in this chapter, the stochastic model is tested by simulating 60 monthly cycles each having 1440 half-hourly wind data sets. For three stations in the modeled area, the frequency of occurrence of wind speeds at defined intervals from all the directions is plotted, as well as the percentage of occurrences from these directions. The three plots at the top of Fig. 4.11 are the direct outputs of the simulations. In this figure the observed data (obtained from Brower et al., 1977) are also plotted in a similar manner. The simulated and observed wind data are not directly comparable, as the model generates from 16 directions, whereas the compiled field data use only eight directions. It will be noted, however, that computations show good agreement with observations.

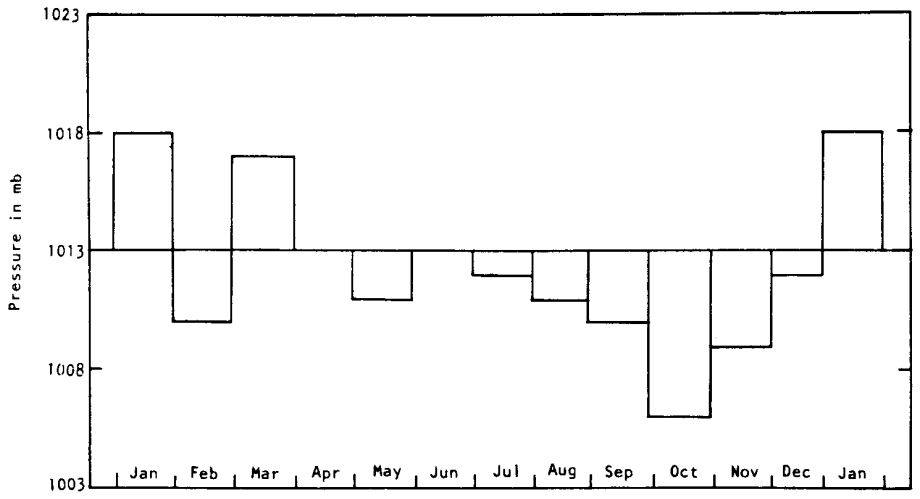

Fig. 4.9—Monthly Meridinal average sea-level pressure over the northern Bering Sea at 65°N latitude.

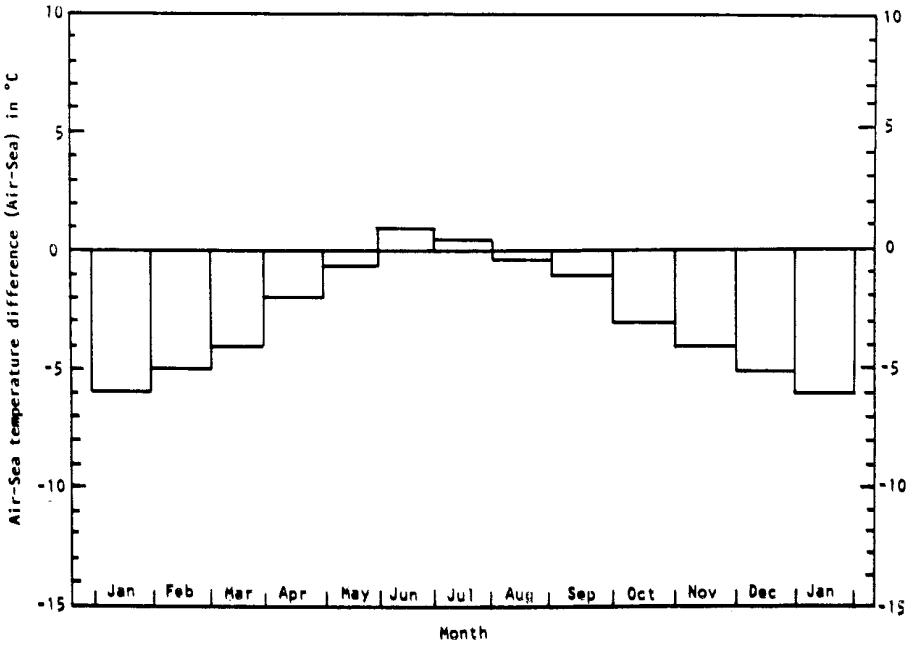

Fig. 4.10—Monthly average air-sea temperature difference over the eastern Bering Sea.

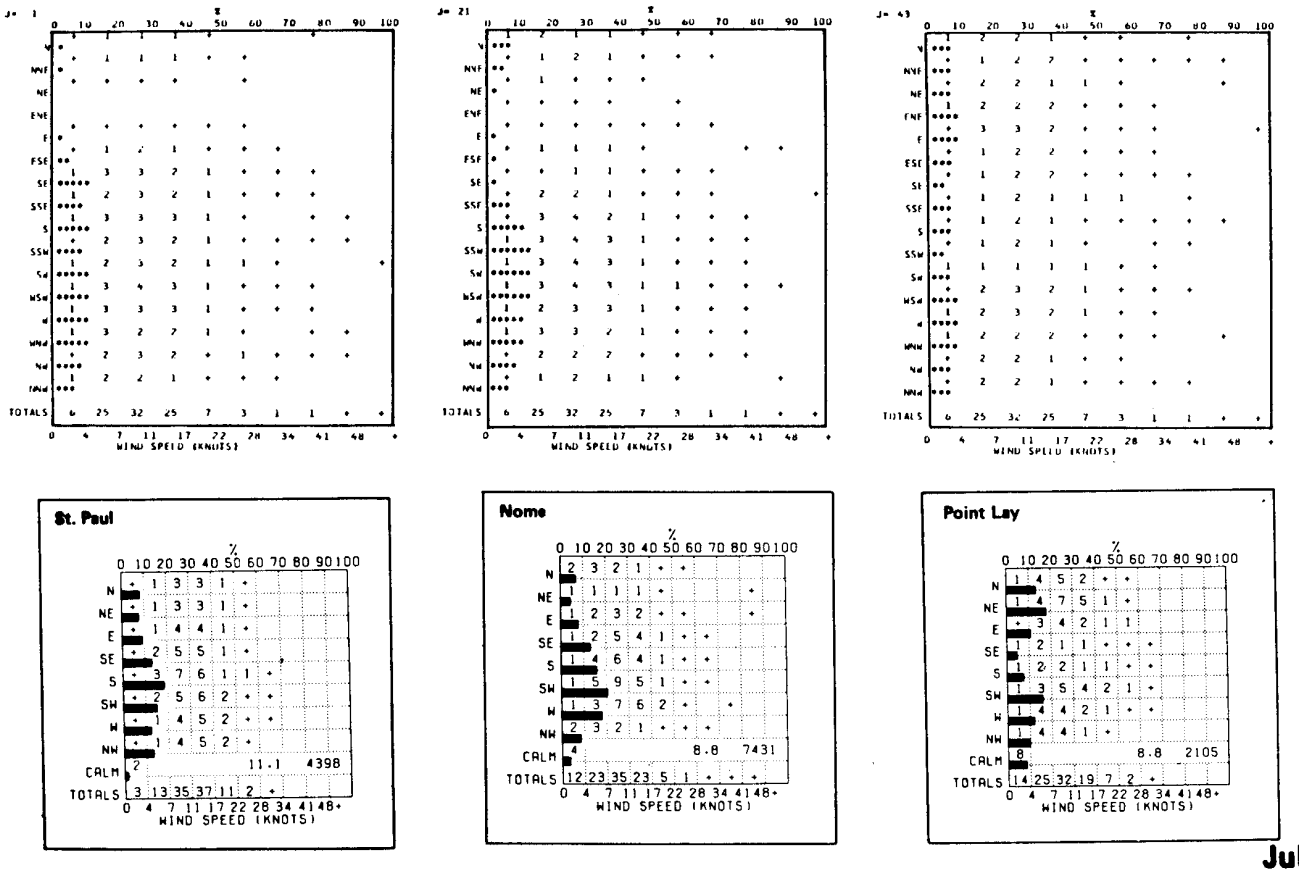

Fig. 4.11—Comparison between the observed wind roses at three land-based stations (Brower et al., 1977) for July, and typical marine winds at nearby locations obtained by long-term (2000) weather sequences interrupted by moving storms.

5. MODELING PACK ICE MOVEMENTS

OBJECTIVES

The primary objective of our study of pack ice movement in the Bering Sea, Chukchi Sea, and the Beaufort Sea is to provide information for an oil spill trajectory model. This model, described in the next chapter, simulates the movement of spilled oil. As spilled oil is trapped in or under the ice during winter and subsequently released during the spring/summer period, it is important in our overall modeling effort to establish ice pack movements. Consequently, our interest is centered around the movement of the ice pack rather than the mechanics of solid ice or shore-fast ice, which received considerable scientific attention some years ago (Parmerter and Coon, 1972; Hibler et al., 1972; Pritchard, 1975). This has been changed recently (Thorndike and Colony 1982; Pritchard, 1984). They have even shown that highly simplified free-drift ice computations can provide reasonable ice trajectories even in the Beaufort Sea during winter in areas other than the near-shore land-fast ice region. In the shore-fast region, ice moves vertically with tides, yet no major displacement in the horizontal direction occurs. Oil spill during winter would be released the following summer when the ice melted.

ICE CONDITIONS AND THE DYNAMICS OF ICE PACK

Within our modeled area, the Beaufort Sea is covered with ice almost the entire year with only seasonal variations in concentration. Only during summer are there open areas close to shore. Figure 5.1 shows the percentage of ice coverage during the summer as it is schematized in the five-layer Beaufort Sea model. The figure also shows the thickness of multiyear ice in the model. This thickness ranges from 1.7 m near the open area to nearly 3 m in the north. During winter the latitudinal variation in the thickness of pack ice ranges from approximately 1 meter to nearly 4 meters north of the 75° latitude. The ice cover contained, at that time, young ice (first year), and multiyear ice. The near-shore area, as well as the lagoons behind the barrier islands, are almost completely covered with shore-fast ice with minimum horizontal displacement throughout the entire winter season.

Outside the narrow shelf in deep water, most of the ice is pack ice, which drifts as a result of wind and current forcing. The mean annual net drifts vary from 0.4 to 4.8 km/day and move in a westerly direction, being part of the general circulation around the North Pole (Arctic Gyre). However, under storm conditions ice displacement can be considerable. Weeks and Weller (1984) reported that under winds of 90 km/hr, pack ice can move 40 km in five hours, suggesting a drift ratio of nearly 8.9 percent of the wind speed. Our model results sometimes show even higher drift speeds. For example, in an area southwest of Point Barrow, one simulation showed a drift speed of nearly 10 km/hr during very high winds in the vicinity.

High drift speed along the coastal areas between Point Barrow and the Bering Strait (except Kotzebue Sound, which is occupied by shore-fast ice) is attributable to two major causes. First, when the winter Siberian High is coupled to an easterly moving Aleutian Low, the direction and speed of the resulting air flow can cause ice movement in the eastern Chukchi Sea to reverse and break out of the Bering Strait to the south. Second, as we discussed

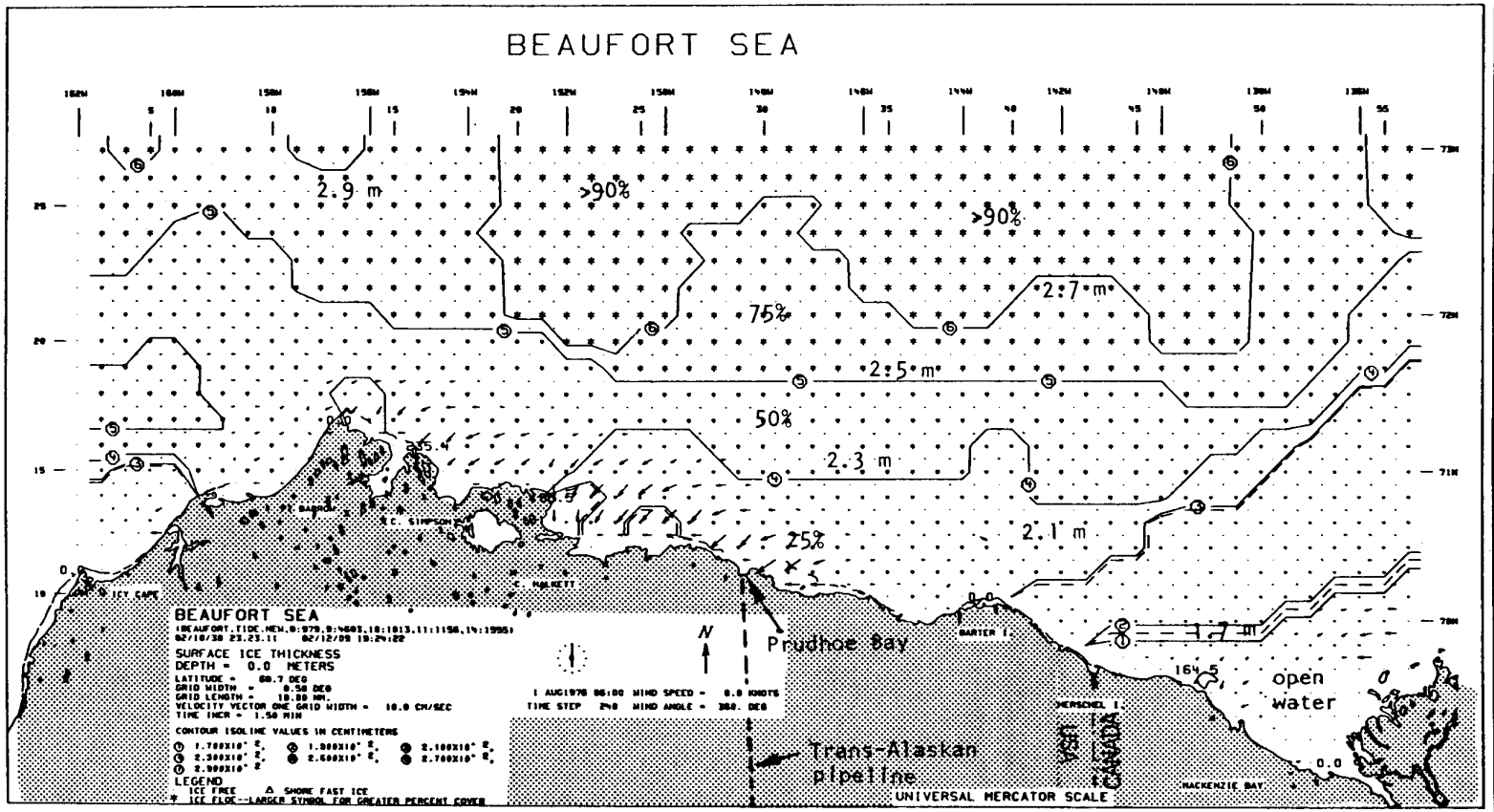

Fig. 5.1—Spatial distribution of ice concentration and thickness as compiled from existing data for the summer period.

above, because of the orientation of the coastline when the atmospheric pressure gradient creates a current reversal, coastal jets in that area would add a substantial advective component to the along-shore wind drift of ice pack.

The coverage of ice in the Bering Sea during winter is limited to the shelf area with interannual variability. The normal limit of ice during winter extends from Point Navarin southeast to the vicinity of Point Mueller. The thickness of pack ice varies considerably with larger thickness at higher latitudes. In the simulation with the Chukchi Sea/Bering Sea models of winter conditions, the ice thickness distribution shown in Fig. 5.2 was used.

During late fall when the predominant wind shifts from the southwest to the northeast, the surface cooling of water columns induces a strong vertical convective process over the eastern shelf area.

In the near-shore area, upwelling, associated with the northeasterly wind stress, reinforces this convective process. Accelerated by these two dynamic processes, temperatures of the homogeneous coastal water would reach the freezing point associated with its salinity (–1.65°C for a salinity of 32 g/kg at that point in time).

As ice is being formed, the freezing process releases a certain amount of salt—the amount is inversely proportional to the rate of freezing. However, this local process cannot continue indefinitely. The northeasterly wind, which produces ice through cooling, transports the locally produced young ice away from shore. This transport is not exactly with the prevailing wind but in a west southwesterly direction because of Coriolis effects.

As the ice factory of the Bering Sea, the northeastern coastal waters have higher salinity and lower temperatures than the deep Bering Basin near the end of the winter season. Near the shelf break, ice that has been formed near shore melts because of higher water temperatures and therefore leaves a layer of stable, fresher waters beneath the ice.

The dynamics of ice in the marginal ice zone are affected by the baroclinic field. Fresh water beneath the ice suppresses the generation of turbulence, therefore creating a discontinuity in the vertical shear coupling. This fresh water beneath the ice not only increases the drifting speed but also reduces the turning angle. In the marginal ice zone, ice also interacts with the short-wave field, reducing wave heights and the Stokes' transport.

In modeling the ice movements, we have tried to incorporate as much of the aforementioned dynamics as they have been understood since our modeling effort began in 1978. Wind stress and water/ice stress coefficients used in the model have been updated from published works (Ovsiyenko, 1976; Martin et al., 1978; Reynolds and Pease, 1982; Langleben, 1982; Macklin, 1983; Pease et al., 1983; Overland et al., 1984). The final drag coefficient used for the air/ice interface is 0.003 and the drag coefficient used for the ice/water interface is 0.018 with water velocity evaluated at the middle of the top layer. For the Bering Sea this is approximately 2.5 meters from the surface and 1.5 meter from the bottom of the ice.

COMPUTATIONAL FORMULAS AND DATA REQUIREMENTS

The computations of the movements of pack ice are based on the consideration of the change in momentum in the horizontal plane by wind stress at the upper surface, stress at the ice/water interface, Coriolis force, momentum transfer within the ice pack, thermodynamics, vertical stability associated with the growth/melting process, and the sea/surface tilt.

Since the model considers only the movements of pack ice, the size of an individual ice floe is assumed to be smaller than the computational grid size. Lacking actual field

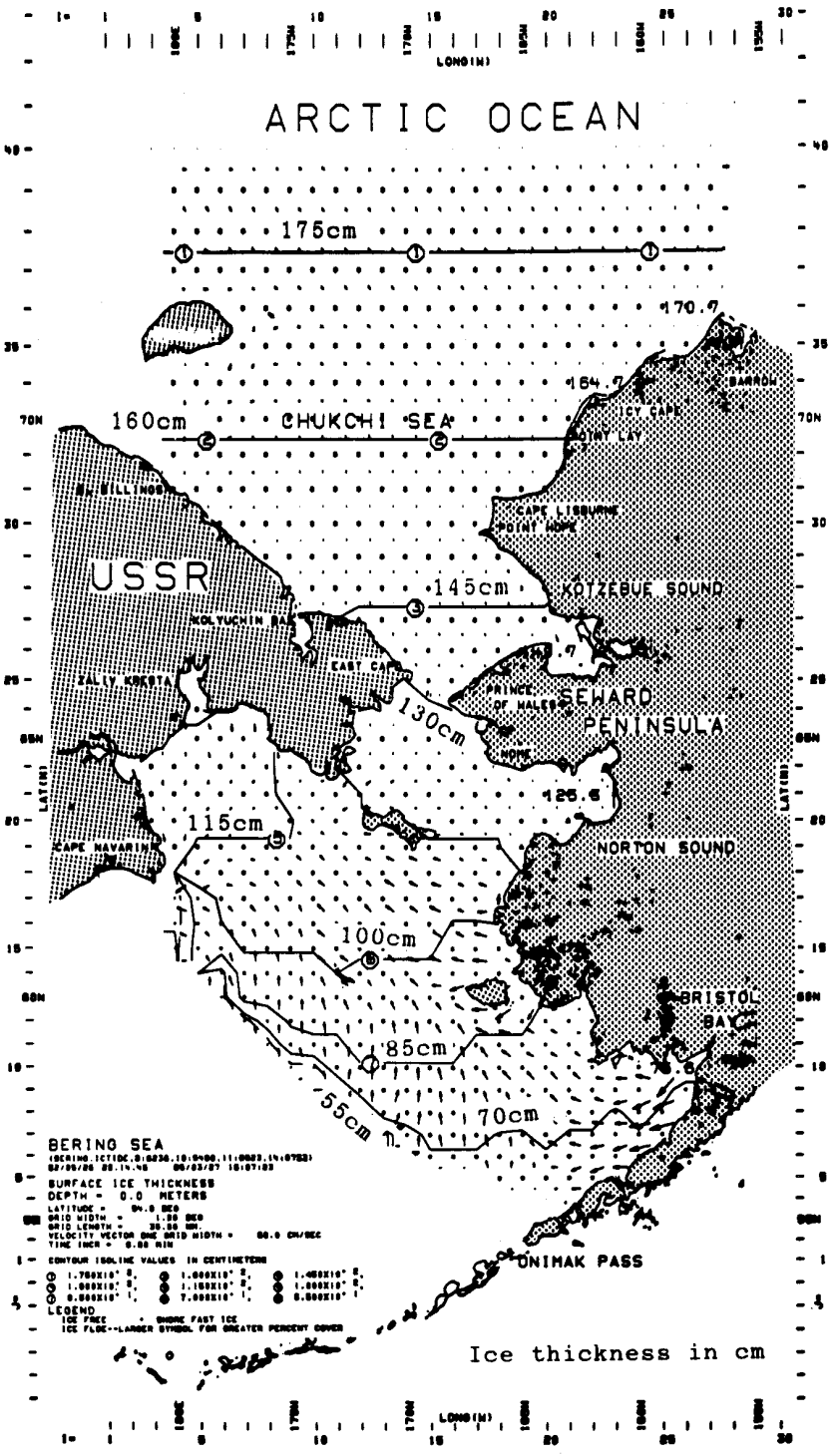

Fig. 5.2—Spatial distribution of average pack ice thickness in the Bering/Chukchi Sea model near the end of January.

measurements, we assume the vertical temperature gradient within the ice to be linear. The rate of momentum transfer within the pack ice in the computational grid is estimated as a function of ice concentration according to the four-third power law of the subgrid momentum transfer.

The balance of momentum for the ice in the horizontal direction, if written directly in finite difference form, is

$$\overline{\overline{\delta_t(\bar{H}^x u')}^t} = -\delta_x\left(\overline{\overline{\bar{H}^x u'}^x \overline{u'}^x}\right) - \delta_y\left(\overline{\overline{\bar{H}^y v'}^x \overline{u'}^y}\right) + f\bar{H}^x\overline{v'}^{xy} - \frac{1}{\bar{\rho}^x}\bar{H}^x\delta_x p$$

$$+ \frac{1}{\bar{\rho}^x}\left[C^*\rho_a W_a^2 \sin\psi - \left(E_x'\delta_z\overline{u'}^{2t}\right)_{k-3/2} + \delta_x\left(HA_x'\delta_x u\right)_- + \delta_y\left(\overline{\bar{H}^x\overline{A_y'}^x}^y \delta_y u'\right)_-\right] \tag{5.1}$$

at $i+\frac{1}{2}$, j, l, n

$$\overline{\overline{\delta_t(\bar{H}^y v')}^t} = -\delta_x\left(\overline{\overline{\bar{H}^x u'}^y \overline{v'}^x}\right) - \delta_y\left(\overline{\overline{\bar{H}^y v'}^y \overline{v'}^y}\right) - f\bar{H}^y\overline{u'}^{xy} - \frac{1}{\bar{\rho}^y}\bar{H}^y\delta_x p$$

$$+ \frac{1}{\bar{\rho}^y}\left[C^*\rho_a W_a^2 \cos\psi - \left(E_y'\delta_z\overline{v'}^{2t}\right)_{k-3/2} + \delta_x\left(\overline{\bar{H}^y\overline{A_x'}^y}^x \delta_x v\right)_- + \delta_y\left(HA_y'\delta_y v'\right)_-\right] \tag{5.2}$$

at $i, j+\frac{1}{2}$, l, n

where H = local ice thickness,
u' = ice velocity in x direction,
v' = ice velocity in y direction,
C^* = wind stress coefficient,
ρ_a = density of air,
ρ = density of ice,
W_a = wind speed,
ψ = wind angle from the y coordinate, and
f = Coriolis force term.

In these momentum equations, we have on the left side of the equals sign the change in momentum. The first two terms on the right are advection terms, the third term is the Coriolis force term, the fourth term is the pressure term, and the fifth, wind stress.

The sixth term represents the momentum transfer to the flowing water underneath the ice, and the last two terms give a rough approximation of shear between ice.[1]

With the last two terms we are able to couple part of the ice field to land by use of very high horizontal momentum exchange terms, or represent a certain area with unbroken thick ice coverage. In the latter case we have then assumed that in these areas ice does not elastically or plastically reform. This was recently found quite reasonable by Thorndike and Colony (1982) and by Pritchard (1984).

[1]A much more complicated formulation of the shear, similar to formulations in soil mechanics, was used initially. The use of that formulation required much computation and the results were nearly identical with the simple shear representation in Eq. (5.1) and (5.2).

Similar to the bottom stress of a fluid flow model, the momentum exchange coefficient at the bottom of the ice can be expressed:

$$E'_x = \frac{\rho g (\bar{h}^z)^2 \left[(\hat{\delta}_z u)^2_- + (\hat{\delta}_z \overline{v}^{xy})^2_- \right]^{1/2}}{(C_s)^2}$$

$$\text{at } i+\tfrac{1}{2},\ j,\ l,\ n \tag{5.3}$$

$$E'_y = \frac{\rho g (\bar{h}^z)^2 \left[(\hat{\delta}_z \overline{u}^{xy})^2_- + (\hat{\delta}_z v)^2_- \right]^{1/2}}{(C_s)^2}$$

$$\text{at } i,\ j+\tfrac{1}{2},\ l,\ n \tag{5.4}$$

where the density (ρ) and the thickness of the ice layer are computed locally by the parametric relationship presented later.

The Chezy coefficient (C_s) between the ice water interlayers is used not only for the momentum transfer computation but also for the computation of turbulence energy generation with respect to the transport of subgrid scale energy in the surface layer of water. In the computation of the ice cover model, a Chezy value of 420 $cm^{1/2}/sec$ is used. This value was converted from the stress coefficient described above.

In the presence of ice, the local top-layer thickness for the water computation is adjusted according to ice displacement, which is also a function of local ice thickness and ice water density differences.

If ice is present in part of the modeled area, then the change of momentum is computed at the grid points as a function of the wind stress, stress at the ice water interface, Coriolis force, internal ice stress, and sea surface tilt.

The internal stress between ice floes is evaluated according to the degree of ice coverage by means of variable horizontal diffusion coefficients. Quantitatively, these coefficients range from one obtained by the four-thirds power law of the characteristic length scale (grid dimension) for the ice-free condition, to an arbitrarily large value for the fully covered condition. In the case of full coverage, shear stress terms at the ice water interface are reevaluated considering the random spacing of draft beneath the pressure ridges associated with the local ice thickness (Whittmann and Schule, 1966).

Before a simulation of winter conditions can be made with the three-dimensional model with ice cover, we need, in addition to the hydrodynamic forcing function at the open boundaries of the model, wind information and initial conditions such as ice thickness and ice coverage. Since it can be expected that very limited information about the ice thickness would be available during some winter periods, an initial ice thickness model is designed to estimate the ice thickness at the start of a simulation. Critical information to determine the ice thickness includes the average value of the total degree-days (below zero) at the starting time of the simulation and the spatial salinity distribution at the beginning of the winter season.

To initiate the ice simulation at each grid location, local water salinity is used to estimate the freezing point. This value is then stored for later use. The freezing point of sea water for various salinities can be estimated (Neumann and Pierson, 1966).

$$T_f = -0.003 - 0.527S_w - 0.00004S_w^2 \tag{5.5}$$

where s_w is the local sea water salinity.

From weather statistics, an averaged value of total degree-days (below zero) can be obtained that corresponds to the starting time of the simulation. From this information, the freezing point of sea water, depth, salinity, and initial temperature, and the "effective" local total degree-days below sea water freezing point can be computed. Once the freezing point has been reached, salt is rejected from the ice, thus it is no longer a function of local sea water but of the ambient freezing temperature. The relationship between the salt content and the ice temperature can be expressed as:

$$S_i = 2.3 - 0.1883T_a \tag{5.6}$$

T_i represents the ice temperature, which may be assumed to be the same as the ambient air temperature, T_a.

From the salinity of ice, the density of young ice is approximately:

$$\rho_i = 0.918 + 0.0008S_i \tag{5.7}$$

To estimate the local ice thickness, the local latent heat of fusion of ice, λ, can be computed also from the salinity of ice mentioned above.

$$\lambda_i = 80.0 - 4.267S_i \tag{5.8}$$

The initial local ice thickness at each grid location can be computed (in cgs units) according to:

$$H_i = \left[\frac{2\ell}{\lambda_i \rho_i}(D - T_f) \times 24 \times 3600\right]^{1/2} \tag{5.9}$$

where denotes the coefficient of thermoconductivity, which is approximately 0.0055 cal degree^{-1} sec^{-1}, and D represents the total degree-days below the freezing point locally. These data are obtained from Brower et al. (1977). During computation the formation and melting of ice are computed assuming linear vertical temperature gradient within ice:

$$\frac{\Delta h}{\Delta t} = -\frac{\ell}{\lambda_i \rho_i}\left[\frac{T_a - T_f}{h}\right] \tag{5.10}$$

The recursion formula in the finite-difference form is:

$$H^{n+1} = H^n \frac{\ell(T_a - T_f)(2\Delta t)}{\lambda_i \rho_i H^{n-1}} \tag{5.11}$$

In the subsequent computation the amount of salt rejection or formation is computed as the source or sink terms in the salt balance equation for the top-layer water simulation.

$$S = \left(H_i^{t+\Delta t} - H_i^{t-\Delta t} \right) \cdot \frac{\rho_i^t \, S_i^t \times 1000}{2\Delta t \; \rho_w^t \; H_w^t} \tag{5.12}$$

where ρ_w and H_w represent the density and surface layer thickness of water.

If ice is present at the model's open boundaries, then the nonlinear advection and diffusion terms are neglected in the momentum equation near the boundary in the same manner as is done in the flow computations. The same procedure is applied to all the internal open ice edges.

When land-fast ice exists in the model area we either assign locally an extremely large momentum diffusion coefficient or set locally the horizontal ice velocity components to zero. The vertical movements of land-fast ice are computed, however.

Sea ice distribution in the modeled area is expressed in Okta. By international agreement the Okta system is used to report the extent of the ice cover. An ice concentration of 1 Okta (one-eighth) or more, defines the edge of pack ice. Total ice coverage is 8 Oktas (Brower et al., 1977). More recent literature seems to report ice concentrations in the 0–10 system with a scale of 10 to represent full coverage. For example, charts issued by the Navy/NOAA Joint Ice Center are in the scale 10 system (Stringer et al., 1982).

For our model inputs we have adapted the Okta system, since the existing ice data at the beginning of our modeling effort were nearly all in Oktas. A value of 9 was created to denote a shore-fast ice zone. In the computation, the Okta scale is also used as a computational flag to classify approximately the type of ice, as well as a parameter for computing the horizontal momentum transfer within the ice pack.

The parametric relationship for the ice growth described here has been tested against the observed data at Norton Sound and Beaufort Sea (Stringer and Hufford, 1982; Stringer et al., 1982). Using typical values of degree days, the formula gives reasonable ice thickness for the entire winter season as compared with the local data.

ICE/WATER INTERACTION UNDER THE FORCES OF WIND AND CURRENTS

Pack ice moves because of the momentum transfer from currents underneath the ice to the ice mass, and because of the momentum transfer from wind to the ice. Ice motions are nonlinear functions in space and time because of nonlinear terms in the equations that describe the ice motions, Eqs. (5.1) and (5.2).

To test computational procedures and to understand the behavior of the system we were working with at that time, we made a number of experiments. One of these experiments is of particular importance, as it revealed considerable differences in the movement of ice in relation to the underlying water. The experiments were made with the submodel of Norton Sound for winter conditions typically occurring in March. Figure 5.3 shows the initial distribution of ice thickness. Open water exists in the northeast part of the bay where ice has been removed by the predominant wind from the north-northeast. The vertical water column is nearly homogeneous throughout the area except for the surface salt input associated with ice generation in the northeast part of the Sound. Other than in areas near the Yukon Delta and at the head of the Sound where shore-fast ice is found, Norton Sound is covered with ice floes that range in size from a few meters to one or two kilometers. The diurnal tide is

dominant in the eastern part of the Sound, whereas in the western part of the model area, the semidiurnal tide is stronger. The thickness of the ice ranged from 0.8 to 1.05 meters.

To study the ice/water interaction, we exerted a constant wind of 18 knots from the north-northeast, the predominant wind for this month. Ice moves under the influence of wind and tide, and typical ice velocities are shown in Fig. 5.4. Note that the ice movements deviate considerably from the wind direction. The influence of the current stress and the stress exerted by the neighboring ice appears to be quite strong.

The velocity of the water in the top layer just underneath the ice is quite variable, as shown in Fig. 5.5. Near Kwikpak Pass the water velocity is nearly zero and, in this case, the direction of the ice movement is approximately 35° to the right of the direction of the wind. At this location the speed of ice is approximately 3.3 percent of the wind speed. However, a short distance away where larger water velocities exist, the speed of ice approaches 4.5 percent of the wind speed.

It will be noted also that the speed of ice near the shore-fast ice zones is reduced in comparison with its speed farther away. In many cases rotational effects in the ice movement may be observed near the boundary of land-fast ice. The model experiment also shows that shore-fast ice considerably reduces the water velocities in the layer immediately underneath the ice.

In a subsequent experiment we evaluated the movement of ice over a certain period. At the beginning of this experiment only the tidal motions were simulated until the starting transient had disappeared. Subsequently, the wind stress was applied over a 12-hour period and for the following 12 hours the wind was stopped again. The direction of the wind was from the northeast and the wind velocity was 10 knots.

To obtain insight into the transient effect of wind on the ice field, plots of ice displacements were made for a number of locations in the model. These pathways are shown in Fig. 5.6 and are the pathways resulting from a 12-hour period of wind followed by a 12-hour period without wind. The movement of the ice in the eastern Sound is influenced by the underlying diurnal tidal excursion, whereas in the southwestern part of the model the semidiurnal tide exerts the most influence. If we look at the movement over a 24-hour period, as shown in Fig. 5.7, it can be seen that the net displacement varies considerably over the area in displacement and in direction. The drift distance is typically from 6 to 9 km for this period in which the wind stress was applied for only 12 hours. To study the inertia component of the ice's movement, the wind stress is exerted only in the first 12 hours of the day simulated.

After this experiment, which was made in 1980, field data became available from sea/ice trajectories determined by Landsat imagery as shown in Fig. 5.8 (Stringer and Hufford, 1982). The daily movements of ice range from 7 km to 14.5 km, which is approximately twice the displacement during the 12-hour experiment; wind directions are quite well in agreement with those of our aforementioned simulation. Unfortunately, no wind data were obtained at stations in the Sound during that period. The wind conditions were typical for that season with air pressure difference between Point Barrow and Nome being 0.4 inches.

The comparison between the long-term observed ice trajectories and the simulated long-term trajectories under the areawide wind forcing is presented in the next chapter. It is our opinion that the long-term ice trajectories should be verified together with the wind model that will be used for the oil spill trajectory simulation.

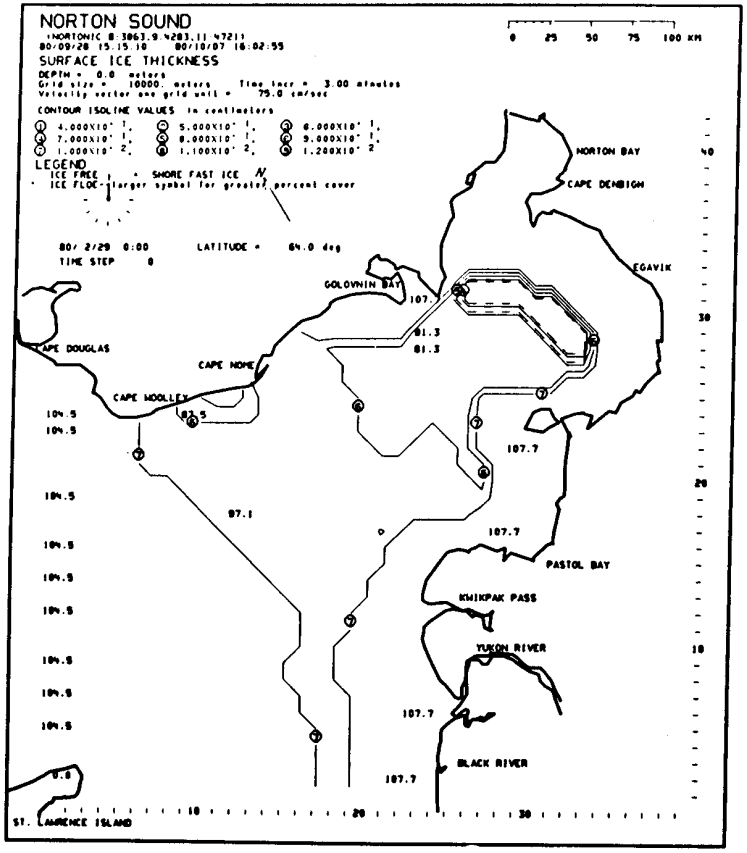

Fig. 5.3—Initial distribution of ice thickness. Area near the Yukon Delta and at the head of the Sound is covered by shore-fast ice. Areas near Golovin Bay and south of it are ice-producing areas.

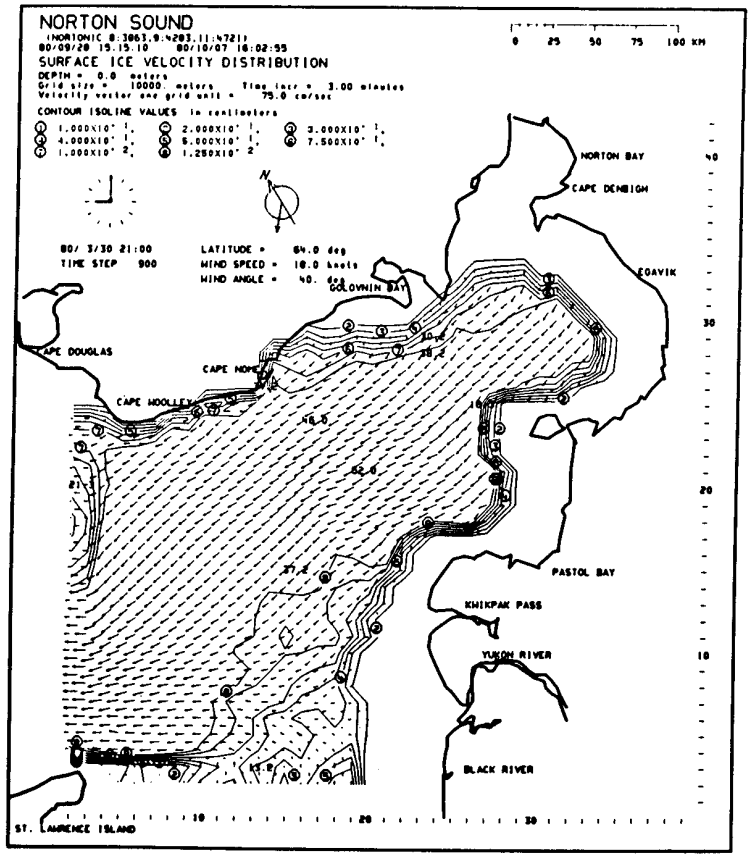

Fig. 5.4—Ice floe movement under northeast wind (10 kn) combined with tidal movement. Displacements immediately neighboring shore-fast ice zones are limited with rotational behavior induced by strong ice-ice interactions.

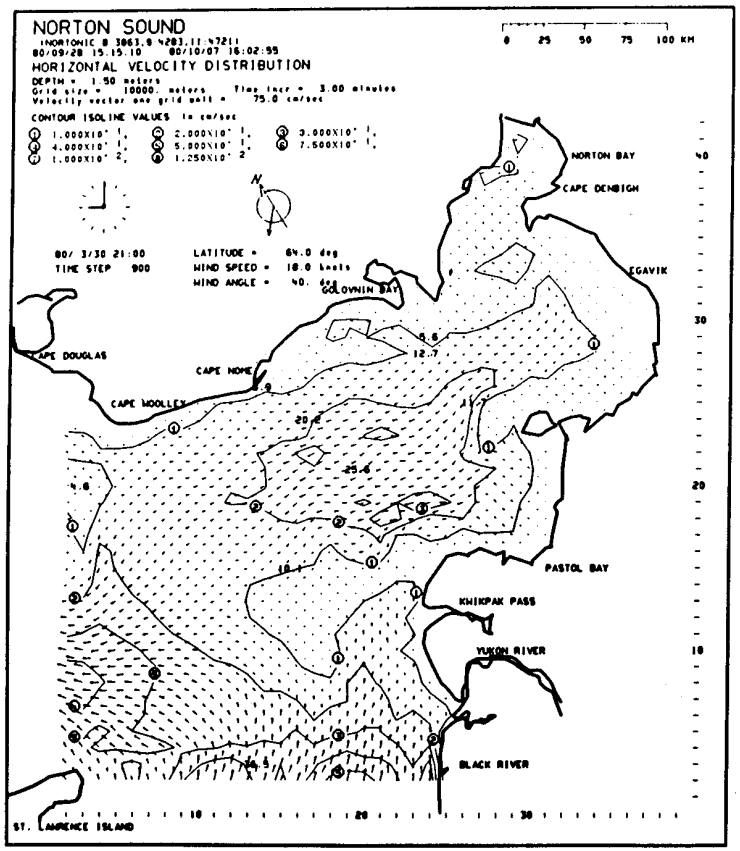

Fig. 5.5—Water movements beneath the ice. They are driven by tidal forces and wind stresses transmitted through the ice.

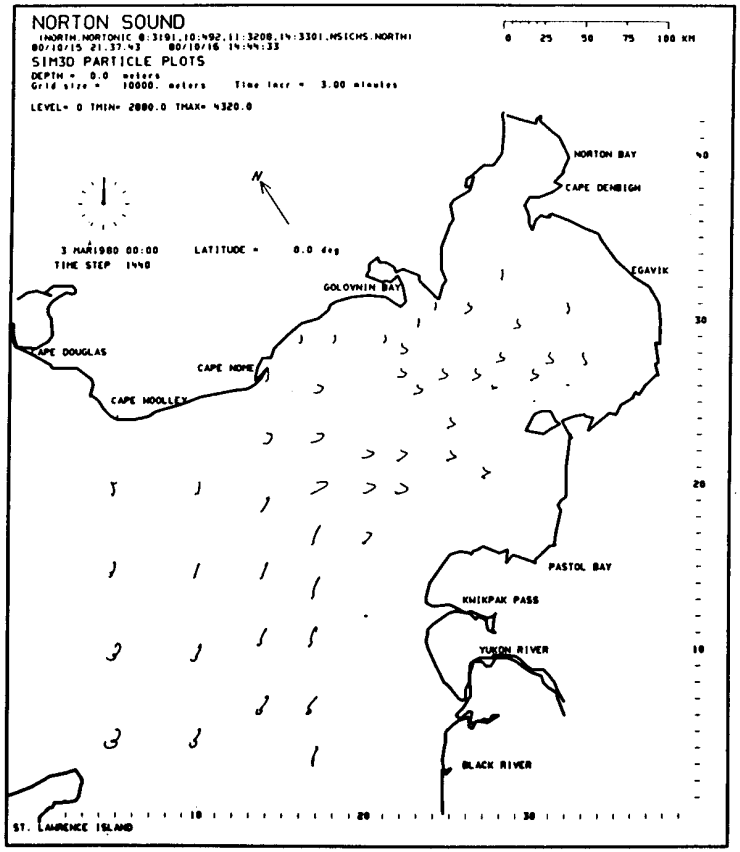

Fig. 5.6—24-hour ice trajectories, driven by tidal excursion and 10 kn wind from the northeast for the first 12 hours.

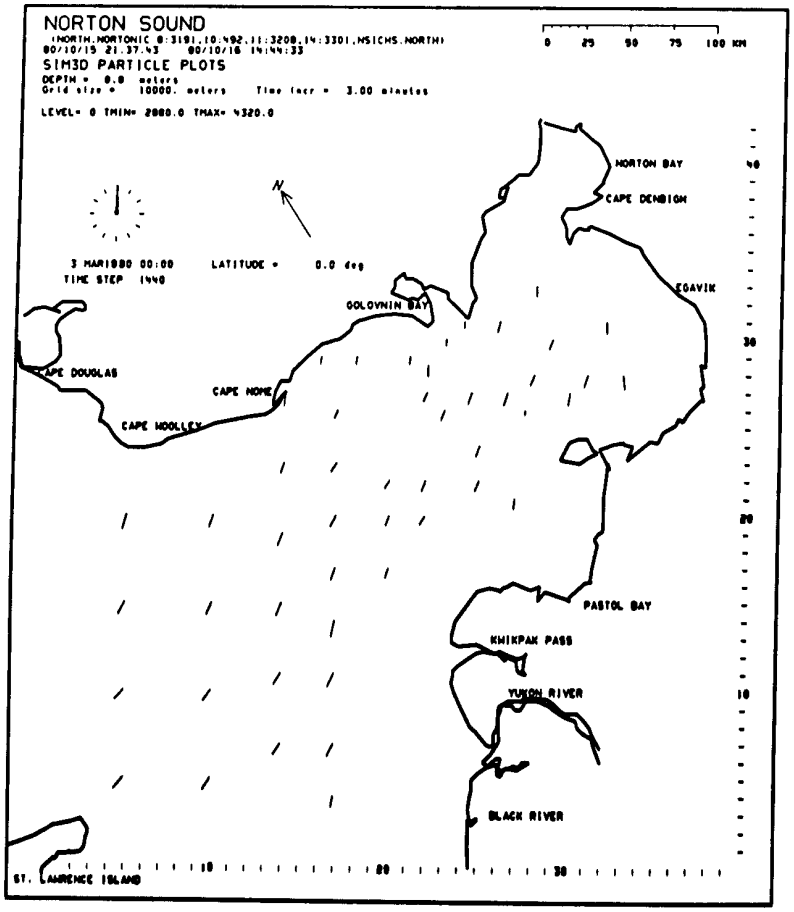

Fig. 5.7—24-hour net ice displacements, induced by tidal-residual current and 10 kn wind from the northeast for the first 12 hours. Daily displacements under 24-hour wind stress would be approximately twice the amount shown.

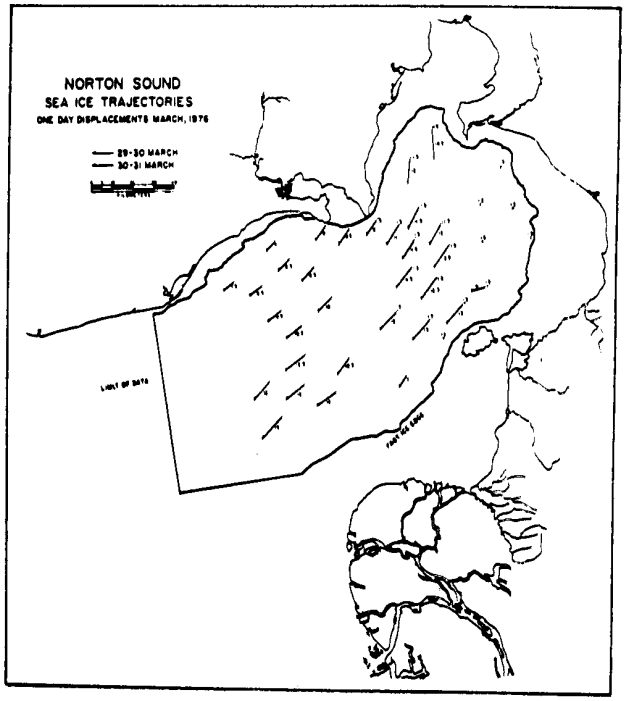

Fig. 5.8—Pattern of daily ice floe movement of 30-31 March 1976 (Stringer and Hufford, 1980) when the pressure difference between Barrow and Nome was approximately 0.4 inches.

6. MODELING OIL TRAJECTORIES

OBJECTIVES

Before decisions are made concerning which specific offshore areas to lease for exploration or exploitation, the responsible governmental agency (U.S. Department of Interior) must balance orderly resource development against the protection of human, marine, and coastal environments, to ensure that the public receives a fair return for these resources. In studies made for this purpose, the impact of hypothetical oil spills are considered. To assess the impact of these oil spills on resource areas, simulations of the pathways of oil spills are required for representative weather conditions for specified periods of the year. A relatively large number of simulations are required from each spill site to obtain sufficient data for statistical analysis.

Not only are oil spill pathways required for the impact analysis, in certain instances knowledge about the extent of oil spills is required as well as about the oil concentrations that would occur in the water column.

THE MODELING APPROACH FOR LONG DURATION WIND DRIVEN CURRENTS

As the three-dimensional models made of the different offshore areas of Alaska simulate the movements of water, and as a model is available to simulate wind sequences offshore, it would be logical to use these models in the computation of oil spill movements. To use these models effectively, we have developed a method to compute wind driven currents. This method retains the dynamic detail of the three-dimensional model and yet is approximately two orders of magnitude more efficient than the simulations with the three-dimensional model; it is called the "wind-driven response function method." In essence, the method extends the basic idea of the "drift ratio" between the wind speed and current speed except that the ratio changes in time and over space and is derived from the three-dimensional model.

The traditional, simple fixed drift-ratio method has many difficulties when applied in the Alaskan coastal waters. It is applicable only for cases of steady wind with constant speed blows over water with finite depth and with no boundaries. However, the concept of the "drift ratio" is a good one—but we need to include more dynamics in it.

In examining the fundamental dynamics of wind-driven currents, even under the assumption of steady (in time), constant (over space) wind and an infinitely long straight coastline, wind-driven currents over water of finite depth do vary both in direction and speed at the surface and at different levels to satisfy the law of conservation of mass. Using information on the distance from shore, wind direction, and local depth, Ekman (1905) worked out the variabilities of drift currents by using highly simplified terms in the equations of motion. On the other hand, to include more terms would require the solution of the complete three-dimensional model.

In our study, time-varying response functions under various wind conditions were developed using wind stress associated with the marine wind speed. Reverse procedures (convolution) were then used during the oil trajectory simulation; therefore, they are not

linear with respect to local wind speed. Since the response functions for all layers are derived from the three-dimensional model, time-varying effects (such as a moving storm, deepening of a mixed layer, and inertia components) are included in the oil spill trajectory computation. The method is very efficient, however, the oil spill trajectory model was programmed so that the drift ratio and deflection angle from field observations under various conditions over an entire area can, as an option, still be used for the computation of oil movement.

Wind driven currents over stratified waters vary with the degree of vertical stability associated with the stratification. To illustrate this point we use a simple case where the time series of water movement at two nearby locations in Norton Sound is plotted (Fig. 6.1), and wind from the east is applied for a duration of 12 hours (close to the inertial period) over the water. The response of surface water at two nearby locations is not the same to satisfy the continuity principle of water within a bay. Response functions over the water column of the entire modeled area are calculated by the three-dimensional model.

To generate the complete set of response functions, five computer simulation runs are needed. One computer run is without wind but with tide. The other four computer runs are with tides and with wind from each of four directions. The four response functions set are derived from the difference between them and the one with tide as the only forcing function. The level of tidal currents at different areas produces variable wind responses under the same wind, so the tide has to be included when deriving wind response functions, otherwise they will be overestimated. This is why in a coastal area with strong tidal currents the drift ratio would be lower than in the open ocean because of the quadratic nature of the bottom friction.

When response functions are saved in discrete time intervals (30 minutes was used) the drift velocity at a certain time is computed by numerical convolution.

$$U_{ij}(n\,\Delta t) = \Delta t \sum_{k=0}^{n} (W^2) h_{ij}(n\,\Delta t - k\,\Delta t) \tag{6.1}$$

where W = wind speed from a certain direction,
U_{ijk} = velocity at a particular point (i, j, k), and
h_{ijk} = time domain response function between squared wind speed and velocity at point (k, j, k).

With this formula the velocity at point i, j, k can be determined if the wind speed from a specific direction is known, as well as the response function.

The same principle applies for complex wind scenarios, then the vectorial decomposition is involved.

COMPUTING OIL BEHAVIOR UNDER ICE

In the absence of a current, oil released in a water column will rise and be trapped underneath the ice. Under porous young ice during formation, oil will initially undergo a certain degree of vertical migration through the vertical brine channels. Most oil is initially in the form of droplets until a lateral slick is formed. The oil sheet tends to spread with an obtuse contact angle. For typical Alaska Prudhoe Bay crude oil, the average observed values of interfacial surface tension, density, and the contact angle are 31 dynes/cm, 0.911 g/cc, and 20°, respectively (Kovacs et al., 1980). The static thickness of the same oil is approximately

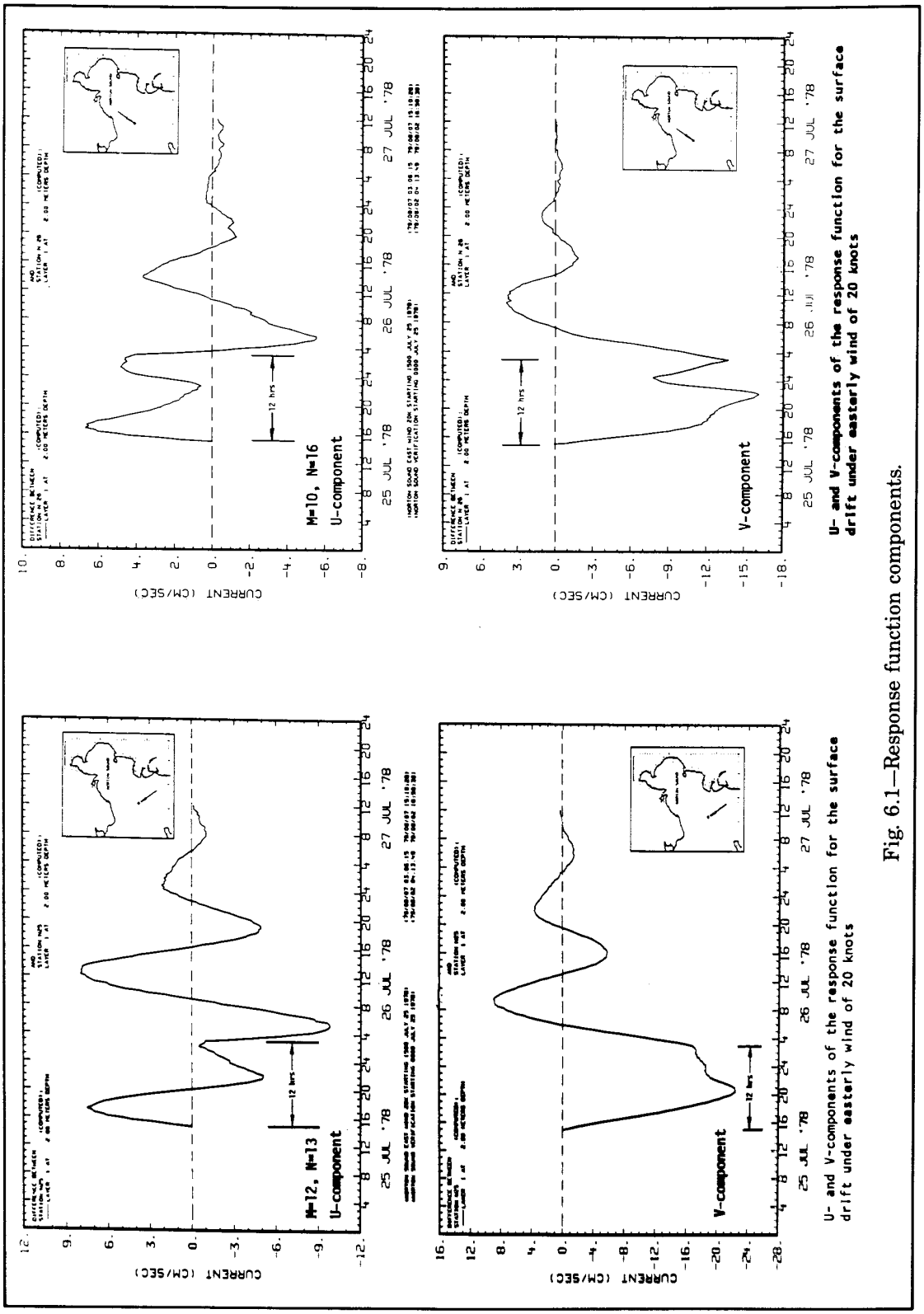

Fig. 6.1—Response function components.

1.2 cm. Since the dynamic pressure exerted by a moving current on an oil slick of finite length tends to balance between the front and the back faces, the equilibrium thickness should be the same for both unaccelerated and static slicks.

The bottom roughness of ice not only determines the amount of oil that may be trapped beneath it, it also influences the speed of oil movement under moving currents. Using a radar echo sounding system, Cox et al. (1980) made extensive measurements of ice bottom morphology and found the standard variation of ice thickness to be 3.1 cm over a mean thickness of 1.53 m in an undeformed shore-fast ice zone near Prudhoe Bay. The thickness of ice was also found to be inversely proportional to the thickness of snow cover over it. The snow acts as an insulator that reduces heat exchange from the sea water through the ice to the atmosphere and thus retards the growth rate. Consequently, a substantial quantity of oil can be retained underneath the pack ice. Under weak currents, trapped oil will travel with the pack ice. The movement of oil under this condition would be identical to the computed movement of ice described above but the shear stress coefficients between water and ice are reduced.

Under strong "relative currents" (between water and ice), oil will travel at a speed different from the ice and currents. To compute the movement of oil under these conditions, in the three-dimensional model we adapted a method developed by Cox et al. (1980) with parameters evaluated from laboratory tests. This method involves the evaluation of a critical relative velocity between ice and water. Using ρ_w to represent the density of sea water in the surface layer of our computation, the critical velocity for the incipient motion with large roughness is approximately:

$$u_{\text{critical}} = 1.5 \left[\left(\frac{\rho_o + \rho_w}{\rho_o \rho_w} \right) \left(\sigma_{o/w} g (\rho_w - \rho_o) \right)^{1/2} \right]^{1/2} \tag{6.2}$$

in which ρ_o, $\sigma_{o/w}$ are, respectively, the density of oil and the surface tension at the oil/water interface. With the aforementioned typical values observed in the Beaufort Sea, this critical value is approximately 21 cm/sec.

Equation (6.2) is developed considering the formation of Kelvin-Helmholtz type instability, which exerts a limit on the thickness of an oil slick near the head region. A multiplier of 1.5 on the right-hand side of Eq. (6.2) was used considering the actual velocity that would cause droplet tearing. Ultimate slick failure occurs at about twice the critical velocity.

According to Cox et al. (1980), the critical velocity at which oil begins to move relative to the water when the relative velocity between ice and water is:

$$u_{\text{oil}} = u_{\text{water}} \left[1 - \left(\frac{\kappa}{A F_\delta^2 + B} \right)^{1/2} \right] \tag{6.3}$$

where κ is the amplification factor and F_δ is a slick densimetric Froude number defined by:

$$F_\delta = \frac{u_{\text{water}}}{\sqrt{[(\rho_w - \rho_o)/\rho_w] g \delta}} \tag{6.4}$$

in which δ represents the equilibrium slick thickness.

Equation (6.3) is derived from the momentum balance between form drag, oil/water interfacial shear stress, and the retarding of oil/ice frictional force. Constants A and B in the equation contain the effects of frontal shear and plane shear, as well as the normal force from oil's buoyance against the ice. For the field conditions of the model areas, the values of these coefficients are 1.75 and 0.115. The amplification factor κ equals unity for a hydrodynamic smooth region and is greater than zero for rough surfaces. For the field conditions in the model areas, the factor was given a value of 1.105. To determine the equilibrium oil slick thickness from the density of the oil, we used an empirical relation. The empirical difference is:

$$\delta = 1.67 - 8.5\,(\rho_w - \rho_o)(\text{cm}) \tag{6.5}$$

In the three-dimensional model the local density of water is evaluated by the equation of state of sea water. The density of oil can be computed by a table look-up procedure.

In our computation, the local density of sea water associated with the ice formation/salt rejection and advection was evaluated and updated. The results of oil movement beneath the ice under various wind conditions, in the form of response functions computed from the three-dimensional simulation, were recorded on magnetic tape as subsequent inputs to the oil spill trajectory computation.

We found that oil will generally move with ice except under two conditions that cause it to travel at a different speed. The first condition is beneath the shore-fast ice in an area where tidal currents are strong. The second condition is when pack ice is located very close to a passing storm center, when drifting ice abruptly changes direction. Under this condition a high relative velocity between the water and ice can be reached..

Because of the pronounced nonlinear vertical shear coupling, and at high latitude, the direction of an oil movement appears to be extremely variable. Therefore, the vertical shear coupling should be included in the computation even though spilled oil beneath the ice may not seem to be in constant motion with appreciable magnitude.

MODELING OIL SPILL TRAJECTORIES

Oil spill trajectory computations involve two parts—the first part calculates the movement of oil mainly by advective transport, and the second part calculates the movement of dispersive mechanisms, including weathering, diffusion, and dissolution processes. In this section we will describe the modeling of advective transport only.

Oil transported by advective mechanisms contains several major components. The method used to compute each component is as follows:

Oil Transport by Mean Wind Drift. During this computational step, oil movement resulting from wind stress at the surface layer and at different levels in the water column is calculated by the response function technique. The response function represents local advective transient response to a given wind stress. If a three-dimensional model is used to develop these response functions, the effects of transient inertia, bottom, shoreline, and vertical stratification are all included. The computed movement using this response technique gives only the movement near the middle of the surface layer (typically 5 meters) schematized in the 3D model. For the surface movement the results are extrapolated for speed and direction near the surface using an analytical solution of the Ekman type assuming constant density within that surface (mixed) layer.

Stokes' Transport. When wind blows over the water surface it generates Stokes' transport in addition to the mean wind-driven current. This transport is caused by the nonlinear residual orbital motion associated with the local wind waves field. The magnitude of this transport is a function of the intensity and age of the wave field. The direction is nearly identical to the wave-propagating direction. In the oil spill trajectory model, a special subroutine is used to compute the direction and speed of this transport. According to measurements in the field and in the laboratory, Stokes' transport is approximately 1.6 percent of the local wind speed if the wave field is not limited by wind duration and fetch length. The wind used to compute the Stokes' transport is obtained from the wind field model described in Chapter 4.

Tidal and Baroclinic Residual Component over the Alaskan Outer Continental Shelf Area. Because of the complex tidal regime and density field, tidal residual and baroclinic circulation components are quite essential. We have discussed their dynamics in great detail in Chapter 3.

To simulate a number of trajectories with the trajectory model, many data are needed from other models that we have previously described. Figure 6.2 gives an overview of the data flow between these models. As illustrated in the diagram, when computing the oil movement, the oil/trajectory model plays the role of data synthesizer. As physical parameters involved in calculating oil movements are difficult and expensive to measure over the entire Alaskan waters, the model is programmed with flexibility in mind, so that any field data, if available, can be used to drive the model in its simplest mode. On the other hand, the trajectory model would link results from the other models. To perform this task, it contains the basic physical parameters of the entire lease area as well as the grid network of the entire model and submodels within the system.

During the study period, spill trajectory analyses were made on a lease-area basis. For each lease sale, approximately 30 to 40 launch points were selected by the Minerals Management Service according to the potential petroleum resource. The movements of oil were then tracked for a period of time, typically a month during the summer period, to as long as six months during winter.

From each launch location 40 to 60 trajectories are computed under different weather scenarios. For each trajectory, half-hourly positions are computed and landfall locations are recorded where possible. As described above, the wind-driven component of the oil movements is computed using the wind-driven response function technique through the convolution procedure. To maintain accuracy, each response function has half-hourly weighting elements for each wind direction, each computational grid, each layer, and each season. One magnetic tape is required to store all response functions from each of four wind directions. For the computation of oil spill trajectories, this information is transferred to disk storage.

Results from a typical simulation are presented in Fig. 6.3. In the figure, the computational grid of the three-dimensional model of the Beaufort Sea is superimposed over the oil trajectory model, which also covers the eastern portion of the Chukchi Sea. The response functions and net-current field over that area are averages obtained from the two models.

On top of the graph, computed 12-hour wind vectors sampled at Point Barrow are plotted. The mean winds and half-hourly varying winds from the simulation are also presented in the form of wind roses for speed and direction, also at Point Barrow. The wind direction rose represents the frequency of occurrence of wind direction toward which wind is blowing. A wind speed rose represents the average marine wind speed associated with each of the 16 wind directions mentioned above. The plotting scale of the highest speed in the rose is 12 knots as indicated under the rose.

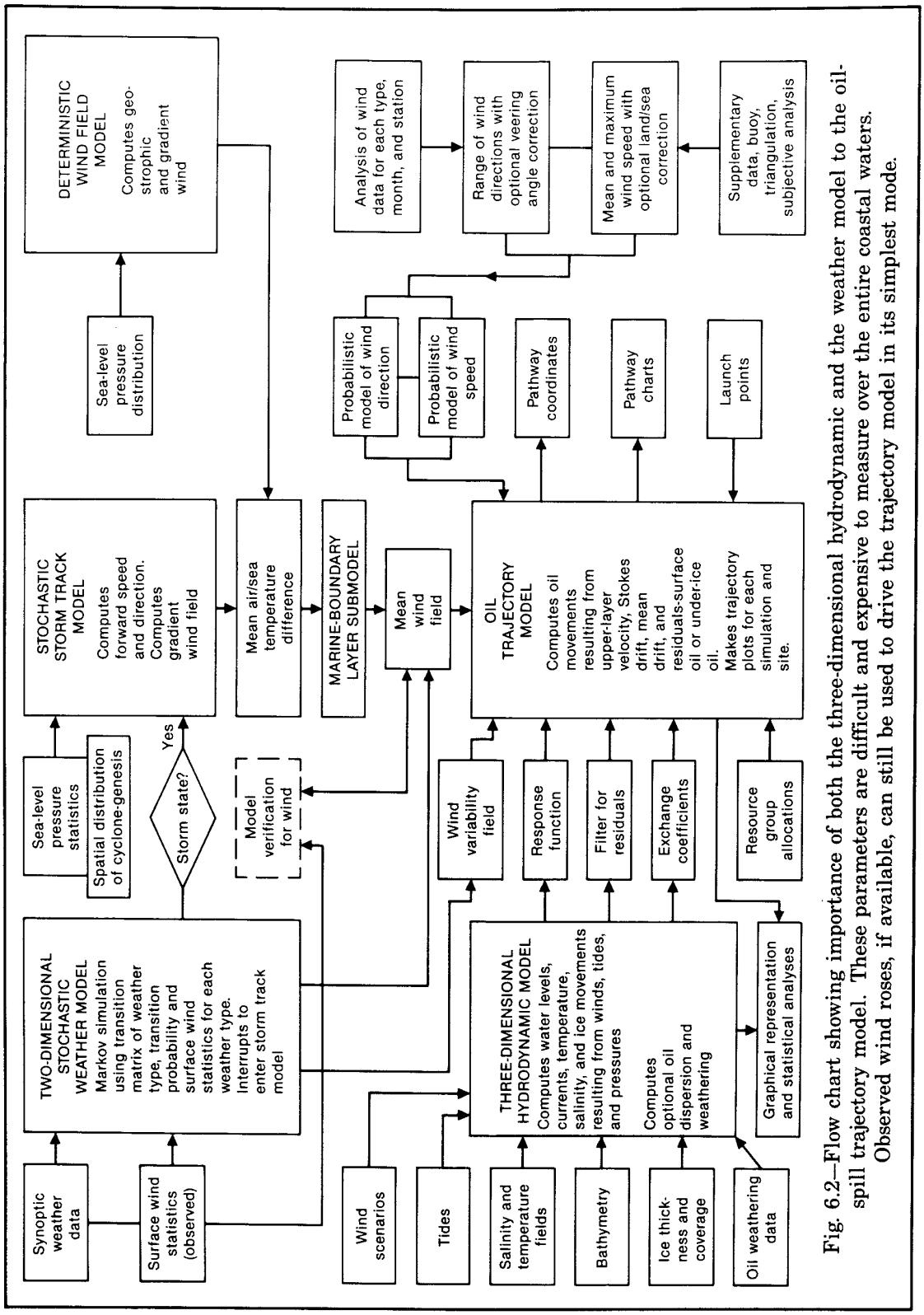

Fig. 6.2—Flow chart showing importance of both the three-dimensional hydrodynamic and the weather model to the oil-spill trajectory model. These parameters are difficult and expensive to measure over the entire coastal waters. Observed wind roses, if available, can still be used to drive the trajectory model in its simplest mode.

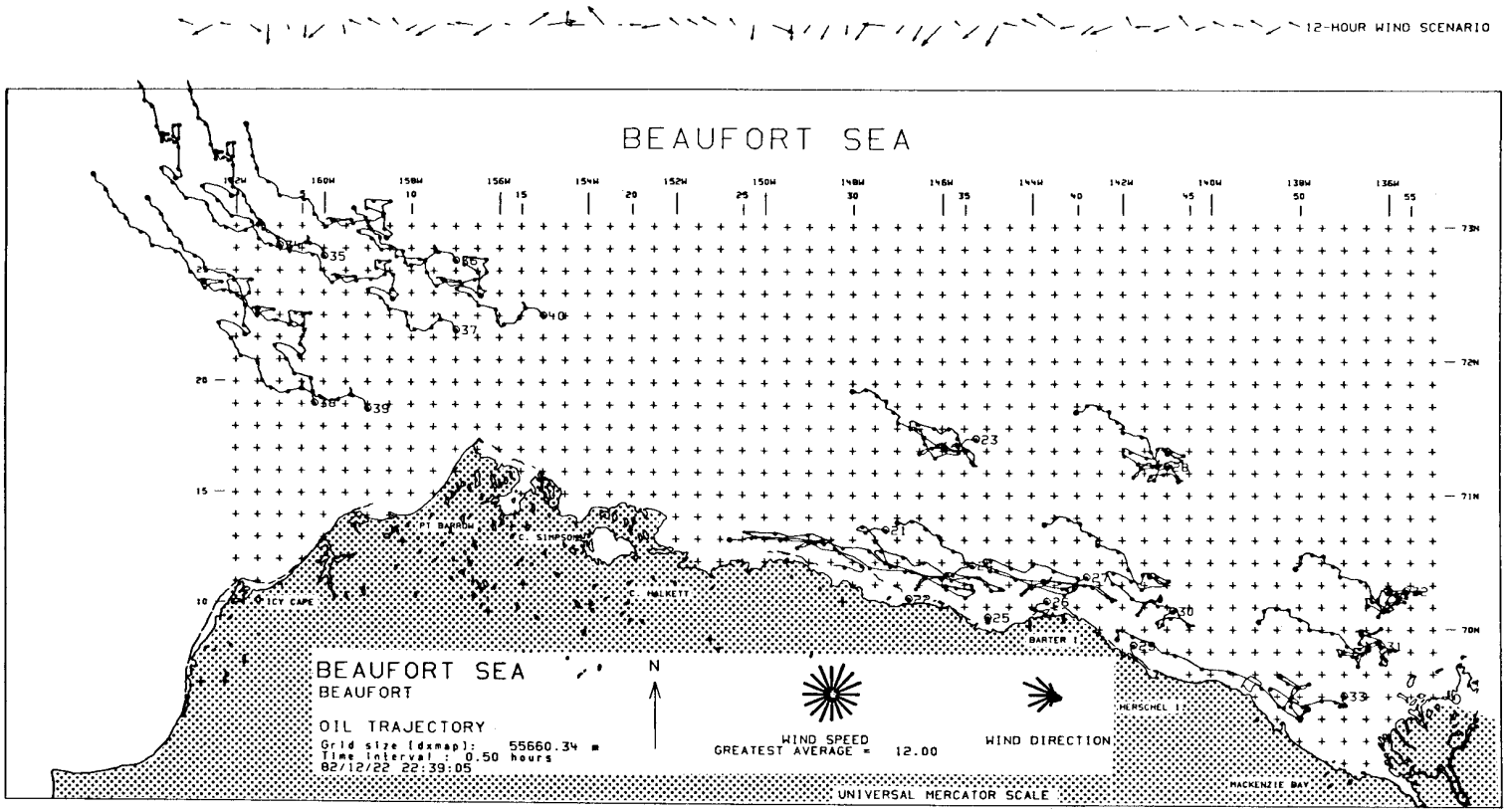

Fig. 6.3—Daily movements of oil originated from launch points 21 through 40.

Each dot in the oil trajectory represents daily displacement originating from the launch point, which is marked by a number. When examining the trajectories one would notice the following interesting aspects:

1. The predominant wind during a summer period is from the east-southeast.
2. Oil spilled closer to the shore travels faster, in a downwind position.
3. Oil spilled offshore moves in a more random direction and has a larger deflection angle. This can be attributed to the greater water depth and the existence of ice floes.
4. Oil spilled further offshore travels in a direction approximately the same as the Arctic Gyre (Colony and Thorndike, 1984, U.S. Coast Guard buoy data, Fig. 6.4). The simulation in Fig. 6.4 was made in December 1982.

The trajectories shown in Fig. 6.3 represent oil movements under a given 30-day weather scenario. In Fig. 6.5 comparison between satellite-tracked buoys (Murphy et al., 1981) and trajectories computed using the coupled trajectory-weather model is shown. During the summer period, the average observed movement of ice is approximately 140 nautical miles per month. The same is found in the computed monthly average displacement. The observed and the computed trajectory patterns in the Mackenzie Bay are quite irregular. This may be due, in part, to the cyclonic local eddy described above.

Without observed wind fields and the variability of winds, tracing the deterministic motion of a particular ice floe is not as desirable as comparing a group of observed trajectories to a group of computed trajectories using a weather model. The same weather model will be used for the statistical trajectory analyses below.

In the trajectories it can be seen that the impact of a moving storm can sometimes be seen as a loop in a trajectory. The size and shape of the loop vary because of their location relative to the moving storm.

The computed trajectories for the winter season have the similar direction of predominant movement. Figure 6.6 shows the general direction of movement launched from three selected points. The residence time within the modeled area is approximately two to three months. If all launch points for a given season are considered, one can assess the oil spill risk by counting the number of contact occurrences within each square area whose length is 10 nautical miles in the north-south direction (Fig. 6.7). In Fig. 6.7 the size of a circle represents the spatial distribution of landfall frequencies. If oil is trapped in a near-shore lagoon, a continuous contact is assumed for the remaining period. In preparing the map, analysis is made using two-hour counting method. Plotting scale for the circle is 21211, two-hour exposure periods equals one latitudinal grid spacing for the radius of the circle.

If the near-shore entrapments are excluded, a similar diagram (Fig. 6.8) gives the spatial distribution for the marine resource contact frequencies. In this case, each latitudinal grid spacing equals 1872 two-hour contact period for the radius of a circle. From graphs like Fig. 6.7 and 6.8, one would be able to obtain a general assessment of contact risk associated with the oil spill. However, sometimes it is more desirable to estimate the concentration of oil, if a contact is made.

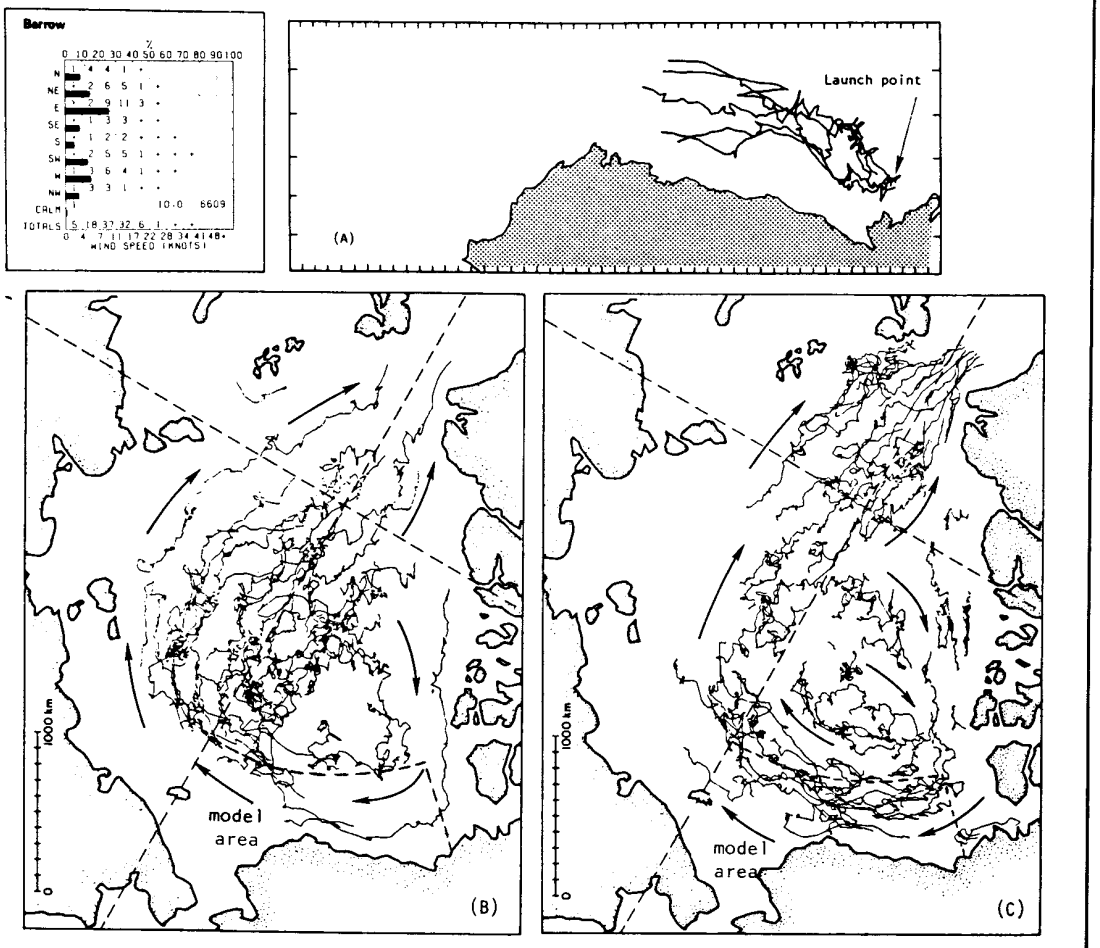

Fig. 6.4—Three groups of ice drift data. (A) Coast Guard drogues for 3 months during the summer of 1979; (B) composite trajectories compiled using data from 1893-1972 by Colony and Thorndike (1984); and (C) trajectories of automatic data buoys (1979-1982), also from Colony and Thorndike (1984).

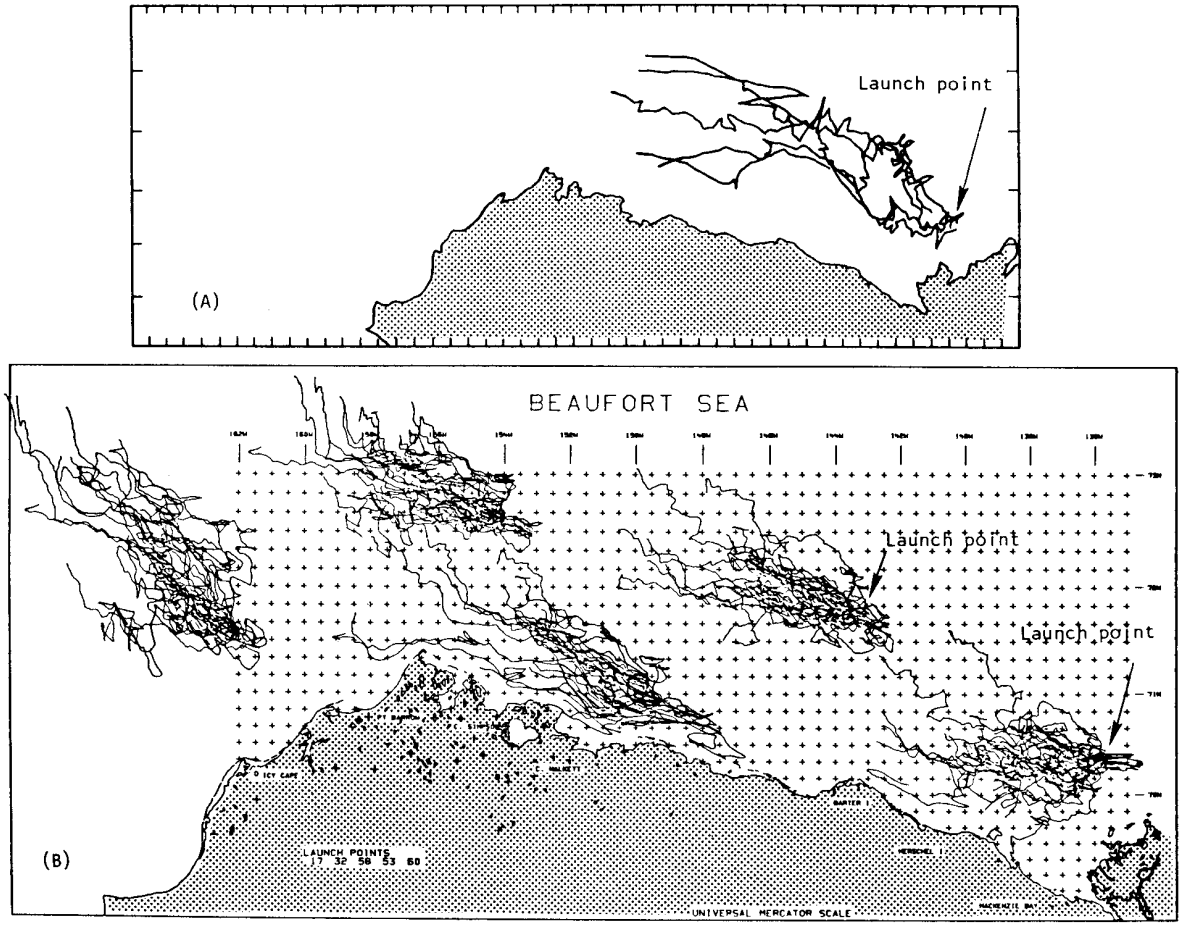

Fig. 6.5—Comparison between (A) trajectories of five satellite-tracked buoys deployed by the U.S. Coast Guard August to October, 1979, from eastern Mackenzie Bay, Canada, and (B) 30-day trajectories launched from five locations and computed by the RAND oil trajectory model and the two-dimensional stochastic weather simulation model.

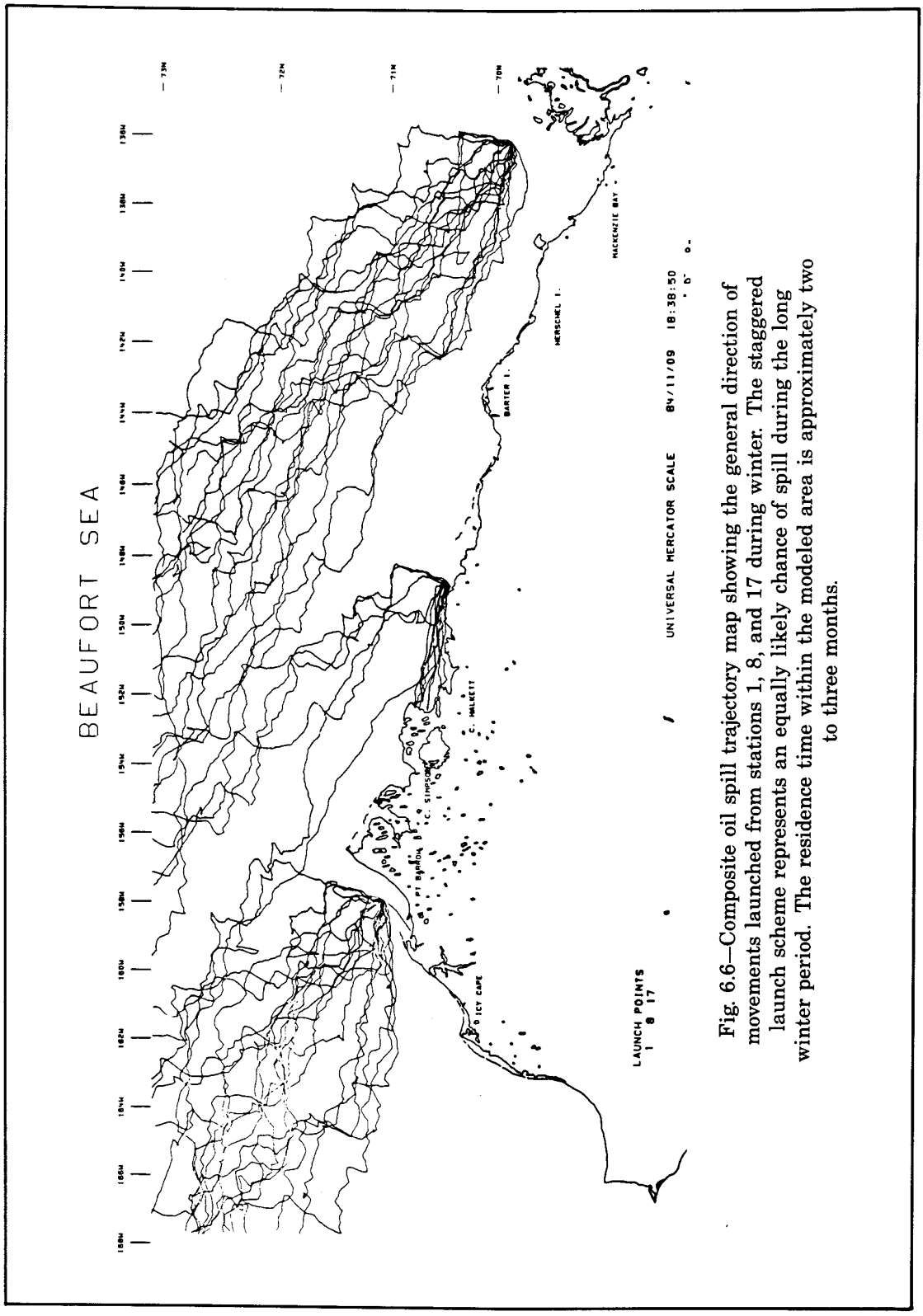

Fig. 6.6—Composite oil spill trajectory map showing the general direction of movements launched from stations 1, 8, and 17 during winter. The staggered launch scheme represents an equally likely chance of spill during the long winter period. The residence time within the modeled area is approximately two to three months.

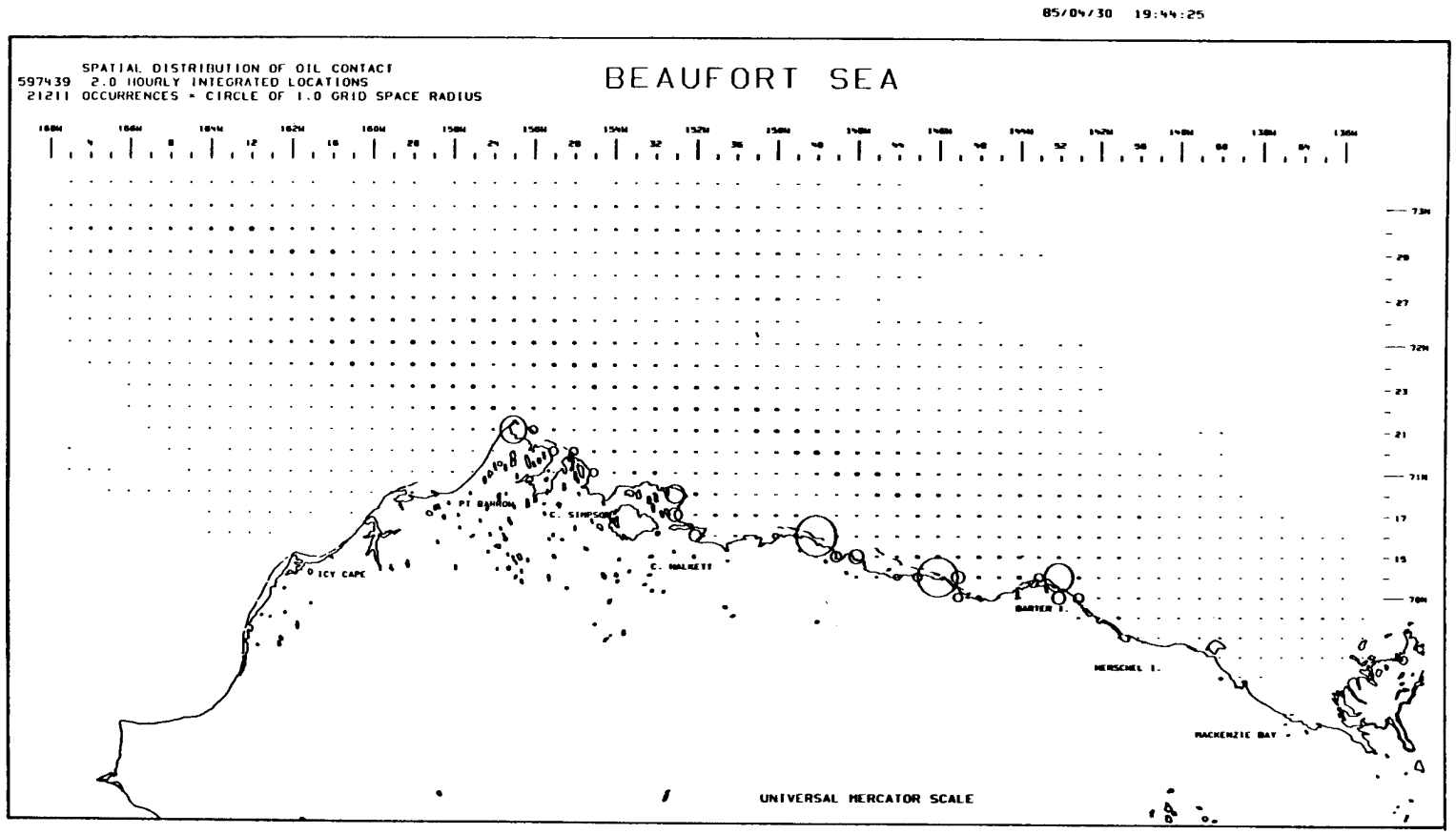

Fig. 6.7—Spatial distribution of oil contact frequencies. If oil is trapped in a near-shore lagoon, a continuous contact is assumed for the remaining period. Analysis is made using two-hour counting method. Plotting scale for the circle is 21211, two-hour exposure periods equal one latitudinal grid spacing for the radius of the circle.

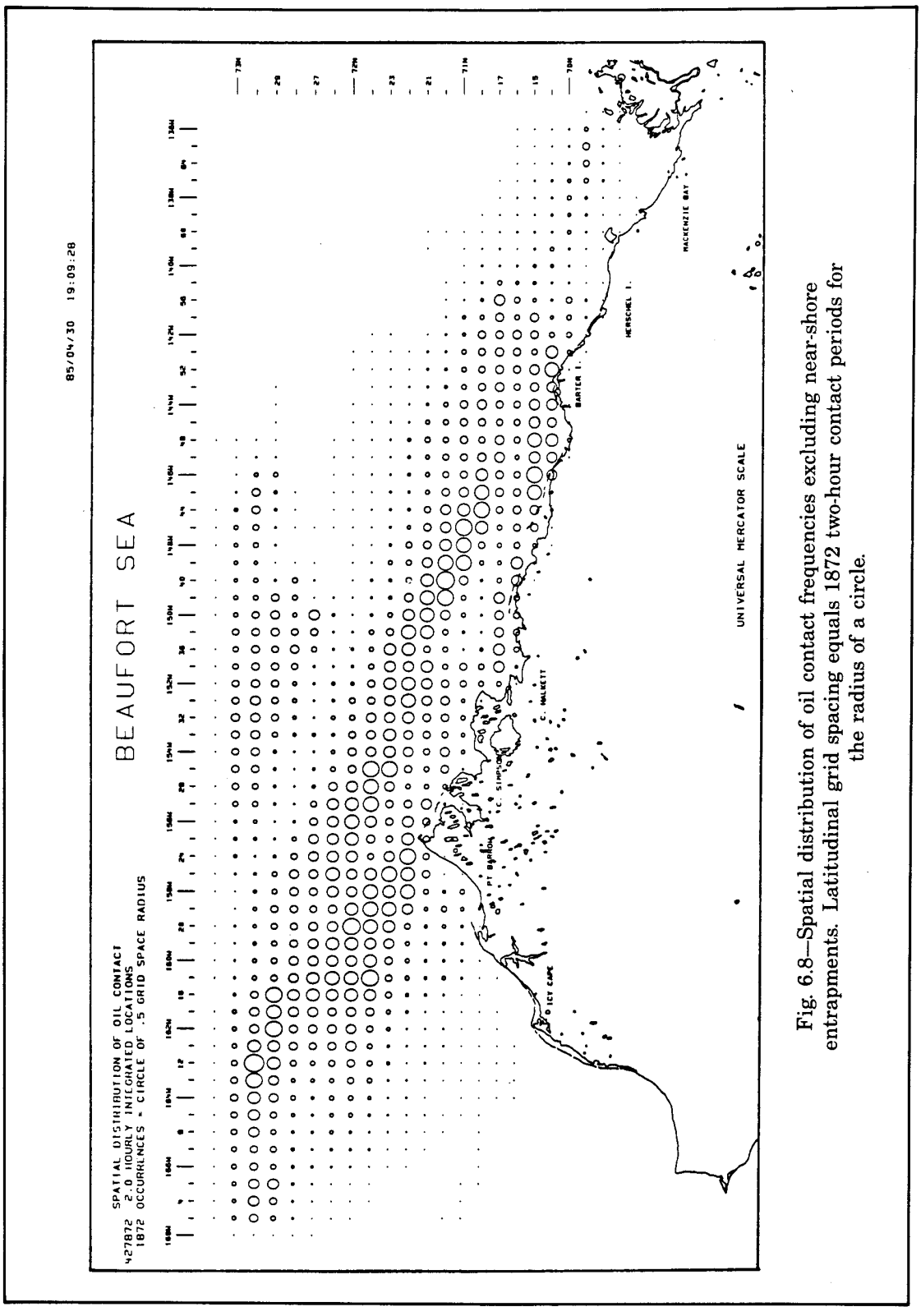

Fig. 6.8—Spatial distribution of oil contact frequencies excluding near-shore entrapments. Latitudinal grid spacing equals 1872 two-hour contact periods for the radius of a circle.

DETERMINING THE OIL CONCENTRATION FIELD

When released in water, fresh crude oil will undergo major changes in its composition while being transported and dispersed. The spreading of oil at the surface is mainly due to mechanisms associated with viscosity, surface tension, and inertia. As time progresses the major process responsible for the spreading of spilled oil are advection and turbulent dispersion. While oil is being advected and dispersed, its concentration decreases as a result of evaporation, photochemical degradation, and biodegradation. These processes are called weathering.

In modeling an oil concentration field, advection, dispersion, and weathering are considered as well as the transport of oil. The rates of evaporation and the bio- and photochemical degradation were evaluated under field conditions by other investigators (Payne et al., 1983). The oil decay rates for the simulation were estimated by these investigators on the basis of turbulence levels determined by means of the three-dimensional models for the different areas.

To illustrate the diffusion process induced by the turbulent oscillating flow, it is more convenient to demonstrate the magnitude of diffusion over the vertical plane in the absence of surface energy input from the wind. In other words, in this illustration the turbulence is generated primarily at the bottom by tide. To show the turbulent diffusion processes one hundred particles are released in each vertical layer near the Pribilof Island and half-hourly displacements are plotted there for a period of 24 hours (Fig. 6.9). The elevations for the eight layers are 2.5, 7.5, 12.5, 17.5, 25, 35, 85, and 240 meters, respectively.

In each layer the movements of particles are caused by advection and diffusion processes. For instance, the hourly displacement of the particle group in the first layer starts from the upper position, gradually moving with the tidal motion. As the group moves the distance between the particles increases because of the turbulent diffusion. In a stricter sense, the separation of particles is the combined result of diffusion and the nonuniformity of the current field. The combined process is called the turbulent dispersion. In shear flow, such as the one illustrated here, the major mechanism responsible for dilution of a soluble is dispersion. This is evident from the amount of dispersion experienced by the particle groups in the lower layers where the velocity gradient is much sharper than in the upper five layers. These five layers are located above the sharp pycnocline, which partially isolates the upward momentum transport.

Also of interest are the distances between the first and the last particle group within each layer. They represent the net displacement over a period of two days. The changes in net transport over the vertical are quite common in the coastal area, to satisfy the law of conservation of mass.

The example presented here illustrates the dispersion mechanism associated primarily with bottom stress and nonuniform velocity distribution. Dispersion effects can also be induced by shore line irregularity through the variability of the velocity field. For each of the large modeled areas, submodels are used to compute near-shore oil movements (Fig. 6.10). The turbulent diffusion coefficients averaged over ten tidal cycles, as computed by the three-dimensional model for each large area and for each layer, are stored on magnetic tapes. These diffusion coefficients became very useful for diffusion analysis in a limited near-shore area. Figure 6.11 represents the results of oil dispersion analysis in which crude oil is released instantaneously from five locations near the Bering Strait. Displacement of the one-part-per-billion concentration envelopes are plotted every five days. The influence of the

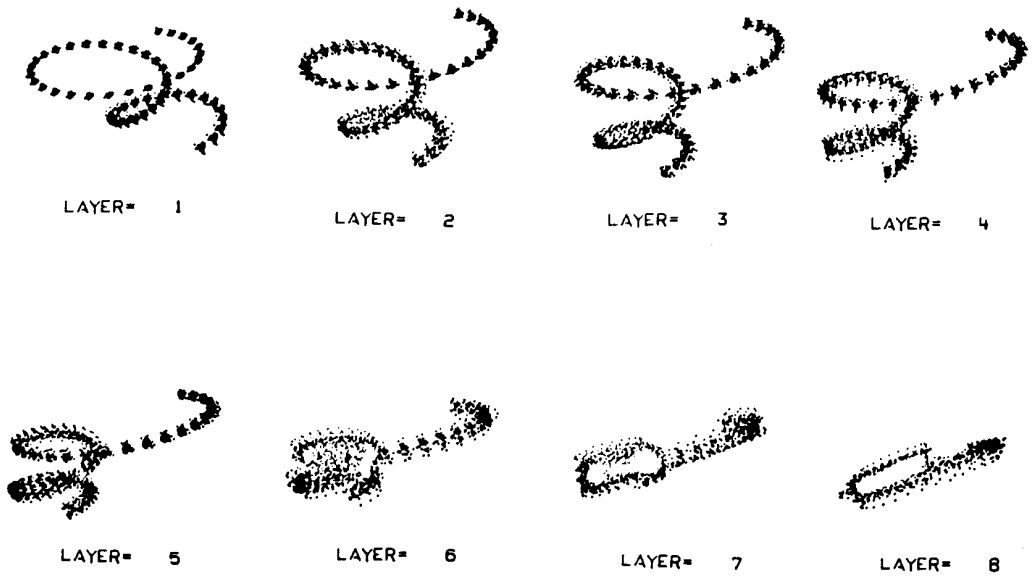

Fig. 6.9—Pathways of particle groups released in different layers of the model. Partially insulated by the pycnocline, 24-hour trajectories of particle groups released in the upper five layers experience less turbulent diffusion than the lower layers when the system is forced only with tidal energies.

shoreline and the variability of local advective/diffusive mechanisms (Fig. 6.11) are quite evident, as seen by the changing speed and direction of the oil movement.

Under a scenario of continuous release, the distribution of surface oil concentration is presented in Fig. 6.11. When oil moves through the Bering Strait, the strong local current tends to elongate the oil. Also notice the cumulation effects when the oil reaches the coastal area, where the on-shore current components drop and the along-shore currents strengthen. This near-shore effect tends to redirect the oil while slowing it down. The speed of an oil transport can be seen from the top diagram of Fig. 6.12, where daily displacements of the advancing plume are plotted. The daily traveling speed of oil is governed by the evolutionary weather state as well as the local circulation pattern.

To illustrate the effects of weather and local baroclinic circulation, a group of six trajectories are launched from five hypothetical spill locations in the Chukchi Sea/Barrow Arch lease area (Fig. 6.13). The net displacement for the northern trajectories during the eight-month period ranges between 3–5° latitude, which represents a daily movement of 1.4 to 2.31 km (Fig. 6.14). Oil launched near Point Hope travels substantially slower than its northern counterpart, which moves predominantly within the Arctic Gyre. The simulated direction and speed of ice movements within the Chukchi Sea agree with the observed values reported

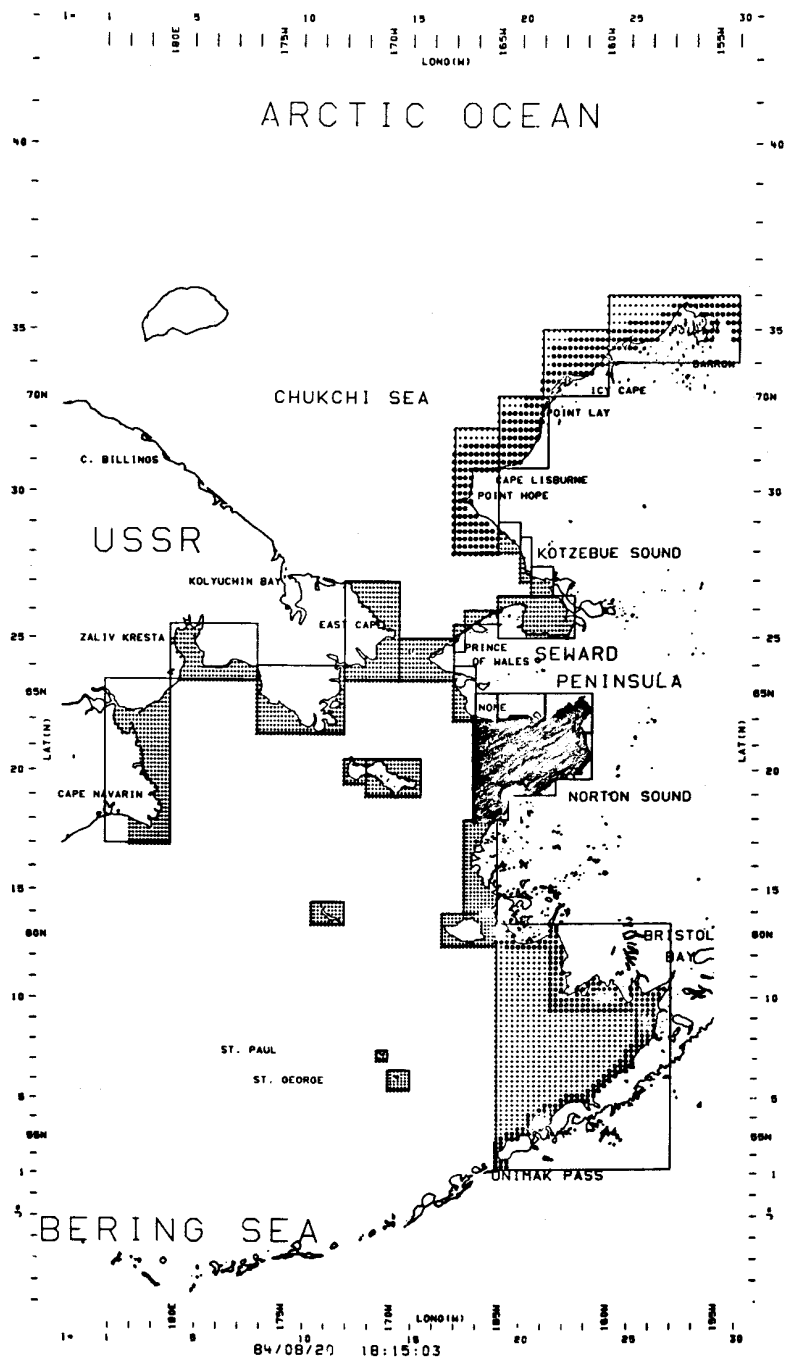

Fig. 6.10—Submodels are used to improve the near-shore resolution of the trajectory computation. The computational grids of the submodel are nested within the larger model's computational grid (Liu and Leendertse, 1984).

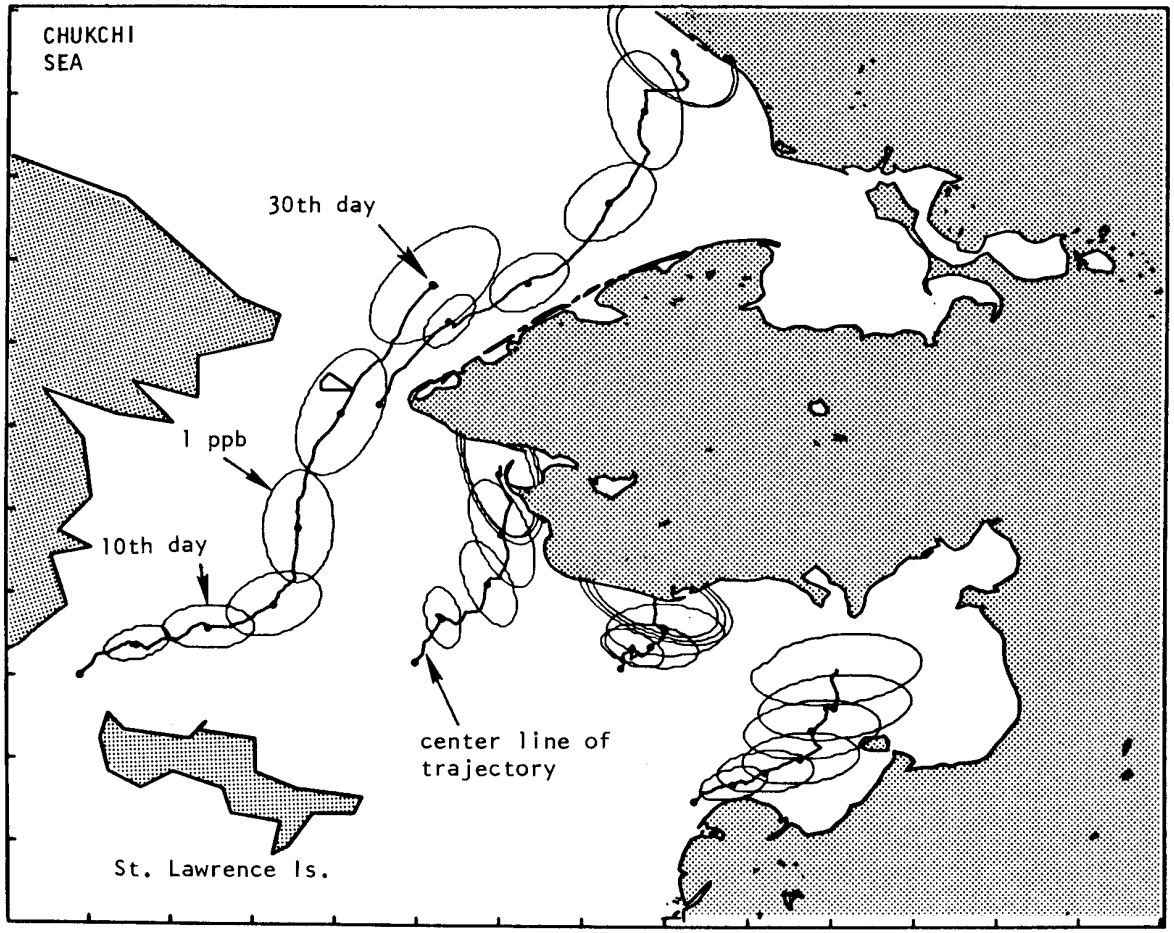

Fig. 6.11—Displacements of the one-part-per billion concentration envelope every five days for an instantaneous release of 700,000 barrels of crude oil from five hypothetical launch points during the summer. The variability of local advective and diffusive mechanisms is illustrated by the changing speed and direction of the oil's movements.

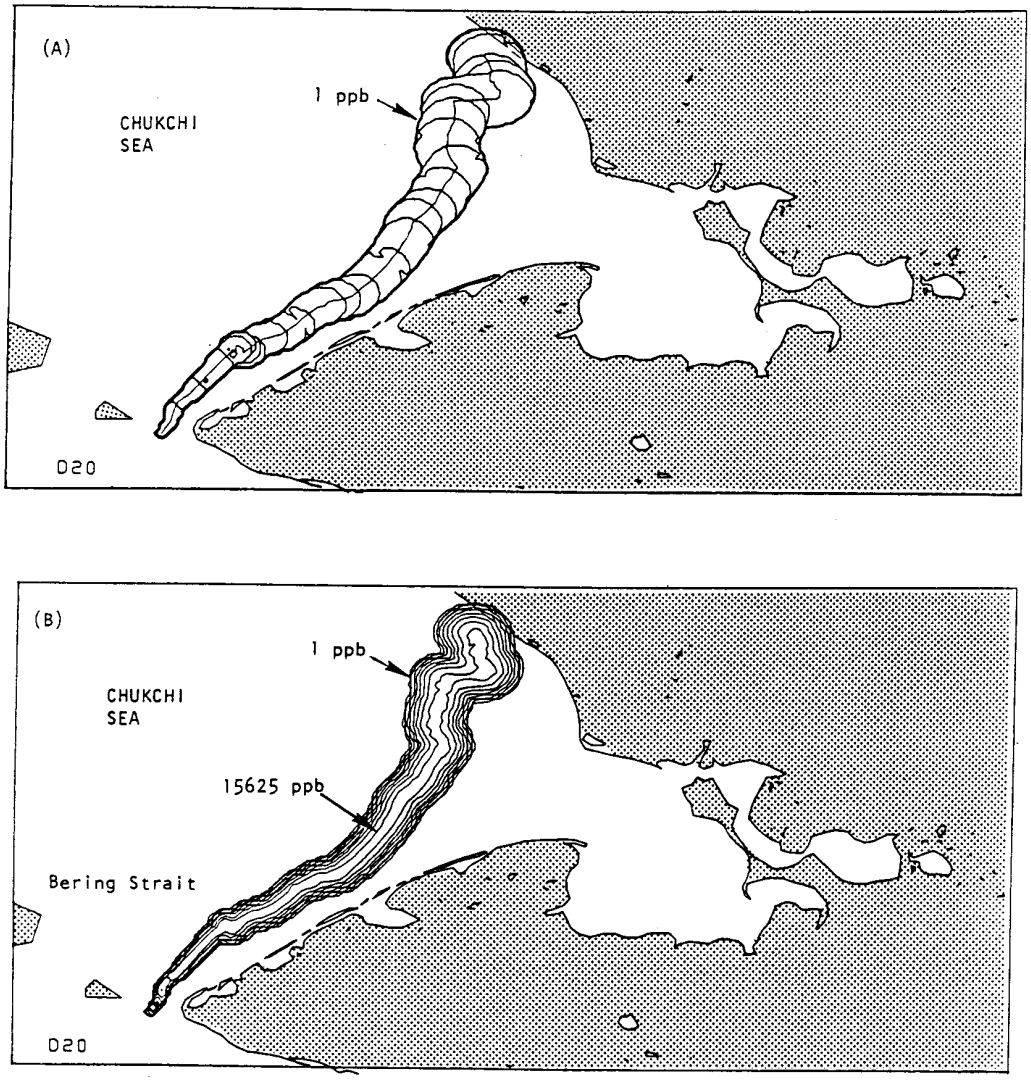

Fig. 6.12—Oil spill trajectory launched in the middle of the Bering Strait under a 30-day stochastic weather scenario during the summer. (A) illustrates the progressive daily displacements of the 1 part per billion concentration envelope for the continuous discharge of 2000 barrels of crude oil. The traveling speed of oil is governed by the evolutionary weather state as well as the local circulation pattern. (B) illustrates the concentration contour of the oil. Notice the cumulation effects when the oil reaches the coastal area where the on-shore current components drop and the along-shore currents strengthen. This near-shore effect tends to redirect the oil while slowing it down somewhat.

by Gordienko (1958), and Hibler (1979), who made computations using ice models including nonlinear plastic flow effects by means of viscous-plastic constitutive law.

Perhaps it is more illustrative to show and analyze a group of trajectories launched near an embayment so that the shore effects can be seen. The launch point is located between St. Lawrence Island and the Gulf of Anadyr, USSR (see the insert map of Fig. 6.15). Twenty-one groups of 30-day oil spill trajectories are sampled every two hours. These sampled data are then analyzed for their direction and speed. For a 30-day duration there are 360 two-hour samples for current directions and speeds. Since the directions and speeds of currents at every two hours are located over a different area, local residual circulation and the relative distance from the shore-fast ice make the movement of oil contained in ice different from that of free-drifting pack ice. Consequently, there are more random ice motions under the local wind stress than the oil movements in the water column resulting from inertia and momentum filtering effects.

Figure 6.16 indicates that most oil spill trajectories move in a predominantly northwesterly direction. For the summer period (Fig. 6.16), however, most contacts are closer to the eastern shore. It should be noted that the plotting scale of Fig. 6.17 is four times that of the one shown in Fig. 6.16. The western Chukchi Sea receives much less impact during the summer season than in the winter period. On the average, oil travels a shorter distance and moves more randomly under the summer winds. During summer, winds have higher variabilities and, as a consequence, the inertial current components have a substantial contribution toward the overall current direction. The area of greatest impact is located near Icy Cape.

Another method using the oil spill trajectory simulation results is to trace back from a given marine resource contact location to the location of oil released. If the marine area is ecologically sensitive, then the area near the launch point should not be considered for oil exploration. This type of "trace-back" analysis was made, for example, for the Chukchi Sea lease area. Partial results for winter and summer are listed in Tables 6.1 and 6.2, respectively. The tables are for illustrative purposes only. For example, in Table 6.1, the location of the marine area is represented by the (I,J) grid of the model as listed in the first two columns in the table. The third column is the number of trajectories hitting this area during this period. The subsequent numbers are the launch points where the oil was released. In the first row of Table 6.1, at marine area I=3, J=17 as shown in Fig. 6.13, oil was released from stations J14, J15, J16, J20, and J36. The area is relatively safe during summer as indicated in Table 6.2 from the launch points considered for this particular simulation run. Analyses such as these are sometimes instrumental in marine pollution analysis where the location of a point source is to be selected to avoid a particular marine resource area.

The marine resource group risk exposure time can be evaluated by the spatial distribution of oil contact frequencies from the spill trajectories. In Fig. 6.17 the contact frequencies are plotted at each marine area with the size of circle proportional to the contact time.

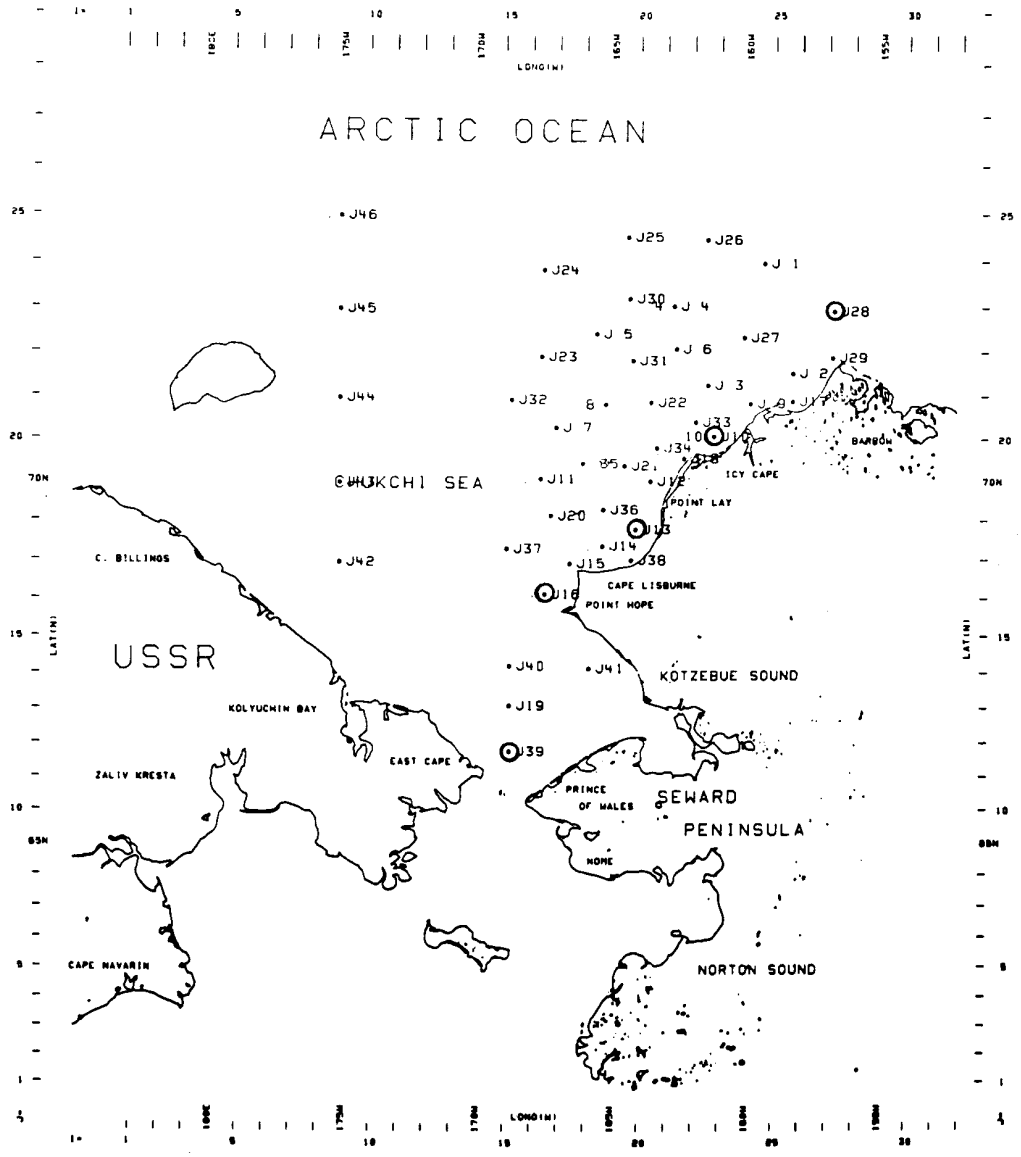

Fig. 6.13—Location of 46 launch points specified for the oil spill trajectory computation. Barrow Arch lease area (No. 109).

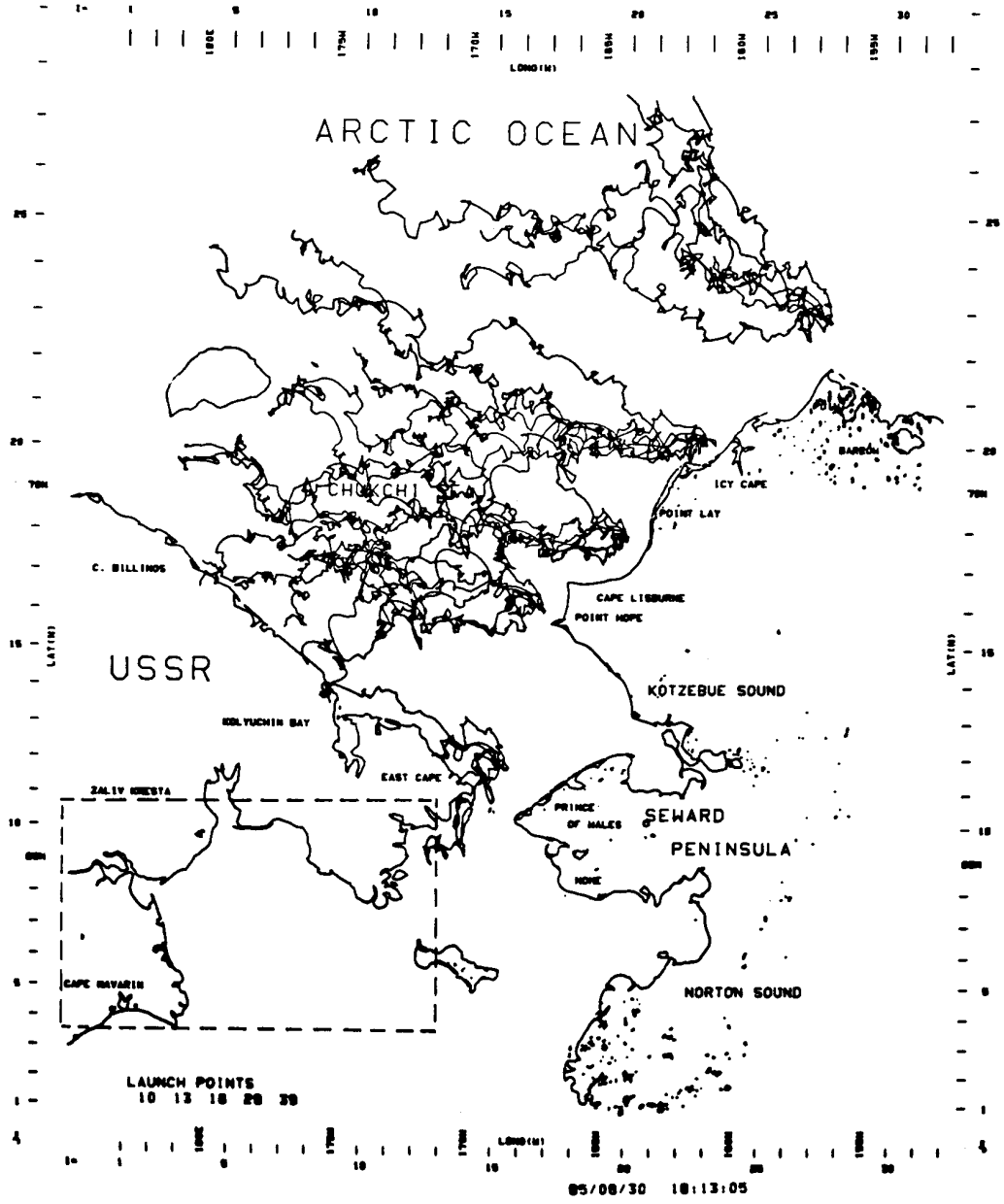

Fig. 6.14—Five sets of randomly selected trajectories from launch points 10, 13, 16, 28, and 39; under the staggered-launch mode, each spill has about equally likely chance of occurrence during the winter. Spill launched near the Bering Strait can move either south or north depending on the weather sequence.

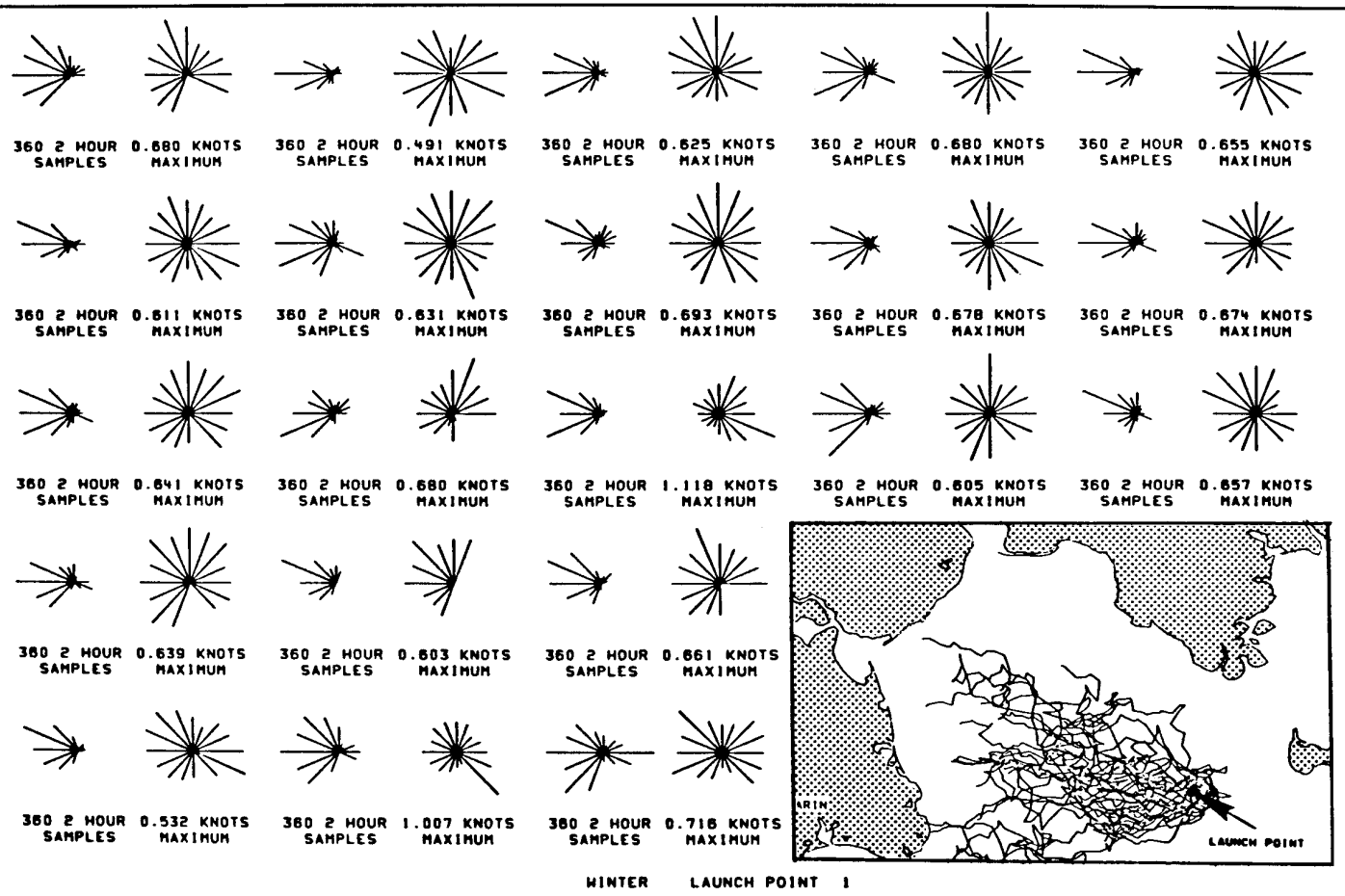

Fig. 6.15—Current roses analyzed from twenty-one 30-day oil spill trajectories for winter, launched near a point between St. Lawrence Island and the Gulf of Anadyr, USSR (see insert map). Local residual and the relative distance from the shore-fast ice make the oil containing ice move differently from the free-drifting pack ice. Consequently, there are more random ice motions under the local wind stress than the oil movements in the water column resulting from inertia and momentum filtering effects.

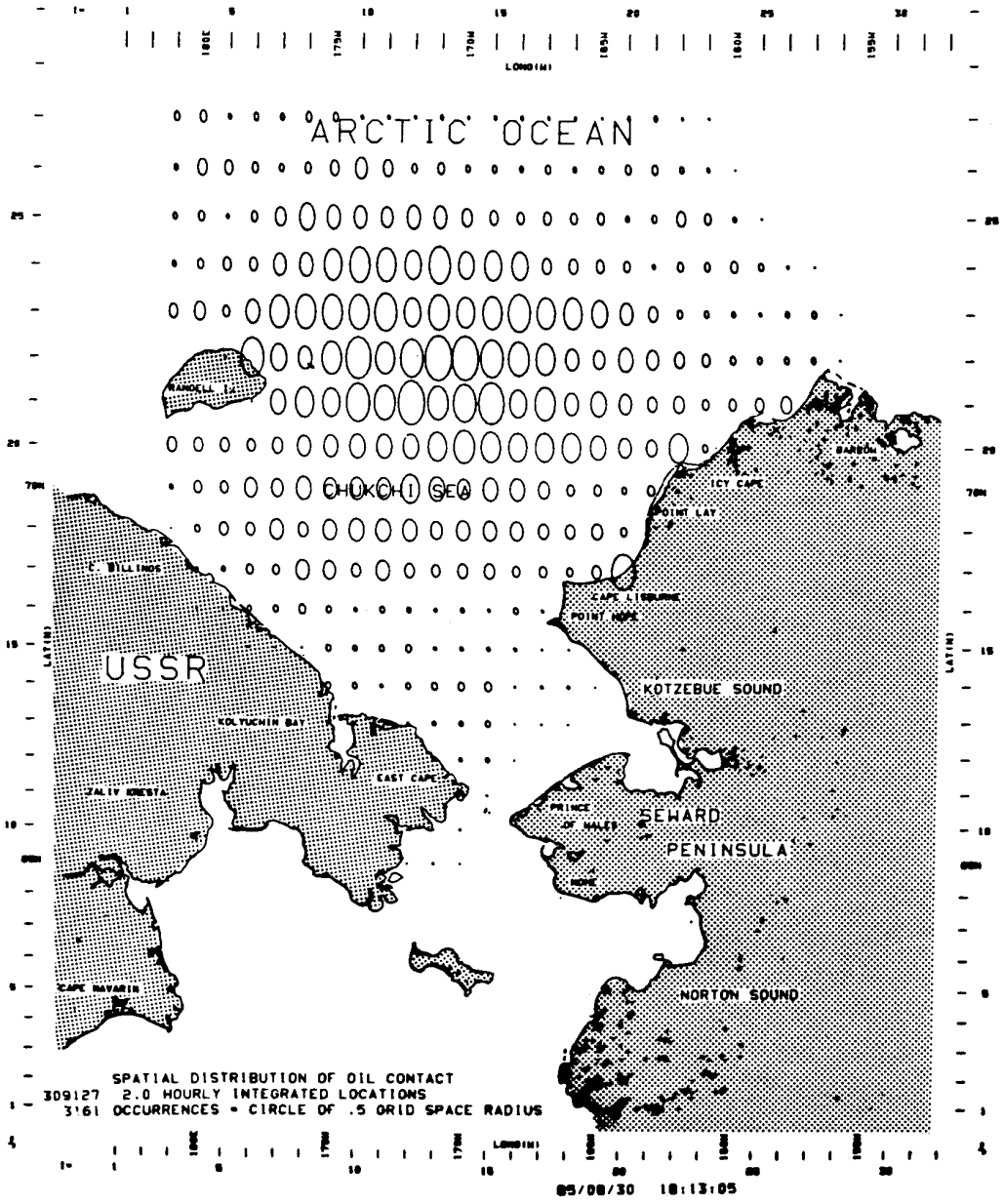

Fig. 6.16—Spatial distribution of oil contact frequencies during winter. Latitudinal grid spacing equals 3161 two-hour contact periods for the long axis of the ellipse.

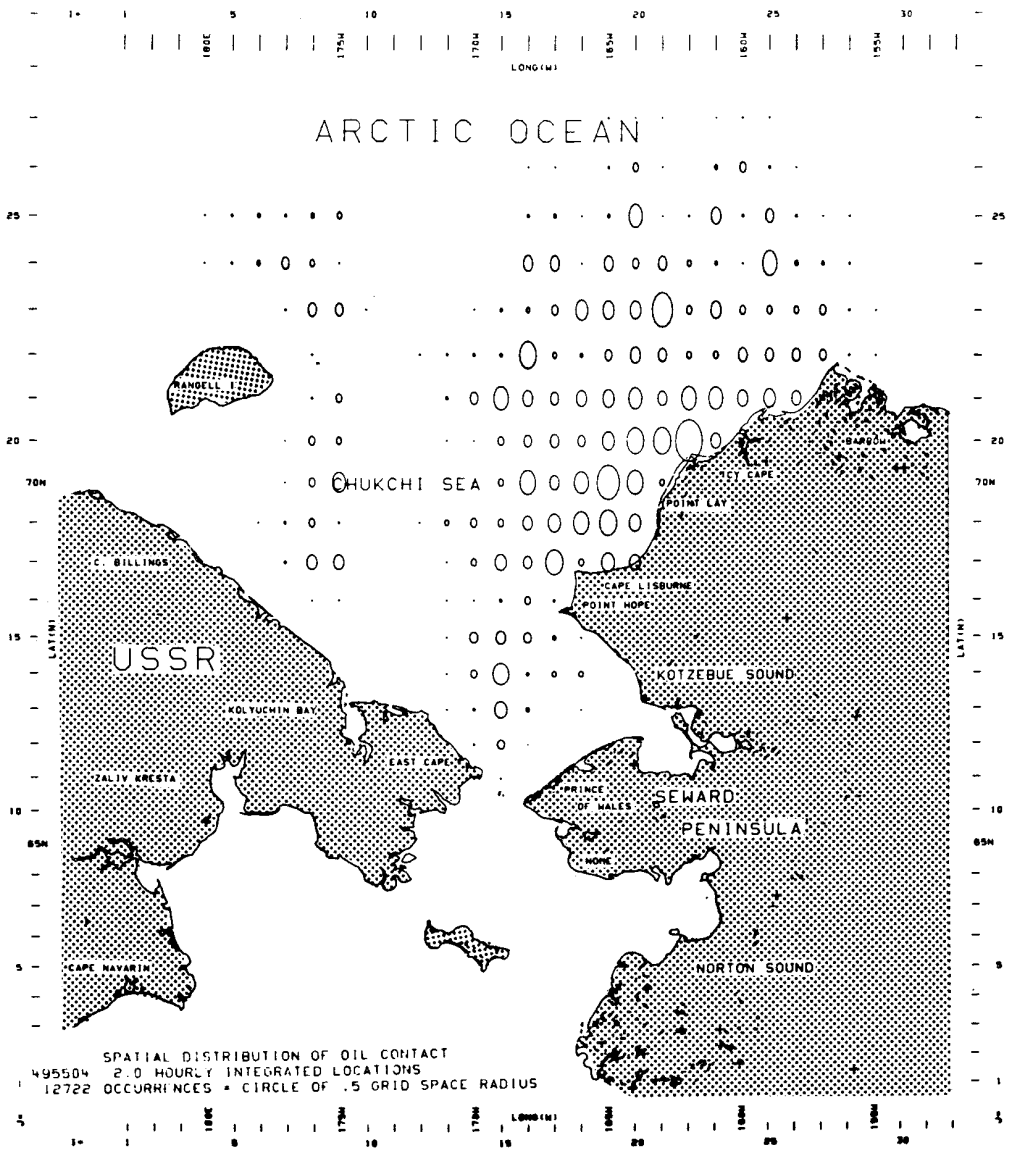

Fig. 6.17—Spatial distribution of oil contact frequencies during summer. Latitudinal grid spacing equals 12722 two-hour contact periods for the long axis of the ellipse.

Table 6.1

CHUKCHI SEA WINTER OIL SPILL TRAJECTORY ANALYSES (SALE 109). TABULATED "TRACE-BACK" OF OIL SPILL CONTACT BETWEEN CONTACT LOCATION AND LAUNCH POINT. "*" INDICATES LANDFALL AND "#" INDICATES TRAJECTORY MOVED OUT OF THE MODELED AREA

I	J	NO	LAUNCH POINTS TERMINATING AT (I,J)
3	17	9	*J14 *J15 *J15 *J16 *J16 *J16 *J20 *J36 *J36
3	18	8	J11 J14 J14 J15 J15 J37 J37 J37
3	19	28	J 7 J11 J12 J13 J13 J13 J13 J14 J14 J15 J16 J16 J20 J20 J20 J20 J21 J32 J32 J35 J35 J36 J36 J37 J37 J37 J37 J40
3	20	15	J 8 J 8 J12 J14 J15 J16 J20 J20 J20 J20 J23 J34 J36 J37 J37
3	21	1	*J11
3	23	16	J 2 J 5 J 5 J 7 J 8 J 8 J 8 J 9 J 9 J22 J23 J23 J30 J32 J34 J35
3	24	24	J 2 J 3 J 5 J 5 J 6 J 8 J11 J22 J22 J22 J23 J23 J23 J23 J24 J24 J25 J25 J30 J31 J32 J32 J32 J35
3	25	16	J 3 J 4 J 5 J 6 J 7 J 8 J23 J23 J23 J23 J24 J27 J30 J31 J31 J31
3	26	14	J 5 J 5 J 5 J 5 J 6 J 6 J24 J24 J24 J25 J25 J27 J30 J31
3	27	13	J 4 J 4 J 6 J24 J24 J24 J24 J27 J30 J30 J30 J30 J32
3	28	2	#J23 #J24
4	16	5	*J15 *J16 *J38 *J37 *J38
4	17	7	*J16 J16 *J19 J20 J36 *J37 *J41
4	18	10	J11 J12 J13 J15 J15 J23 J35 J37 J41 J41
4	19	9	J 7 J12 J14 J14 J21 J34 J35 J36 J36
4	20	6	J 5 J 7 J 8 J20 J33 J36
4	21	1	*J12
4	22	1	*J22
4	23	10	J 3 J 4 J 4 J 4 J12 J21 J21 J31 J32 *J33
4	24	10	J 6 J 6 J10 J17 J18 J25 J29 J31 J33 J34
4	25	9	J 2 J 4 J 5 J 8 J10 J22 J27 J30 J33
4	26	12	J 3 J 3 J 4 J 9 J24 J24 J25 J28 J29 J30 J31 J31
4	27	5	J 1 J 2 J 5 J 6 J25
4	28	1	#J26
5	16	16	*J 7 *J11 *J14 *J14 *J15 *J16 *J20 *J20 *J21 *J35 *J37 *J40 *J40 *J40 *J41 *J41
5	17	3	J15 *J16 J38
5	18	4	J 8 J15 J36 J38
5	19	4	J14 J21 J21 J31
5	20	6	J13 J18 J22 J34 J36 J37
5	21	9	*J11 *J13 *J15 *J20 *J21 *J22 *J23 *J33 *J38
5	22	39	*J 3 *J 3 *J 4 *J 5 *J 5 *J 6 *J 7 *J 7 *J 7 *J 8 *J 8 *J 8 *J 8 *J 8 *J 9 *J10 *J12 *J12 *J18 *J18 *J20 *J21 *J22 *J22 *J22 *J23 *J23 *J24 *J30 *J30 *J31 *J31 *J32 *J32 *J32 *J33 *J34 *J35 *J36
5	23	9	J 7 J 8 J 9 J12 *J25 J27 J30 J33 *J36
5	24	1	J23
5	25	2	J25 J33
5	26	6	J 4 J 9 J22 J26 J29 J30
5	27	2	J24 J26
5	28	4	#J 4 #J25 #J27 #J30
6	15	4	*J11 *J12 *J19 *J41
6	16	2	*J16 *J40
6	17	1	J14
6	18	2	J22 J40
6	19	4	J12 J14 J15 J16
6	20	4	J 6 J 9 J10 J13
6	21	75	*J 3 *J 3 *J 3 *J 3 *J 4 *J 5 *J 5 *J 6 *J 7 *J 7 *J 7 *J 7 *J 8 *J 9 *J 9 *J10 *J11 *J11 *J11 *J11 *J11 *J11 *J11 *J11 *J12 *J12 *J12 *J12 *J13 *J13 *J14 *J14 *J16 *J18 *J20 *J20 *J21 *J21 *J21 *J21 *J21 *J21 *J21 *J21 *J22 *J22 *J22 *J23 *J24 *J30 *J31 *J31 *J31 *J32 *J32 *J32 *J33 *J34 *J34 *J34 *J34 *J34 *J35 *J35 *J35 *J35 *J35 *J35 *J36 *J36 *J36 *J37 *J37 *J38
6	22	20	J 2 *J 6 J 6 *J 7 *J 7 *J 7 J 7 J10 J13 J14 *J15 J17 *J24 J31 *J32 *J32 *J32 J33 *J34 J34
6	23	6	J 3 J 4 J 9 J 9 J17 J27
6	24	7	J 2 J 5 J 6 J18 J18 J22 J32
6	25	2	J31 J34
6	26	3	J 3 J17 J23

Table 6.2

CHUKCHI SEA SUMMER OIL SPILL TRAJECTORY ANALYSES (SALE 109). TABULATED "TRACE-BACK" OF OIL SPILL CONTACT BETWEEN CONTACT LOCATION AND LAUNCH POINT. "*" INDICATES LANDFALL AND "#" INDICATES TRAJECTORY MOVED OUT OF THE MODELED AREA

I	J	NO	LAUNCH POINTS TERMINATING AT (I,J)																									
4	24	1	J45																									
4	25	1	J46																									
5	24	19	J45	J45	J45	J46	J46	J46	J46	J46	J46	J46	J46	J46	J46	J46	J46	J46	J46	J46	J46							
5	25	8	J46	J46	J46	J46	J46	J46	J46	J46																		
6	18	1	J43																									
6	24	18	J45	J45	J45	J45	J45	J45	J45	J45	J45	J45	J45	J45	J45	J45	J45	J45	J46	J46								
6	25	3	J46	J46	J46																							
7	17	13	J42	J42	J42	J42	J42	J42	J42	J42	J42	J42	J42	J43	J43													
7	18	15	J43	J43	J43	J43	J43	J43	J43	J43	J43	J43	J43	J43	J43	J43	J44											
7	19	1	J44																									
7	20	2	J44	J44																								
7	23	1	J45																									
7	24	4	J45	J45	J45	J45																						
8	17	16	J42	J42	J42	J42	J42	J42	J42	J42	J42	J42	J42	J42	J42	J42	J42	J42										
8	18	11	J43	J43	J43	J43	J43	J43	J43	J43	J43	J43	J44															
8	19	21	J43	J44	J44	J44	J44	J44	J44	J44	J44	J44	J44	J44	J44	J44	J44	J44	J44	J44	J44	J44	J44	J44	J44			
8	20	1	J44																									
8	23	3	J45	J45	J45																							
8	24	2	J45	J45																								
9	16	2	J42	J42																								
9	17	1	J42																									
9	19	5	J43	J43	J44	J44	J44																					
9	20	1	J44																									
12	18	4	J37	J37	J37	J37																						
12	22	1	J32																									
13	13	3	J39	J39	J39																							
13	14	1	J19																									
13	15	1	J40																									
13	16	1	J40																									
13	17	4	J37	J37	J37	J37																						
13	18	17	J37	J37	J37	J37	J37	J37	J37	J37	J37	J37	J37	J37	J37	J37	J37	J37										
13	21	13	J32	J32	J32	J32	J32	J32	J32	J32	J32	J32	J32	J32	J32													
13	22	7	J32	J32	J32	J32	J32	J32	J32																			
14	11	1	J39																									
14	12	3	J39	J39	J39																							
14	13	5	J39	J39	J39	J39	J39																					
14	14	22	J19	J19	J19	J19	J19	J19	J19	J19	J19	J19	J19	J19	J19	J19	J19	J19	J19	J19	J39	J39	J39	J39	J40			
14	15	29	J19	J19	J19	J19	J19	J19	J40	J40	J40	J40	J40	J40	J40	J40	J40	J40	J40	J40	J40	J40	J40	J40	J40	J40	J40	J40
			J40	J40	J40	J40	J40																					
14	16	3	J16	J16	J40																							
14	17	20	J16	J16	J16	J16	J16	J16	J16	J16	J16	J16	J16	J16	J16	J16	J16	J16	J16	J16	J37	J37						
14	18	3	J37	J37	J37																							
14	19	1	J20																									
14	20	1	J11																									
14	21	9	J 7	J 7	J 7	J 7	J32	J32	J32	J32	J32																	
14	22	5	J 7	J32	J32	J32	J32																					
14	23	2	J23	J23																								
15	13	4	J19	J39	J39	J39																						
15	14	10	J19	J19	J19	J39	J39	J39	J39	J39	J39	J41																
15	15	10	J19	J19	J40	J40	J41	J41	J41	J41	J41	J41																
15	16	5	J15	J40	J41	J41	J41																					
15	17	9	J15	J15	J16	J16	J16	J16	J16	J16	J16																	
15	18	11	J15	J15	J16	J16	J20	J20	J20	J20	J20	J20	J20															
15	19	18	J11	J11	J11	J11	J20	J20	J20	J20	J20	J20	J20	J20	J20	J20	J20	J20	J20	J20	J20							
15	20	20	J 7	J11	J11	J11	J11	J11	J11	J11	J11	J11	J11	J11	J11	J11	J11	J11	J11	J11	J11	J11	J11					

7. CONCLUSIONS

This report presents the methodologies, data analyses, and the modeling efforts related to the hydrodynamic processes of the Alaskan coastal waters. The following conclusions were reached during the course of the study:

1. The hydrodynamic processes of the Alaskan coastal waters possess different characteristic scales both in time and over space, depending on their depth and the relative distance from the coast. This, when coupled with the shoreline configuration, requires nested models of various scale to resolve the dynamic process of our primary concern. Because of this, we have developed models that range in size from 1.5 million square kilometers (Gulf of Alaska model, 43,000 grid points) to lagoon models, which have grid spacings of only a few hundred meters.
2. In 1980 the results of the three-dimensional model of the Bering/Chukchi Sea indicated an amphidromic system in the lower Chukchi Sea. Its location varied slightly depending on the seasonal variability of ice coverage and the vertical stratification. The computational results are presented in Liu and Leendertse (1982).
3. The baroclinic spin-up time ranged from a few hours for a small coastal tidal model to more than ten days for a large model such as the Gulf of Alaska. For the eastern Bering shelf, which has an average depth of 75 meters, and over 90 percent of the energy is of tidal origin, the time to reach equilibrium is approximately five to seven days. The computed baroclinic circulation pattern over the shelf with the tidal bands filtered out agrees with the observed patterns.
4. A hydrodynamic model coupled to an areawide weather or wind model is required to simulate the complete water movements in the Alaskan coastal waters. At the present time, the global weather data grid network over the Alaskan area does not have enough resolution to compute realistic wind fields associated with a strong moving storm and cannot be used for accurate oil spill simulations.
5. A parametric wind model based upon statistical data can be used very effectively and with a high degree of accuracy as input for oil spill simulations.
6. In addition to the hydrodynamics computation algorithm, extensive software developments are required for the oil spill simulation and subsequent processing of results for impact assessments.
7. Short intervals are required for accurate computation of trajectories near shore locations. Also, the weathering of oil in the simulations requires a short time interval for accurate computation of oil concentrations. This is particularly true for the computation of weathering shortly after a release, as then the evaporation rates are high.
8. For oil spill impact risk analysis, not only is information about the trajectory required, but also information about the dispersion of oil. The computation of this dispersion requires a rather extensive computational effort.
9. Hydrodynamic models with much resolution of the pycnocline are required to properly model the physical processes in this stratification zone without appreciable numerical diffusion. Numerical models using vertical coordinate transformations appear to be insufficient for resolving the pycnocline.

10. Shear stress coefficients for the air/ice and ice/water interfaces should be calculated based on data using the exact model for which they will be used later, ideally for the areas with similar ice coverage. Otherwise, coefficients derived from models of lower dimensions would overestimate the amount of momentum transfer if they were used in a model of higher dimensions. Fewer terms are involved that represent the overall momentum transport process in the lower dimension models than in those with higher dimensions. The same is true for diffusion coefficients. Fitting the same data group, a one-dimensional model would result in higher diffusion coefficients than a two-dimensional model, as the latter has more terms to resolve the diffusive process.
11. At the present time, the available turbulence-closure schemes still need improvements when turbulence is strongly influenced by body forces acting in a preferred direction, such as the buoyancy forces. The ice melting process creates strong stratification in the Alaskan offshore waters; therefore, it is more difficult to simulate turbulent processes in these waters. More studies are needed to compute the dispersion in nonhomogeneous waters.
12. For the turbulence-closure computation in this modeling study, a parametric relationship considering energy transfer from the wind field is used as an input energy source term. The amount of energy input is evaluated according to the equilibrium condition considering the Miles-Phillip mechanism and uses shallow water wave/current data measured by our colleagues of the Netherlands Rijkswaterstaat. These data are measured over the southern North Sea under the influence of the Icelandic Low. Both the depth and wind conditions are quite similar to the oceanic conditions of the Alaskan shelf waters during an ice free condition. This is quite different from the traditional approach in which the upper boundary is treated as a moving or nonmoving wall like the bottom. It is the authors' belief that storm-induced surface diffusion and transport are extremely important in an oil spill risk analysis. The likelihood of a spill is much higher during storm conditions. The wall-generated turbulence does not behave the same as the storm generated surface turbulence. In the present k-ε formulation, there is little experimental information at the surface that could be used as the basis for specifying the length scale (Rodi, 1980). Certainly more research is needed in this area.
13. This study has developed a general data base on the tidal propagation and residual circulation pattern over the Alaskan coastal waters so that they can be used as boundary and initial conditions for the nested models of higher resolution. Baroclinic residual currents coexisted with the tidal energy over the broad Bering/Chukchi Sea shelf and results are tabulated in Tables A.1 through A.6. It is more economical and reliable to use the circulation produced in this manner than to have those small models generate baroclinic current fields themselves.

Appendix

COMPUTED RESIDUAL CURRENTS IN THE BERING AND CHUKCHI SEAS

Table A.1

COMPUTED EAST-WEST COMPONENT OF TIDAL/BAROCLINIC RESIDUAL CURRENTS IN THE BERING AND CHUKCHI SEAS (cm/sec)

	181W 0.0'	180W 30.0'	180W 0.0'	179W 30.0'	179W 0.0'	178W 30.0'	178W 0.0'	177W 30.0'	177W 0.0'	176W 30.0'	176W 0.0'	175W 30.0'	175W 0.0'	174W 30.0'	174W 0.0'	173W 30.0'	173W 0.0'	172W 30.0'	172W 0.0'	171W 30.0'
72 0.0'N	-1.748	-2.152	-2.555	-1.368	-0.181	0.068	0.316	-0.913	-2.142	-1.826	-1.511	-1.828	-2.144	-1.114	-0.084	-1.058	-2.032	-1.921	-1.810	-1.624
71 45.0'N	-0.874	-1.076	-1.278	-0.684	-0.090	0.740	1.571	1.181	0.791	0.789	0.787	-0.373	-1.534	-1.754	-1.974	-1.786	-1.599	-1.502	-1.405	-1.266
71 30.0'N	0.0	0.0	0.0	0.0	0.0	1.413	2.825	3.274	3.723	3.404	3.085	1.081	-0.923	-2.393	-3.864	-2.515	-1.165	-1.083	-1.000	-0.908
71 15.0'N	0.0	0.0	0.0	0.0	0.0	0.706	1.413	1.503	1.594	1.506	1.419	0.151	-1.116	-1.871	-2.626	-2.010	-1.395	-1.178	-0.962	-0.893
71 0.0'N	0.0	0.0	0.0	0.0	0.0	0.0	0.0	-0.268	-0.535	-0.391	-0.247	-0.778	-1.310	-1.349	-1.388	-1.506	-1.624	-1.274	-0.924	-0.877
70 45.0'N	-3.963	-2.782	-1.601	-0.734	0.133	0.903	1.673	1.282	0.891	0.130	-0.630	-1.463	-2.297	-1.168	-0.039	-1.178	-2.316	-1.518	-0.720	-0.482
70 30.0'N	-7.925	-5.564	-3.202	-1.468	0.265	1.805	3.346	2.831	2.317	0.652	-1.013	-2.148	-3.283	-0.987	1.310	-0.849	-3.008	-1.762	-0.516	-0.088
70 15.0'N	-2.845	-3.102	-3.358	-2.883	-2.409	-1.609	-0.810	0.415	1.639	0.921	0.202	-0.107	-0.416	0.335	1.086	-0.307	-1.700	-1.719	-1.739	-0.772
70 0.0'N	2.234	-0.640	-3.514	-4.298	-5.082	-5.024	-4.965	-2.002	0.962	1.189	1.417	1.934	2.451	1.657	0.863	0.236	-0.391	-1.677	-2.962	-1.456
69 45.0'N	-0.406	-1.772	-3.137	-3.739	-4.341	-4.781	-5.221	-3.870	-2.520	-2.119	-1.718	-1.314	-0.911	-1.541	-2.172	-1.414	-0.656	-1.386	-2.115	-1.836
69 30.0'N	-3.046	-2.903	-2.761	-3.180	-3.599	-4.537	-5.476	-5.739	-6.002	-5.427	-4.852	-4.563	-4.273	-4.740	-5.206	-3.064	-0.922	-1.095	-1.269	-2.217
69 15.0'N	-1.523	-1.441	-1.360	-1.379	-1.398	-1.312	-1.226	-1.845	-2.464	-2.570	-2.677	-1.942	-1.207	-1.958	-2.709	-2.227	-1.744	-1.193	-0.641	-1.623
69 0.0'N	0.0	0.021	0.041	0.422	0.803	1.913	3.023	2.049	1.074	0.286	-0.502	0.679	1.860	0.824	-0.212	-1.389	-2.566	-1.290	-0.014	-1.030
68 45.0'N	0.0	0.010	0.021	0.211	0.401	2.334	4.266	3.910	3.554	2.087	0.620	1.075	1.530	0.891	0.252	-1.318	-2.888	-1.810	-0.732	-1.271
68 30.0'N	0.0	0.0	0.0	0.0	0.0	2.754	5.509	5.771	6.033	3.887	1.741	1.471	1.200	0.958	0.716	-1.247	-3.209	-2.330	-1.450	-1.511
68 15.0'N	0.0	0.0	0.0	0.0	0.0	1.377	2.754	2.885	3.017	3.486	3.955	2.397	0.839	1.736	2.633	0.662	-1.308	-0.976	-0.644	-1.087
68 0.0'N	0.0	0.0	0.0	0.0	0.0	0.0	0.0	0.0	0.0	3.085	6.169	3.323	0.478	2.514	4.551	2.571	0.592	0.377	0.161	-0.663
67 45.0'N	0.0	0.0	0.0	0.0	0.0	0.0	0.0	0.0	0.0	1.542	3.085	2.775	2.465	3.717	4.969	3.784	2.599	1.240	-0.120	0.186
67 30.0'N	0.0	0.0	0.0	0.0	0.0	0.0	0.0	0.0	0.0	0.0	0.0	2.226	4.452	4.920	5.388	4.997	4.607	2.102	-0.402	1.035
67 15.0'N	0.0	0.0	0.0	0.0	0.0	0.0	0.0	0.0	0.0	0.0	0.0	1.113	2.226	2.460	2.694	2.499	2.304	0.871	-0.562	0.181
67 0.0'N	0.0	0.0	0.0	0.0	0.0	0.0	0.0	0.0	0.0	0.0	0.0	0.0	0.0	0.0	0.0	0.0	0.0	-0.361	-0.722	-0.673
66 45.0'N	0.0	0.0	0.0	0.0	0.0	0.0	0.0	0.0	0.0	0.0	0.0	0.0	0.0	0.0	0.0	0.0	0.0	0.0	-0.181	-0.289
66 30.0'N	0.0	0.0	0.0	0.0	0.0	0.0	0.0	0.0	0.0	0.0	0.0	0.0	0.0	0.0	0.0	0.0	0.0	0.0	0.0	-1.905
66 15.0'N	0.0	0.0	0.0	0.0	0.0	0.0	0.0	0.0	0.0	0.0	0.0	0.0	0.0	0.0	0.0	0.0	0.0	0.0	0.0	-0.952
66 0.0'N	0.0	0.0	0.0	0.0	0.0	0.0	0.0	0.0	0.0	0.0	0.0	0.0	0.0	0.0	0.0	0.0	0.0	0.0	0.0	0.0
65 45.0'N	0.0	0.0	0.0	0.0	0.0	0.0	0.0	0.0	0.0	0.0	0.0	0.0	0.0	0.0	0.0	0.0	0.0	0.0	0.0	-0.221
65 30.0'N	0.0	0.0	0.0	0.0	0.0	0.0	0.0	0.0	0.0	0.0	0.0	0.0	0.0	0.0	0.0	0.0	0.0	0.0	0.0	-0.441
65 15.0'N	0.0	-0.122	-0.245	0.132	0.508	0.529	0.549	0.334	0.119	0.059	0.0	0.0	0.0	0.0	0.0	0.0	0.0	0.561	1.122	1.308
65 0.0'N	0.0	-0.245	-0.490	0.264	1.017	1.057	1.097	0.667	0.237	0.119	0.0	0.0	0.0	0.0	0.0	0.0	0.0	1.122	2.244	3.056
64 45.0'N	0.188	0.057	-0.074	-0.095	-0.116	0.388	0.892	1.043	1.193	1.358	1.523	1.155	0.787	0.393	0.0	0.0	0.0	1.692	3.384	2.874
64 30.0'N	0.376	0.359	0.342	-0.453	-1.248	-0.281	0.686	1.418	2.149	2.597	3.046	2.310	1.574	0.787	0.0	0.0	0.0	2.262	4.524	2.692
64 15.0'N	0.006	0.289	0.573	0.465	0.356	1.395	2.434	1.804	1.173	0.976	0.780	0.169	-0.442	0.684	1.811	2.301	2.792	4.145	5.499	3.547
64 0.0'N	-0.364	0.220	0.805	1.382	1.960	3.071	4.182	2.190	0.197	-0.644	-1.486	-1.972	-2.459	0.582	3.622	4.603	5.584	6.028	6.473	4.402
63 45.0'N	0.050	0.701	1.352	1.022	0.691	0.138	-0.415	-0.152	0.111	-0.664	-1.439	-0.211	1.018	2.184	3.350	3.985	4.621	3.929	3.236	2.201
63 30.0'N	0.464	1.181	1.899	0.661	-0.577	-2.795	-5.012	-2.493	0.025	-0.684	-1.392	1.551	4.494	3.786	3.078	3.368	3.658	1.829	0.0	0.0
63 15.0'N	0.232	-0.682	-1.596	-1.161	-0.726	-2.800	-4.873	-3.121	-1.369	-0.889	-0.408	1.402	3.214	3.134	3.055	2.636	2.217	1.983	1.750	1.850
63 0.0'N	0.0	-2.546	-5.092	-2.984	-0.875	-2.805	-4.734	-3.749	-2.763	-1.094	0.575	1.254	1.933	2.483	3.032	1.903	0.775	2.137	3.500	3.699
62 45.0'N	0.0	-1.315	-2.631	-1.364	-0.097	-0.579	-1.060	-0.816	-0.571	0.265	1.102	1.312	1.521	1.773	2.026	1.542	1.059	1.889	2.719	2.781
62 30.0'N	0.0	-0.085	-0.169	0.256	0.681	1.648	2.614	2.118	1.621	1.625	1.628	1.369	1.109	1.064	1.019	1.182	1.344	1.641	1.938	1.862
62 15.0'N	4.113	3.393	2.673	2.138	1.603	1.283	0.962	0.994	1.027	0.713	0.399	1.193	1.987	1.848	1.709	1.575	1.442	1.525	1.608	1.592
62 0.0'N	8.225	6.870	5.515	4.020	2.526	0.918	-0.691	-0.129	0.432	-0.200	-0.831	1.016	2.864	2.631	2.398	1.969	1.540	1.408	1.277	1.321
61 45.0'N	5.127	4.519	3.910	3.105	2.299	1.358	0.418	1.060	1.701	0.352	-0.996	0.629	2.255	2.017	1.779	1.326	0.873	0.899	0.924	1.218
61 30.0'N	2.029	2.168	2.306	2.189	2.071	1.799	1.527	2.249	2.970	0.904	-1.162	0.242	1.646	1.403	1.160	0.684	0.207	0.389	0.572	1.115
61 15.0'N	1.099	1.378	1.657	1.898	2.140	1.772	1.404	1.950	2.496	0.512	-1.471	0.200	1.871	1.554	1.236	1.098	0.960	0.573	0.186	0.480
61 0.0'N	0.169	0.588	1.007	1.607	2.208	1.744	1.281	1.651	2.022	0.121	-1.781	0.158	2.096	1.704	1.313	1.513	1.713	0.757	-0.199	-0.156
60 45.0'N	0.085	0.058	0.030	0.526	1.021	0.636	0.251	0.573	0.896	-0.972	-2.840	-0.633	1.574	1.115	0.656	0.757	0.857	0.275	-0.307	-0.443
60 30.0'N	0.0	-0.473	-0.946	-0.556	-0.167	-0.472	-0.778	-0.504	-0.230	-2.065	-3.900	-1.424	1.052	0.526	0.0	0.0	0.0	-0.207	-0.414	-0.730
60 15.0'N	0.0	-0.236	-0.473	-0.417	-0.362	-0.362	-0.363	-0.161	0.041	-1.032	-2.106	0.218	2.542	1.558	0.575	0.627	0.679	0.728	0.777	0.302
60 0.0'N	0.0	0.0	0.0	-0.279	-0.557	-0.252	0.052	0.183	0.313	0.001	-0.312	1.860	4.031	2.590	1.149	1.253	1.358	1.663	1.969	1.334
59 45.0'N	0.0	0.0	0.0	-0.139	-0.279	-0.420	-0.561	0.649	1.859	-0.075	-2.008	-0.110	1.789	1.016	0.244	0.655	1.067	1.094	1.121	0.932
59 30.0'N	0.0	0.0	0.0	0.0	0.0	-0.588	-1.175	1.114	3.404	-0.150	-3.705	-2.079	-0.454	-0.558	-0.661	0.057	0.776	0.525	0.274	0.531
59 15.0'N	0.0	0.0	0.0	0.0	0.0	-0.294	-0.588	1.416	3.420	-0.283	-3.987	-3.616	-3.244	-3.581	-3.917	-1.853	0.211	0.467	0.723	0.425
59 0.0'N	0.0	0.0	0.0	0.0	0.0	0.0	0.0	1.718	3.437	-0.416	-4.269	-5.152	-6.035	-6.604	-7.173	-3.764	-0.354	0.409	1.172	0.319
58 45.0'N	0.0	0.0	0.0	0.0	0.0	0.0	0.0	0.0	0.859	1.718	-0.288	-2.293	-2.731	-3.169	-3.901	-4.634	-3.773	-2.912	-1.286	0.339	0.147
58 30.0'N	0.0	0.0	0.0	0.0	0.0	0.0	0.0	0.0	0.0	0.0	-0.159	-0.317	-0.310	-0.303	-1.199	-2.094	-3.782	-5.470	-2.982	-0.494	-0.026
58 15.0'N	0.0	0.0	0.0	0.0	0.0	0.0	0.0	0.0	0.0	0.0	-0.079	-0.159	-0.455	-0.751	-0.816	-0.882	-2.818	-4.754	-4.450	-4.145	-2.448
58 0.0'N	0.0	0.0	0.0	0.0	0.0	0.0	0.0	0.0	0.0	0.0	0.0	-0.599	-1.198	-0.434	0.331	-1.854	-4.039	-5.917	-7.796	-4.870
57 45.0'N	0.0	0.0	0.0	0.0	0.0	0.0	0.0	0.0	0.0	0.0	0.0	-0.300	-0.599	-0.441	-0.283	-1.252	-2.221	-3.673	-5.125	-4.048
57 30.0'N	0.0	0.0	0.0	0.0	0.0	0.0	0.0	0.0	0.0	0.0	0.0	0.0	0.0	-0.448	-0.896	-0.650	-0.403	-1.428	-2.454	-3.226
57 15.0'N	0.0	0.0	0.0	0.0	0.0	0.0	0.0	0.0	0.0	0.0	0.0	0.0	0.0	-0.224	-0.448	-0.528	-0.609	-0.988	-1.367	-1.577
57 0.0'N	0.0	0.0	0.0	0.0	0.0	0.0	0.0	0.0	0.0	0.0	0.0	0.0	0.0	0.0	0.0	-0.407	-0.814	-0.548	-0.281	0.071
56 45.0'N	0.0	0.0	0.0	0.0	0.0	0.0	0.0	0.0	0.0	0.0	0.0	0.0	0.0	0.0	0.0	-0.204	-0.407	-0.361	-0.315	-0.184
56 30.0'N	0.0	0.0	0.0	0.0	0.0	0.0	0.0	0.0	0.0	0.0	0.0	0.0	0.0	0.0	0.0	0.0	0.0	-0.174	-0.348	-0.439
56 15.0'N	0.0	0.0	0.0	0.0	0.0	0.0	0.0	0.0	0.0	0.0	0.0	0.0	0.0	0.0	0.0	0.0	0.0	-0.087	-0.174	-0.326
56 0.0'N	0.0	0.0	0.0	0.0	0.0	0.0	0.0	0.0	0.0	0.0	0.0	0.0	0.0	0.0	0.0	0.0	0.0	0.0	0.0	-0.213
55 45.0'N	0.0	0.0	0.0	0.0	0.0	0.0	0.0	0.0	0.0	0.0	0.0	0.0	0.0	0.0	0.0	0.0	0.0	0.0	0.0	-0.107
55 30.0'N	0.0	0.0	0.0	0.0	0.0	0.0	0.0	0.0	0.0	0.0	0.0	0.0	0.0	0.0	0.0	0.0	0.0	0.0	0.0	0.0
55 15.0'N	0.0	0.0	0.0	0.0	0.0	0.0	0.0	0.0	0.0	0.0	0.0	0.0	0.0	0.0	0.0	0.0	0.0	0.0	0.0	0.0
55 0.0'N	0.0	0.0	0.0	0.0	0.0	0.0	0.0	0.0	0.0	0.0	0.0	0.0	0.0	0.0	0.0	0.0	0.0	0.0	0.0	0.0

Table A.2

COMPUTED EAST-WEST COMPONENT OF TIDAL/BAROCLINIC RESIDUAL CURRENTS IN THE BERING AND CHUKCHI SEAS (cm/sec)

		171W 0.0'	170W 30.0'	170W 0.0'	169W 30.0'	169W 0.0'	168W 30.0'	168W 0.0'	167W 30.0'	167W 0.0'	166W 30.0'	166W 0.0'	165W 30.0'	165W 0.0'	164W 30.0'	164W 0.0'	163W 30.0'	163W 0.0'	162W 30.0'	162W 0.0'	161W 30.0'
72	0.0'N	-1.437	-1.266	-1.096	-0.587	-0.077	0.348	0.773	1.378	1.983	1.978	1.973	1.914	1.855	2.186	2.517	3.084	3.652	3.727	3.802	3.256
71	45.0'N	-1.127	-0.800	-0.473	-0.436	-0.399	-0.315	-0.231	0.149	0.529	1.458	2.386	2.168	1.950	2.165	2.381	2.546	2.711	2.736	2.760	2.658
71	30.0'N	-0.816	-0.333	0.151	-0.285	-0.720	-0.978	-1.236	-1.080	-0.924	0.938	2.800	2.422	2.045	2.144	2.244	2.008	1.771	1.744	1.717	2.059
71	15.0'N	-0.823	-0.474	-0.125	-0.365	-0.604	-0.232	0.140	-0.162	-0.464	0.016	0.496	-0.102	-0.701	-0.713	-0.724	-0.837	-0.949	-1.330	-1.712	-2.357
71	0.0'N	-0.829	-0.616	-0.402	-0.445	-0.488	0.514	1.515	0.756	-0.003	-0.906	-1.808	-2.627	-3.446	-3.570	-3.693	-3.681	-3.670	-4.405	-5.141	-6.773
70	45.0'N	-0.244	-0.327	-0.409	-0.309	-0.210	0.180	0.570	0.250	-0.070	-0.505	-0.939	-2.006	-3.154	-2.951	-2.749	-2.953	-3.157	-3.770	-4.383	-4.293
70	30.0'N	0.341	-0.038	-0.416	-0.174	0.068	-0.153	-0.374	-0.255	-0.136	-0.103	-0.071	-1.466	-2.861	-2.333	-1.805	-2.224	-2.644	-3.134	-3.625	-1.813
70	15.0'N	0.195	0.426	0.657	0.737	0.816	-0.144	-1.105	-1.442	-1.780	-1.291	-0.802	-0.753	-0.705	-0.533	-0.361	-0.841	-1.322	-1.567	-1.813	-0.906
70	0.0'N	0.050	0.890	1.731	1.647	1.564	-0.135	-1.835	-2.629	-3.424	-2.478	-1.532	-0.060	1.452	1.267	1.083	0.542	0.0	0.0	0.0	0.0
69	45.0'N	-1.557	-0.967	-0.378	-0.203	-0.028	-0.193	-0.359	-0.628	-0.896	-0.716	-0.536	0.095	0.725	0.481	0.236	0.118	0.0	0.0	0.0	0.0
69	30.0'N	-3.165	-2.825	-2.486	-2.052	-1.619	-0.251	1.117	1.374	1.631	1.046	0.461	0.230	-0.001	-0.306	-0.612	-0.306	0.0	0.0	0.0	0.0
69	15.0'N	-2.605	-2.527	-2.449	-2.364	-2.279	-0.909	0.462	0.342	0.221	0.619	1.017	0.925	0.833	0.263	-0.306	-0.153	0.0	0.0	0.0	0.0
69	0.0'N	-2.046	-2.229	-2.412	-2.676	-2.939	-1.566	-0.193	-0.691	-1.189	0.193	1.574	1.620	1.666	0.833	0.0	0.0	0.0	0.0	0.0	0.0
68	45.0'N	-1.809	-1.114	-0.419	-1.297	-2.176	-1.094	-0.012	0.055	0.121	0.454	0.787	0.810	0.833	0.417	0.0	0.0	0.0	0.0	0.0	0.0
68	30.0'N	-1.573	0.001	1.575	0.081	-1.413	-0.622	0.170	0.800	1.430	0.715	0.0	0.0	0.0	0.0	0.0	0.0	0.0	0.0	0.0	0.0
68	15.0'N	-1.530	-0.914	-0.298	-1.159	-2.020	-1.843	-1.666	-0.847	-0.029	-0.014	0.0	0.0	0.0	0.0	0.0	0.0	0.0	0.0	0.0	0.0
68	0.0'N	-1.487	-1.829	-2.171	-2.399	-2.627	-3.064	-3.501	-2.494	-1.488	-0.744	0.0	0.0	0.0	0.0	0.0	0.0	0.0	0.0	0.0	0.0
67	45.0'N	0.492	0.040	-0.411	-0.538	-0.665	-1.459	-2.253	-2.268	-2.282	-1.591	-0.819	-0.381	0.057	0.029	0.0	0.0	0.0	0.0	0.0	0.0
67	30.0'N	2.472	1.910	1.348	1.322	1.297	0.146	-1.006	-2.041	-3.077	-2.357	-1.638	-0.762	0.115	0.057	0.0	0.0	0.0	0.0	0.0	0.0
67	15.0'N	0.924	0.983	1.042	1.754	2.465	1.925	1.384	0.688	-0.008	-0.346	-0.683	-0.350	-0.016	0.043	0.102	0.051	0.0	0.0	0.0	0.0
67	0.0'N	-0.623	0.057	0.737	2.185	3.634	3.704	3.774	3.417	3.060	1.666	0.271	0.063	-0.146	0.028	0.203	0.102	0.0	0.0	0.0	0.0
66	45.0'N	-2.216	-2.114	-2.011	0.357	2.726	2.978	3.231	3.011	2.791	1.724	0.656	0.291	-0.073	0.014	0.102	0.085	0.068	0.034	0.0	0.0
66	30.0'N	-3.809	-4.284	-4.759	-1.470	1.819	2.253	2.688	2.605	2.523	1.781	1.040	0.520	0.0	0.0	0.0	0.068	0.135	0.068	0.0	0.0
66	15.0'N	-1.905	-2.142	-2.380	-0.426	1.527	2.253	2.978	2.120	1.261	0.891	0.520	0.260	0.0	0.0	0.0	0.034	0.068	0.034	0.0	0.0
66	0.0'N	0.0	0.0	0.0	0.617	1.235	2.252	3.269	1.634	0.0	0.0	0.0	0.0	0.0	0.0	0.0	0.0	0.0	0.0	0.0	0.0
65	45.0'N	-0.441	0.253	0.946	1.551	2.156	1.895	1.634	0.817	0.0	0.0	0.0	0.0	0.0	0.0	0.0	0.0	0.0	0.0	0.0	0.0
65	30.0'N	-0.882	0.505	1.892	2.484	3.076	1.538	0.0	0.0	0.0	0.0	0.0	0.0	0.0	0.0	0.0	0.0	0.0	0.0	0.0	0.0
65	15.0'N	1.493	2.011	2.529	1.665	0.802	-0.139	-1.080	-0.540	0.0	0.0	0.0	0.0	0.0	0.0	0.0	0.0	0.0	0.0	0.0	0.0
65	0.0'N	3.868	3.517	3.165	0.846	-1.473	-1.817	-2.161	-1.080	0.0	0.0	0.0	0.0	0.0	0.0	0.0	0.0	0.0	0.0	0.0	0.0
64	45.0'N	2.364	2.909	3.454	1.582	-0.291	-1.181	-2.071	-1.916	-1.761	-0.880	0.0	0.0	0.0	0.0	0.0	0.0	0.0	0.0	0.0	0.0
64	30.0'N	0.860	2.301	3.743	2.317	0.892	-0.544	-1.980	-2.751	-3.521	-1.761	0.0	0.0	0.0	0.0	0.0	0.0	0.0	0.0	0.0	0.0
64	15.0'N	1.596	1.599	1.603	1.098	0.593	-0.047	-0.686	-1.684	-2.683	-1.792	-0.901	-0.180	0.541	0.054	-0.432	-0.650	-0.867	-0.666	-0.464	-0.232
64	0.0'N	2.332	0.898	-0.536	-0.121	0.294	0.451	0.608	-0.618	-1.844	-1.824	-1.803	-0.361	1.082	0.109	-0.865	-1.299	-1.733	-1.331	-0.929	-0.464
63	45.0'N	1.166	0.449	-0.268	0.543	1.353	1.553	1.753	0.883	0.014	-0.249	-0.511	0.352	1.216	0.257	-0.702	-0.883	-1.064	-0.764	-0.464	-0.232
63	30.0'N	0.0	0.0	0.0	1.206	2.413	2.655	2.898	2.385	1.872	1.326	0.781	1.065	1.349	0.405	-0.540	-0.468	-0.395	-0.198	0.0	0.0
63	15.0'N	1.949	2.047	2.146	2.233	2.320	1.525	0.730	0.706	0.682	0.692	0.702	0.688	0.675	0.202	-0.270	-0.234	-0.198	-0.099	0.0	0.0
63	0.0'N	3.899	4.095	4.291	3.259	2.227	0.394	-1.439	-0.973	-0.507	0.057	0.622	0.311	0.0	0.0	0.0	0.0	0.0	0.0	0.0	0.0
62	45.0'N	2.842	2.477	2.112	1.877	1.642	-0.052	-1.745	-0.974	-0.202	0.054	0.311	0.155	0.0	0.0	0.0	0.0	0.0	0.0	0.0	0.0
62	30.0'N	1.786	0.859	-0.068	0.495	1.057	-0.497	-2.052	-0.975	0.103	0.051	0.0	0.0	0.0	0.0	0.0	0.0	0.0	0.0	0.0	0.0
62	15.0'N	1.576	0.752	-0.072	0.313	0.698	-0.173	-1.044	-0.252	0.539	0.270	0.0	0.0	0.0	0.0	0.0	0.0	0.0	0.0	0.0	0.0
62	0.0'N	1.365	0.644	-0.077	0.131	0.339	0.152	-0.036	0.470	0.976	0.488	0.0	0.0	0.0	0.0	0.0	0.0	0.0	0.0	0.0	0.0
61	45.0'N	1.512	1.022	0.532	0.458	0.384	0.396	0.407	0.448	0.488	0.244	0.0	0.0	0.0	0.0	0.0	0.0	0.0	0.0	0.0	0.0
61	30.0'N	1.659	1.400	1.141	0.785	0.430	0.640	0.850	0.425	0.0	0.0	0.0	0.0	0.0	0.0	0.0	0.0	0.0	0.0	0.0	0.0
61	15.0'N	0.773	0.965	1.156	1.052	0.948	0.869	0.789	0.351	-0.087	-0.044	0.0	0.0	0.0	0.0	0.0	0.0	0.0	0.0	0.0	0.0
61	0.0'N	-0.113	0.529	1.172	1.319	1.467	1.097	0.728	0.277	-0.174	-0.087	0.0	0.0	0.0	0.0	0.0	0.0	0.0	0.0	0.0	0.0
60	45.0'N	-0.579	0.044	0.668	0.768	0.868	0.581	0.294	0.200	0.107	0.254	0.402	0.201	0.0	0.0	0.0	0.0	0.0	0.0	0.0	0.0
60	30.0'N	-1.045	-0.441	0.164	0.217	0.269	0.065	-0.140	0.123	0.387	0.596	0.804	0.402	0.0	0.0	0.0	0.0	0.0	0.0	0.0	0.0
60	15.0'N	-0.173	-0.043	0.087	0.188	0.288	0.109	-0.070	0.062	0.194	0.298	0.402	0.201	0.0	0.0	0.0	0.0	0.0	0.0	0.0	0.0
60	0.0'N	0.699	0.355	0.010	0.158	0.307	0.153	0.0	0.0	0.0	0.0	0.0	0.0	0.0	0.0	0.0	0.0	0.0	0.0	0.0	0.0
59	45.0'N	0.743	0.511	0.279	0.388	0.497	0.423	0.349	0.391	0.433	0.419	0.405	0.353	0.301	0.234	0.166	0.065	-0.037	-0.018	0.0	0.0
59	30.0'N	0.788	0.668	0.548	0.618	0.688	0.693	0.697	0.781	0.865	0.837	0.809	0.706	0.603	0.468	0.333	0.130	-0.073	-0.037	0.0	0.0
59	15.0'N	0.127	0.342	0.557	0.442	0.328	0.431	0.534	0.603	0.671	0.528	0.384	0.679	0.974	0.833	0.693	0.562	0.391	0.195	0.0	0.0
59	0.0'N	-0.534	0.016	0.565	0.266	-0.032	0.169	0.372	0.425	0.478	0.219	-0.041	0.652	1.345	1.199	1.053	0.954	0.855	0.427	0.0	0.0
58	45.0'N	-0.046	0.175	0.397	0.129	-0.139	0.331	0.800	0.701	0.601	0.115	-0.371	0.022	0.414	0.490	0.566	0.662	0.759	0.162	-0.436	-0.455
58	30.0'N	0.441	0.335	0.229	-0.009	-0.246	0.492	1.229	0.977	0.725	0.012	-0.701	-0.609	-0.517	-0.219	0.079	0.371	0.663	-0.104	-0.871	-0.910
58	15.0'N	-0.752	-0.559	-0.366	-0.183	-0.000	0.270	0.540	0.859	1.177	0.149	-0.880	-0.998	-1.117	-0.706	-0.296	0.260	0.815	0.106	-0.602	-0.790
58	0.0'N	-1.944	-1.453	-0.961	-0.358	0.246	0.049	-0.149	0.740	1.629	0.285	-1.059	-1.387	-1.716	-1.193	-0.670	0.148	0.967	0.317	-0.333	-0.670
57	45.0'N	-2.971	-2.578	-2.185	-1.243	-0.300	-0.203	-0.105	0.771	1.648	1.240	0.832	-0.049	-0.931	-0.411	0.109	0.572	1.034	1.169	1.303	0.219
57	30.0'N	-3.998	-3.704	-3.409	-2.128	-0.846	-0.454	-0.062	0.803	1.667	2.195	2.724	1.289	-0.146	0.372	0.889	0.995	1.102	2.020	2.939	1.108
57	15.0'N	-1.788	-2.280	-2.773	-2.579	-2.385	-1.421	-0.458	0.449	1.356	1.848	2.340	1.558	0.777	0.690	0.604	0.590	0.577	1.279	1.980	0.861
57	0.0'N	0.423	-0.857	-2.137	-3.031	-3.925	-2.389	-0.853	0.096	1.046	1.501	1.957	1.828	1.700	1.009	0.318	0.186	0.053	0.537	1.021	0.613
56	45.0'N	-0.054	-0.746	-1.437	-2.405	-3.373	-3.325	-3.276	-1.295	0.685	1.732	2.778	2.193	1.609	1.031	0.452	0.434	0.416	0.482	0.549	0.451
56	30.0'N	-0.531	-0.634	-0.738	-1.780	-2.822	-4.260	-5.699	-2.687	0.325	1.962	3.599	2.559	1.518	1.052	0.586	0.682	0.779	0.427	0.076	0.288
56	15.0'N	-0.479	-0.682	-0.885	-0.439	0.007	-1.406	-2.819	-2.836	-2.854	-1.094	0.665	0.169	-0.327	-0.139	0.049	0.427	0.806	0.422	0.038	0.144
56	0.0'N	-0.427	-0.730	-1.032	0.902	2.836	1.449	0.061	-2.986	-6.032	-4.150	-2.269	-2.221	-2.173	-1.331	-0.489	0.172	0.833	0.417	0.0	0.0
55	45.0'N	-0.213	-0.365	-0.516	0.451	1.418	1.431	1.444	-1.714	-4.872	-4.442	-4.012	-3.590	-3.168	-2.715	-2.261	-0.922	0.417	0.208	0.0	0.0
55	30.0'N	0.0	0.0	0.0	0.0	0.0	1.414	2.828	-0.443	-3.713	-4.734	-5.755	-4.959	-4.164	-4.099	-4.034	-2.017	0.0	0.0	0.0	0.0
55	15.0'N	0.0	0.0	0.0	0.0	0.0	0.707	1.414	-0.391	-2.195	-2.980	-3.764	-3.060	-2.357	-2.187	-2.017	-1.009	0.0	0.0	0.0	0.0
55	0.0'N	0.0	0.0	0.0	0.0	0.0	0.0	0.0	-0.339	-0.678	-1.226	-1.773	-1.161	-0.549	-0.275	0.0	0.0	0.0	0.0	0.0	0.0

Table A.3

COMPUTED EAST-WEST COMPONENT OF TIDAL/BAROCLINIC RESIDUAL CURRENTS IN THE BERING AND CHUKCHI SEAS (cm/sec)

		161W 0.0'	160W 30.0'	160W 0.0'	159W 30.0'	159W 0.0'	158W 30.0'	158W 0.0'	157W 30.0'	157W 0.0'	156W 30.0'	156W 0.0'
72	0.0'N	2.709	2.661	2.612	2.052	1.492	0.769	0.047	-2.828	-5.703	-2.851	0.0
71	45.0'N	2.556	2.153	1.750	1.005	0.261	0.032	-0.197	-4.618	-9.040	-4.520	0.0
71	30.0'N	2.402	1.644	0.887	-0.041	-0.969	-0.705	-0.441	-6.409	******	-6.189	0.0
71	15.0'N	-3.002	-2.213	-1.423	-1.624	-1.825	-1.023	-0.220	-3.204	-6.189	-3.094	0.0
71	0.0'N	-8.406	-6.069	-3.732	-3.207	-2.681	-1.341	0.0	0.0	0.0	0.0	0.0
70	45.0'N	-4.203	-3.035	-1.866	-1.603	-1.341	-0.670	0.0	0.0	0.0	0.0	0.0
70	30.0'N	0.0	0.0	0.0	0.0	0.0	0.0	0.0	0.0	0.0	0.0	0.0
70	15.0'N	0.0	0.0	0.0	0.0	0.0	0.0	0.0	0.0	0.0	0.0	0.0
70	0.0'N	0.0	0.0	0.0	0.0	0.0	0.0	0.0	0.0	0.0	0.0	0.0
69	45.0'N	0.0	0.0	0.0	0.0	0.0	0.0	0.0	0.0	0.0	0.0	0.0
69	30.0'N	0.0	0.0	0.0	0.0	0.0	0.0	0.0	0.0	0.0	0.0	0.0
69	15.0'N	0.0	0.0	0.0	0.0	0.0	0.0	0.0	0.0	0.0	0.0	0.0
69	0.0'N	0.0	0.0	0.0	0.0	0.0	0.0	0.0	0.0	0.0	0.0	0.0
68	45.0'N	0.0	0.0	0.0	0.0	0.0	0.0	0.0	0.0	0.0	0.0	0.0
68	30.0'N	0.0	0.0	0.0	0.0	0.0	0.0	0.0	0.0	0.0	0.0	0.0
68	15.0'N	0.0	0.0	0.0	0.0	0.0	0.0	0.0	0.0	0.0	0.0	0.0
68	0.0'N	0.0	0.0	0.0	0.0	0.0	0.0	0.0	0.0	0.0	0.0	0.0
67	45.0'N	0.0	0.0	0.0	0.0	0.0	0.0	0.0	0.0	0.0	0.0	0.0
67	30.0'N	0.0	0.0	0.0	0.0	0.0	0.0	0.0	0.0	0.0	0.0	0.0
67	15.0'N	0.0	0.0	0.0	0.0	0.0	0.0	0.0	0.0	0.0	0.0	0.0
67	0.0'N	0.0	0.0	0.0	0.0	0.0	0.0	0.0	0.0	0.0	0.0	0.0
66	45.0'N	0.0	0.0	0.0	0.0	0.0	0.0	0.0	0.0	0.0	0.0	0.0
66	30.0'N	0.0	0.0	0.0	0.0	0.0	0.0	0.0	0.0	0.0	0.0	0.0
66	15.0'N	0.0	0.0	0.0	0.0	0.0	0.0	0.0	0.0	0.0	0.0	0.0
66	0.0'N	0.0	0.0	0.0	0.0	0.0	0.0	0.0	0.0	0.0	0.0	0.0
65	45.0'N	0.0	0.0	0.0	0.0	0.0	0.0	0.0	0.0	0.0	0.0	0.0
65	30.0'N	0.0	0.0	0.0	0.0	0.0	0.0	0.0	0.0	0.0	0.0	0.0
65	15.0'N	0.0	0.0	0.0	0.0	0.0	0.0	0.0	0.0	0.0	0.0	0.0
65	0.0'N	0.0	0.0	0.0	0.0	0.0	0.0	0.0	0.0	0.0	0.0	0.0
64	45.0'N	0.0	0.0	0.0	0.0	0.0	0.0	0.0	0.0	0.0	0.0	0.0
64	30.0'N	0.0	0.0	0.0	0.0	0.0	0.0	0.0	0.0	0.0	0.0	0.0
64	15.0'N	0.0	0.0	0.0	0.0	0.0	0.0	0.0	0.0	0.0	0.0	0.0
64	0.0'N	0.0	0.0	0.0	0.0	0.0	0.0	0.0	0.0	0.0	0.0	0.0
63	45.0'N	0.0	0.0	0.0	0.0	0.0	0.0	0.0	0.0	0.0	0.0	0.0
63	30.0'N	0.0	0.0	0.0	0.0	0.0	0.0	0.0	0.0	0.0	0.0	0.0
63	15.0'N	0.0	0.0	0.0	0.0	0.0	0.0	0.0	0.0	0.0	0.0	0.0
63	0.0'N	0.0	0.0	0.0	0.0	0.0	0.0	0.0	0.0	0.0	0.0	0.0
62	45.0'N	0.0	0.0	0.0	0.0	0.0	0.0	0.0	0.0	0.0	0.0	0.0
62	30.0'N	0.0	0.0	0.0	0.0	0.0	0.0	0.0	0.0	0.0	0.0	0.0
62	15.0'N	0.0	0.0	0.0	0.0	0.0	0.0	0.0	0.0	0.0	0.0	0.0
62	0.0'N	0.0	0.0	0.0	0.0	0.0	0.0	0.0	0.0	0.0	0.0	0.0
61	45.0'N	0.0	0.0	0.0	0.0	0.0	0.0	0.0	0.0	0.0	0.0	0.0
61	30.0'N	0.0	0.0	0.0	0.0	0.0	0.0	0.0	0.0	0.0	0.0	0.0
61	15.0'N	0.0	0.0	0.0	0.0	0.0	0.0	0.0	0.0	0.0	0.0	0.0
61	0.0'N	0.0	0.0	0.0	0.0	0.0	0.0	0.0	0.0	0.0	0.0	0.0
60	45.0'N	0.0	0.0	0.0	0.0	0.0	0.0	0.0	0.0	0.0	0.0	0.0
60	30.0'N	0.0	0.0	0.0	0.0	0.0	0.0	0.0	0.0	0.0	0.0	0.0
60	15.0'N	0.0	0.0	0.0	0.0	0.0	0.0	0.0	0.0	0.0	0.0	0.0
60	0.0'N	0.0	0.0	0.0	0.0	0.0	0.0	0.0	0.0	0.0	0.0	0.0
59	45.0'N	0.0	0.0	0.0	0.0	0.0	0.0	0.0	0.0	0.0	0.0	0.0
59	30.0'N	0.0	0.0	0.0	0.0	0.0	0.0	0.0	0.0	0.0	0.0	0.0
59	15.0'N	0.0	0.0	0.0	0.0	0.0	0.0	0.0	0.0	0.0	0.0	0.0
59	0.0'N	0.0	0.0	0.0	0.0	0.0	0.0	0.0	0.0	0.0	0.0	0.0
58	45.0'N	-0.474	-0.237	0.0	0.0	0.0	0.0	0.0	0.0	0.0	0.0	0.0
58	30.0'N	-0.949	-0.474	0.0	0.0	0.0	0.0	0.0	0.0	0.0	0.0	0.0
58	15.0'N	-0.978	-0.506	-0.033	0.015	0.062	0.031	0.0	0.0	0.0	0.0	0.0
58	0.0'N	-1.008	-0.537	-0.066	0.029	0.124	0.062	0.0	0.0	0.0	0.0	0.0
57	45.0'N	-0.865	-0.474	-0.083	0.148	0.379	0.202	0.024	0.012	0.0	0.0	0.0
57	30.0'N	-0.723	-0.412	-0.100	0.267	0.633	0.341	0.048	0.024	0.0	0.0	0.0
57	15.0'N	-0.259	-0.000	0.258	0.287	0.317	0.170	0.024	0.012	0.0	0.0	0.0
57	0.0'N	0.206	0.411	0.617	0.308	0.0	0.0	0.0	0.0	0.0	0.0	0.0
56	45.0'N	0.352	0.330	0.308	0.154	0.0	0.0	0.0	0.0	0.0	0.0	0.0
56	30.0'N	0.499	0.250	0.0	0.0	0.0	0.0	0.0	0.0	0.0	0.0	0.0
56	15.0'N	0.250	0.125	0.0	0.0	0.0	0.0	0.0	0.0	0.0	0.0	0.0
56	0.0'N	0.0	0.0	0.0	0.0	0.0	0.0	0.0	0.0	0.0	0.0	0.0
55	45.0'N	0.0	0.0	0.0	0.0	0.0	0.0	0.0	0.0	0.0	0.0	0.0
55	30.0'N	0.0	0.0	0.0	0.0	0.0	0.0	0.0	0.0	0.0	0.0	0.0
55	15.0'N	0.0	0.0	0.0	0.0	0.0	0.0	0.0	0.0	0.0	0.0	0.0
55	0.0'N	0.0	0.0	0.0	0.0	0.0	0.0	0.0	0.0	0.0	0.0	0.0

Table A.4

COMPUTED NORTH-SOUTH COMPONENT OF TIDAL/BAROCLINIC RESIDUAL CURRENTS IN THE BERING AND CHUKCHI SEAS (cm/sec)

	181W 0.0'	180W 30.0'	180W 0.0'	179W 30.0'	179W 0.0'	178W 30.0'	178W 0.0'	177W 30.0'	177W 0.0'	176W 30.0'	176W 0.0'	175W 30.0'	175W 0.0'	174W 30.0'	174W 0.0'	173W 30.0'	173W 0.0'	172W 30.0'	172W 0.0'	171W 30.0'
72 0.0'N	0.549	0.549	0.549	-1.815	-4.179	-0.615	2.950	4.257	5.564	3.800	2.035	1.378	0.722	-0.063	-0.847	-1.514	-2.181	-1.257	-0.333	-1.301
71 45.0'N	0.275	0.275	0.275	-0.907	-2.090	0.154	2.397	3.113	3.829	2.363	0.897	0.156	-0.586	-1.861	-3.137	-2.726	-2.316	-1.132	0.052	-0.647
71 30.0'N	0.0	0.0	0.0	0.0	0.0	0.922	1.844	1.969	2.095	0.927	-0.240	-1.067	-1.893	-3.660	-5.426	-3.939	-2.451	-1.006	0.438	0.007
71 15.0'N	0.0	0.0	0.0	0.0	0.0	0.461	0.922	2.898	4.874	3.077	1.280	-1.143	-3.566	-4.452	-5.338	-2.605	0.129	0.203	0.278	-0.064
71 0.0'N	0.0	0.0	0.0	0.0	0.0	0.0	0.0	3.826	7.652	5.226	2.800	-1.220	-5.239	-5.244	-5.250	-1.271	2.708	1.413	0.119	-0.136
70 45.0'N	0.0	0.0	0.0	0.0	0.0	0.0	0.0	1.554	3.109	0.259	-2.592	-4.819	-7.047	-5.744	-4.440	-1.653	1.135	0.961	0.788	0.228
70 30.0'N	0.0	0.0	0.0	0.0	0.0	0.0	0.0	-0.717	-1.435	-4.709	-7.983	-8.419	-8.855	-6.243	-3.630	-2.034	-0.438	0.510	1.457	0.593
70 15.0'N	3.995	3.995	3.995	2.672	1.349	1.046	0.743	-2.030	-4.803	-5.940	-7.078	-5.484	-3.890	-2.713	-1.536	-1.071	-0.605	0.527	1.660	1.141
70 0.0'N	7.990	7.990	7.990	5.344	2.698	2.092	1.486	-3.342	-8.170	-7.172	-6.173	-2.550	1.074	0.816	0.558	-0.107	-0.773	0.545	1.863	1.688
69 45.0'N	3.628	3.628	3.628	3.095	2.563	0.605	-1.352	-4.224	-7.095	-6.157	-5.218	-3.682	-2.146	-1.705	-1.265	-1.351	-1.437	-0.149	1.139	1.557
69 30.0'N	-0.734	-0.734	-0.734	0.847	2.427	-0.882	-4.191	-5.105	-6.020	-5.141	-4.262	-4.813	-5.365	-4.227	-3.089	-2.595	-2.102	-0.843	0.415	1.425
69 15.0'N	-0.367	-0.205	-0.043	0.142	0.328	-2.362	-5.051	-4.998	-4.944	-4.327	-3.710	-3.770	-3.830	-2.717	-1.605	-0.415	0.776	0.527	0.278	1.466
69 0.0'N	0.0	0.324	0.648	-0.562	-1.771	-3.842	-5.912	-4.890	-3.868	-3.513	-3.157	-2.726	-2.295	-1.208	-0.121	1.766	3.653	1.898	0.142	1.507
68 45.0'N	0.0	0.162	0.324	-0.281	-0.886	-2.921	-4.957	-4.288	-3.620	-2.129	-0.638	-0.690	-0.741	-0.470	-0.198	0.992	2.182	1.566	0.950	1.350
68 30.0'N	0.0	0.0	0.0	0.0	0.0	-2.001	-4.002	-3.687	-3.372	-0.745	1.881	1.347	0.813	0.268	-0.276	0.218	0.712	1.235	1.758	1.194
68 15.0'N	0.0	0.0	0.0	0.0	0.0	-1.000	-2.001	-1.843	-1.686	-2.365	-3.043	-1.930	-0.817	-1.826	-2.835	-1.224	0.387	1.171	1.956	1.897
68 0.0'N	0.0	0.0	0.0	0.0	0.0	0.0	0.0	0.0	0.0	-3.984	-7.967	-5.207	-2.447	-3.921	-5.395	-2.666	0.063	1.108	2.154	2.600
67 45.0'N	0.0	0.0	0.0	0.0	0.0	0.0	0.0	0.0	0.0	-1.992	-3.984	-3.430	-2.876	-3.787	-4.698	-2.843	-0.989	0.259	1.508	1.993
67 30.0'N	0.0	0.0	0.0	0.0	0.0	0.0	0.0	0.0	0.0	0.0	0.0	-1.652	-3.304	-3.653	-4.001	-3.021	-2.041	-0.590	0.861	1.387
67 15.0'N	0.0	0.0	0.0	0.0	0.0	0.0	0.0	0.0	0.0	0.0	0.0	-0.826	-1.652	-1.826	-2.000	-1.510	-1.020	-1.045	-1.069	0.913
67 0.0'N	0.0	0.0	0.0	0.0	0.0	0.0	0.0	0.0	0.0	0.0	0.0	0.0	0.0	0.0	0.0	0.0	0.0	0.0	-1.500	-3.000	0.439
66 45.0'N	0.0	0.0	0.0	0.0	0.0	0.0	0.0	0.0	0.0	0.0	0.0	0.0	0.0	0.0	0.0	0.0	0.0	-0.750	-1.500	1.041
66 30.0'N	0.0	0.0	0.0	0.0	0.0	0.0	0.0	0.0	0.0	0.0	0.0	0.0	0.0	0.0	0.0	0.0	0.0	0.0	0.0	1.643
66 15.0'N	0.0	0.0	0.0	0.0	0.0	0.0	0.0	0.0	0.0	0.0	0.0	0.0	0.0	0.0	0.0	0.0	0.0	0.0	0.0	0.822
66 0.0'N	0.0	0.0	0.0	0.0	0.0	0.0	0.0	0.0	0.0	0.0	0.0	0.0	0.0	0.0	0.0	0.0	0.0	0.0	0.0	0.0
65 45.0'N	0.0	0.0	0.0	-0.128	-0.255	-0.128	0.0	0.0	0.0	0.0	0.0	0.0	0.0	0.0	0.0	0.0	0.0	0.0	0.0	0.0
65 30.0'N	0.0	0.0	0.0	-0.255	-0.510	-0.255	0.0	0.0	0.0	0.0	0.0	0.0	0.0	0.0	0.0	0.0	0.0	0.0	0.0	0.0
65 15.0'N	0.0	0.0	0.0	-0.316	-0.632	-0.316	0.0	-0.022	-0.045	-0.022	0.0	0.0	0.0	0.0	0.0	0.0	0.0	0.0	0.0	0.024
65 0.0'N	0.0	0.0	0.0	-0.377	-0.754	-0.377	0.0	-0.045	-0.089	-0.045	0.0	0.0	0.0	0.0	0.0	0.0	0.0	0.0	0.0	0.049
64 45.0'N	0.0	-0.055	-0.109	-0.010	0.089	-0.105	-0.299	-0.373	-0.448	-0.477	-0.506	-0.253	0.0	0.0	0.0	0.0	0.0	0.443	0.886	0.853
64 30.0'N	0.0	-0.109	-0.219	0.356	0.931	0.167	-0.598	-0.702	-0.807	-0.909	-1.012	-0.506	0.0	0.0	0.0	0.0	0.0	0.886	1.772	1.657
64 15.0'N	0.172	-0.036	-0.243	0.084	0.412	-0.099	-0.609	-0.093	0.422	-0.251	-0.924	-2.168	-3.411	-2.732	-2.054	-1.027	0.0	2.138	4.277	3.111
64 0.0'N	0.344	0.038	-0.267	-0.188	-0.108	-0.364	-0.621	0.515	1.651	0.408	-0.836	-3.829	-6.822	-5.465	-4.107	-2.054	0.0	3.391	6.782	4.565
63 45.0'N	-0.193	0.050	0.292	0.441	0.590	0.973	1.357	1.090	0.824	-1.513	-3.851	-4.773	-5.695	-3.787	-1.878	0.485	2.847	3.479	4.111	2.642
63 30.0'N	-0.729	0.061	0.852	1.070	1.288	2.311	3.335	1.666	-0.003	-3.434	-6.865	-5.717	-4.569	-2.108	0.352	3.023	5.694	3.567	1.440	0.720
63 15.0'N	-0.364	0.955	2.274	1.346	0.417	0.515	0.612	-0.205	-1.023	-2.990	-4.958	-3.136	-1.314	0.748	2.809	3.044	3.280	1.633	-0.015	-0.007
63 0.0'N	0.0	1.848	3.696	1.622	-0.453	-1.281	-2.110	-2.076	-2.042	-2.546	-3.050	-0.554	1.941	3.603	5.265	3.065	0.866	-0.302	-1.469	-0.735
62 45.0'N	0.0	0.535	1.071	-0.374	-1.819	-1.561	-1.303	-0.515	0.274	-0.783	-1.840	0.095	2.031	2.699	3.367	1.461	-0.444	-0.689	-0.934	-0.088
62 30.0'N	0.0	-0.777	-1.555	-2.369	-3.184	-1.840	-0.496	1.047	2.589	0.980	-0.630	0.745	2.120	1.794	1.468	-0.143	-1.754	-1.076	-0.399	0.559
62 15.0'N	0.496	0.108	-0.281	-0.231	-0.180	0.199	0.578	0.533	0.489	0.456	0.424	2.141	3.858	2.736	1.615	0.294	-1.028	-0.386	0.255	0.550
62 0.0'N	0.993	0.993	0.993	1.908	2.823	2.237	1.651	0.019	-1.612	-0.067	1.478	3.536	5.595	3.679	1.762	0.730	-0.302	0.304	0.910	0.541
61 45.0'N	-1.272	-1.272	-1.272	-0.817	-0.362	-0.057	0.249	-0.609	-1.466	0.421	2.308	3.443	4.578	2.539	0.500	-0.019	-0.537	-0.010	0.518	-0.029
61 30.0'N	-3.536	-3.536	-3.536	-3.542	-3.548	-2.350	-1.153	-1.237	-1.321	0.909	3.139	3.350	3.560	1.399	-0.762	-0.767	-0.773	-0.324	0.126	-0.598
61 15.0'N	-2.173	-2.173	-2.173	-2.403	-2.633	-1.680	-0.727	-1.008	-1.288	0.938	3.165	3.581	3.997	1.860	-0.276	-0.611	-0.945	-0.475	-0.005	-0.194
61 0.0'N	-0.809	-0.809	-0.809	-1.263	-1.718	-1.009	-0.300	-0.778	-1.255	0.968	3.191	3.812	4.433	2.321	0.209	-0.454	-1.116	-0.626	-0.135	0.211
60 45.0'N	-0.405	-1.015	-1.625	-1.730	-1.835	-1.473	-1.111	-1.496	-1.882	0.205	2.292	3.245	4.199	2.068	-0.062	-0.310	-0.558	-0.596	-0.634	-0.324
60 30.0'N	0.0	-1.220	-2.441	-2.196	-1.952	-1.937	-1.921	-2.215	-2.509	-0.557	1.394	2.679	3.964	1.816	-0.333	-0.166	0.0	-0.567	-1.133	-0.859
60 15.0'N	0.0	-0.610	-1.220	-1.221	-1.223	-1.560	-1.898	-2.337	-2.776	-0.573	1.629	2.910	4.191	1.597	-0.998	-0.499	0.0	-0.603	-1.206	-0.791
60 0.0'N	0.0	0.0	0.0	-0.246	-0.493	-1.184	-1.874	-2.458	-3.042	-0.589	1.865	3.141	4.418	1.378	-1.663	-0.831	0.0	-0.639	-1.278	-0.722
59 45.0'N	0.0	0.0	0.0	-0.123	-0.246	-0.925	-1.603	-2.510	-3.417	-0.242	2.933	4.470	6.008	2.387	-1.234	-1.160	-1.085	-1.059	-1.033	-0.594
59 30.0'N	0.0	0.0	0.0	0.0	0.0	-0.666	-1.333	-2.562	-3.792	0.105	4.002	5.799	7.597	3.396	-0.806	-1.488	-2.170	-1.479	-0.788	-0.466
59 15.0'N	0.0	0.0	0.0	0.0	0.0	-0.333	-0.666	-1.412	-2.158	0.625	3.408	3.714	4.021	0.730	-2.560	-1.830	-1.100	-0.981	-0.863	-0.599
59 0.0'N	0.0	0.0	0.0	0.0	0.0	0.0	0.0	-0.262	-0.523	1.145	2.814	1.629	0.444	-1.935	-4.313	-2.171	-0.029	-0.483	-0.937	-0.732
58 45.0'N	0.0	0.0	0.0	0.0	0.0	0.0	0.0	-0.131	-0.262	0.183	0.628	0.865	1.102	-0.337	-1.776	-0.701	0.374	0.701	1.027	-0.434
58 30.0'N	0.0	0.0	0.0	0.0	0.0	0.0	0.0	0.0	0.0	-0.778	-1.557	0.102	1.761	1.261	0.761	0.769	0.778	1.884	2.991	-0.135
58 15.0'N	0.0	0.0	0.0	0.0	0.0	0.0	0.0	0.0	0.0	-0.389	-0.778	-0.330	0.118	0.052	-0.013	0.811	1.635	1.817	1.999	-0.292
58 0.0'N	0.0	0.0	0.0	0.0	0.0	0.0	0.0	0.0	0.0	0.0	0.0	-0.763	-1.526	-1.156	-0.787	0.853	2.493	1.750	1.008	-0.449
57 45.0'N	0.0	0.0	0.0	0.0	0.0	0.0	0.0	0.0	0.0	0.0	0.0	-0.381	-0.763	-0.672	-0.581	0.273	1.128	1.125	1.122	-0.375
57 30.0'N	0.0	0.0	0.0	0.0	0.0	0.0	0.0	0.0	0.0	0.0	0.0	0.0	-0.187	-0.374	-0.306	-0.238	0.499	1.236	0.301	
57 15.0'N	0.0	0.0	0.0	0.0	0.0	0.0	0.0	0.0	0.0	0.0	0.0	0.0	0.0	-0.094	-0.187	-0.263	-0.339	0.060	0.459	-0.381
57 0.0'N	0.0	0.0	0.0	0.0	0.0	0.0	0.0	0.0	0.0	0.0	0.0	0.0	0.0	0.0	0.0	-0.220	-0.440	-0.379	-0.318	-0.462
56 45.0'N	0.0	0.0	0.0	0.0	0.0	0.0	0.0	0.0	0.0	0.0	0.0	0.0	0.0	0.0	0.0	-0.110	-0.220	-0.365	-0.509	-0.585
56 30.0'N	0.0	0.0	0.0	0.0	0.0	0.0	0.0	0.0	0.0	0.0	0.0	0.0	0.0	0.0	0.0	0.0	0.0	-0.350	-0.700	-0.709
56 15.0'N	0.0	0.0	0.0	0.0	0.0	0.0	0.0	0.0	0.0	0.0	0.0	0.0	0.0	0.0	0.0	0.0	0.0	-0.175	-0.350	-0.597
56 0.0'N	0.0	0.0	0.0	0.0	0.0	0.0	0.0	0.0	0.0	0.0	0.0	0.0	0.0	0.0	0.0	0.0	0.0	0.0	0.0	-0.484
55 45.0'N	0.0	0.0	0.0	0.0	0.0	0.0	0.0	0.0	0.0	0.0	0.0	0.0	0.0	0.0	0.0	0.0	0.0	0.0	0.0	-0.242
55 30.0'N	0.0	0.0	0.0	0.0	0.0	0.0	0.0	0.0	0.0	0.0	0.0	0.0	0.0	0.0	0.0	0.0	0.0	0.0	0.0	0.0
55 15.0'N	0.0	0.0	0.0	0.0	0.0	0.0	0.0	0.0	0.0	0.0	0.0	0.0	0.0	0.0	0.0	0.0	0.0	0.0	0.0	0.0
55 0.0'N	0.0	0.0	0.0	0.0	0.0	0.0	0.0	0.0	0.0	0.0	0.0	0.0	0.0	0.0	0.0	0.0	0.0	0.0	0.0	0.0

Table A.5

COMPUTED NORTH-SOUTH COMPONENT OF TIDAL/BAROCLINIC RESIDUAL CURRENTS IN THE BERING AND CHUKCHI SEAS (cm/sec)

		171W 0.0'	170W 30.0'	170W 0.0'	169W 30.0'	169W 0.0'	168W 30.0'	168W 0.0'	167W 30.0'	167W 0.0'	166W 30.0'	166W 0.0'	165W 30.0'	165W 0.0'	164W 30.0'	164W 0.0'	163W 30.0'	163W 0.0'	162W 30.0'	162W 0.0'	161W 30.0'
72	0.0'N	-2.269	-1.847	-1.425	-0.818	-0.212	0.152	0.516	0.216	-0.084	0.334	0.751	0.848	0.944	0.882	0.820	0.871	0.922	1.561	2.200	2.177
71	45.0'N	-1.346	-1.230	-1.114	-0.389	0.336	0.445	0.554	0.829	1.103	1.325	1.546	1.206	0.865	1.137	1.409	1.395	1.380	1.824	2.268	2.162
71	30.0'N	-0.423	-0.614	-0.804	0.040	0.884	0.738	0.592	1.441	2.290	2.316	2.341	1.564	0.787	1.392	1.998	1.918	1.839	2.087	2.335	2.148
71	15.0'N	-0.407	-0.327	-0.246	0.322	0.890	0.507	0.124	1.539	2.955	3.131	3.307	2.123	0.939	1.487	2.035	2.052	2.070	2.247	2.424	2.220
71	0.0'N	-0.391	-0.040	0.311	0.604	0.897	0.276	-0.344	1.638	3.620	3.946	4.272	2.682	1.092	1.582	2.072	2.186	2.300	2.407	2.513	2.292
70	45.0'N	-0.331	0.253	0.838	0.643	0.447	0.735	1.022	2.922	4.821	3.623	2.424	0.766	-0.892	0.266	1.425	0.949	0.473	0.911	1.349	0.191
70	30.0'N	-0.272	0.547	1.365	0.681	-0.003	1.193	2.389	4.206	6.023	3.299	0.576	-1.151	-2.877	-1.049	0.779	-0.288	-1.355	-0.585	0.184	-1.910
70	15.0'N	0.621	0.727	0.834	0.456	0.077	1.579	3.080	3.339	3.599	1.052	-1.494	-1.981	-2.467	-0.530	1.406	1.010	0.614	0.353	0.092	-0.955
70	0.0'N	1.514	0.908	0.303	0.230	0.158	1.964	3.771	2.473	1.174	-1.195	-3.564	-2.810	-2.057	-0.012	2.033	2.308	2.583	1.291	0.0	0.0
69	45.0'N	1.974	1.993	2.011	1.274	0.537	1.006	1.476	1.226	0.976	0.138	-0.701	-0.757	-0.812	0.053	0.919	0.898	0.876	0.438	0.0	0.0
69	30.0'N	2.434	3.077	3.720	2.318	0.916	0.048	-0.820	-0.021	0.778	1.470	2.162	1.297	0.432	0.118	-0.196	-0.513	-0.830	-0.415	0.0	0.0
69	15.0'N	2.653	2.656	2.659	1.703	0.747	0.844	0.941	0.798	0.656	0.901	1.146	0.193	-0.761	0.320	1.401	0.493	-0.415	-0.208	0.0	0.0
69	0.0'N	2.871	2.234	1.597	1.087	0.577	1.640	2.702	1.618	0.534	0.332	0.131	-0.911	-1.953	0.523	2.999	1.499	0.0	0.0	0.0	0.0
68	45.0'N	1.751	1.483	1.216	1.729	2.241	3.017	3.792	2.038	0.284	1.000	1.716	0.370	-0.977	0.261	1.499	0.750	0.0	0.0	0.0	0.0
68	30.0'N	0.631	0.733	0.835	2.370	3.905	4.394	4.883	2.458	0.034	1.667	3.301	1.650	0.0	0.0	0.0	0.0	0.0	0.0	0.0	0.0
68	15.0'N	1.838	1.689	1.540	2.201	2.863	3.619	4.374	3.029	1.684	2.179	2.675	1.337	0.0	0.0	0.0	0.0	0.0	0.0	0.0	0.0
68	0.0'N	3.045	2.605	2.245	2.033	1.821	2.843	3.866	3.600	3.334	2.692	2.049	1.024	0.0	0.0	0.0	0.0	0.0	0.0	0.0	0.0
67	45.0'N	2.479	1.843	1.206	1.490	1.774	2.634	3.495	3.430	3.365	3.137	2.909	1.454	0.0	0.0	0.0	0.0	0.0	0.0	0.0	0.0
67	30.0'N	1.913	1.040	0.168	0.947	1.726	2.425	3.124	3.260	3.396	3.582	3.768	1.884	0.0	0.0	0.0	0.0	0.0	0.0	0.0	0.0
67	15.0'N	2.895	1.808	0.721	1.435	2.148	2.078	2.008	3.051	4.093	4.376	4.659	2.777	0.895	0.394	-0.108	-0.054	0.0	0.0	0.0	0.0
67	0.0'N	3.877	2.576	1.275	1.922	2.569	1.731	0.892	2.841	4.790	5.170	5.549	3.670	1.790	0.788	-0.215	-0.108	0.0	0.0	0.0	0.0
66	45.0'N	3.582	2.525	1.469	2.064	2.660	1.628	0.596	1.996	3.396	3.783	4.171	2.714	1.257	0.575	-0.107	-0.098	-0.089	-0.044	0.0	0.0
66	30.0'N	3.287	2.475	1.663	2.207	2.750	1.525	0.300	1.150	2.001	2.397	2.793	1.758	0.723	0.362	0.0	-0.089	-0.177	-0.089	0.0	0.0
66	15.0'N	1.643	1.237	0.832	3.986	7.141	4.780	2.420	2.406	2.392	1.894	1.396	0.879	0.362	0.181	0.0	-0.044	-0.089	-0.044	0.0	0.0
66	0.0'N	0.0	0.0	0.0	5.766	11.532	8.036	4.540	3.662	2.784	1.392	0.0	0.0	0.0	0.0	0.0	0.0	0.0	0.0	0.0	0.0
65	45.0'N	0.0	0.0	0.0	4.801	9.602	7.278	4.954	3.173	1.392	0.696	0.0	0.0	0.0	0.0	0.0	0.0	0.0	0.0	0.0	0.0
65	30.0'N	0.0	0.0	0.0	3.836	7.673	6.521	5.369	2.684	0.0	0.0	0.0	0.0	0.0	0.0	0.0	0.0	0.0	0.0	0.0	0.0
65	15.0'N	0.049	0.914	1.780	4.476	7.173	6.381	5.589	2.795	0.0	0.0	0.0	0.0	0.0	0.0	0.0	0.0	0.0	0.0	0.0	0.0
65	0.0'N	0.098	1.828	3.559	5.117	6.674	6.242	5.810	2.905	0.0	0.0	0.0	0.0	0.0	0.0	0.0	0.0	0.0	0.0	0.0	0.0
64	45.0'N	0.820	2.529	4.237	4.958	5.679	5.845	6.011	4.032	2.053	1.026	0.0	0.0	0.0	0.0	0.0	0.0	0.0	0.0	0.0	0.0
64	30.0'N	1.543	3.229	4.915	4.800	4.685	5.449	6.213	5.159	4.105	2.053	0.0	0.0	0.0	0.0	0.0	0.0	0.0	0.0	0.0	0.0
64	15.0'N	1.945	2.774	3.603	3.124	2.644	3.369	4.094	3.607	3.121	1.948	0.775	0.388	0.0	0.0	0.0	0.0	0.0	-0.530	-1.060	-0.530
64	0.0'N	2.348	2.319	2.291	1.447	0.603	1.289	1.974	2.056	2.137	1.844	1.550	0.775	0.0	0.0	0.0	0.0	0.0	-1.060	-2.120	-1.060
63	45.0'N	1.174	1.160	1.146	1.766	2.387	2.599	2.811	2.766	2.722	2.618	2.514	1.842	1.169	0.805	0.441	0.633	0.824	0.085	-0.653	-0.327
63	30.0'N	0.0	0.0	0.0	2.086	4.172	3.909	3.647	3.477	3.307	3.393	3.478	2.908	2.338	1.610	0.883	1.265	1.648	1.231	0.814	0.407
63	15.0'N	0.0	0.0	0.0	2.355	4.710	4.121	3.533	3.550	3.567	3.122	2.677	3.098	3.519	1.980	0.441	0.633	0.824	0.616	0.407	0.204
63	0.0'N	0.0	0.0	0.0	2.624	5.248	4.333	3.418	3.623	3.827	2.852	1.877	3.288	4.700	2.350	0.0	0.0	0.0	0.0	0.0	0.0
62	45.0'N	0.759	0.817	0.875	1.750	2.625	2.795	2.964	2.940	2.915	1.975	1.035	1.693	2.350	1.175	0.0	0.0	0.0	0.0	0.0	0.0
62	30.0'N	1.517	1.633	1.749	0.876	0.003	1.256	2.510	2.256	2.003	1.098	0.193	0.097	0.0	0.0	0.0	0.0	0.0	0.0	0.0	0.0
62	15.0'N	0.845	0.968	1.092	0.660	0.229	0.908	1.587	1.490	1.393	0.940	0.488	0.244	0.0	0.0	0.0	0.0	0.0	0.0	0.0	0.0
62	0.0'N	0.172	0.303	0.434	0.445	0.455	0.560	0.665	0.724	0.782	0.782	0.782	0.391	0.0	0.0	0.0	0.0	0.0	0.0	0.0	0.0
61	45.0'N	-0.575	-0.134	0.306	0.391	0.476	0.453	0.430	0.719	1.008	0.700	0.391	0.196	0.0	0.0	0.0	0.0	0.0	0.0	0.0	0.0
61	30.0'N	-1.322	-0.572	0.178	0.338	0.498	0.346	0.194	0.714	1.234	0.617	0.0	0.0	0.0	0.0	0.0	0.0	0.0	0.0	0.0	0.0
61	15.0'N	-0.383	-0.120	0.142	0.085	0.027	0.389	0.751	1.024	1.297	0.648	0.0	0.0	0.0	0.0	0.0	0.0	0.0	0.0	0.0	0.0
61	0.0'N	0.556	0.332	0.107	-0.168	-0.443	0.432	1.307	1.333	1.360	0.680	0.0	0.0	0.0	0.0	0.0	0.0	0.0	0.0	0.0	0.0
60	45.0'N	-0.015	-0.125	-0.235	-0.285	-0.334	0.273	0.880	0.751	0.621	0.249	-0.123	-0.062	0.0	0.0	0.0	0.0	0.0	0.0	0.0	0.0
60	30.0'N	-0.585	-0.582	-0.578	-0.402	-0.225	0.114	0.454	0.168	-0.117	-0.182	-0.246	-0.123	0.0	0.0	0.0	0.0	0.0	0.0	0.0	0.0
60	15.0'N	-0.376	-0.381	-0.386	-0.491	-0.597	-0.185	0.226	0.084	-0.059	-0.091	-0.123	-0.378	-0.633	-0.316	0.0	0.0	0.0	0.0	0.0	0.0
60	0.0'N	-0.166	-0.180	-0.194	-0.581	-0.968	-0.485	-0.002	-0.001	0.0	0.0	0.0	-0.633	-1.266	-0.633	0.0	0.0	0.0	0.0	0.0	0.0
59	45.0'N	-0.155	-0.351	-0.548	-0.742	-0.937	-0.753	-0.568	-0.284	0.0	0.0	0.0	-0.649	-1.297	-0.649	0.0	0.0	0.0	0.0	0.0	0.0
59	30.0'N	-0.144	-0.522	-0.901	-0.904	-0.906	-1.020	-1.134	-0.567	0.0	0.0	0.0	-0.665	-1.329	-0.665	0.0	0.0	0.0	0.0	0.0	0.0
59	15.0'N	-0.335	-0.627	-0.919	-1.043	-1.166	-1.266	-1.367	-0.808	-0.249	-0.095	0.060	-0.692	-1.444	-0.793	-0.142	-0.124	-0.106	-0.005	0.097	0.048
59	0.0'N	-0.527	-0.732	-0.938	-1.182	-1.426	-1.513	-1.599	-1.049	-0.499	-0.189	0.120	-0.719	-1.559	-0.921	-0.284	-0.248	-0.212	-0.009	0.193	0.097
58	45.0'N	-1.894	-1.782	-1.671	-1.515	-1.358	-1.400	-1.442	-1.033	-0.624	-0.424	-0.225	-0.652	-1.080	-0.635	-0.190	-0.153	-0.117	-0.193	-0.270	-0.135
58	30.0'N	-3.261	-2.833	-2.404	-1.848	-1.291	-1.288	-1.284	-1.016	-0.748	-0.659	-0.569	-0.586	-0.602	-0.349	-0.096	-0.059	-0.022	-0.377	-0.733	-0.367
58	15.0'N	-2.583	-2.180	-1.777	-1.544	-1.310	-1.252	-1.194	-1.382	-1.569	-1.832	-2.096	-1.538	-0.980	-0.745	-0.509	-0.642	-0.774	-1.012	-1.250	-0.617
58	0.0'N	-1.905	-1.528	-1.150	-1.240	-1.329	-1.217	-1.105	-1.747	-2.389	-3.006	-3.623	-2.491	-1.359	-1.141	-0.923	-1.224	-1.526	-1.647	-1.767	-0.866
57	45.0'N	-1.871	-1.873	-1.875	-1.278	-0.680	-0.842	-1.003	-1.473	-1.942	-2.240	-2.538	-1.926	-1.313	-0.623	0.067	-0.246	-0.559	-0.851	-1.144	-0.588
57	30.0'N	-1.838	-2.219	-2.601	-1.316	-0.031	-0.466	-0.901	-1.198	-1.496	-1.474	-1.453	-1.360	-1.268	-0.105	1.057	0.733	0.409	-0.056	-0.520	-0.309
57	15.0'N	-1.221	-0.976	-0.731	-0.602	-0.472	-0.431	-0.389	-0.706	-1.023	-1.363	-1.703	-1.192	-0.681	0.383	1.448	1.156	0.863	0.315	-0.233	0.216
57	0.0'N	-0.605	0.267	1.138	0.113	-0.913	-0.395	0.123	-0.214	-0.551	-1.252	-1.954	-1.025	-0.095	0.872	1.840	1.579	1.318	0.686	0.055	0.741
56	45.0'N	-0.662	-0.262	0.138	-0.089	-0.317	-0.051	0.214	0.142	0.069	-0.886	-1.841	-1.404	-0.968	-0.097	0.774	0.679	0.585	0.497	0.410	0.788
56	30.0'N	-0.719	-0.791	-0.862	-0.292	0.279	0.293	0.306	0.498	0.689	-0.519	-1.728	-1.784	-1.840	-1.066	-0.291	-0.220	-0.148	0.308	0.765	0.836
56	15.0'N	-0.843	-0.908	-0.974	-0.788	-0.602	-0.579	-0.557	0.534	1.625	1.221	0.817	-0.491	-1.800	-1.178	-0.557	-0.193	0.171	0.377	0.584	0.519
56	0.0'N	-0.968	-1.026	-1.085	-1.283	-1.482	-1.451	-1.420	0.571	2.562	2.962	3.363	0.801	-1.760	-1.291	-0.822	-0.167	0.489	0.447	0.404	0.202
55	45.0'N	-0.484	-0.513	-0.542	-0.642	-0.741	-0.658	-0.575	0.812	2.199	2.066	1.933	-0.947	-3.828	-2.334	-0.841	-0.643	-0.444	-0.121	0.202	0.101
55	30.0'N	0.0	0.0	0.0	0.0	0.0	0.135	0.271	1.054	1.837	1.170	0.504	-2.696	-5.895	-3.378	-0.860	-1.119	-1.377	-0.689	0.0	0.0
55	15.0'N	0.0	0.0	0.0	0.0	0.0	0.068	0.135	0.037	-0.061	0.348	0.756	-0.931	-2.618	-1.245	0.129	-0.280	-0.689	-0.344	0.0	0.0
55	0.0'N	0.0	0.0	0.0	0.0	0.0	0.0	0.0	-0.979	-1.958	-0.475	1.008	0.834	0.659	0.888	1.118	0.559	0.0	0.0	0.0	0.0

Table A.6

COMPUTED NORTH-SOUTH COMPONENT OF TIDAL/BAROCLINIC RESIDUAL CURRENTS IN THE BERING AND CHUKCHI SEAS (cm/sec)

		161W 0.0'	160W 30.0'	160W 0.0'	159W 30.0'	159W 0.0'	158W 30.0'	158W 0.0'	157W 30.0'	157W 0.0'	156W 30.0'	156W 0.0'
72	0.0'N	2.154	1.408	0.662	0.714	0.766	1.100	1.434	4.568	7.703	7.703	7.703
71	45.0'N	2.057	1.093	0.128	0.102	0.076	-0.366	-0.807	3.718	8.242	8.242	8.242
71	30.0'N	1.960	0.778	-0.405	-0.510	-0.614	-1.831	-3.048	2.867	8.782	8.782	8.782
71	15.0'N	2.015	0.516	-0.983	-1.497	-2.012	-2.529	-3.046	0.673	4.391	4.391	4.391
71	0.0'N	2.070	0.255	-1.560	-2.485	-3.410	-3.227	-3.044	-1.522	0.0	0.0	0.0
70	45.0'N	-0.967	-0.874	-0.780	-1.242	-1.705	-1.613	-1.522	-0.761	0.0	0.0	0.0
70	30.0'N	-4.004	-2.002	0.0	0.0	0.0	0.0	0.0	0.0	0.0	0.0	0.0
70	15.0'N	-2.002	-1.001	0.0	0.0	0.0	0.0	0.0	0.0	0.0	0.0	0.0
70	0.0'N	0.0	0.0	0.0	0.0	0.0	0.0	0.0	0.0	0.0	0.0	0.0
69	45.0'N	0.0	0.0	0.0	0.0	0.0	0.0	0.0	0.0	0.0	0.0	0.0
69	30.0'N	0.0	0.0	0.0	0.0	0.0	0.0	0.0	0.0	0.0	0.0	0.0
69	15.0'N	0.0	0.0	0.0	0.0	0.0	0.0	0.0	0.0	0.0	0.0	0.0
69	0.0'N	0.0	0.0	0.0	0.0	0.0	0.0	0.0	0.0	0.0	0.0	0.0
68	45.0'N	0.0	0.0	0.0	0.0	0.0	0.0	0.0	0.0	0.0	0.0	0.0
68	30.0'N	0.0	0.0	0.0	0.0	0.0	0.0	0.0	0.0	0.0	0.0	0.0
68	15.0'N	0.0	0.0	0.0	0.0	0.0	0.0	0.0	0.0	0.0	0.0	0.0
68	0.0'N	0.0	0.0	0.0	0.0	0.0	0.0	0.0	0.0	0.0	0.0	0.0
67	45.0'N	0.0	0.0	0.0	0.0	0.0	0.0	0.0	0.0	0.0	0.0	0.0
67	30.0'N	0.0	0.0	0.0	0.0	0.0	0.0	0.0	0.0	0.0	0.0	0.0
67	15.0'N	0.0	0.0	0.0	0.0	0.0	0.0	0.0	0.0	0.0	0.0	0.0
67	0.0'N	0.0	0.0	0.0	0.0	0.0	0.0	0.0	0.0	0.0	0.0	0.0
66	45.0'N	0.0	0.0	0.0	0.0	0.0	0.0	0.0	0.0	0.0	0.0	0.0
66	30.0'N	0.0	0.0	0.0	0.0	0.0	0.0	0.0	0.0	0.0	0.0	0.0
66	15.0'N	0.0	0.0	0.0	0.0	0.0	0.0	0.0	0.0	0.0	0.0	0.0
66	0.0'N	0.0	0.0	0.0	0.0	0.0	0.0	0.0	0.0	0.0	0.0	0.0
65	45.0'N	0.0	0.0	0.0	0.0	0.0	0.0	0.0	0.0	0.0	0.0	0.0
65	30.0'N	0.0	0.0	0.0	0.0	0.0	0.0	0.0	0.0	0.0	0.0	0.0
65	15.0'N	0.0	0.0	0.0	0.0	0.0	0.0	0.0	0.0	0.0	0.0	0.0
65	0.0'N	0.0	0.0	0.0	0.0	0.0	0.0	0.0	0.0	0.0	0.0	0.0
64	45.0'N	0.0	0.0	0.0	0.0	0.0	0.0	0.0	0.0	0.0	0.0	0.0
64	30.0'N	0.0	0.0	0.0	0.0	0.0	0.0	0.0	0.0	0.0	0.0	0.0
64	15.0'N	0.0	0.0	0.0	0.0	0.0	0.0	0.0	0.0	0.0	0.0	0.0
64	0.0'N	0.0	0.0	0.0	0.0	0.0	0.0	0.0	0.0	0.0	0.0	0.0
63	45.0'N	0.0	0.0	0.0	0.0	0.0	0.0	0.0	0.0	0.0	0.0	0.0
63	30.0'N	0.0	0.0	0.0	0.0	0.0	0.0	0.0	0.0	0.0	0.0	0.0
63	15.0'N	0.0	0.0	0.0	0.0	0.0	0.0	0.0	0.0	0.0	0.0	0.0
63	0.0'N	0.0	0.0	0.0	0.0	0.0	0.0	0.0	0.0	0.0	0.0	0.0
62	45.0'N	0.0	0.0	0.0	0.0	0.0	0.0	0.0	0.0	0.0	0.0	0.0
62	30.0'N	0.0	0.0	0.0	0.0	0.0	0.0	0.0	0.0	0.0	0.0	0.0
62	15.0'N	0.0	0.0	0.0	0.0	0.0	0.0	0.0	0.0	0.0	0.0	0.0
62	0.0'N	0.0	0.0	0.0	0.0	0.0	0.0	0.0	0.0	0.0	0.0	0.0
61	45.0'N	0.0	0.0	0.0	0.0	0.0	0.0	0.0	0.0	0.0	0.0	0.0
61	30.0'N	0.0	0.0	0.0	0.0	0.0	0.0	0.0	0.0	0.0	0.0	0.0
61	15.0'N	0.0	0.0	0.0	0.0	0.0	0.0	0.0	0.0	0.0	0.0	0.0
61	0.0'N	0.0	0.0	0.0	0.0	0.0	0.0	0.0	0.0	0.0	0.0	0.0
60	45.0'N	0.0	0.0	0.0	0.0	0.0	0.0	0.0	0.0	0.0	0.0	0.0
60	30.0'N	0.0	0.0	0.0	0.0	0.0	0.0	0.0	0.0	0.0	0.0	0.0
60	15.0'N	0.0	0.0	0.0	0.0	0.0	0.0	0.0	0.0	0.0	0.0	0.0
60	0.0'N	0.0	0.0	0.0	0.0	0.0	0.0	0.0	0.0	0.0	0.0	0.0
59	45.0'N	0.0	0.0	0.0	0.0	0.0	0.0	0.0	0.0	0.0	0.0	0.0
59	30.0'N	0.0	0.0	0.0	0.0	0.0	0.0	0.0	0.0	0.0	0.0	0.0
59	15.0'N	0.0	0.0	0.0	0.0	0.0	0.0	0.0	0.0	0.0	0.0	0.0
59	0.0'N	0.0	0.0	0.0	0.0	0.0	0.0	0.0	0.0	0.0	0.0	0.0
58	45.0'N	0.0	0.0	0.0	0.0	0.0	0.0	0.0	0.0	0.0	0.0	0.0
58	30.0'N	0.0	0.0	0.0	0.0	0.0	0.0	0.0	0.0	0.0	0.0	0.0
58	15.0'N	0.017	0.450	0.883	0.441	0.0	0.074	0.148	0.074	0.0	0.0	0.0
58	0.0'N	0.034	0.900	1.765	0.883	0.0	0.148	0.295	0.148	0.0	0.0	0.0
57	45.0'N	-0.031	0.983	1.997	1.265	0.533	0.348	0.163	0.089	0.016	0.008	0.0
57	30.0'N	-0.097	1.066	2.229	1.648	1.066	0.549	0.031	0.031	0.031	0.016	0.0
57	15.0'N	0.665	1.084	1.502	1.125	0.748	0.382	0.016	0.016	0.016	0.008	0.0
57	0.0'N	1.427	1.101	0.775	0.603	0.430	0.215	0.0	0.0	0.0	0.0	0.0
56	45.0'N	1.167	0.742	0.316	0.266	0.215	0.108	0.0	0.0	0.0	0.0	0.0
56	30.0'N	0.907	0.382	-0.143	-0.071	0.0	0.0	0.0	0.0	0.0	0.0	0.0
56	15.0'N	0.454	0.191	-0.071	-0.036	0.0	0.0	0.0	0.0	0.0	0.0	0.0
56	0.0'N	0.0	0.0	0.0	0.0	0.0	0.0	0.0	0.0	0.0	0.0	0.0
55	45.0'N	0.0	0.0	0.0	0.0	0.0	0.0	0.0	0.0	0.0	0.0	0.0
55	30.0'N	0.0	0.0	0.0	0.0	0.0	0.0	0.0	0.0	0.0	0.0	0.0
55	15.0'N	0.0	0.0	0.0	0.0	0.0	0.0	0.0	0.0	0.0	0.0	0.0
55	0.0'N	0.0	0.0	0.0	0.0	0.0	0.0	0.0	0.0	0.0	0.0	0.0

BIBLIOGRAPHY

Aagaard, K., L. K. Coachman, and E. Carmarck, "On the Halocline of the Arctic Ocean," *Deep Sea Res.*, Vol. 28A, No. 6, 1981, pp. 529–545.

Abraham, G., "Jet Diffusion in Liquid of Greater Density," *J. of Hydraulic Div., Proc. Am. Soc. of Civil Engr.*, Vol. 86, HY6, 1960, pp. 1–3.

Abramowitz, M., and L. A. Stegun, *Handbook of Mathematical Functions*, National Bureau of Standards, Washington, D.C., 1964.

Ahlnas, K., and G. Wendler, "Sea Ice Observations by Satellite in the Bering, Chukchi, and Beaufort Sea," *Proc. Fifth Inter. Conf. Port and Ocean Eng. Under Arctic Conditions*, POAC 79, Trondheim, Norway, 1979, pp. 313–329.

Aitken, J., "On the Effects of Oil on a Stormy Sea," *Roy. Soc. Edinburgh*, Vol. 12, 1882, pp. 56–75.

Anderson, D.L.T., and P. D. Killworth, "Spin-Up of a Stratified Ocean with Topography," *Deep Sea Res.*, Vol. 24, 1977, pp. 709–732.

Arsen'ev, V. S., *Circulation in the Bering Sea*, No. 13, Akad. Nauka SSSR, Moscow, 1965, pp. 61–65.

Arsen'ev, V. S., *Currents and Water Masses of the Bering Sea*, Akad. Nauka SSSR, Moscow, 1967.

Barry, R. G., "Further Climatological Studies of Baffin Island, Northwest Territories," *Inland Water Directories*, Technical Report 65, Ottawa, Canada, 1972.

Barry, R. G., and A. H. Perry, *Synoptic Climatology*, Methnen and Co., Ltd, London, 1973.

Bowles, P., H. Bums, F. Hudswell, and R.T.P. Wipple, "Sea Disposal of Low Activity Effluent," *Second International Conference on the Peaceful Use of Atomic Energy*, United Nations, New York, 1958, p. 376.

Brower, W. A., H. F. Diaz, A. S. Prechtel, H. W. Searby, and J. L. Wise, *Climatic Atlas of the Outer Continental Shelf Waters and Coastal Regions of Alaska*, Publ. 8-77, AEIDIC, 1977.

Brown, B. G., R. W. Katz, and A. H. Murphy, "Time Series Models to Simulate and Forecast Wind Speed and Wind Power," *J. Climate and Appl. Meteor.*, Vol. 23, 1984, pp. 1184–1195.

Brown, R. A., and W. T. Liu, "An Operational Large-Scale Marine Planetary Boundary Layer Model," *J. Appl. Meteor.*, Vol. 21, 1982, pp. 261–269.

Cardon, V. J., *Specification of the Wind Distribution in the Marine Boundary Layer for Wave Forecasting*, New York University, Geophysical Sciences Lab, TR69–1, 1969.

Coachman, L. K., and K. Aagaard, "Reevaluation of Water Transports in the Vicinity of Bering Strait," in D. W. Hood and J. A. Calder (eds.), *The Eastern Bering Sea Shelf: Oceanography and Resources*, Vol. 1, University of Washington Press, Seattle, Washington, 1981, pp. 95–110.

Colony, R., and A. S. Thorndike, "Sea Ice Strain During 1979," *Sixth Intern. Conf. Port and Ocean Eng. Under Arctic Conditions*, POAC, Quebec, Canada, 1981.

Colony, R., and A. S. Thorndike, "A Estimate of the Main Field of Arctic Sea Ice Motion," *J. Geophys. Res.*, Vol. 89, No. 6, November 1984, pp. 10623–10629.

Conradsen, K., L. B. Nielsen, and L. P. Prahm, "Review of Weibull Statistics for Estimation of Wind Speed Distributions," *J. Climate and Appl. Meteor.*, Vol. 23, 1984, pp. 1173–1183.

Cox, J. C., L. A. Shultz, R. P. Johnson, and R. A. Sheley, "The Transport and Behavior of Oil Spilled In and Under Sea Ice," *Arctic Fac. Report*, No. 460C, 1980.

Danielsen, E. F., W. V. Burt, and M. Rattray, "Intensity and Frequency of Severe Storms in the Gulf of Alaska," *Trans. A.G.U.*, Vol. 38, No. 1, pp. 44–49.

Defant, A., *Physical Oceanography*, The MacMillian Co., New York, 1961.

Dell'osso, L., and L. Bengtsson, "Prediction of a Typhoon Using a Fine Mesh NWP Model," *Tellus*, Vol. 37A, 1985, pp. 97–105.

Drury, W. H., C. Ramsdell, and J. B. French, Jr., "Progress Report to NOAA/OCSEAP," Vol. 11, Anchorage, Alaska, 1981, pp. 175–487.

Dvoryaninov, G. S., and A. V. Prusov, "Theoretical Model of Mass Transport by Gravity and Tidal Waves," *Okeanologiya*, Vol. 18, No. 6, 1978, pp. 640–647.

Ekman, V. W., "On the Influence of the Earth's Rotation on Ocean Currents," *Ark. Math. Astr. Fysik.* Kong, Su. Vetenskap. Akad., Stockholm, Vol. 2, No. 11, 1905, p. 52.

Elliott, A. J., "Measurements of the Turbulence in an Abyssal Boundary Layer," *J. Phys. Ocean.*, Vol. 14, No. 11, 1984, pp. 1779–1786.

Essenwanger, O.M., "Analyzed Procedures for the Quality of Control of Meteorological Data," *Meteor. Monogr.*, Am. Meteor. Soc., No. 33, pp. 141–147.

Fan, L. N., and N. H. Brooks, *Numerical Solution of Turbulent Buoyant Jet Problems*, Keck Lab., Report No. KH-R-18, California Institute of Technology, 1969.

Favorite, F., "The Alaskan Stream," *Inter. N. Pac. Fish. Comm. Bull.*, Vol. 21, 1967, p. 20.

Favorite, F., A. J. Dodimimead, and K. Nasu, "Oceanography of the Subarctic Pacific Region," *Inter. N. Pac. Fish Comm. Bull.*, Vol. 33, 1976, p. 187.

Fay, J. A., and D. P. Hoult, "Physical Processes in the Spread of Oil on a Water Surface," U.S. Coast Guard R&D Report No. 714107/A/001, 1971.

Finzi, G., P. Bonelli, and G. Bacci, "A Statistic Model of Surface Wind for Air Quality Control Processes," *J. Climate and Appl. Meteor.*, Vol. 23, 1984, pp. 1354–1361.

Fisher N. I., Comment on "A Method for Estimating the Standard Deviation of Wind Directions," *J. Appl. Meteor.*, Vol. 22, 1983, p. 1971.

Fisher, N. I., and T. Lewis, "Estimating the Common Mean Direction of Several Circular or Spectral Distributions with Differing Dispersions," *BIOMETRIKA*, Vol. 70, 1983, pp. 333–341.

Franklin, B., "Of the Stilling of Waves by Means of Oil," in J. Sparks (ed.), *The Works of Benjamin Franklin*, Childs and Peterson Books, Philadelphia, Pennsylvania, 1840.

Gabriel, K. R., and J. Newmann, "On a Distribution of Weather Cycles by Lengths," *Quart. J. R. Meteor. Soc.*, Vol. 83, 1957, pp. 375-380.

Gabriel, K. R., and J. Newmann, "A Markov Chain Model for Daily Rainfall Occurrence at Tel Aviv," *Quart. J. R. Meteor. Soc.*, Vol. 88, 1962, pp. 90–95.

Garratt, J. R., "Review of Drag Coefficients over Oceans and Continents," *Mon. Wea. Rev.*, Vol. 105, 1977, pp. 915–929.

Gordienko, P., "Arctic Ice Drift," *Proc. Conf. on Arctic Sea Ice*, Published by the National Academy of Sciences and the National Research Council, Washington, D.C., 1958, pp. 210–220.

Gordon, R. L., "Internal Wave Climate near the Coast of Northwest Africa during JOINT-1," *Deep Sea Res.*, Vol. 25, 1978, pp. 625–643.

Harleman, D.R.F., and G. H. Jirka, "Buoyant Discharge from Submerged Multiport Diffusers," *Coastal Engineering*, Vol. 14, 1974, pp. 2180–2198.

Harris, R. A., *Manual of Tides*, Report of the Superintendent, U.S. Coast and Geodetic Survey, Washington, D.C, 1904, p. 313.

Hasting, C., *Approximations for Digital Computers,* Princeton University Press, 1955.

Heathershaw, A. D., "The Turbulent Structure of the Bottom Boundary Layer in a Tidal Current," *Geophys. J. Roy. Astron. Soc.*, Vol. 58, 1979, pp. 395–430.

Hesse, L., "On the Surface to Geostrophic Wind Relationship at Sea and the Stability of Dependence of the Resistance Law," *Beitr. Phys. Atmosph.*, Vol. 47, 1974, p. 45.

Hesse, L., and V. Wagner, "On the Relationship Between Geostrophic and Surface Wind at Sea," *Mon. Wea. Rev.*, Vol. 99, 1971, pp. 255–259.

Hibler, W. D. III., "A Dynamic Thermodynamic Sea Ice Model," *Phys. Oceano.*, Vol. 9, No. 7, 1979, pp. 815–846.

Hibler, W. D., W. F. Weeks, and S. J. Mock, "Statistical Aspects of Sea-Ice Ridge Distributions," *J. Geophys. Res.*, Vol. 77, No. 30, 1972, pp. 5954–5970.

Hinze, J. O., *Turbulence,* McGraw Hill, New York, 1959.

Hirst, E., "Buoyant Jets Discharged to Quiescent Stratified Ambients," *J. Geophys. Res.*, Vol. 76, No. 30, 1971.

Holl, M., and B. Mendenhall, "FIB-Fields by Information Bending," *Naval Fleet Numerical Weather Central.*, Proj. M-167, Final Report, 1971.

Holt, D. P., "Oil Spreading on the Sea," *Annual Review, Fluid Mechanics,* Vol. 4, 1972, pp. 341–368.

Hunt, J. N., and F. Johns, "Currents Induced by Tides and Gravity Waves," *Tellus,* Vol. 15, No. 4, 1963.

Ichiye, T., "The Theory of Turbulence," *Oceanographical Magazine,* Vol. 3, 1951, pp. 83–87.

Jenne, R. L., *Data Sets for Meteorological Research,* National Center for Atmospheric Research, Boulder, Colorado, TN/1A-111, 1975.

Johns, F., "On the Mass Transport Induced by Oscillatory Flow in a Turbulent Boundary Layer," *J. Fluid Mech.*, Vol. 43, Part 1, 1970.

Joppe, K., *Turbulence Models for Horizontal Layered Flow,* Delft Hydraulics Laboratory/Technological University, S656 (in Dutch), Delft, Netherlands, 1985.

Jowett, J., and D. Vere-Jones, "The Prediction of Point Processes," in P.A.W. Lewis (ed.), *Stochastic Point Processes,* J. Wiley Co., New York, 1972.

Kerr, R. A., "Fingers of Salt Help Mix the Sea," *Science,* Vol. 211, 1981, pp. 155–157.

Kinder, T. H., *The Hydrographic Structure over the Continental Shelf near Bristol Bay,* Department of Oceanography, University of Washington, Vol. 11, M77-3, 1977.

Kinder, T., L. K. Coachman, and J. A. Galt, "The Bering Slope Current System," *J. Phys. Oceano.*, Vol. 5, 1975, pp. 231–245.

Kinder, T., J. D. Schumacher, and D. V. Hansen, "Observation of a Baroclinic Eddy: An Example of Mesoscale Variability in the Bering Sea," *J. Phys. Oceano.*, Vol. 10, No. 8, 1980, pp. 1227–1245.

Kirstein, B. E., J. R. Payne, and R. T. Redding, *Multivariate Analysis of Petroleum Weathering in the Marine Environment Sub-Arctic,* NOAA, OCSEAP, Report No. 22, Anchorage, Alaska, 1984.

Klein, W. H., "Principal Tracks and Mean Frequencies of Cyclone and Anticyclones in the Northern Hemisphere," U.S. Weather Bureau, Research Paper No. 40, 1957.

Koh, R.C.Y., and N. H. Brooks, "Fluid Mechanics of Waste Water Disposal in the Ocean," *Annual Rev. of Fluid Mech., 1975.*

Kolmogoroff, A. N., "A Refinement of Previous Hypotheses Concerning the Local Structure of Turbulence in a Viscous Incompressible Fluid at High Reynolds Number," *J. Fluid Mech.*, Vol. 13, No. 1, 1962, pp. 82–85.

Kranenberg, C., "Wind-Induced Entrainment in a Stably-Stratified Fluid," *J. Fluid Mech.*, Vol. 145, 1984.

Kranenberg, C., *A K-Model for Stably-Stratified Turbulent Flow, Part 1, Formulation,* Report No. 4–85, Laboratory of Fluid Mechanics, Department of Civil Engineering, Delft University of Technology, Delft, Netherlands, 1985.

Kondo, J., "Air-Sea Bulk Transfer Coefficients in Diabatic Condition," *Boundary Layer Meteor.*, Vol. 9, 1975, pp. 91–112.

Kovacs, A., "Sea Ice Thickness Profiling and Under Ice Oil Entrapment," *Proc. Ninth Annual Offshore Tech. Conf.*, OTC, Houston, Texas, 1977, p. 2949.

Kovacs, A., "Oil Pooling Under Sea Ice," *Environmental Assessment of the Alaskan Continental Shelf,* Vol. 8, 1979, pp. 310–353.

Kovacs, A., R. M. Morey, and D. Cundy, "Oil Pooling Under Sea Ice," *Environmental Assessment of the Alaskan Continental Shelf, Annual Report,* Vol. 5, 1980, pp. 333–339.

Kozo, T., personal communication, 1984.

Kusunoki, K., J. Mugurama, and K. Higuchi, *Oceanographic Observations at Fletcher's Ice Island (T-3) in the Arctic Ocean in 1959–1960,* Sci. Report No. 4, AFCRL-62-479, GRD, Air Force Cambridge Research Laboratory, Bedford, Massachusetts, 1962.

Lamb, H., *Hydrodynamics,* Dover Publishing, New York, 1945.

Lambert, R. B., "On the Vertical Transport Due to Fingers in Double Diffusion Convection," *J. Fluid Mech.*, Vol. 54, 1972, pp. 627–640.

Langleben, M. P., "A Study of the Roughness Parameters of Sea Ice from Wind Profiles," *J. Geophys. Res.*, Vol. 77, No. 30, 1972, pp. 5935–5944.

Langleben, M. P., "Water Drag Coefficient of First-Year Sea Ice," *J. Geophys. Res.*, Vol. 87, No. C1, 1982, pp. 573–578.

Laufer, J., *The Structure of Turbulence in Fully Developed Pipe Flow,* National Advisory Commission on Aeronautics, TR-1174, Washington, D.C., 1954.

Launder, B. E., and D. B. Spalding, *Mathematical Models of Turbulence,* Academic Press, New York, 1972.

Leendertse, J. J., R. C. Alexander, and S. K. Liu, *A Three-Dimensional Model for Estuaries and Coastal Seas: Vol. 1, Principles of Computation,* The RAND Corporation, R-1417-OWRR, December 1973.

Leendertse, J. J., and S. K. Liu, *A Three-Dimensional Model for Estuaries and Coastal Seas: Vol. II, Aspects of Computation,* The RAND Corporation, R-1764-OWRT, June 1975.

Leendertse, J. J., and S. K. Liu, *A Three-Dimensional Model for Estuaries and Coastal Seas: Vol. IV, Turbulent Energy Computation,* The RAND Corporation, R-2187-OWRT, May 1977.

Linden, P. F., "On the Structure of Salt Fingers," *Deep Sea Res.*, Vol. 20, 1973, pp. 325–340.

List, E. J., and J. Imberger, "Turbulent Entrainment in Buoyant Jets and Plumes," *Proc. J. Hydro. Div.*, Vol. 99, 1973, p. 1461.

Liu, S. K., and A. B. Nelson, *A Three-Dimensional Model for Estuaries and Coastal Seas: Vol. V, Turbulent Energy Program,* The RAND Corporation, R-2188-OWRT, May 1977.

Liu, S. K., and J. J. Leendertse, "Multidimensional Numerical Models of Estuaries and Coastal Seas," *Advances in Hydroscience,* Vol. II, Academic Press, New York, 1978, pp. 95–164.

Liu, S. K., and J. J. Leendertse, *A Three-Dimensional Model for Estuaries and Coastal Seas: Vol. VI, Bristol Bay Simulations,* The RAND Corporation, R-2405-NOAA, September 1979.

Liu, S. K., and J. J. Leendertse, "A 3-D Oil Spill Model With and Without Ice Cover," *Mechanics of Oil Slicks*, Association Amicale des Ingenieurs, and International Association for Hydraulic Research, Paris, France, 1981a, pp. 247–265.

Liu, S. K., and J. J. Leendertse, "A Three-Dimensional Model of Norton Sound Under Ice Cover," *Proc. Sixth Inter. Conf. Port and Ocean Eng. Under Arctic Conditions*, POAC, Quebec, Canada, 1981b, pp. 433–443.

Liu, S. K., and J. J. Leendertse, "Three-Dimensional Model of Bering and Chukchi Sea," *Coastal Engineering*, Vol. 18, American Society of Civil Engineers, New York, 1982, pp. 598–616.

Liu, S. K., and J. J. Leendertse, "A Three-Dimensional Model of Beaufort Sea," *Coastal Engineering*, Vol. 19, American Society of Civil Engineering, New York, 1984.

Liu, S. K., and J. J. Leendertse, "A Three-Dimensional Model of the Gulf of Alaska," *Coastal Engineering*, American Society of Civil Engineering, New York, 1987.

Mackay, D., and Medir, "The Interfacial Behavior of Oil Under Ice," *Canadian J. of Chem. Engineering*, Vol. 54, February 1976.

Macklin, S. A., "Wind Drag Coefficient over First-Year Sea Ice in the Bering Sea," *J. Geophys. Res.*, Vol. 88, No. C5, 1983, pp. 2845–2852.

Macklin, S. A., C. H. Pease, and R. M. Reynolds, *Bering Air-Sea Ice Study* (BASICS), NOAA-ERL-PMEL-52, Seattle, Washington, 1984.

Macklin, S. A., R. L. Brown, J. Gray, and R. L. Lindsay, *METLIB-II—A Program Library for Calculating and Plotting Atmospheric and Oceanic Fields*, NOAA, ERL PMEL-54, Seattle, Washington, 1984.

Martin, S., *The Seasonal Variation of Oil Entrainment in First-Year Arctic Sea Ice, A Comparison of NORCOR/OCS Observations*, Department of Oceanology, University of Washington, March 1977.

Martin, S., P. Kauffman, and S. Soltar, *Field Report on March Field Traverse of Ice Temperature, Salinity and Thickness in Norton Sound*, Department of Oceanography, University of Washington, Special Report, September 1978.

McWilliams, B., and D. Sprevak, "The Estimation of the Parameters of the Distribution of Wind Speed and Direction," *Wind Engineering*, Vol. 4, No. 4, 1980, pp. 227–238.

McWilliams, B., and D. Sprevak, "Stochastic Model of Wind Speed and Direction," in O. D. Anderson (ed.), *Time Series Analysis: Theory and Practice*, Vol. 7, Elsevier Science Publisher, Amsterdam, Netherlands, 1985, pp. 195–203.

Mofjeld, H. O., "Effects of Vertical Viscosity on Kelvin Waves," *J. Phys. Oceano.*, Vol. 10, 1980, pp. 1040–1050.

Mofjeld, H. O., "Recent Observations of Tides and Tidal Currents from the Northeastern Bering Sea Shelf," PMEL/NOAA Technical Report, PMEL-57, Seattle, Washington, 1984.

Mofjeld, H. O., and J. D. Schumacher, "Residual Tidal Currents and Current Records from the Eastern Bering Sea Shelf," PMEL/NOAA, Seattle, Washington, 1983.

Mofjeld, H. O., and J. W. Lavelle, "Bottom Boundary Layer Studies in Tidally-Dominated Regimes," XVIII General Assembly of the Union of Geodesy and Geophysics, Hamburg, Federal Republic of Germany, IAPSO Programme and Abstracts, 1983.

Mofjeld, H. O., J. D. Schumacher, and D. J. Pashinski, *Theoretical and Observed Profiles of Tidal Currents at Two Sites on the Southeastern Bering Shelf*, NOAA Technical Memorandum, ERL PMEL-62, Seattle, Washington, 1984.

Monin, A. S., and A. M. Yaglom, "Statistical Fluid Mechanics," *Mechanics of Turbulence*, Vol. 2, Springer-Verlag, Berlin, 1975.

Mountain, D. G., L. K. Coachman, and K. Aagaard, "On the Flow Through Barrow Canyon," *J. Phys. Oceano.*, Vol. 6, 1976, pp. 461–470.

Muench, R. D., and K. Ahlnas, "Ice Movement and Distribution in the Bering Sea from March to June 1974," *J. Geophys. Res.*, Vol. 81, No. 24, 1976, pp. 4467–4476.

Muench, R. D., and J. D. Schumacher, *Physical Oceanographic and Meteorological Conditions in the Northwestern Gulf of Alaska,* NOAA Technical Memorandum ERL PMEL-22, Seattle, Washington, 1980.

Muench, R. D., J. D. Schumacher, and C. A. Pearson, *Circulation in the Lower Cook Inlet, Alaska,* NOAA Technical Memorandum ERL PMEL-28, Seattle, Washington, 1981.

Muench, R. D., and J. D. Schumacher, "On the Bering Sea Ice Edge Front," *J. Geo. Res.*, Vol. 90, No. C2, 1985, pp. 3185–3197.

Munk, W. H., G. C. Ewing, and R. R. Revelle, "Diffusion in Bikini Lagoon," *Trans. A.G.U.*, 1949, pp. 59–66.

Munk, W. H., and G. F. Carrier, "On the Wind-Driven Circulation in Ocean Basins of Various Shapes," *Tellus,* Vol. 2, 1950, pp. 158–167.

Murphy, D. L., P. A. Tebeau, and L. M. Lissuer, *Long-Term Movement of Satellite-Tracked Buoys in the Beaufort Sea,* Office of Research and Development, U.S. Department of Transportation, CG-D-48-82, 1981.

Murray, S. P., "Trajectories and Speeds of Wind-Driven Currents Near the Coast," *J. Phys. Oceano.*, Vol. 5, 1975, pp. 347–360.

Mysak, L. A., R. D. Muench, and J. D. Schumacher, "Baroclinic Instability in a Down Stream Varying Channel: Shelikof Strait, Alaska," *J. Phys. Oceano.*, Vol. 11, No. 7, 1981, pp. 950–969.

National Academy of Sciences, *Petroleum in the Marine Environment,* National Academy of Science, Washington, D.C., 1975.

Neumann, G., *Ocean Currents,* Elsevier Publishing Co., New York, 1968.

Neumann, G., and J. W. Pierson, Jr., *Principle of Physical Oceanography,* Prentice Hall, Englewood Cliffs, New Jersey, 1966.

Neyman, J., and E. L. Scott, "A Theory of the Spatial Distribution of Galaxies," *Astrophys. J.*, Vol. 116, 1952, pp. 144–163.

Niebauer, H. J., J. Roberts, and T. C. Royer, "Shelf Break Circulation in the Northern Gulf of Alaska," *J. Geophys. Res.*, Vol. 86, 1981, pp. 4231–4242.

Oboukhov, A. M., "Some Special Features of Atmospheric Turbulence," *J. Fluid Mechanics,* Vol. 13, No. 1, 1962.

Okubo, A., "Equation Describing the Diffusion of an Introduced Pollutant in a One-Dimensional Estuary," *Studies on Oceanography,* Tokyo, 1964, pp. 216–226.

Overland, J. E., R. A. Brown, and C. D. Mobley, *METLIB—A Program Library for Calculating and Plotting Marine Boundary Layer Wind Fields,* NOAA Technical Memorandum ERL PMEL-20, 1980.

Overland, J. E., "Progress Report on the Observed Wind over Norton Sound, Alaska to NOAA/OCSEAP," Anchorage, Alaska, 1980.

Overland, J. E., R. Reynolds, and C. H.Pease, "A Model of the Atmospheric Boundary Layer Over the Marginal Ice Zone," *J. Geophys. Res.*, Vol. 88, C5, 1983, pp. 2836–2840.

Overland, J. E., H. O. Mofjeld, and C. H. Pease, "Wind-Driven Ice Drift in a Shallow Sea," *J. Geophys. Res.*, Vol. 89, No. C4, 1984, pp. 6525–6531.

Ovsiyenko, S. N., "Numerical Modelling of the Drift of Ice," *Izvestiya, Atmo. and Oceanic Physics,* Vol. 12, No. 11, 1976, pp. 1201–1206.

Parmerter, R. R., and M. D. Coon, "Model of Pressure Ridge Formation in Sea Ice," *J. Geophys. Res.*, Vol. 77, No. 33, 1972, pp. 6565–6575.

Payne, J. R., *A Review of the Formation and Behavior of Water-in-Oil Emulsion (mousse) from Spilled Petroleum, and Tar Ball Distributions Chemistries and Fates in the World's Oceans,* National Academy of Sciences, Ocean Sciences Board Workshop, Clearwater Beach, Florida, 1981.

Payne, J. R., B.E. Kirstein, G. D. McNabb, J. L. Lamback, C. deOliveira, and W. Hom, "Multivariate Analysis of Petroleum Hydrocarbon Weathering in the Subarctic Environment," *Proc. 1983 Oil Spill Conference,* pp. 423–434.

Pearson, C. A., H. O. Mofjeld, and R. B. Tripp, "Tides of the Eastern Bering Sea Shelf," in D. W. Hood and J. A. Calder (eds.), *The Eastern Bering Sea Shelf: Oceanography and Resources,* Vol. 1, University of Washington Press, Seattle, Washington, 1981a, pp. 111–130.

Pearson, C. A., J. D. Schumacher, and R. D. Muench, "Effects of Wave-Induced Mooring Noise on Tidal and Low Frequency Current Observations," *Deep Sea Res.*, Vol. 28A, No. 10, 1981b, pp. 1223–1229.

Pease, C. H., S. A. Salo, and J. E. Overland, "Drag Measurements for the First-Year Ice over a Shallow Sea," *J. Geophys. Res.*, Vol. 88, C5, 1983, pp. 2853–2862.

Pease, C. H., and J. E. Overland, "An Atmospherically Driven Sea-Ice Model for the Bering Sea," *Am. J. of Glaciology,* Vol. 5, 1984, pp. 111–114.

Pitman, R. W., *Oceanographic Data from the Bering, Chukchi and Beaufort Sea,* Report to NOAA, WASC-83-00114, Brown and Caldwell, Anchorage, Alaska, 1984.

Plutchak, N. B., and R. L. Kolpack, "Numerical Simulation of Oil Spreading on Water," *Mechanics of Oil Slicks,* Int. Assoc. for Hydraulic Research, Paris, France, 1981.

Pritchard, R. S., "An Elastic-Plastic Constitutive Law for Sea Ice," *J. of Appl. Mechanics,* June 1975, pp. 379–384.

Pritchard, R. S., "Beaufort Sea Ice Motions," in P. W. Barnes, D. M. Schell, and E. Reimnitz, (eds.), *The Alaskan Beaufort Sea Ecosystem and Environments,* Academic Press, New York, 1984, pp. 95–113.

Putnins, P., "The Sequences of Baric Pressure Patterns over Alaska," *Studies on the Meteorology of Alaska,* Environmental Data Service, ESSA, Washington, D.C., 1966.

Reed, R. K., "Flow of the Alaskan Stream and Its Variations," *Deep Sea Res.*, Vol. 31, No. 4, 1984, pp. 369–386.

Reed, R. K., and J. D. Schumacher, "Additional Current Measurements in the Alaskan Stream Near Kodiak Island," *J. of Phys. Oceano.*, Vol. 14, No. 7, 1984, pp. 1239–1246.

Reiner, R. W., "Ice Breakout in the Bering Strait," M.S. Thesis, College of Engineering, University of Washington, Seattle, Washington, 1979.

Reynolds, M., and C. H. Pease, *Drift Characteristics of Northeastern Bering Sea During 1982,* NOAA, Tech. Memo ERL, PMEL-55, 1982.

Richardson, L. F., "Atmospheric Diffusion Shown on a Distance-Neighbor Graph," *Proc. Roy. Soc. London,* Vol. A110, pp. 709–727.

Richardson, L. F., and H. Stommel, "Note on Eddy Diffusion at Sea," *J. of Meteor.*, Vol. 5, pp. 234–240.

Riera, J. D., A. J. Viollaz, and J. C. Reimundin, "Some Recent Results on Probabilistic Models of Extreme Wind Speed," *J. of Indust. Aerodynamics,* Vol. 2, 1977, pp. 271–287.

Rodi, W., "Turbulence Models and Their Application in Hydraulics," *International Assoc. for Hydraulic Res.*, 1980.

Rodriguez, E., and R. E. Huschke, *The RAND Weather Data Bank (RAWDAB): An Evolving Base of Accessible Weather Data,* The RAND Corporation, R-1269-PR, March 1974.

Royer, T. C., and W. J. Emery, "Circulation in the Bering Sea 1982–83, Based on Satellite-Tracked Drifter Observations," *J. of Phys. Oceanography,* Vol. 14, 1984, pp. 1914–1920.

Salo, S. A., J. D. Schumacher, and L. K. Coachman, *Winter Currents on the Eastern Bering Sea Shelf,* NOAA/PMEL Technical Report, Seattle, Washington, 1983.

Schumacher, J. D., R. K. Reed, M. Grigsby, and D. Dreves, *Circulation and Hydrography Near Kodiak Island, September to November, 1977,* NOAA Technical Memorandum ERL PMEL-13, U.S. Government Printing Office, Washington, D.C., 1979-0-677-072/1279.

Schumacher, J. D., T. H. Kinder, D. J. Pashinski, and R. L. Charnell, "A Structure Front Over the Continental Shelf of the Eastern Bering Sea," *J. Phy. Oceano.,* Vol. 9, No. 1, 1979, pp. 79–87.

Schumacher, J. D., and R. D. Muench, *Physical Oceanography and Meteorological Conditions in the Northwest Gulf of Alaska,* NOAA, TM-ERL-PMEL-22, Seattle, Washington, October 1980.

Schumacher, J. D., and R. K. Reed, "Coastal Flow in the Northwest Gulf of Alaska: The Kenai Current," *J. Geo. Res.,* Vol. 85, No. C11, 1980, pp. 6680–6688.

Schumacher, J. D., C. A. Pearson, and J. E. Overland, "On Exchange of Water Between the Gulf of Alaska and the Bering Sea Through the Unimak Pass," *J. Geo. Res.,* Vol. 87, No. C7, 1982, pp. 5785–5795.

Schumacher, J. D., and T. H. Kinder, "Low Frequency Current Regimes over the Bering Sea Shelf," *J. Phys. Oceano.,* Vol. 13, 1983, pp. 607–623.

Schumacher, J. D., K. Aagaard, and R. B. Tripp, "Effects of a Shelf Polynya on Flow and Water Properties in the Northern Bering Sea," *J. Geo. Res.,* Vol. 88, No. C5, 1983, pp. 2723–2732.

Schumacher, J. D., S. A. Macklin, and L. S. Ineze, *Background and Research Plan for the Northwest Gulf of Alaska Fishery Oceanography Experiment,* Pacific Marine Environmental Lab., NOAA/PMEL-734, 1984, Seattle, Washington, 1984.

Schutz, C., *Synoptic Performance Characteristic of the Two-Level Atmospheric Model,* The RAND Corporation, R-1689-ARPA, August 1975.

Schutz, C., and W. L. Gates, *Global Climatic Data for Surface, 800MB, 400MB: January,* The RAND Corporation, R-915-ARPA, November 1971.

Schutz, C., and W. L. Gates, *Global Climatic Data for Surface, 800MB, 400MB: July,* The RAND Corporation, R-1029-ARPA, November 1972.

Schutz, C., and W. L. Gates, *Global Climatic Data for Surface, 800MB, 400MB: April,* The RAND Corporation, R-1317-ARPA, December 1973.

Schutz, C., and W. L. Gates, *Global Climatic Data for Surface, 800MB, 400MB: October,* The RAND Corporation, R-1425-ARPA, March 1974.

Schwiderski, E. W., *Global Ocean Tides,* TR-3866, Surface Weapons Center, Dahlgren, Virginia, 1978.

Semenov, Y. V., and B. M. Taran, "Numerical Model of the Wind Drift of Ice, Taking into Account the Appearance of Zones of Maximum Solidity," *Izvestiya, Atmo. and Oceanic Physics,* Vol. 18, No. 9, 1982, pp. 775–778.

SethuRaman, S., and J. Tichler, "Statistical Hypothesis Tests of Some Micrometeorological Observations," *J. Appl. Meteor.,* Vol. 16, No. 5, 1977, pp. 455–461.

Smith, O. E., "Application of Distribution Derived from the Bivariate Normal Density Function," *Probability and Statistics in Atmospheric Sciences,* Proc. of Int. Sym. held in Honolulu, Hawaii, 1971, p. 162–168.

Stern, M. E., "The 'Salt Fountain' and Thermohaline Convection," *Tellus*, Vol. 12, 1960, pp. 172–175.

Stern, M. E., and J. S. Turner, "Salt Fingering and Convective Layer," *Deep Sea Res.*, Vol. 16, 1969, pp. 497–511.

Stringer, W. J., and G. L. Hufford, "Interaction of Bering Sea and Norton Sound Pack Ice," *Arctic and Alpine Research*, Vol. 14, No. 2, 1982, pp. 149–156.

Stringer, W. J., and R. D. Henzler, "Norton Sound Ice Floe Trajectories Observed Between March 29 and 31, 1976," *Proc. Syn. Meeting, The Norton Sound Environment and Possible Consequences of Planned Oil and Gas Development*, NOAA, Anchorage, Alaska, February 1982.

Stringer, W. J., J. E. Groves, R. D. Henzler, L. K. Schreurs, and J. Zender-Romick, "Ice Concentration in the Eastern Beaufort Sea," *Geophys. Inst. Rep.*, University of Alaska, Fairbanks, Alaska, 1982.

Stroop, D. V., *Report on Oil Pollution Experiments, Behavior of Fuel Oil on the Surface of the Sea*, U.S. Department of Commerce, Bureau of Standards, Washington, D.C., 1927.

Sunderman, J., "The Semi-Diurnal Principal Lunar Tide M2 in the Bering Sea," *Deutsche Hydrographische Zeitschrift*, Vol. 30, 1977, pp. 91–101.

Tait, R. I., and M. R. Howe, "Thermocline Staircase," *Nature*, Vol. 231, 1971, pp. 178–179.

Takenouti, A. Y., and K. Ohtani, "Currents and Water Masses in the Bering Sea: A Review of Japanese Work," in D. W. Hood and E. J. Kelley (eds.), *Oceanography of the Bering Sea with Emphasis on Renewable Resources*, University of Washington, Seattle, Washington, 1974.

Thorndike, A. S., and R. Colony, "Sea Ice Motion in Response to Geostrophic Winds," *J. Geophys. Res.*, Vol. 87, No. C7, 1982, pp. 5845–5852.

Tripp, R. B., L. K. Coachman, K. Aagaard, and J. D. Schumacher, "Low Frequency Components of Flow in the Bering Strait System," American Geophysical Union Meeting, Seattle, Washington, September 1978.

Tuller, S. E., and A. C. Brett, "The Characteristics of Wind Velocity That Favor the Fitting of a Weibull Distribution in Wind Speed Analysis," *J. Climate and Appl. Meteor.*, Vol. 23, 1984, pp. 124–134.

Turner, J. S., "Salt Fingers Across a Density Interface," *Deep Sea Res.*, Vol. 14, 1967, pp. 599–611.

U.S. Navy Fleet Weather Facility, *Arctic Sea Ice Analyses 1972–1975*, Suitland, Maryland, 1979.

Uzuner, S., F. Weiskopf, J. Cox, and L. A. Schultz, *Transport of Oil Slicks Under a Uniform Smooth Ice Cover*, Environmental Protection Agency, Report No. EPA-600/3-79-041, Corvallis, Oregon, April 1979.

Van Bebber, W. J., "Die Zugstrassen der baromefrischen Minima nach den Bahnenkarten der Deutschen Seewarte fur den Zeitraum," *Met. Zeit., Vol. 8, 1891, pp. 361–366.*

Van Bebber, W. J., and W. Koppen, "The Isobaric Type of the North Atlantic Ocean and the Western Europe" (in German), *Arch. dtsch. Seewarte*, Hamburg, Vol. 18, 1895.

Verrall, K. A., and R. L. Williams, "A Method for Estimating the Standard Deviation of Wind Directions," *J. Appl. Meteor.*, Vol. 21, 1982, pp. 1922–1925.

Walter, B. A., J. E. Overland, and R. O. Gilmer, "Air-Ice Drag Coefficients for First Year Sea-Ice Derived from Aircraft Measurements," *J. Geophy. Res.*, Vol. 89, No. C3, 1984, pp. 3550–3560.

Weeks, W. F., and G. Weller, "Offshore Oil in the Alaskan Arctic," *Science*, Vol. 225, No. 4660, 1984, pp. 371–378.

Wiseman, W. J., and L. J. Rouse, Jr., "A Coastal Jet in the Chukchi Sea," *Arctic*, Vol. 33, 1980, pp. 21–29.

Whittmann, W., and J. J. Schule, "Comments on the Mass Budget of Arctic Pack Ice," in J. O. Fletcher (ed.), *Proc. of Symposium on Arctic Heating Budget and Atmospheric Circulation*, The RAND Corporation, RM-5233-NSF, December 1966.

Wu, J., "Wind Stress Coefficients over Sea Surface from Breeze to Hurricane," *J. Geophys. Res.*, Vol. 87, 1982, pp. 9704–9706.

Zeman, O., and J. L. Lumley, "Modeling Salt-Fingering Structures," *J. Mar. Res.*, Vol. 40, No. 2, 1982, pp. 315–330.

Zisman, W. A., "The Spreading of Oil on Water," *J. Chem. Physics*, Vol. 9, 1941, pp. 789–793.